From Photonic Crystals to Photonic Glasses through disorder

(De los cristales fotónicos a los vidrios fotónicos a través del desorden)

Memoria presentada para optar al grado de Doctor en Física por:

Pedro David García Fernández

Tesis dirigida por:

Prof. Dr. Ceferino López Fernández

Tutor:

Prof. Dr. José Manuel Calleja Pardo

Departamento de Física de Materiales
Facultad de Ciencias
Universidad Autónoma de Madrid

Insituto de Ciencia de Materiales de Madrid
Consejo Superior de Investigaciones Científicas

Diciembre de 2008

Summary

This thesis is the result of a four-year doctorate on light propagation and emission though complex systems, done in the Material Science Institute of Madrid (which belongs to the national research council, CSIC) and Unidad Asociada CSIC-Vigo University under the supervision of Prof. Dr. Ceferino López. All the samples studied so far in this thesis have been grown at the ICMM laboratory as well as the static optical measurements and the experiments on resonant random and ZnO lasing. ZnO refractive index contrast was measured by ellipsometry with the help of Dr. R. Serna, from Institute of Optics-CSIC. Dynamic measurements performed with the streak camera were done in the laboratory of ultrafast spectroscopy at the Materials Physics Department-UAM with the collaboration of Prof. Dr. L. Viña. Dynamic measurements performed with the optical gating technique are the result of an international scientific exchange of four months in the Laboratory for non-linear spectroscopy in Florence (LENS) under the supervision of Dr. D. S. Wiersma. The quantum dots used in chapter 4 were provided by Dr. N. Gaponik from the Technical University of Dresden, also as an international collaboration. Scanning electron microscopy from ZnO inverse opals was performed at the Vigo University with the help of Prof. Dr. Luis Liz. The international collaborations with Dr. D. Wiersma and Dr. N. Gaponik are result of the fruitful scientific European Network of excellence *Phoremost*. The work described in this thesis has been published in the following papers:

- *Density of states governs light scattering in photonic crystals*
  P. D. Garcia, R. Sapienza, L. S. Froufe-Perez, C. Lopez, arXiv:0811.4494 (2008).

- *Resonant light transport through Mie modes in Photonic Glasses.*
  P. D. Garcia, R. Sapienza, J. Bertolotti, M. D. Martin, A. Blanco, A. Altube, L. Viña, D.S. Wiersma, C. Lopez, Phys. Rev. A, **78**, 023823 (2008).

- *Resonance-driven random lasing.*
  S. Gottardo, Riccardo Sapienza, P. D. Garcia, A. Blanco, D. S. Wiersma, C. Lopez, Nature Photonics, **2**, 429 (2008). Cover letter.

- *Observation of Resonant Behavior in the Energy Velocity of Diffused Light.*
  R. Sapienza, P. D.Garcia, J. Bertolotti, M. D. Martin, A. Blanco, L. Viña, C. Lopez, D. S. Wiersma, Phys. Rev. Lett. **99**, 233902 (2007).

- *Photonic Glass: a novel random material for light.*
  P. D. García, R. Sapienza, A. Blanco, C. López, Adv. Mater. **19**, 2597, (2007).

- *Quantum dot thin layers templated on ZnO inverse opals.*
  P. D. Garcia, A. Blanco, A. Shavel, N. Gaponik, A. Eychmüller, B. Rodríguez, L. Liz, C. López, Adv. Mater. **18**, 2768 (2006).

- *Optical study of Gamma-L high energy photonic pseudogaps in ZnO Inverted Opals.*
  P. D. Garcia, C. López, J. Appl. Phys. **99**, 046103 (2006).

- *Tuning and optical study of the Gamma-X and Gamma-L photonic pseudogaps in opals.*
  P. D. Garcia, J. F. Galisteo-López, C. López, Appl. Phys. Lett. **87**, 201109 (2005).

- *ZnO inverse opals by chemical vapour deposition.*
  B.H. Juárez, P. D. Garcia, D. Golmayo, A. Blanco, C. López, Adv. Mater. **17**, 2765 (2005).

Hunc igitur terrorem animi tenebrasque necessest non radii solis neque lucida tela diei discutiant, sed naturae species ratioque

Este terror, pues, y estas tinieblas del espíritu, necesario es que las disipen, no los rayos del sol ni los lúcidos dardos del día, sino la contemplación de la naturaleza y la ciencia.

Our terrors and our darknesses of mind must be dispelled, not by the sunshine's rays, not by those shining arrows of the light, but by insight into nature, and a scheme of systematic contemplation.

TITUS LUCRETIUS CARUS, *De rerum natura*, (I, 146-148)

DON'T PANIC!!

COLDPLAY, *Parachutes.*

A la memoria de mi padre.

A mi madre.

Contents

Chapter 1

Introduction

In the early 1800s, the double-slit experiments performed by Young and Fresnel provided strong evidence for wave-like nature of light [1]. This happened more than a century before L. de Broglie established that all matter, in particular the electron, has also a wave-like behavior [2]. Despite the time delay between both statements, solid state physics has motivated important goals in the field of light transport though complex dielectric media. These materials are dielectric structures in which the dielectric function varies on length scales comparable to the wavelength of light. The analogy is carried out by substituting matter waves for classical waves and electrostatic potential for dielectric function. Two paradigmatic examples suggested by this analogy between photons and electrons are photonic crystals [3, 4] and *Anderson* localization of light [5, 6, 7].

The control of light transport is crucial not only to solve fundamental questions but also to design and tailor new photonic devices for optical performance in the same manner as governing electron transport gave rise to the semiconductor and electronic technology. Nevertheless and contrary to what happens with atomic crystals which are provided by nature very efficiently, optical science and technologies had to exploit natural optical materials and engineer new devices from them. In the last years a new frontier has emerged, with the goal of controlling light propagation through interference in artificially engineered optical materials and metamaterials. An extraordinary progress has been made in the fabrication of nano-photonic structures, with many novel optical properties. While (ordered) periodic photonic media, i.e. photonic crystals, take advantage of the periodicity in the dielectric constant and the consequent long-range correlation to mold the flow of light, disordered ones, with no positional order, can still strongly affect light transport [8]. Furthermore, photonic materials with structures between order and disorder have been for the first time accessible, and are widely studied.

Figure 1.1**a** schematizes the interplay between order and disorder in dielectric complex media. With the same building block, a dielectric sphere with size comparable to the wavelength of light, two extreme systems can be built: a perfectly ordered arrangement (a so-called photonic crystal) and a completely ran-

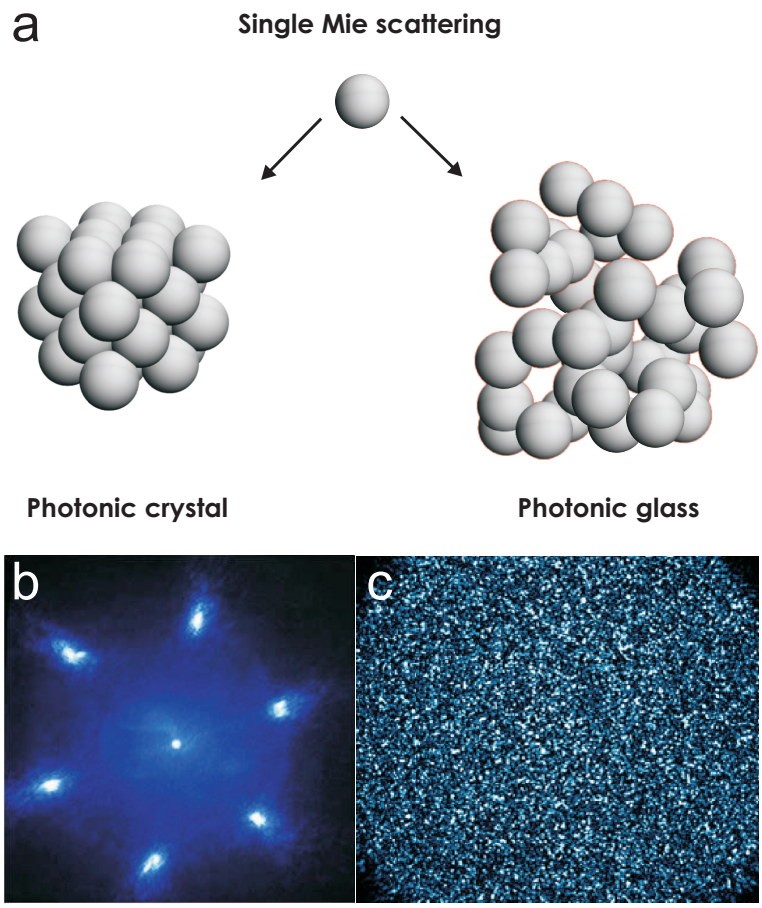

Figure 1.1: **(a)** Ordered and disordered packing of a single-scattering building block, a dielectric sphere in this case. **(b)** and **(c)** Light speckle pattern arising from an ordered fcc arrangement of dielectric microspheres and from a random arrangement of the same spheres, respectively and collected on a far field screen.

dom arrangement of spheres (a so-called photonic glass). Figure 1.1**b** shows the light speckle pattern from an ordered fcc arrangement of microspheres (photonic crystal) and figure 1.1**c** shows the same physical phenomenon from a random arrangement of the same microspheres (photonic glass). In the ordered case, the speckle pattern adopts a particular distribution due to the underlaying lattice structure.

This introduction will briefly show the principles of light scattering with nanostructured dielectrics. Contrary to common introductions, which provide a state of the art in nanophotonics, this introduction wants to give the basic tool and a general view to the field of light scattering with ordered and disordered complex systems. Fundamental concepts related to single light scattering as the scattering matrix and the scattering cross section will be shown firstly. In this thesis the fundamental building block is the dielectric sphere; for this reason, the solution to the Maxwell equations for such scatterer will be briefly

explained. Then, we will move into the more complicated topic of multiple scattering, both through disordered and ordered nanostructures. In the first case, we will approach this complicated issue with a diffusion approximation, neglecting interference effects in a first approximation, which accounts fairly well for the systems analyzed in this thesis. On the contrary, lith interference is at the heart of multiple scattering of light in photonic crystals. It will be seen how this fact has strong consequences on the light dispersion relation and the electromagnetic density of states, which can be engineered very efficiently in photonic crystals to perform the desired optical performances. Light emission and light transport are strongly affected by this facts.

The aim of this thesis, its motivation, is to obtain and to show how disordered dielectric nanostructures are also able to control the flow of light but, at the same time, how the introduction of disorder in an, otherwise, perfectly ordered structure in a controlled manner increases it performances. The interplay between order and disorder in dielectric nanostructures is at the basis of this thesis.

1.1. Single light scattering

Light propagates along straight lines from the luminous body to the body illuminated and bends or breaks those lines (scatters) *when passing out of one medium into another* [9]. As pointed by Newton, light scattering is a basic phenomenon in light transport. Furthermore, it is nearly impossible to observed the light directly from its source. Most of the light emitted by a source is spread out due to scattering and reaches our eyes in an indirect way. The straight propagation of light is disturbed by inhomogeneities or a change in the speed of light. The speed of light in a medium is characterized though the refractive index n, which is defined as the ratio between the speed of light in vacuum and in the medium. An interface between two media gives rise to a deviation in light direction of propagation, due to the different refractive index of the media. A scatterer is an inhomogeneity in an overall homogenous medium. The interaction of light with a scatterer is a scattering event, which in this thesis will be only considered to be elastic: the scattering event only changes the light wavevector but not light energy.

The regime in which light interacts only once with a scatterer is called single scattering. When a (sound, electromagnetic, matter, etc) wave scatters with an object, the whole physical process can be express as follows:

$$\psi_{scatt}(\overrightarrow{r}) = \mathbf{S}\psi_0(\overrightarrow{r}) \tag{1.1}$$

where the scattering matrix, $\mathbf{S}$, transforms the incident wave into the scattered wave. The elements of the scattering matrix, the so-called scattering amplitude functions s_i, are all complex functions that depend on the directions of incidence and scattering and on the particle size and morphology. The scattered wave in the far field is a spherical, outgoing wave which amplitude can be expressed in terms of the scattering amplitudes as:

$$E_{scatt}(\overrightarrow{r}) = s\frac{e^{ikr}}{r}E_0(\overrightarrow{r}) \tag{1.2}$$

and also for the magnetic field components whose states that light emitted from the scatterers is a superposition of spherical waves. The, so-called, Stokes parameters (I, Q, U, V) are a complete set of quantities expressed in terms of the components of the EM fields which completely characterize the intensity and state of polarization of a light beam. In particular, the first stoke parameter, I, is the intensity of the field, the energy flow per unit area. Any given transformation process of the field as, for example, a scattering process, can be expressed as:

$$(I, Q, U, V) = \mathbf{F}(I_0, Q_0, U_0, V_0) \tag{1.3}$$

where $\mathbf{F}$ is a transformation matrix which elements are expressed in terms of those of the scattering matrix, $\mathbf{S}$. Without entering in detail about the relationship between $F_{i,j}$ and s_i (which, otherwise, can be found in [10]), in the particular case of spherical particles, the off-diagonal scattering matrix elements are null and the scattered intensity can be written as:

$$I_{scatt} = \frac{d\sigma}{d\Omega}I_0 = \frac{\Sigma_i|s_i(\theta,\phi)|^2}{2k^2r^2}I_0 \tag{1.4}$$

Under energy conservation, let the total energy scattered in all directions be equal to the energy of the incident wave falling on the area σ, the so-called scattering cross-section:

$$\sigma = \frac{1}{2k^2}\int \Sigma_i|s_i(\theta,\phi)|^2 d\Omega \tag{1.5}$$

where the differential cross-section is, then:

$$\frac{d\sigma}{d\Omega} = \frac{\Sigma_i|s_i(\theta,\phi)|^2}{2k^2} \tag{1.6}$$

This magnitude is of paramount importance since it contains all the information related to the scattering process, it indicates in which directions the wave scattering is more efficient.

According to the relative ratio between the scatterer size and the light wavelength (λ), different scattering scenarios can be described. If the scatterer size is much smaller than λ, the *Rayleigh* scattering amplitudes depend only on the particle polarizability (α) and on light frequency, ω, as:

$$\sigma = \frac{2}{3}\frac{\omega^4}{c^4}\frac{|\alpha|^2}{4\pi} \tag{1.7}$$

where c is the vacuum speed of light. A detailed discussion about this kind of scattering can be found in [10].

When the scatterer size is comparable to λ, the scattering is in the, so-called, *Mie* regime and can be solved analytically in the case of a spherical scatterer. Scattering in this regime is resonant and anisotropic and, since all the scatterers analyzed in this thesis are Mie dielectric spherical scatterers, it is of paramount

importance to understand, at least briefly, the fundamentals of the solution proposed by Mie to the Maxwell equations. In the following, by Mie sphere it should be understood a dielectric sphere scatterer with size comparable to the wavelength of light.

For completeness it will be mentioned that the final scattering regime is that one called geometrical optics, when the scatterer size is much larger than the light wavelength. Geometric optics, or ray optics, describes light propagation in terms of *rays* which are defined to be perpendicular to the wavefronts of the actual optical waves. Geometric optics provides rules for propagating these rays through an optical system, which indicates how the actual wavefront will propagate. This is a significant simplification of optics, and fails to account for many important optical effects such as diffraction and polarization.

1.1.1. Mie solution to the Maxwell's equations

The main scatterer analyzed in this thesis is a dielectric sphere. It will appear in random arrangements as well as in ordered structures. It is capital, therefore, to understand the underlying physics of light-sphere interaction before going a step beyond into the ensemble. The Maxwell equations in absence of free charges of currents may be expressed as:

$$\begin{aligned} \nabla \times \mathbf{H}(\mathbf{r},t) - \frac{1}{c}\frac{\partial \mathbf{D}(\mathbf{r},t)}{\partial t} = 0, \qquad & \nabla \cdot \mathbf{B}(\mathbf{r},t) = 0 \\ \nabla \times \mathbf{E}(\mathbf{r},t) + \frac{1}{c}\frac{\partial \mathbf{B}(\mathbf{r},t)}{\partial t} = 0, \qquad & \nabla \cdot \mathbf{D}(\mathbf{r},t) = 0 \end{aligned} \tag{1.8}$$

A complete and comprehensive derivation of the Mie solution to these equations can be find in [10]. Here, the basic results will be briefly shown. The modes of a spherical dielectric particle were first investigated by Mie at the beginning of the 19th century, in the context of light scattering from small spherical metal particles [11]. These optical modes are confined by continuous total internal reflection at the sphere-air interface and are often referred to as whispering-gallery modes. This description was originated from the *problem of the whispering-gallery* which Lord Rayleigh published in early 20th century [12] describing the phenomenon of acoustical waves he had observed propagating around the interior gallery of the Saint Paul's Cathedral dome. When plane-polarized light of frequency ω is incident on a dielectric sphere, a resonant situation is possible whenever ω matches the frequency of an EM eigenmode of the sphere. These eigenmodes are spherical waves labelled by two integer numbers, just as in the case of electronic quantum orbitals in atoms, and are generally electric or magnetic oscillating multipoles. Sourceless Maxwell equations for harmonic EM fields can be calculated exactly for the spherical scatterer by solving the fully retarded vector Helmholtz equation in spherical coordinates.

$$(\nabla^2 + n^2 k^2)\Phi = 0 \tag{1.9}$$

where n is the refractive index, $k = \omega/c$ is the wavevector, Φ represents either the electric field $\mathbf{E}$ or the magnetic field $\mathbf{H}$. A common route to obtain a general

solution to the vectorial equation is to obtain a solution to the scalar Helmholtz equation, ψ, and then generate two independent, zero-divergence and orthogonal solutions as:

$$\begin{aligned} \mathbf{U}_\psi &= \nabla \times (\mathbf{r}\psi) \\ \mathbf{V}_\psi &= \frac{\nabla \times \mathbf{U}_\psi}{nk} \end{aligned} \tag{1.10}$$

The generating function ψ, solution to the scalar Helmholtz equation obtained with the variable separation method, is a linear combination of Legendre polynomials, $P_m^l(\cos\theta)$, and spherical Bessel functions, $z_m(x)$:

$$\psi_{l,m} = \begin{pmatrix} \cos(l\theta) \\ \sin(l\theta) \end{pmatrix} P_m^l(\cos\theta) z_m(nkr) \tag{1.11}$$

where l and m are integer numbers which satisfy $l \geq m \geq 0$.

Finally, two possible solutions to the Maxwell equations can be generated by a linear combination of vector harmonics $\mathbf{U}_\psi$ as:

$$\begin{aligned} \mathbf{E} &= \mathbf{U}_\psi + i\mathbf{V}_\mu \\ \mathbf{H} &= n(-\mathbf{U}_\mu + i\mathbf{V}_\psi) \end{aligned} \tag{1.12}$$

The problem to find solutions to the Maxwell equations in this specific case reduces to the simpler problem of finding two solutions, ψ and μ, to the scalar Helmholtz equation. The full solution is analytic but expressed in the form of infinite series of spherical harmonics.

The spherical components of both fields in the far field ($r \to \infty$) can be expressed as a combination of spherical harmonics:

$$\begin{aligned} E_\theta(r,\theta,\phi) &= s_2(\theta)\frac{e^{ikr}}{kr}E_0\cos\phi &&= s_2(\theta)\frac{e^{ikr}}{kr}E_\theta^0(r,\theta,\phi) \\ E_\phi(r,\theta,\phi) &= -s_1(\theta)\frac{e^{ikr}}{kr}E_0\sin\phi &&= s_1(\theta)\frac{e^{ikr}}{kr}E_\phi^0(r,\theta,\phi) \\ E_r(r,\theta,\phi) &= 0 \end{aligned} \tag{1.13}$$

and analogously for the components of the magnetic field $\mathbf{H}$. According to equation 1.2, $s_i(\theta)$ are the scattering amplitudes:

$$
\begin{aligned}
s_1(\theta) &= \sum_{m=1}^{\infty} \frac{2m+1}{m(m+1)} [a_m \zeta_m(\cos\theta) + b_m \xi_m(\cos\theta)] \\
s_2(\theta) &= \sum_{m=1}^{\infty} \frac{2m+1}{m(m+1)} [b_m \zeta_m(\cos\theta) + a_m \xi_m(\cos\theta)]
\end{aligned}
\tag{1.14}
$$

where a_m, b_m, ζ_m and ξ_m are also linear combinations of Legendre polynomials and Bessel functions [10]. In particular, $a_m(x,y)$, $b_m(x,y)$, where the arguments $x = \pi d/\lambda$ and $y = \pi n d/\lambda$ (d is the sphere diameter) define the dependence of the EM modes on the ratio nd/λ. These modes, defined by $\mathbf{E}_{l,m}(r,\theta,\phi)$ and $\mathbf{H}_{l,m}(r,\theta,\phi)$, are the EM eigenmodes of a dielectric sphere. Figure 1.2 shows the modulus of the scattered EM field for a sphere with diameter d at two different energies ($\lambda \simeq d$) [13]. These resonant electromagnetic modes in dielectric spheres are analogous to electronic orbitals in atoms [14]. The field confinement in the sphere depends on the ratio $d \cdot n/\lambda$ and is stronger when $d \cdot n/\lambda$ increases (higher energies). It is worth to mention that when increasing the refractive index of the sphere, also the EM field confinement increases.

The total scattering cross section can be calculated from equation 1.5 and 1.14 as:

$$
\sigma_{tot} = \frac{1}{2k^2} \int S(\theta,\phi) d\Omega = \frac{2\pi}{k^2} \sum_{m=1}^{\infty} (2m+1) \Re(a_m + b_m) \tag{1.15}
$$

which is the analytical solution to the scattering problem of a plane-wave and a dielectric sphere.

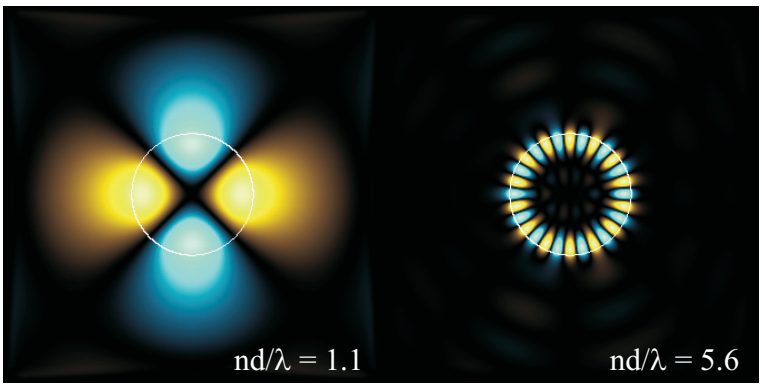

Figure 1.2: Modulus of the scattered EM field for a sphere diameter $d = 1100$ nm and refractive index $n = 3.4$ in the case of low $(d/\lambda = 0.33)$ and high energy $(d/\lambda = 1.65)$. The confinement of the mode in the spheres increases with the field energy.

1.2. Multiple light scattering in random systems

In the previous section we have treated the problem of single light scattering in the particular case that the scatterer is a dielectric sphere. As pointed by Newton, when light propagates from the source to the detector it does it in a straight line (apart from general relativity corrections). In that case, light propagation is said to be straight or ballistic and is the characteristic propagation regime through a homogenous medium. Nevertheless, when light travels through a very disordered system it is multiply scattered. Straight or ballistic propagation cannot accurately describe the transport of light. The multiple scattering process can be intuitively distinguished from the ballistic transport in the following example. When light propagates though the two systems shown in figure 1.3, it undergoes two different regimes of transport. In the first case (**1**), apart from a small absorption (inelastic scattering) revealed in the change of color of white light impinging the system, light does not scatter with the medium. The boundaries between medium (**1**) and air are the unique source of elastic scattering. If we, for example, place a piece of paper with something written there, we are able to read it if we place the paper on the other side of medium (**1**). Light is said to follow a ballistic transport since it does not change its direction of propagation. On the contrary, when light propagates through the second medium (**2**), it performs a very complicated multiple scattering process before escaping the system. It undergoes a random walk and, if the scattering strength is not very high (relatively low refractive index contrast between the materials which compose the system) the whole transport regime can be accurately described as a diffusion process. In that case, interference effects can be obviated in a first approximation. Light entering in such medium is scattered numerous times and when it emerges from the material conserves of the color of the incident light, whatever the incident direction. Since ambient light is visible (contains all the wavelengths of the visible spectrum), the diffusive medium appears white. All white materials owe their color to multiple light scattering. We will here briefly review the standard diffusion model used to quantitatively describe light transport in an isotropic random dielectric medium.

1.2.1. Diffusion approximation

The multiple scattering of light has a very complicated solution in terms of Maxwell equations when many scatterers have to be taken into account. A model to solve this problem is the radiative transfer equation of the dilute medium where phase and light interference are neglected. The solution of the radiative transfer equation can be considerably simplified by introducing further approximations. The diffuse approximation considers a random walk of photons and imposes a continuity equation for the light intensity $I(\mathbf{r}, t)$ disregarding interference effects. Propagation of light can, therefore, be viewed as a diffusion process such as gasses diffuse in a partial pressure gradient. The most important parameter is the scattering mean free path, ℓ_s, which is the average distance between two consecutive scattering events. This parameter sets the limits of the diffusive approximation

as: $\lambda << \ell_s << L$ (many scattering events occur before the light leaves the system, where L is the system size, hereafter sample thickness) and $k \cdot \ell_s >> 1$ (limits the approximation to a dilute medium, where k is the light wave vector). After several scattering events, the light propagation is completely randomized. The transport mean free path, ℓ_t, is defined as the average distance after which the intensity distribution becomes isotropic and is the characteristic length in the regime of multiple scattering. The transport of ballistic or unscattered light in such a medium in space (r) and time (t) is dictated by Lambert-Beer equation, $I(\mathbf{r},t) = I(0,t) \cdot exp(-\mathbf{r}/\ell_s)$, while diffuse light propagates according to the diffusion equation as follows:

$$\frac{\partial I(\mathbf{r},t)}{\partial t} = \mathcal{D}\nabla^2 I(\mathbf{r},t) - \frac{\nu_e}{\ell_i} I(\mathbf{r},t) + S(\mathbf{r},t) \tag{1.16}$$

where $S(\mathbf{r},t)$ is the light source, v_e is the velocity of the energy [66, 67] and ℓ_i is the absorption length, over which light is attenuated by a factor e^{-1}. The diffusion equation is a very general and practical description of numerous transport processes in physics: an ink droplet in a glass of water, the particles of a gas in a pressure gradient, the neutrons in a nuclear reactor. In the particular case of light diffusion, it describes how light intensity spreads through the system with a rate of transport dictated by the diffusion constant, $\mathcal{D}$. The larger the diffusion constant, the faster the transport process. The whole diffuse transport may be truncated by absorption, which is introduced in the diffusion equation through the inelastic scattering term $\tau_i = \nu_e/\ell_i$, where the inelastic or absorption time τ_i is the characteristic time over which light is absorbed in the sample.

As previously explained, usually, disordered media are opaque and white, i.e. non dispersive. In such a disordered medium, the group velocity can only be associated with the ballistic (or unscattered) component, and therefore cannot

Figure 1.3: Ballistic light transport (**1**) and multiple scattering transport (**2**) are shown in this figure.

be applied to describe the transport of energy, which, for large enough optical thicknesses, is governed by the scattered light. When this regime of diffusive propagation is set up, not only phase but also group velocity fail to give an account of light transport and a new quantity describing the transport of energy in the new diffusive regime is required. The velocity of the scattered light propagation inside disordered media needs to be defined by the velocity of the transported energy and is given by the ratio of the energy flux to the energy density in any point of the sample. This, in general, is very complex and given neither by the group velocity nor the phase velocity [66, 67]. Transport parameters and, in particular, energy velocity must be drastically altered in the presence of scattering resonances: in an extreme case of light diffusion in a cold atomic cloud, the atomic energy spectrum can be so resonant to the incident light, that the energy velocity can be as low as few thousands meter per second ($v_e/c \sim 10^{-5}$) [144].

Multiple scattering increases the interaction between light and the system. When the material which composes the system presents absorption, its effect is increased in a diffusive propagation. The inelastic absorption length, ℓ_i, is the average depth which light propagates ballistically (straight forward) in an homogeneous medium before being attenuated by a factor e. The diffusive absorption length, ℓ_a, is the distance light propagates diffusively before being absorbed. Inside a diffusive and absorbing material, ℓ_a is the penetration depth of the diffuse light. Diffuse light propagates a greater distance than in a homogeneous material to reach the same depth. For this reason, ℓ_a is shorter than ℓ_i. However, both are not independent functions but are related to ℓ_t as [8]:

$$\ell_a = \sqrt{(\ell_t \cdot \ell_i)/3} \tag{1.17}$$

The experimental systems treated in this work have a slab geometry which imposes certain boundary conditions on the diffusion equation: the system can be considered infinite for x and y directions and limited between $z = 0$ and $z = L$. An incident plane wave is originated at $z = -\infty$ and, due to multiple scattering, decays exponentially inside the system according to Lambert-Beer equation. Dirichlet Boundary conditions to the diffusion equation are:

$$I(z) = 0 \quad at \begin{cases} z = -z_{e1} \\ z = L + z_{e2} \end{cases} \tag{1.18}$$

where $z_{e1,2}$ are the extrapolation lengths, of the order of ℓ_s, which are the positions where the diffusive light intensity would be zero if the light source would be placed inside the system and, eventually, may be different at the front and back surfaces (if their reflectivities are different).

1.2.2. Stationary solution

Within the diffusion approximation, only diffusive light can be handled and therefore, an incident plane wave can not be inserted as source in the diffusion equation: it decays exponentially inside the system. The incoming coherent flux is replaced by a source of diffusive radiation at the plane $z = z_p$, where z_p is the so-called penetration length. A common phenomenological way to introduce a source

[15] is to consider or an exponentially decaying one, $S(z) = S(0) \cdot exp(-z/z_p)$ or a delta one, $S(z) = S(0) \cdot \delta(z - z_p)$.

The solution of the stationary diffusion equation with boundary conditions 1.18 and for a delta source leads to the total transmission of light through a photonic glass slab given by [16]:

$$I(z) = I(z_p) \begin{cases} sinh[\alpha(z_e + z)]/sinh[\alpha(z_p + z_e)] & z < z_p \\ sinh[\alpha(L + z_e - z)]/sinh[\alpha(L + z_p + z_e)] & z > z_p \end{cases} \tag{1.19}$$

where

$$\begin{aligned} I(z_p) &= \frac{S(0)}{\alpha \mathcal{D}} \frac{sinh[\alpha(z_p + z_e)] sinh[\alpha(L + z_e - z_p)]}{sinh[\alpha(L + 2z_e)]} \\ z_e &= \frac{1}{2\alpha} \ln[\frac{1 + \alpha z_0}{1 - \alpha z_0}] \\ z_0 &= \frac{2}{3} \ell_t(\lambda) \left(\frac{1 + R}{1 - R} \right) \end{aligned} \tag{1.20}$$

In the solution, $\alpha = 1/\ell_i$ is the inverse absorption length and R is the polarization and angular averaged reflectivity of the boundaries [17]. Figure 1.4 reproduces the solution to the stationary diffusion equation, $I(z)$, assuming an exponential source (full line) and a delta source (dashed line) for a slab geometry system with the parameters related to the diffusion equation such as z_e and z_p, which are typically set to be identical ($z_e = z_p$).

A very important function to take into account is the total transmission of light integrated over all the angles, which is defined as the total flux at $z = L$ divided by the incident flux $S(0)$ [16]:

$$T(L, \lambda) = \frac{1 - R}{\alpha} \frac{\sinh[\alpha(z_p + z_e)] \sinh[\alpha z_e)]}{\sinh[\alpha(L + 2z_e)]} \tag{1.21}$$

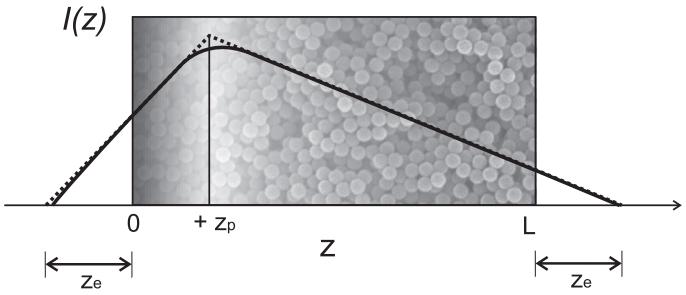

Figure 1.4: Plot of the light intensity vs. distance in a slab of a photonic glass. The full line represents the solution to the diffusion equation assuming an exponential source at $z = z_p$ whereas the dashed line represents the solution assuming a delta source placed at the same position. Extrapolation length z_e and penetration length z_p are shown.

In absence of absorption and taking into account $L \gg \ell_t$, the total light transmission 1.21 can be approximated as:

$$T(L,\lambda) \simeq \frac{2z_e}{L+2z_e} \propto \frac{\ell_t}{L} \tag{1.22}$$

where $z_e \sim \ell_t$. The total light transmission through a multiple scattering slab in the absence of absorption is directly proportional to the transport mean free path, ℓ_t, and inversely proportional to the slab thickness, $T(\lambda) \sim \ell_t(\lambda)/L$. As in electronic transport and in the absence of absorption, the optical conductance (transmission) is inversely proportional to the (optical) conductor thickness. Doubling the thickness of the (optical) conductor halves the transmission. This is known as photonic Ohm's law. The diffusion of light in a disordered dielectric slab and, in particular, a multiple scattering medium leads, therefore, to the photonic Ohm's law. With static measurements of the total light transmission through a given slab with known thickness it is possible to obtain the absolute value of the transport mean free path, ℓ_t.

1.2.3. Dynamic solution

The full solution of the time-dependent diffusion equation with boundary conditions is given by [18]:

$$\begin{aligned} T(t,\lambda) &= \frac{\exp(-t/\tau_i)}{4\,t\,(4\pi t\mathcal{D}(\lambda))^{3/2}}\,[\sum_{j=-\infty}^{+\infty} A_j \exp(-A_j^2/4\mathcal{D}(\lambda)t) \\ &- \sum_{j=-\infty}^{+\infty} B_j \exp(-B_j^2/4\mathcal{D}(\lambda)t)] \end{aligned} \tag{1.23}$$

$$\begin{aligned} A_j &= (1-2j)(L+2z_e) - 2(z_p+\ell_t) \\ B_j &= (2j+1)(L+2z_e) \\ \tau_i &= \frac{\ell_i^2}{\mathcal{D}} \end{aligned} \tag{1.24}$$

where the inelastic absorption length, $\ell_i(\lambda)$, turns into an absorption or inelastic time $\tau_i(\lambda)$. The rate of diffuse light transport in the photonic glass is defined by the diffusion constant, $\mathcal{D}$, given by Fick's law [19]. This is, therefore, a dynamic variable and a time-resolved measurement of light transmission is needed to obtain its value. The physical meaning of the summatory in equation (1.23) can be understood as follows: light which follows shorter optical paths thought the slab is transmitted at earlier times while light which performs longer random walks emerges much later. The total transmission is therefore given by the sum of all these contributions. This would produce a time-spread of an initial pulse, which depends on the diffusion constant. The behavior at long time is dominated by

the least decaying exponential, giving the time tail decay rate $\tau_d = \pi^2 \cdot \mathcal{D}/(L + z_{e1} + z_{e2})$.

1.3. Multiple light scattering in Photonic Crystals

If a light plane wave encounters a Mie sphere, a scattering process takes place as explained in previous sections. Scattering is what allow us to observe a small sphere as, for example, an air bubble embedded in a glass. If a second sphere is placed in the vicinity of the first one, the situation becomes a little bit more complicated due to interference effects between the scattered waves emerging from both scatterers. Let us imagine that these spheres have the same size comparable to the light wavelength; if we place N of these spheres close one another the process becomes unmanageable and the single scattering is replaced by a multiple scattering problem. But, in that case, an observer is still able to distinguish the spheres ensemble (as we can observe the beer foam in figure 1.3). Between all the possible position configurations of these N Mie spheres, a very intriguing and fascinating case happens when they are placed in an ordered fashion. In that very particular case, light undergoes a very peculiar propagation and, for a large interval of frequencies, the ensemble is no longer visible for an observer. The system becomes transparent for that wide energy range. But, as a consequence, there is an energy window, the so-called photonic band gap (PBG), for which the system becomes opaque. No light can propagate through the system in that frequency range. This is the case of a perfect *photonic crystal*, where the waves scattered by each sphere interfere in such a way to cause total transparency for a large energy interval with just a change in the overall energy velocity. Photonic crystals composed by Mie spheres, as all those used in this thesis, are a particular realization of such system. The underlaying lattice allow us to apply the Bloch theorem and to treat the problem of multiple scattering with the very well known formalism used in solid state physics for atomic crystals. Actually, every kind of waves (sound, electromagnetic, matter) propagating though a lattice of a particular periodic potential V give rise to the same effects. This particular potential V has a different nature in each case: electrostatic potential, V_e, for electrons in an atomic crystal, dielectric function, ε, for photons in a photonic crystal.

Due to this remarkable property, photonic crystals manipulate electromagnetic modes and control fundamental aspects of light-matter interaction: light emission [3] and light transport [4], much like semiconductors control electrons. By modifying the vacuum modes, they change the available phase space for light propagation opening frequency gaps in which propagation in some (or even all) directions is inhibited, while the density of states, $\rho(\omega)$, near the band-gap edge frequencies is increased. In addition, to the first prediction by Yablonovich, followed many experiments where redistribution and inhibition of the emission was proven [20, 21, 22] and, furthermore, interesting phenomena are observed in photonic crystals such as anomalous refraction [23], small group velocity [24] and, for certain structures, the opening of a complete photonic band gap [25].

This introduction is not thought to be a compendium of physical phenomena observed in photonic crystals nor a summary of the fabrication methods or state of the art. A recent and very useful review about that can be found in reference [26]. In this section the main properties of multiple scattering of light in photonic crystals and the basic tools and approximations to understand the propagation of light through these systems will be briefly analyzed .

1.3.1. Dispersion relation in Photonic Crystals

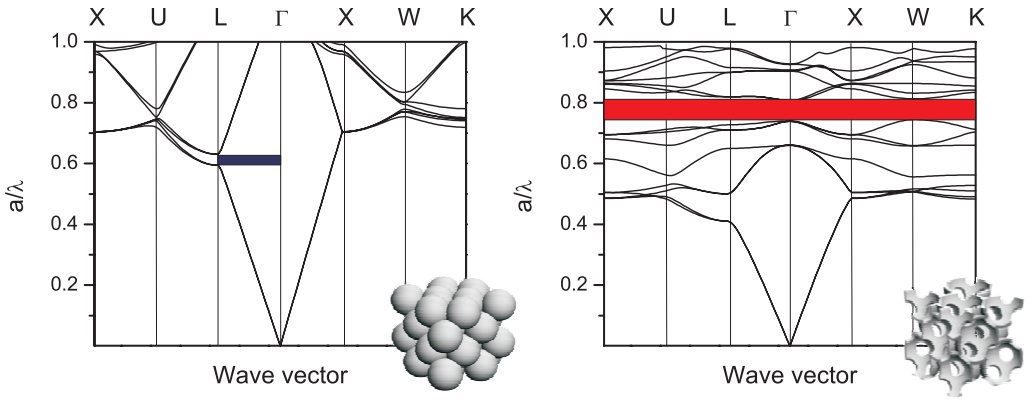

Figure 1.5: **(a)** Band structure for an fcc arrangement of dielectric spheres (n=1.6) in air, calculated along the high symmetry points defining the irreducible Brillouin zone. Pseudogap along the ΓL direction is denoted as a blue band. **(b)** Band structure for an arrangement of air spheres in a dielectric matrix (n=3.45). In this case it is possible to observe a complete photonic band gap (red band). Insets show the corresponding systems in real space.

The main property of photonic crystals is that the dispersion relation, $\omega = \omega(k)$, adopts a complicated behavior in terms of photonic bands. In the case of ordered dielectrics, the analogy with the electron propagation through an atomic crystal becomes very useful. Maxwell equations (1.8) can be combined to obtain a wave equation for any of the fields as:

$$\nabla \times [\frac{1}{\varepsilon(\mathbf{r})} \nabla \times] \mathbf{H}(\mathbf{r}) = (\frac{c^2}{\omega^2}) \mathbf{H}(\mathbf{r}) \tag{1.25}$$

This is an eigenvalue equation with eigenvetors $\mathbf{H}(\mathbf{r})$ and eigenvalues $(\frac{c}{\omega})^2$. The operator acting on $\mathbf{H}(\mathbf{r})$ is Hermitian, so the eigenvalues are real and the eigenvectors form an orthogonal set of solutions. Due to the existence of a periodic *potential*, which in the case of light waves is the periodic dielectric function $\varepsilon(\mathbf{r})$, the Bloch theorem applied to Eq. 1.25 states that:

$$\mathbf{H}_{n\mathbf{k}}(\mathbf{r}) = e^{i\mathbf{kr}} u_{n\mathbf{k}}(\mathbf{r}) \tag{1.26}$$

where k is a wave vector of the first Brillouin zone. These solutions can be expressed as a plane wave envelope function and a periodic function (periodic

Bloch function) $u_{n\mathbf{k}}$ which has the same periodicity as the potential. This fact constrains the possible eigenvectors to the first Brillouin zone and folds the dispersion relation which organizes into, so-called, bands (photonic, in this case) labelled with an integer n. Both the functions $u_{n\mathbf{k}}$ and also the *photonic potential* $\varepsilon(\mathbf{r})^{-1}$ can be expanded into Fourier series of reciprocal lattice vectors G due to periodicity:

$$u_{n\mathbf{k}} = \sum_G u_{n\mathbf{k},G} e^{iGr}, \quad \frac{1}{\varepsilon(\mathbf{r})} = \sum_G \phi_G e^{iGr} \tag{1.27}$$

The dispersion relation folded to the Brillouin zone for two different systems is shown in Figure 1.5. The fist case, corresponds to an fcc arrangement of polystyrene (PS) spheres in air background whereas the second case corresponds to an fcc arrangement of air spheres in a Silicon background. In both, the wavevector is represented in the horizontal axis while the energy is represented in the vertical axis. The wave vector tip follows a trajectory within the Brillouin zone linking high symmetry points which define its irreducible part and the energy is represented in reduced units of a/λ, where a is the lattice parameter and λ the wavelength of light in vacuum. The convenient use of such units is justified by the scalability of the solutions of the problem.

The absence of a fundamental length scale in the Maxwell equations, contrary to the case of electrons in an atomic crystal, implies that a change in the length scale of the system is translated into a corresponding change in the energy scale of the eigenvalues so that the product ωa remains fixed. For the fcc direct arrangement of spheres, figure 1.5**(a)**, it is possible to observe a frequency interval (blue band) for wavevectors lying in the ΓL direction for a reduced frequency window, $a/\lambda \sim 0.6$, where no states are available. Incoming light with wavevector lying in this crystallographic direction finds no states available to couple to. Light with energies contained in that, so-called, *pseudogap* (pG) cannot propagate through the system for this particular direction. In such a system, it is not possible to find a set of energies forbidden for all the crystallographic directions. The appearance of a so-called *photonic band gap* (PBG) requires a larger refractive index contrast $\Delta n = n_2/n_1$ and a different topology. This is achieved in the case of the inverse structure, figure 1.5**(b)**, where the high refractive index contrast is increased to 3.45 and, together with the new topology, gives rise to the opening of a complete PBG which takes place between the 8th and 9th band at reduced frequencies 0.85 (red band).

Photonic crystals are possible candidates to tailor light properties not only due to the eventual appearance of PBG but to the possibility to engineer light group velocity (the velocity at which the wave energy propagates inside the crystal). This constitutes a very fascinating and promising tool to control light propagation [27]. A novel property of photonic crystals, derived by the complicated dispersion relation, is that the light refraction in these systems obeys no more the snell law:

$$n_1 \sin\ \theta_1 = n_2 \sin\ \theta_2 \tag{1.28}$$

where n_i and θ_i are the refractive index and propagation angle inside each medium. The Snell law is a particularly simpler case of light refraction. The propagation of light from one medium (**1**) into another (**2**) gives rise to a change in the propagation direction. In the reciprocal space, the parallel components of the wave-vector must be conserved. The energy must also be conserved. Light refraction is determined by conservation of the component of the light wavevector, k, parallel to the interface between the two media and also by the dispersion surface (all the allowed wavevectors for a given frequency) in both media and according to the energy conservation. The dispersion surfaces of an homogenous medium are spheres with diameters determined by the refractive index of the medium:

$$k = \frac{\omega}{c} n \tag{1.29}$$

Figure 1.6**(a)** schematizes light refraction between two homogenous media with different refractive index. In a photonic crystal light refraction follows a more complicated behavior. Dispersion surfaces adopt very complicated shapes in these materials due to the complicated dispersion relation which light undergoes in such materials. Figure 1.6**(b)** summarizes the complicated refraction from an homogenous medium into a photonic crystal with a given dispersion surface. This is known as anomalous refraction effect [23]. The wave vector inside the second medium, a photonic crystal, k_2, is determined by the conservation of its component parallel to the interface as in the homogeneous medium case, but it is not parallel to the direction of energy propagation which, in a photonic crystal as well as in a homogenous medium, is given by the group velocity, v_g [24]:

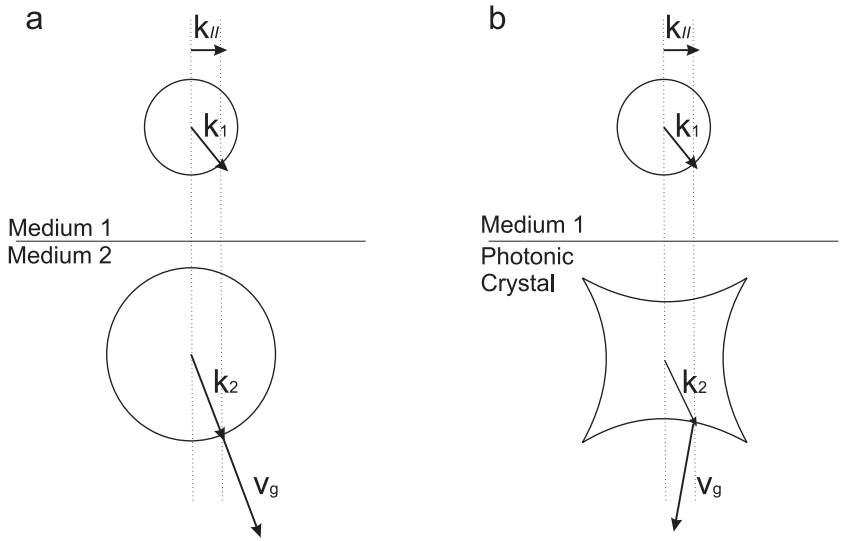

Figure 1.6: **(a)** light refraction between two homogenous media with different refractive index following the Snell law. **(b)** anomalous light refraction from a homogenous medium into a photonic crystal. Dispersion surfaces are, in the latter case, dictated by the complicated dispersion relation. Light refraction no longer obeys the Snell law.

$$\mathbf{v}_g = \nabla_k \omega \tag{1.30}$$

This magnitude is therefore directly related to the band structure of the crystal. In that case, light refraction is not accounted for by the Snell law anymore, but for the particular shape of the dispersion surface in the photonic crystal. A complementary information about dispersion surfaces and light diffraction in photonic crystals can be found in appendix A.

In photonic crystals, therefore, the group velocity can be engineered for light with a certain energy just by selecting the crystallographic direction of propagation through the system and tuning the lattice constant. If a very low group velocity is needed, photonic band edges or photonic weakly dispersive bands can be selected to that purpose and couple light to them. The group velocity associated with *flat* photonic bands becomes small [24], increasing the interaction time between electromagnetic radiation and the materials which form the crystal.

1.3.2. Density of states: light localization and spontaneous emission

The density of states *DOS* in a medium equals the density per unit volume and energy of the number of solutions to Maxwell's equations. A direct consequence of the existence of PBG in the dispersion relation of light through photonic crystals is that, for those energy intervals, the density of available electromagnetic states in the system is zero. The quantum electrodynamical implications of this fact has been widely discussed in the literature [29, 30, 31]. This effect can be engineered in photonic crystals and has two crucial implications: the first one over the spontaneous emission of an emitter placed in a PhC, the second is related to light localization in three-dimensional systems.

A complete PBG entails a complete suppression of the density of states, a modification of the electromagnetic vacuum density of states. A small impurity inside a photonic band gap material will give rise to a confined mode around this impurity, as in atomic crystals. On the other hand, the spontaneous emission of an emitter (atom, molecule, quantum dot) can be controlled and tailored by modification of the properties of the radiation field. This is due to the fact that the total radiative rate Γ of the spontaneous emission is given by the well-known Fermi golden rule:

$$\Gamma(\omega) = \frac{2\pi}{\hbar}\rho(\omega) \tag{1.31}$$

where $\rho(\omega)$ is the photon density of states. For photons in ordinary vacuum ($\omega = ck$),

$$\rho(\omega) = \frac{\omega^2}{\pi^2 c^3} \tag{1.32}$$

In the 1950s E. Purcell proposed the enhancement of spontaneous emission rates of atoms when they are matched in a resonant cavity (the Purcell Effect) [32]. A two level system will decay spontaneously by interaction with a vacuum continuum at a rate proportional to the spectral density of modes per volume

evaluated at the transition frequency. If a local source is placed in a photonic crystal with an electromagnetic band gap, which has zero local density of states, then the spontaneous emission can be rigorously forbidden [3]. Rather, a bound photon-atom state is formed [29]. This effect will occur for an emitter placed in the PhC if the transition energy lies within a complete PBG. However, if the transition energy is near a band edge, where $\rho(\omega)$ is enhanced, an enhancement of the radiative decay is expected. Many different kinds of systems in which the rate of spontaneous emission is modified by the environment are reported, including microcavities [33, 34], two, [35, 36] and three-dimensional [20] photonic crystals to give just a few examples.

Other crucial effect which can be strongly affected by the engineered $\rho(\omega)$ in a PhC is the, so-called, strong or *Anderson* light localization [5]. The inhibition of light propagation was predicted to occur also in the opposite case, as an effect of disorder in some random systems. In analogy to the phenomenon of Anderson localization originally predicted for electrons, if the transport mean free path becomes as short as the wavelength of light itself, interference dominates in the scattering process. One may assist to the formation of localized states, in which light remains trapped, inhibiting light transport. Such an effect has been subject of great interest in disordered materials and can be reached if:

$$\pi^2 c \rho_{loc}(\omega) \ell_t^2 \simeq 1 \tag{1.33}$$

where c is the speed of light in vacuum, $\rho_{loc}(\omega)$ is the photon local density of states at frequency ω, and ℓ_t is the transport mean free path for photons, determined by the degree of disorder in the medium. For photons in a disorder effective medium with refractive index n (1.32), this condition reduces to the Ioffel-Regel criterion, $k\ell_t(\omega) \simeq 1$ [37].

However, in a PhC, a decrease of $\rho_{loc}(\omega)$ in the band-gap and an enhancement at the band-edge reflects the modified phase space available $\triangle k$ for light scattering when the photonic modes are concentrated around few k-directions or the available scattered states are reduced. This is consistent with John's seminal prediction [4] of a need for a modified Ioffe-Regel criterion for scattering in photonic crystals, to include $\triangle k$. The very low density of states near the complete band gap provides a very favorable scenario for the photon localization according to criterion 1.33 even when $k\ell_t(\omega) \gg 1$. Localization in these structures arises from a delicate interplay between order and disorder [38].

1.3.3. Opal-based photonic crystals

From sanscrite *upala* (gemstone), an opal is a self-assembled face centered cubic (fcc) arrangement of monodisperse dielectric microspheres [39]. Natural opals (figure 1.7**a**) are composed by SiO_2 microspheres and show bright visible iridescences due to Bragg reflections from crystallographic planes of the structure. Such a structure acts, therefore, as a three dimensional photonic crystal for visible light (with wavelength comparable to the spheres diameter) with very high quality features. The monodispersity of the spheres defines the minimum free energy configuration to be the fcc structure and, among the possible fabrication methods

used to grow 3D photonic crystals [26], self-assembling gives rise, up to this moment, the best quality samples.

By mimicking nature, it is possible to grow artificial opals with polymeric microspheres such as polystyrene (PS) [40] or polimethilmetacritale (PMMA) [41]. The high monodispersity of these polymer-based microspheres allow very high quality samples, as shown in figure 1.7**(b)**, figure 1.7**(c)**, figure 1.7**(d)**. The first tentative to grow artificial opals was to reproduce the growth process of natural opals: SiO_2 self-assembling by natural sedimentation propitiated by the gravity action. Samples grown by this method [42, 43] present a high amount of disorder (dislocations, mosaic spread, stacking faults) which, usually, spoil the optical performances of the system. Apart from that, these samples are not easy to handle due to its fragility (unless further processing [44] was done to enhance their mechanical stability) and even more, it takes a long time to grow due to the slow sedimentation rate needed to obtain a good crystalline order. To solve these problems and obtain higher quality samples, a new method known as the vertical

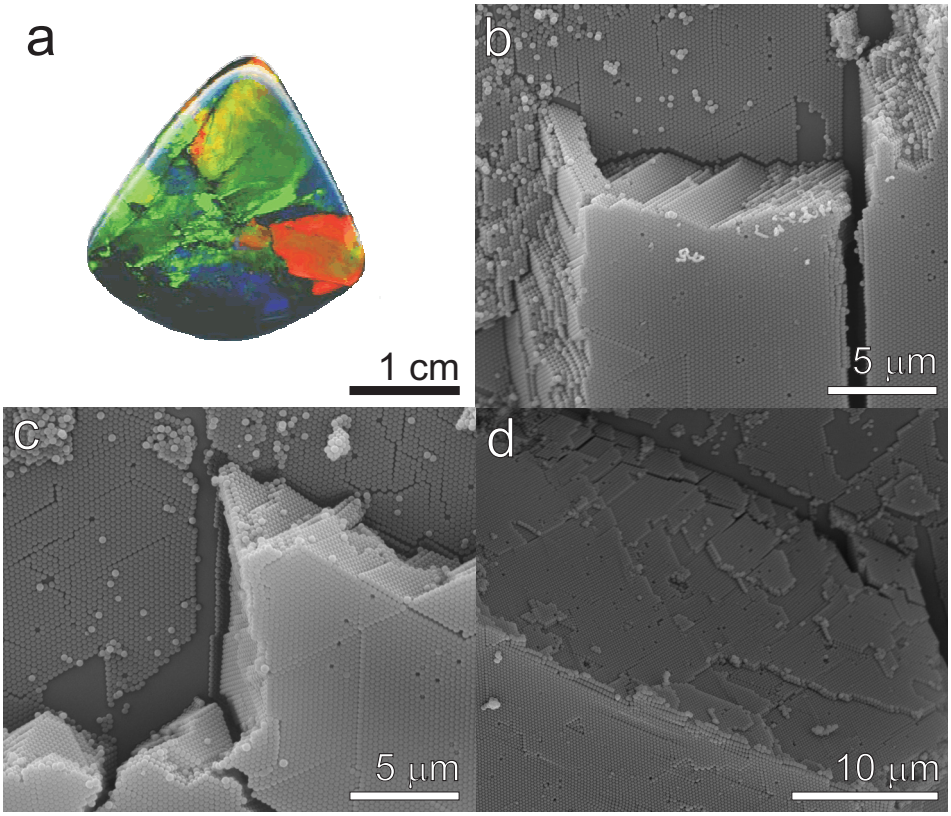

Figure 1.7: **(a)** Picture of a natural grown opal. The bright colors are due to light Bragg reflections on different crystallographic planes due to the mosaic spread composite of the system. **(b)**, **(c)** and **(d)** are scanning electron microscope images from cleaved edges of artificial opals composed by polymer spheres (polystyrene) and grown by vertical deposition. A very high quality and very thick samples (up to 60 layers) can be grown by this method.

deposition [45] was proposed. With this faster fabrication method (just few days are needed compared to sedimentation, which required up to several months) provides samples which present smaller defect concentration (incomparable, up to this moment, with any other fabrication method), controllable thickness (which open a route to systematically study their optical properties) and are easier to handle since they are grown on solid substrates.

A very clear description of this method as well as the optical and morphological characterization of artificial opals grown with it can be found in the PhD thesis of J. F. Galisteo-López [46]. Instead taking advantage from gravity to force the spheres to settle out, a controlled evaporation-assisted vertical deposition on a clean substrate (commonly glass or quartz) is performed. The substrate is hydrophillized by a previous chemical etching which allows the formation of a meniscus forming at the line where the substrate, air and liquid meet (figure 1.8). Then, it is placed in a colloidal suspension of microspheres. Crystal growth begins at the point of the meniscus where its thickness is below the diameter of the sphere [47]. The driving force which pulls the spheres towards the meniscus and force them to self-assemble is the convection. Evaporation of the solvent drives the spheres from the colloidal suspension to the meniscus where an ordered front is formed. Under the appropriate conditions involving colloidal concentration and evaporation rate [47], more than one layer may begin to grow at the meniscus. The self-assembling process seems to be very inefficient at these early stages of the growth process giving rise to, for example, different stacking patterns, [48] high lattice displacements and, even, different stacking order arrangements [49]. Such an extraordinary disorder has been already discussed in the context of op-

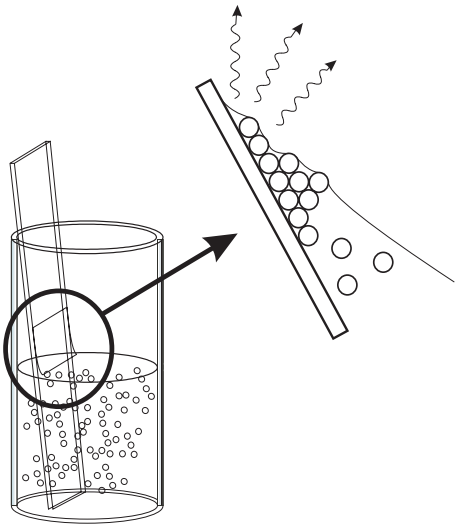

Figure 1.8: Schematic of the vertical deposition growth process. A clean hydrophilic microslide made of glass or quartz is placed in a colloidal suspension of dielectric spheres. The convective forces present at the meniscus between the suspension and the substrate drive the spheres and force them to self-assemble. The controlled evaporation process ensures an effective flow of spheres.

timal self-assembling of the spheres in the colloidal meniscus [50]. The optical performances of a polymer artificial opal are limited by the relative low refractive index of the spheres. These systems are not only interesting by themselves, playing a role of a high quality playground to study fundamental physical phenomena related to photonic crystals, but are also possible templates where it is possible to perform further infiltrations of interesting materials. Different techniques allow the infiltration of a second material and the posterior selective etching of the polymer background. The intermediate and final structure are called composite and inverse opal, respectively. In an inverse opal, a dielectric constant higher than 2.9 ensures the appearance of a complete PBG in the high energy range [51]. The first attempt of an inverse opal was done by O. D. Velev and co workers [52] and the first inverse opal with a complete PBG was archived by A. Blanco and co workers [25]. The main fabrication methods are based on solutions (chemical bath deposition [53] or electrochemistry [54, 55]) and gas phase such as atomic layer deposition [56] (ALD) as well as chemical vapor deposition (CVD) performed in [25] or in the work presented in chapter 2 of this thesis. The gas phase-based method allows a conformal and very controllable growth process which increases notably the optical performances of opal-based photonic crystals.

1.4. Lasing emission in nanostructured materials

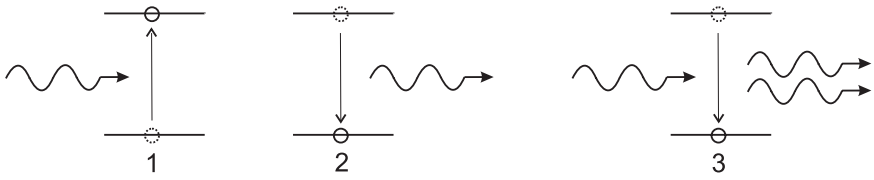

Figure 1.9: The processes of absorption **(1)**, spontaneous emission **(2)** and stimulated emission **(3)** in a photon-particle picture.

When matter absorbs a photon (figure 1.9**a**) and, eventually, radiates it, this emission can be spontaneous or stimulated. Spontaneous emission (figure 1.9**b**) is the process by which a light source in an excited state undergoes a transition to the ground state by interaction with a vacuum continuum and emits a photon. Contrary to this, stimulated emission (figure 1.9**c**) is the process by which an electron, perturbed by a photon having the same energy of the electronic state transition, decays into a lower energy level resulting in the creation of another photon with the same energy and in phase with the initial one. This is at the basis of *laser*, light amplification by stimulated emission of radiation. This phenomenon can be achieved in an optical set up whose essential elements are: **(i)** a *gain medium*, a system with internal electronic states which is able to radiate photons as a result of electronic excitation and decay, **(ii)** an external exciting or *pumping process* and **(iii)** a optical *feedback* mechanism which provides the EM modes necessary for the radiation amplification [61]. The pumping process must provide not merely exited electrons but also *population inversion*, in which

electrons are excited into some higher quantum energy level than in some lower energy lever in the gain medium. In a standard laser, the feedback mechanism is achieved by a resonant optical cavity where standing waves, the modes of the cavity, allow the stimulated emission of the gain medium. The lasing modes of such system are defined by the coupling between the atomic or molecular rate equations of the gain medium and the equations of the optical cavity. A finger print of lasing emission is a threshold behavior. Every feedback mechanism has eventual losses which hampers lasing action. When losses are higher than gain, spontaneous emission dominates. At a high pumping rate, a population inversion large enough to compensate losses and stimulated emission dominates. This two different situations are clearly distinguishable in an output/input emission intensity diagram by a, so-called, threshold. Figure 1.10 shows the output intensity emission from a gain medium as a function of external energy pumping. Two clear rate emissions are revealed: **(1)** the spontaneous emission dominates and **(2)** the stimulated emission dominates. The pumping energy at which the threshold between both situations happens depends on the fraction of spontaneous radiation which contributes to lasing. This is characterized by the, so-called, β-factor which is of paramount importance since it is intimately related to the feedback mechanism losses. The definition of β is the amount of spontaneous emission that contributes to the lasing mode. The rest of the spontaneous emission which does not contribute to the lasing mode is lost. As β represents a fraction, its value is always between 0 (no lasing emission, all the spontaneous emission is lost) and 1 (all the spontaneously emitted photons end up in the laser mode in which is known as threshold-less laser).

One of the challenges of nanophotonics, both ordered or disordered is to engineer a system in which the value of β minimizes with the ultimate goal of obtaining a $\beta = 1$ laser for which stimulated emission dominates for every energy

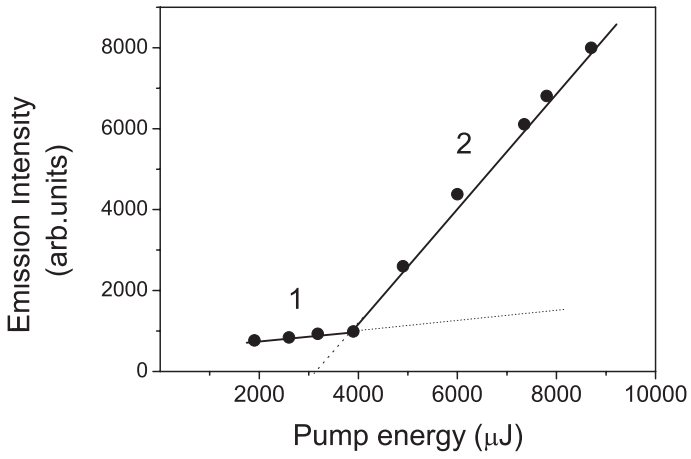

Figure 1.10: Intensity of the maximum emission spectrum vs. pump pulse energy. For pump energy values lower than $4000\ \mu J$ (threshold value) spontaneous emission governs the emission process (**1**) whereas, above threshold, stimulated emission dominates the process (**2**).

pumping value. Photonic crystals where proposed in such a way to minimized losses in the optical cavity and to maximize the value of β [3]. By tuning the emission energy to a complete PBG of the photonic crystal, it is possible to minimize the spontaneous emission which do not contribute to the lasing. As the laser threshold depends on the balance between gain and loss in the system, such a way to engineer the DOS can substantially reduce β.

1.4.1. Random laser

Lasing in nanostructured materials is not only limited to ordered nanostructured dielectrics such as photonic crystals. A very intriguing phenomenon happens when multiple scattering is combined with a gain medium. In such a system it is possible to observe lasing action in a process which is known as *random laser* [62]. This phenomenon was firstly proposed by Letokov in the sixties [63] and experimentally observed by Lawandy [64] in the nineties. In this section we will discuss only diffusive random lasers.

Figure 1.11 shows the comparison between a conventional laser **(a)** and a random laser **(b)**. In a random laser the optical feedback is provided by scattering of light, instead of by a cavity. The necessary condition for a random laser is that the material multiply scatters light, which means that the transport mean free path (the average distance over which the scattered light direction is randomized) is much smaller than L, which is the sample size, $\ell_t << L$. The other fundamental quantity is the gain length ℓ_g that represents the path length over which the intensity is amplified by a factor e^{+1}. The interaction between gain and scattering determines the unique properties of the random laser and, in particular, defines the critical thickness for the sample (in slab geometry) to lase $L_{cr} = \pi\sqrt{\ell_g \ell_t/3}$ [65]. Light transport through a multiple scattering medium can, eventually, be described as a diffusion process characterized by a (transport) mean free path, ℓ_t, and a diffusion constant, $\mathcal{D}$. Diffuse light propagates though such a medium following a diffusion equation 1.16. Optical amplification can be added to the

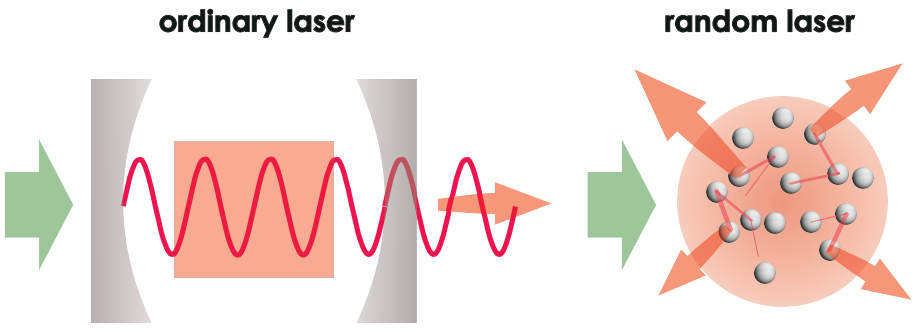

Figure 1.11: **(a)** A conventional laser is composed by a gain medium and an optical cavity which provides the necessary resonant feedback to achieve lasing threshold. **(b)** Unlike ordinary laser, in a random laser the resulting light emission is multidirectional and not really monochromatic, but the threshold behavior, the photon statistics and relaxation oscillations are very similar to those of standard lasers.

diffusion picture described so far. Multiple scattering increases the interaction between light and the system and, when gain is added to this scenario, the system, eventually, lases. The lasing process can be described, to a first approximation, with the four-level rate equation [61] in the presence of diffusion:

$$\begin{aligned} \frac{dN_1(t)}{dt} &= P(t) - \frac{\beta q(t) N_1(t)}{\tau} - \frac{N_1(t)}{\tau}, \\ \frac{dq(t)}{dt} &= \frac{\beta N_1(t)}{\tau}[q(t)+1] - \frac{q(t)}{\tau_c}, \\ \tau_c &= \frac{L^2}{8\mathcal{D}(\lambda)}, \end{aligned} \tag{1.34}$$

where $N_1(t)$ is the number of excited molecules, $P(t)$ is the pump rate, $q(t)$ the number of photons of the laser modes, τ the spontaneous emission lifetime of the gain medium. The differences between a single mode standard laser and a multi-mode random laser lie in the cavity decay time τ_c [68, 69] that becomes dependent on the diffusion constant (and, then, on the transport mean free path) and in the β factor [71] that instead accounts for the average numbers of lasing modes. From Eq. 1.34 it can be seen that the threshold and lasing process can be controlled modifying $D(\lambda)$ and $\ell_t(\lambda)$.

1.4.2. Bloch laser

Photonic crystals where firstly proposed to achieve threshold-less lasers [3]. In a photonic crystal, light-matter interaction can be effectively engineered to enhance light amplification and lasing action [72]. Contrary to the case of (diffuse) random lasers, where the laser mode is randomly spread over the entire system, the lasing mode in a photonic crystal is a linear combination of Bloch modes and is spread over the crystal defined by the symmetry of the structure. This is the reason which explains the isotropic lasing random emission in the first case and the highly directional lasing emission in the second one. In the following, the term *Bloch laser* will be applied to laser in photonic crystals and it is related to the nature of lasing (Bloch) modes in such system. This term has not been used in the literature but it could be useful to distinguish, at least in this thesis, laser in random systems from laser in ordered systems.

As discussed previously, the group velocity of light $\mathbf{v}_g$ is defined by the gradient of the isofrequency surfaces (Eq. 1.30). Consequently, it minimizes when the dispersion relation slope goes to zero. This situation can be achieved, for example, in photonic crystals [27]. At photonic band edges or at weakly dispersive, so-called, *flat* energy bands, the slope of the dispersion relation minimizes for a certain range of wavevector k values. A reduction of $\mathbf{v}_g$ results in an artificially engineered standing wave propagation through the system, compared to that trough the non-structured material. This leads to a stronger interaction and to an enhancement of the optical response of the system. In the particular case that the material which composes the system is a gain material (it is able to radiate photons by means of an external excitation mechanism), an enhancement of the stimulated emission may, eventually, lead to a large reduction in the lasing

threshold [24]. An analogous process occurs in standing wave modes near Bragg diffraction resonance in one-dimensional multilayer stacks. The unique dispersion relation of two- and three-dimensional photonic crystals, which includes, as mentioned, the weakly dispersive *flat* bands at high energy, gives rise to the so-called *group velocity anomaly* [24, 73]. In such case, the reduction of the lasing threshold was brought about by the enhancement of stimulated emission due to the strong interaction between the EM field and the matter. $\mathbf{v}_g$ of the EM eigenmodes is small over the entire energy- and wavevector- range of this bands, leading to this large effective coupling between light and the gain material. This enhancement is similar to that of distributed feedback lasers (DFL) caused by the formation of a standing wave [74]. Actually, DFL is a type of laser where the active region of the device is structured as a Bragg reflector, a one-dimensional photonic crystal. The grating provides optical feedback for the laser during distributed Bragg scattering from the structure and do not use discrete mirrors to form the optical cavity (as are used in conventional laser designs). A three-dimensional photonic crystal *Bloch lasing* in the weakly dispersive *flat* high energy bands is more complicated than a simple Bragg-reflector, but the physics underlying the effect are the same: by nanostructuring the gain material it is possible to obtain a mirror-less laser.

1.5. Outline of this thesis

Figure 1.12 shows the two different systems which provide the tittle and constitute the basis of the work presented in this thesis. Light propagation and light emission though opal-based photonic crystals (**left**) and photonic glasses (**right**). It will be shown how light transport and emission properties can be strongly tailored in such systems. For that purpose, light propagation will be described from two very different approaches: Bloch modes and photonic band structure in the first case and diffusion approximation in the second one. The thesis is divided in three parts: In the first part **(I)**, the effect of a photonic band structure from an ordered system, ZnO inverse opals in this case, is shown on different aspects of light propagation and light emission. In the second part **(II)**, a novel disorder material for light, the photonic glass, will be introduced. Their optical properties as well a particular application of the system for random lasing will also be shown. In the third part **(III)**, a means to perform a controlled transition from an order nanostructure to a disordered one will be developed and, in particular, its implications on ZnO lasing emission.

- Chapter 2 exploits an infiltration technique to obtain ZnO nanostructures based on opals. Ordered and disordered ZnO systems can be obtained with the help of a vapor deposition method. ZnO material and Photoluminescence properties are investigated in this chapter.

- In chapter 3, a method based on ZnO infiltration of opal-based photonic crystals is explained to probe and identify different crystallographic directions of their fcc structure. In particular ΓL and ΓX directions.

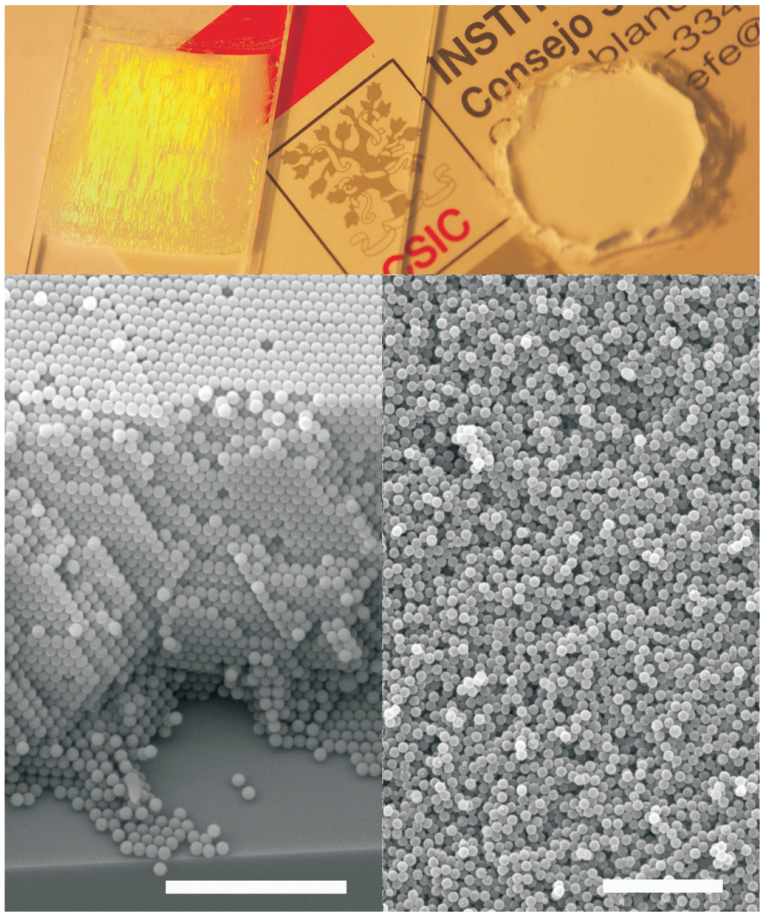

Figure 1.12: **Top:** picture shows an opal-based photonic crystal **(left)** which shows visible iridescences due to Bragg reflections and a photonic glass **(right)** white and without any trace of Bragg features. **Bottom: (left)** Scanning electron microscopy (SEM) image from a photonic crystal cleaved edge (scale bar is 10 μm). **(Right)** SEM image from a photonic glass surface (scale bar is 10 μm). Both samples are made of PS spheres (2% of polidispersity measured by transmission electron microscopy) and have centimeters squared areas and millimeters thickness.

- Chapter 4 it shows an optical study of high energy photonic pseudogaps which appear in ZnO inverse opals. The controlled infiltration of ZnO allows a photonic band engineering which will result crucial to study ZnO high energy bands interaction with quantum dots (QD) emission and ZnO lasing emission. It also develops a method to infiltrate quantum dots, CdTe in this case, in ZnO inverse opals by means of a physical technique. The physical infiltration can be monitored by means of optical spectroscopy of the structure. The interaction of high energy photonic pseudogaps of the ZnO inverse opal with the QD emission undergoes an inhibition and an enhancement. A fine tuning and control can be exerted over the process with posterior ZnO infiltration.

- In chapter 5, a method to obtain a random distribution of monodisperse scatterers is explained. This system is called photonic glass.
- Chapter 6 analyzes the optical properties of photonic glasses by means of static and dynamic measurements and show resonant light diffusion though such a system.
- In chapter 7 the resonant properties of light diffusion are used to control and modify the random lasing action of and organic emitter. It is compared the conventional random lasing in a TiO_2 powder matrix with the resonance-driven random laser in a photonic glass.
- Chapter 8 shows a means to perform a controlled transition from an opal based photonic crystal to a photonic glass. By introducing a controlled amount of vacancies in lattice positions of the original opal a transition of the optical properties, the scattering mean free path and the diffusion constant is observed.
- Finally, in chapter 9 UV ZnO lasing emission is obtained in ordered and disordered nanostructures. UV ZnO lasing is observed in ZnO inverse opals in the high-energy range of the photonic bands provided by the, so-called, *group velocity anomaly*. On the contrary, conventional ZnO random lasing is observed in the case of ZnO inverse photonic glasses and ZnO inverse opals doped with a high amount of vacancies.

Part I

Photonic Crystals

Chapter 2

ZnO: optical and material properties for photonics

Among materials for photonics, ZnO is probably one of the most promising candidates for innovation in the next decade. It has been widely used in numerous applications such as piezoelectric transducers, solar cells, phosphors, and sensors, this wide-gap (3.4 eV) semiconductor has been shown to be a good alternative to other classic materials as a short-wavelength light emitter [76]. Thanks to its large excitonic binding energy (60 meV), lasing at room temperature was demonstrated in thin ZnO films optically pumped in the last decade [77] (it is important to remark the great difficulty which supposes the n/p doping of ZnO to allow electrical pumping). Since then, different ZnO nanostructures have emerged in many different sizes, shapes, and geometries, e.g., nanowires [78, 79], nanobelts [80], or nanoribbons [81, 82], improving its lasing efficiency and boosting its possibilities in photonics. A wide range of novel functionalities can be obtained by nanostructuring ZnO. In particular, there are a number of examples of ZnO-based photonic crystals in one [83], two [84], or three dimensions [85]. In three-dimensional (3D) opal-based photonic crystals, ZnO infiltration of silica opals has been tackled by wet chemical methods [86, 87], and polymeric opals have also been infiltrated with ZnO by sol-gel [88] and electrochemical methods [89].

There are different approaches to growing polycrystalline or epitaxial ZnO. Techniques involving the gas phase are the most widespread, due to the high quality epitaxial growth, and can be directly applied in industry. Furthermore, gas-phase methods have demonstrated their potential in conformal growth for the infiltration of high aspect ratio structures [90, 91, 92]. Atomic layer deposition (ALD) [91, 92] provides atomic-scale thickness control of ZnO films by oxidation of metal-organic precursors such as diethyl zinc (DEZn) or dimethyl zinc (DMZn) (which are highly reactive in air) by alternating metal-organic and water exposures or pulses of a few seconds length in a binary reaction sequence. These methods have, however, never been used in porous environments such as opals even though they are the most appropriate approach for conformal infiltration, which allows a perfect replication of the template.

A controlled process to fabricate large-area high quality ZnO-polystyrene (PS) composites and ZnO inverse opals with fine control over filling volume (nanometric in thickness) by a modified metal-organic chemical vapor deposition (MOCVD) method will be provided in this chapter. The optical properties of such a structure will be analyzed carefully and a deep material characterization will also be carried out.

2.1. ZnO chemical vapor deposition

ZnO has been infiltrated in thin artificial opal films composed by polymeric (PMMA and PS) spheres. These templates are grown by vertical deposition [45] on quartz substrates where a colloidal suspension of PS or PMMA microspheres with a typical concentration of 0.15 wt % is self-assembled. The process takes places along several hours under a controlled temperature ($T = 45\ ^{\circ}C$). The particular templates shown in this chapter have been grown using a sphere diameter $d = 500$ nm, although a wide range of spheres diameters from $d = 200$ nm to $d = 1200$ nm have been tested. The infiltration is peformed by a chemical vapor deposition using as Zn precursor a diluted solution of diethyl-Zinc, $ZnO(CH_3CH_2)_2$, in hexane. Double-distilled water (DDW) was used as oxygen precursor. The diluted metal−organic compound is easier to handle than the pure, highly reactive one. It also provides the key to fine control of the ZnO growth inside the opal. The two precursors are kept separately in glass bubblers at room temperature. Figure 2.1 schematically reproduces the set up use in this process. The precursors were alternately feed into the reactor using nitrogen as

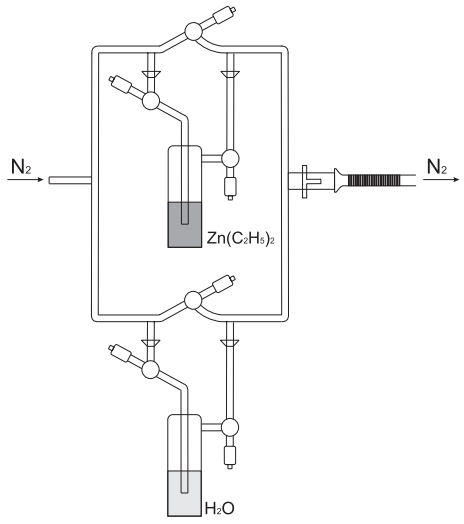

Figure 2.1: Schematic of the CVD set-up to perform the ZnO infiltration of opals. The bare opal is placed on the reactor at $T = 90\ ^{\circ}C$, a continuous flow of nitrogen bubbles diethyl-Zinc and water intermittently to the reactor, where they react forming ZnO conformal shells on the polymer spheres surface.

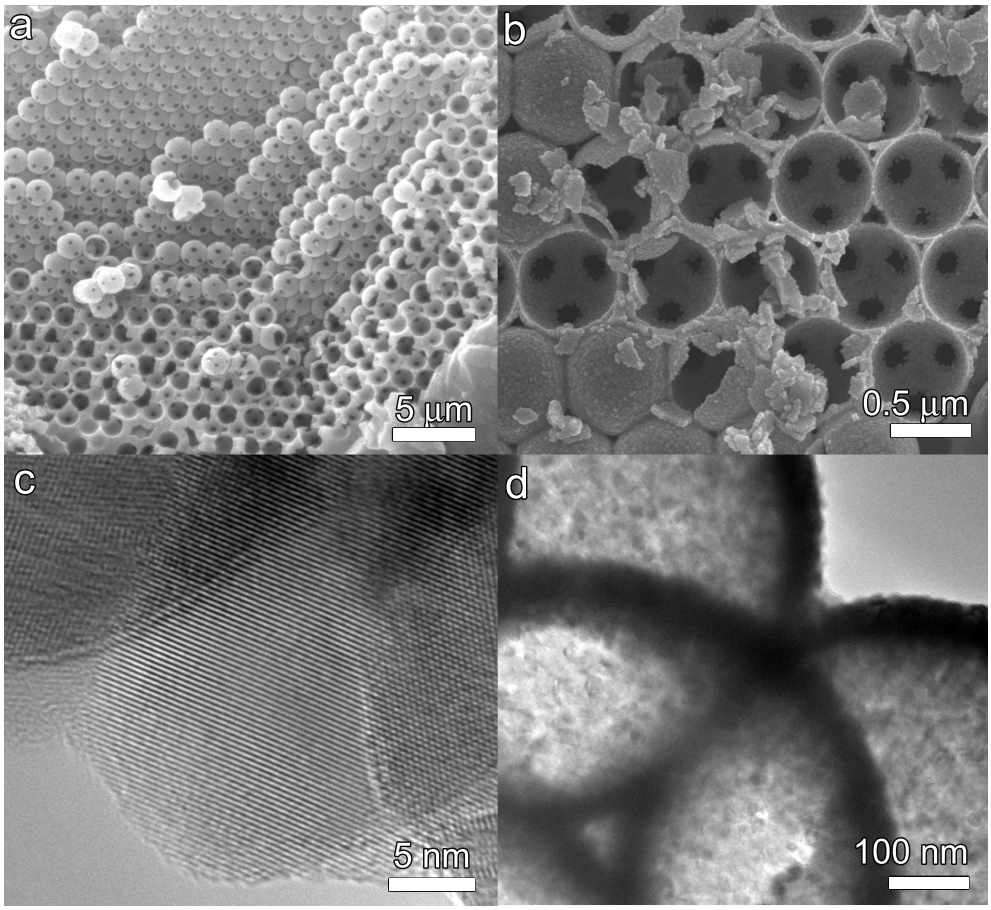

Figure 2.2: Images (SEM) of cleaved edges in ZnO inverse opals (**a**) and (**b**) from 500 nm polystyrene spheres. The images reveal the smoothness and quality of the conformal growth of ZnO shells, which extends for areas of hundreds of square micrometers. Images (TEM) of ZnO grains from ZnO inverted opals (**c**) and (**d**) which show with detail the ZnO atomic planes.

carrier gas at a fixed flow rate. The reactor was kept around $T = 90\ ^{\circ}C$, which is a compromise temperature in order to obtain smooth deposits with fine grains while avoiding the softening of PS. Room temperature conditions yield rough and inhomogeneous deposits. The ZnO film thickness deposited by alternating exposure to the two sources in succession (a cycle) depends on the carrier gas flow rate, temperature, and exposure time of each source. In this particular case, 30 s cycles of water and 20 s cycles of diethyl-Zinc were alternatively bubbled with a fixed nitrogen flow of about 200 ml/min in both cases. A bare opal can be filled in a single cycle or in several cycles. This fact is of paramount importance in order to tune the photonic properties to the desired specifications for optimal performance. Theory predicts particular or functional behavior for a given filling fraction. It is worth mentioning that due to the conformal growth and geometrical constrains the maximum value achievable for the filling fraction is close to

86 %. In addition, conformal growth allows the fabrication of inverse structures even for extremely low ZnO filling fractions.

Inverse opals are obtained after a selective removal of the polymeric background by a calcination process of ZnO@PS composites which comprises on a first step annealing at $T = 90\ ^{\circ}C$ for 6 h, in order to melt the polymer spheres, and a second step at $T = 450\ ^{\circ}C$ for 15 h in air. This process not only removes completely the PS matrix but also recrystallizes the ZnO, as revealed in ZnO photoluminescence measurements shown later on in this chapter. Scanning electron microscopy (SEM), transmission electron microscopy (TEM) and optical spectroscopy have been performed in order to monitor the infiltration process. Figure 3.2 shows SEM images (**a** and **b**) and TEM images (**c** and **d**) from ZnO-based opals grown on quartz substrates. The high quality of the smooth and homogeneous coating can be observed. Figure 3.2**b** and **c** shows the appearance of a cleaved edge of a ZnO inverse opal with an infiltration degree of 60 % of the pore volume. Figure 3.2**c** shows the ZnO grain composition whereas 3.2**d** shows the atomic planes of ZnO grains.

Surface inspections reveal homogeneous growth over square-millimetre areas. The inverse replica order is disturbed only by the usual cracks (hundreds of micrometres apart) which replicates the structural disorder of the templates. The empty interiors of the shells in the inverse replicas are observed only in cracks and the cleaved edges. From these we can give a rough estimate of the ZnO shell thickness of about 20 - 30 nm, in good agreement with the expected value.

2.2. Optical and Material properties

The refractive index of thin ZnO homogenous films (0.4 - 1.6 μm) was measured by ellipsometric techniques to range from 2.2 to 1.9 (shown in Figure 2.3), in good agreement with data previously reported by Yoshikawa and Adachi [93]. Optical microscopy inspection reveals the tuning of the optical properties of the

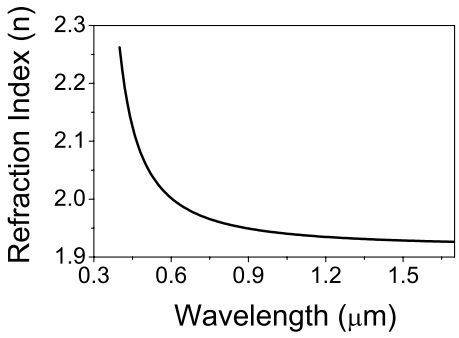

Figure 2.3: Refractive index of ZnO thin films measured by ellipsometry.

system. Optical microscopy was performed with a microscope attached to the spectrometer and a ×4 objective featuring a 0.1 numerical aperture (5.7° angular aperture). Figure 2.4 shows optical microscopy images from the three different stages of the process: the bare opal (**a**), the composite one (**b**) and inverse opal (**c**). The optical responses of ZnO@PS composites and ZnO inverse opals were compared with photonic band calculations [94]. The infilling process has been monitored by the optical reflectance at near normal incidence with respect to the (111) face-centered cubic (fcc) planes taken with the help of an optical microscope from a circular area of about 375 μm diameter. The red-shift in the first-order Bragg peak as the infiltration proceeds accounts for the increase of the average refractive index of the structure due to ZnO infilling.

Figure 2.5 shows the photonic band calculations (**a**) and the reflectance spectra of bare PS opal (**b**), ZnO@PS composite with 80 % pore volume infilling (**c**),

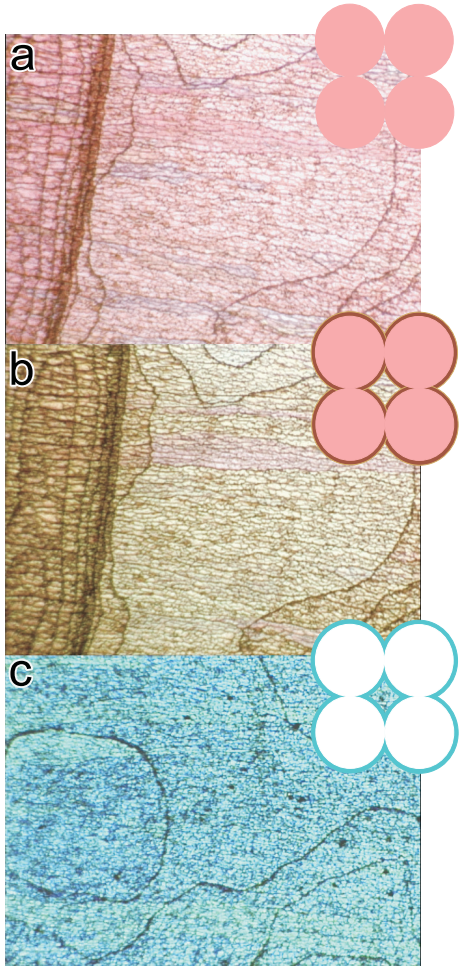

Figure 2.4: Optical microscope images showing the surfaces of the bare opal **(a)**, the ZnO@PS composite one **(b)** and the ZnO inverted opal **(c)**. The different colors arise from the different photonic band structure of each sample, which reflect different colors.

and the same structure after PS calcination (**d**). The parameters used for the calculations were the following: for the bare opal PS spheres arranged in a fcc lattice and with a refractive index of $n_{PS} = 1.59$ were used (pink line in figure 2.5**a**); for the ZnO infiltrated structure (brown line in figure 2.5**a**) a layer of 30 nm with a refractive index of $n_{ZnO} = 1.93$ (taken from ellipsometric data) was added over the PS spheres; finally, for the inverse ZnO replica (blue solid line in figure 2.5**a**) the refractive index of the spheres was replaced by 1 (air) in the inverse structure. Figure 2.5**c** points out the disappearance of the Bragg peak due to index matching (notice the disappearance of the pseudogap in the brown line of (**a**)). In this case, the system behaves as an homogeneous medium with a refractive index of around $n_{eff} = 1.65$ and a thickness of around 5 μ m. After removal of PS by calcination the Bragg peak blue-shifted (figure 2.5**d**), due to the lowering of the average refractive index (from $n_{eff} = 1.65$ to $n_{eff} = 1.2$), and becomes broader (almost double) because of the increase of the refractive index contrast ($n_{ZnO}/n_{air} = 1.9$). It is important to pay attention to the fact that, the color of each structure shown in figure 2.4 does not correspond to the reflectance of the first order pseudogap. Figure 2.5 shows how the light reflectance from the three structures (bare opal, composite one and inverse opal) happens in the infrared (see wavelength axis). The color shown in the optical microscopy pictures is due to high energy photonic features which will be subject of analysis in the following chapters.

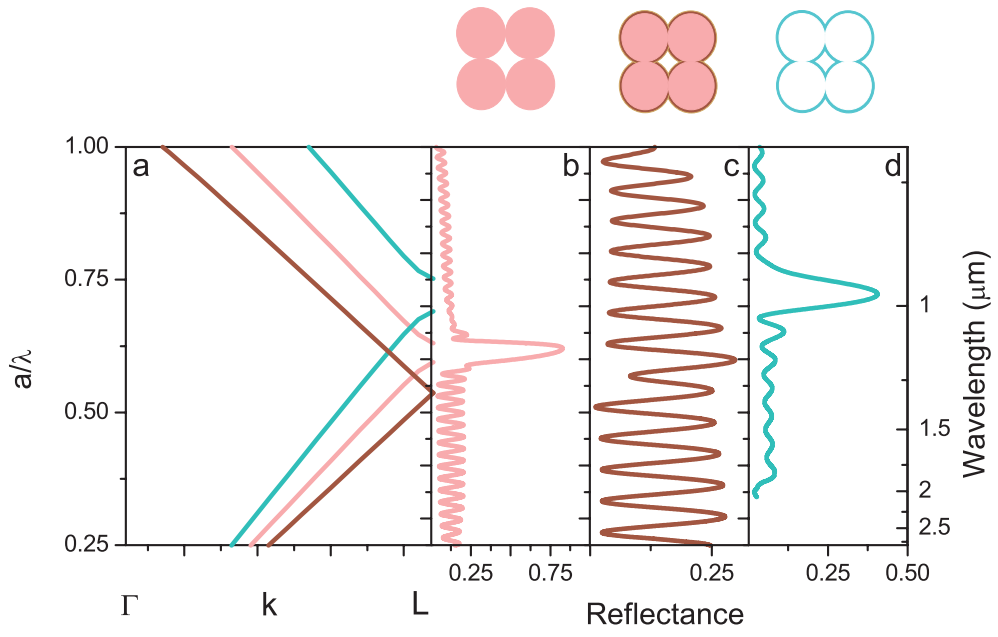

Figure 2.5: Specular reflectance spectra of a PS bare opal **(b)**, 80% ZnO@PS opal composite **(c)**, and ZnO@air inverse structure **(d)**, together with the corresponding photonic band calculations **(a)** for bare (pink), composite (brown), and inverse (blue) structures. This colors correspond to the real structures reflectance.

2.3. ZnO photoluminescence

The optical properties of a semiconductor are connected with both intrinsic and extrinsic impurities. Intrinsic optical transitions take place between the conduction band and the valence band, including excitonic effects due to the Coulomb interaction. Excitons are classified as free or bound. Extrinsic properties are related to dopants or defects, which usually create discrete electronic states in the electronic band gap, and therefore influence both optical-absorption and emission processes. The electronic states of the bound excitons (BEs) depend strongly on the semiconductor material, in particular, the band structure. Other defect-related transitions could be seen in optical spectra such as free to bound (electron-acceptor), bound to bound (donor-acceptor), and the so-called yellow/green luminescence. As in any semiconductor, impurities affect the electrical and optical properties of ZnO. ZnO photoluminescence (PL) emission at room temperature is due to free-exciton at 3.26 eV ($\sim$ 380 nm) (bound exciton is, at this temperature, ionized) and a wide green luminescence band (GL). The nature of the GL, appearing at about 2.5 eV ($\sim$ 600 nm) has been explained in terms of oxygen vacancy (V_O) or Zinc vacancy (V_{Zn}) [95].

The samples were optically pumped by a frequency tripled Q−switched pulsed Nd:YAG laser (9 ns pulse duration), with 10 Hz repetition rate. The spot size was fixed at 2 mm diameter. The pumping beam and the emission beam were along the direction perpendicular to the sample surface (along ΓL crystallographic di-

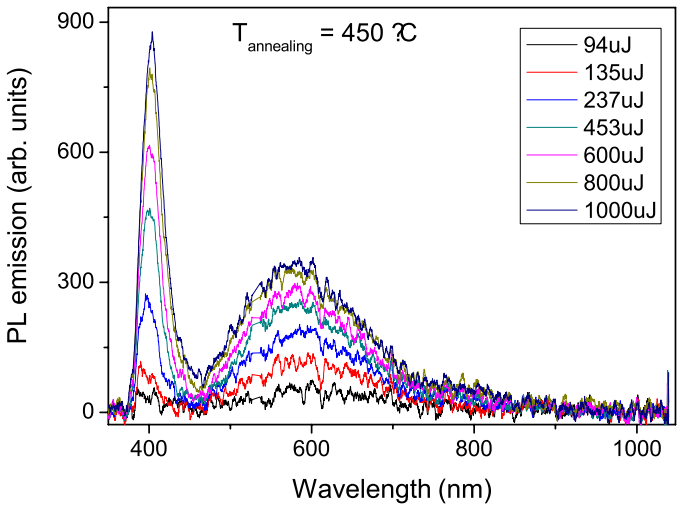

Figure 2.6: Emission from ZnO annealed at $T = 450\ ^{\circ}C$ as a function of pump energy. The spot size is fixed at 2 mm diameter. Two clear bands can be distinguished, from the free-exciton emission ($\lambda = 390$ nm) and from ZnO defects emission ($\lambda = 600$ nm). The intensity of both emissions increases linearly with pump energy, as expected from a spontaneous−like luminescence.

rection). In particular, the emission was monitored with a miniature spectrometer with a resolution of 0.5 nm. Figure 2.6 shows a set of ZnO PL measurements as a function of pump energy. PL measurements show very efficient free-exciton emission and defect emission band in ZnO inverted opals. In this case, the original PS spheres have a diameter $d = 200$ nm and, therefore, the free-exciton emission does not overlap with any photonic feature related to the band-structure of the ZnO inverted opal. For this measurements, ZnO has been annealed at $T = 450\ ^{\circ}C$. Two clear characteristic emissions are shown corresponding to the free-exciton, at $\lambda = 390$ nm as well as to the intrinsic impurities, at $\lambda = 600$ nm. The intensity of both emission bands increases linearly with energy pumping, as expected from a spontaneous emission luminescence.

The relation between ZnO crystalline structure and ZnO PL has been analyzed varying the annealing temperature. The elemental composition of the ZnO inverse structures was studied by energy dispersive X−ray. Figure 2.7 shows the X−ray characterization (**a**) and the PL emission (**b**) as a function of annealing

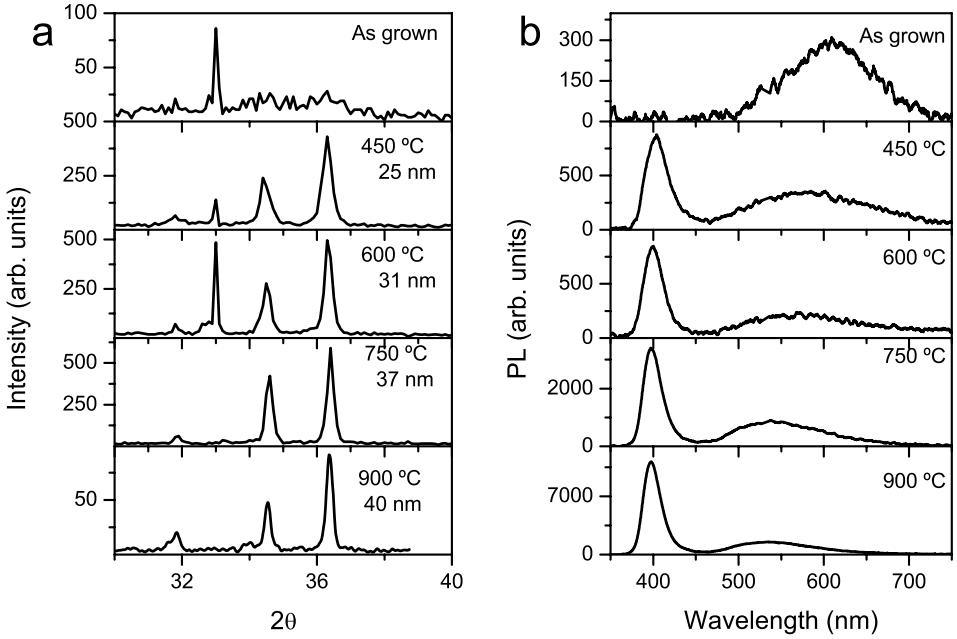

Figure 2.7: **(a)** X−ray diffractograms from the ZnO inverse opals at different annealing temperatures. The grain size grows with temperature from 4 nm in the as-grown case, to 40 nm at $900^{\circ}C$. **(b)** ZnO PL measurements as a function of annealing temperature. All these samples are pumped at with the same energy ($1000\ \mu J \sim 80\ \mu J/mm^2$ per pulse). As-grown ZnO inverse opals do not present free-exciton emission. An increase of annealing temperature allows the ZnO crystallization, a higher free-exciton emission and a decrease of the ZnO structural defects. This is pointed out in a higher value of $I_{exciton}/I_{defects}$, which denotes a higher sample crystallinity.

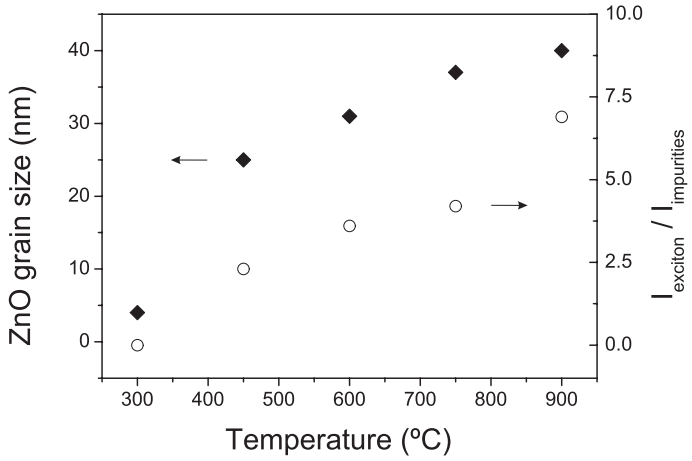

Figure 2.8: **(Right axis)** Dependence of the ratio between of the free-exciton emission and the impurities emission intensity on the annealing temperature. **(Left axis)** Dependence of the ZnO grain size on the annealing temperature

temperature.

The effect of a higher annealing temperature on the ZnO crystal grain is evident. Upon crystallization, sharp peaks are obtained, in agreement with an increase in the grain size. All samples present a polycrystalline nature, the grain size increasing from 4 to $\sim$ 40 nm upon annealing at $T = 900\ ^{\circ}C$, as shown in figure 2.7**a**. Data are estimated by applying the Scherrer formula. This ZnO grain size is of the order of the ZnO shell layer thickness. This fact has important consequences on the inverse structure mechanical stability. ZnO inverse opals annealed at high temperatures (typically $T > 550\ ^{\circ}C$) become very intestable due to shrinkage and structural tensions. On the contrary, grain size and crystallization degree have also a direct consequence on free-excitonic emission. Figure 2.7**b** shows direct measurements of ZnO PL at room temperature at the same pumping energy (175 $\mu J/mm^2$) from samples annealed at different temperatures. The maximum intensity related to the free-exciton emission varies from 0 (as grown ZnO does not present such an emission) to a very efficient emission after annealing at $T = 900\ ^{\circ}C$. Figure 2.8 shows the grain size and the ratio between the free-exciton emission and the impurities band emission ($I_{exciton}/I_{impurities}$). This value is a quality measure of the crystal, increased notably by the annealing process.

The ZnO recrystallization is not only possible by a typical annealing process under controlled temperature but also by the direct and local action of the pumping laser. Figure 2.9 shows ZnO emission PL at room temperature as a function of pump energy. In this particular case, the sample has not been annealed after the growth process. It presents a poor grain crystallization, as shown in figure 2.7**a** for the case of as-grown ZnO. As revealed in the figure, for low pump energy no free-exciton related emission is shown by the system. On the contrary, a strong band emission due to structural ZnO defects (GL) appears at $\lambda = 600$

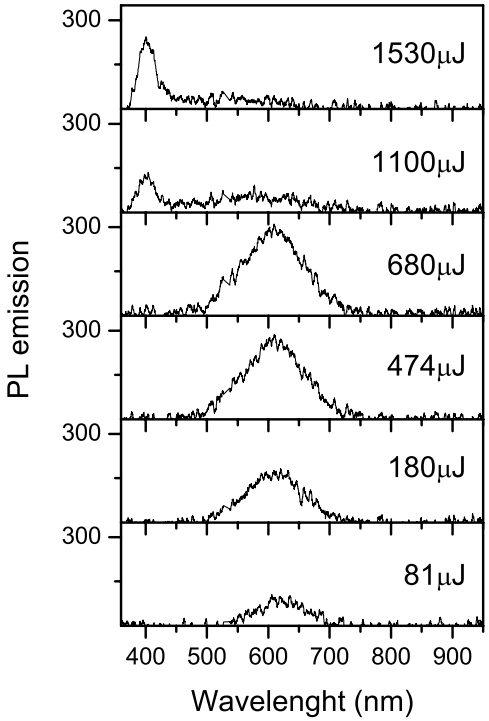

Figure 2.9: PL emission from as-grown ZnO inverted opals. No annealing process has been carried out in this samples. When the pump energy is increased over than $1100\ \mu J \sim 175\ \mu J/mm^2$, a clear free-exciton emission is revealed. The pump laser crystallizes the sample locally and induces free-exciton emission, reducing the ZnO impurities and structural defects and, threfore, GL emission.

nm, pointing out a high extrinsic defects density. The defect related band emission increases linearly with the pump energy. For pump energy value higher than $1100\ \mu J \sim 175\ \mu J/mm^2$ (threshold annealing pump energy value) the appearance of free-exciton emission and the inhibition of defect band emission are revealed. The reason which explains this fact is the direct and local annealing induced by the pump laser beam. This process gives rise to a local material crystallization and happens only by the action of the pump laser beam. Those areas of ZnO inverse opal which are not directly pumped by the laser beam and, consequently, do not suffer an annealing process, remain amorphous. This fact is observed by reducing the pump energy to value lower than the threshold annealing value $175\ \mu J/mm^2$ and pumping a different ZnO area. By doing so, only defect band related emission is observed whereas in an annealed area free-exciton emission is still observable. This effect is, therefore, a local annealing and crystallization induced by the pump laser and is a very interesting property which opens a route to study direct laser writing in ZnO inverted opals.

2.4. Conclusions

In summary, here the use of CVD to grow ZnO in synthetic opals is reported. This method yields large-area, high-quality ZnO@PS and ZnO inverse opals with very precise control of degree of infiltration, which, in terms of thickness, means nanometer-thick layers. For the quality of the deposits and the ease of use, as well as for its inexpensiveness, this may well turn out to be the ultimate method of synthesis for a material that has gained a place on the rostrum of materials for photonics. ZnO grown by this method shows strong UV free-exciton photoluminescence at room temperature, which may be useful to grow ordered or disordered ZnO nanostructures with emission properties.

Chapter 3

Tuning and optical study of ΓX and ΓL pseudogaps in opals

One of the most interesting properties of photonic crystals is that they allow to modify the photon density of states. The latter is determined by the band structure which may be tailored by means of variations in the refractive index and topology for a given symmetry. Although for artificial opals the symmetry is fixed by the growth process, the band structure can be modified, to certain extent, by means of a controlled infiltration with other interesting materials carrying out what can be called band gap engineering [96, 97]. Knowledge of the photonic band structure of synthetic opals and the possible modifications attainable by engineering through infiltration is desirable in order to exploit their potential in applications for light steering such as super refractive devices. For artificial opals at low frequencies ($a/\lambda < 1$, where a is the lattice parameter and λ the wavelength of light in vacuum), pseudogaps appear for propagation along different directions. The width of such pseudogaps is mostly dictated by the magnitude of the Fourier component of the expansion of the dielectric function associated with the reciprocal lattice vector G corresponding to the point in reciprocal space where the gap opens [24]. Therefore, for a fixed symmetry, the interaction and, hence, pseudogap width may be manipulated modifying the refractive index distribution and volume fraction [98] since the symmetry and lattice parameter remain unaltered.

3.1. Morphological characterization

In this chapter, a method to tune the two high-symmetry pseudogaps in artificial opals occurring in the reciprocal space directions ΓL and ΓX which correspond to crystallographic orientations (111) and (100) respectively will be demonstrated. In particular the ΓX gap, closed for bare opals, can be opened. We use areas of the opal that present either of these orientations which naturally appear in artificial opals grown by vertical deposition. They can be identified by the symmetry of the arrangement of spheres in the surface of the sample. Areas of hexagonal (square) arrangement of spheres correspond to (111) (100) planes.

While several high-symmetry directions have been studied in bulk artificial opals by inspecting cleft edges [99], they are difficult to cut, the available areas are small, difficult to locate, orientate and align with the spectroscopic experimental set up. While thin film opals grown by vertical deposition have almost always their (111) planes parallel to the substrate, in some cases naturally occurring (100) oriented regions appear as already reported by several authors [100, 101]. This occurs mostly in the initial stages of growth.

The samples used were grown using polystyrene (PS) spheres 503 nm in diameter (3 % polydispersity) synthesized by a previously published method [40]. ZnO infiltration of the sample was carried out with the modified metal−organic chemical vapor deposition method shown in chapter 2. In order to remove PS spheres to obtain a ZnO inverted opal, the sample was calcinated at $T = 450\ ^{\circ}C$ for 2 hours. A Fourier transform infrared spectrometer was used to record the optical reflectance of the samples at normal incidence in a wide spectral range. A microscope attached to the spectrometer with a $\times 4$ objective featuring a 0.1 numerical aperture (5.7° angular aperture) was used to focus and collect the light. We have performed all measurements in adjacent regions with square and hexagonal planes in areas of 9 and 11 layers of thickness respectively. The thickness was estimated from Fabry-Perot oscillations present in the spectra on either side of the Bragg peak. Optical microscopy (figure 3.1) and scanning electron microscopy (figure 3.2) were used to characterize the morphology of the samples. Optical microscopy was performed with the same objective used for optical measurements. In order to perform the scanning electron microscopy inspection, the

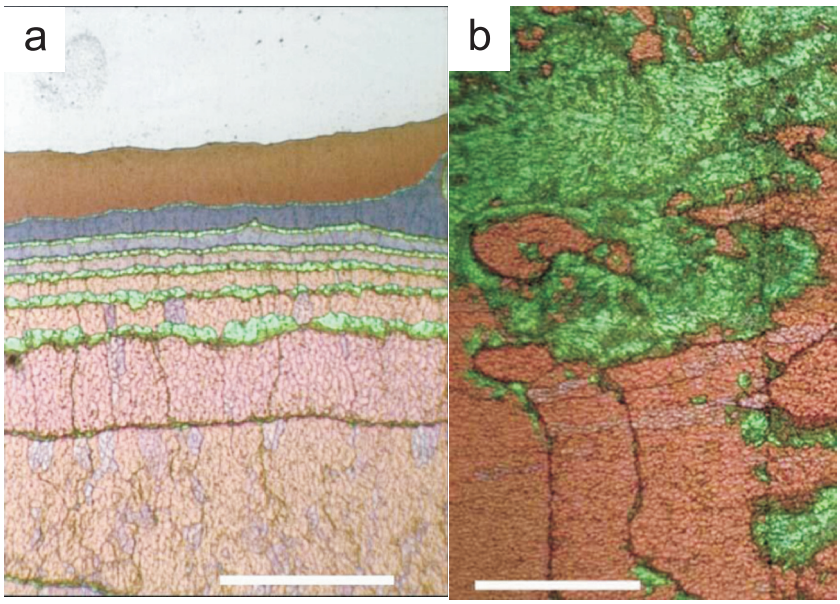

Figure 3.1: Optical microscopy images showing regions with different morphology. **(a)** Initial stages of sample growth at the top of the sample. **(b)** Wide region presenting green and pink colors. Scale bar is 375 μm in both cases.

samples were coated with a thin gold film as customary. Optical microscopy images show sample regions presenting different hue. At the early stages (top of the sample in figure 3.1**a**) growth takes place by the formation of terraces of increasing thickness with steps more or less parallel to the (horizontal) meniscus line. As the sample thickness increases, the color of the terraces varies from brown (1 layer) to pink ($>$ 7 layers). At the boundaries between terraces bright green colors are observed. Even when the sample has reached a stationary thickness (figure 3.1**b**), some regions present fairly wide ($> 1\ mm^2$) green and pink colored areas coexisting. A closer inspection of the above mentioned regions by means of electron microscopy provides structural information at a more local level. Figure 3.2**a** shows the first stages of growth of the sample presented in figure 3.1**a**. In the image, sample thickness grows from one (left) to three (right) layers. Alternation between square and hexagonally arranged planes takes place, and accounts for the different colors observed. Where square arrangements appear green colors are observed, while hexagonal ones account for the brown-pink areas. Such alternation has been previously observed in similar samples [47] and has been accounted for by invoking an optimal filling of the meniscus region where the ordering of the sample takes place [50]. Electron microscopy inspection of large pink (figure 3.2**b**) and green (figure 3.2**c**) areas, as those in figure 3.2**b**, confirms their (111) and (100) orientation. The existence of wide regions with (100) orientation amid the prevailing (111) constitutes a perfect playground to carry out the study of the pseudogap associated with both propagation directions due to their width and thickness.

3.2. Optical study

The whole process is monitored by optical spectroscopy (figure 3.1). For the bare opal, the hexagonal area presents (figure 3.1**a**, left panel) a strong reflectance peak (1160 nm) which corresponds to the calculated [94] pseudogap taking place at the L point. The high energy response ($a/\lambda > 1$) of these regions presents a maximum of intensity for $\lambda = 583$ nm, which accounts for the pink color. Square areas do not present a reflectance peak at low energies (figure 3.1**a**, right panel). This is due to the fact that the pseudogap is closed in the L point for this low refractive index contrast, although a feature in Fabry-Perot oscillations appears in the spectra in the same position ($a/\lambda = 0.7$) where the two sets of degenerate energy bands meet. The green colour of this region is accounted for by the reflectance peak around $\lambda = 517$ nm in the high energy range. Incidentally we wish to say that the high energy response of synthetic opals has been studied before [102, 103, 104] and is known to be a signature of the high quality of the samples. This rules out misgivings about not having a reflectance feature due to low quality of the inspected region.

The degree of infiltration of the opal can be assessed by comparing the spectral position of the first order Bragg from (111) facets with the calculated pseudo-gap in the ΓL direction [105]. Increasing the pore filling fraction with a high index material affects differently the X and L pseudogaps spectral width. A study

performed by means of band structure calculations shows that, for the case of the inverted structure, for which the largest modification of the X-pseudogap is expected, a 35 % filling is optimal for achieving a maximum spectral width for both pseudogaps. Figure 3.1**b** presents the optical response of an opal with such filling fraction. For the infiltrated opal (figure 3.1**b**) a reflectance peak appears in the spectrum from the (100) oriented region due to the opening of a pseudogap in the ΓX direction (0.011 broad in a/λ units). The calculated pseudogap width in the ΓL direction is 0.025 ($\Delta\omega/\omega \sim 0.03$). This difference in breadth explains the different intensity in the peaks corresponding to the two different crystal orientations. That the reflectance peak corresponding to the ΓX direction appears in a spectral position slightly blueshifted compared to the pseudogap predicted by the band diagram in this direction could be explained by finite size effects, previously reported for the ΓL direction [106, 107], but not studied for the ΓX direction yet. After the calcination process and opal inversion, reflectance spectra have been recorded for both crystal orientations (figure 3.1**c**). For the ΓX direction (right panel) reflectance spectra shows a strong (18 %)

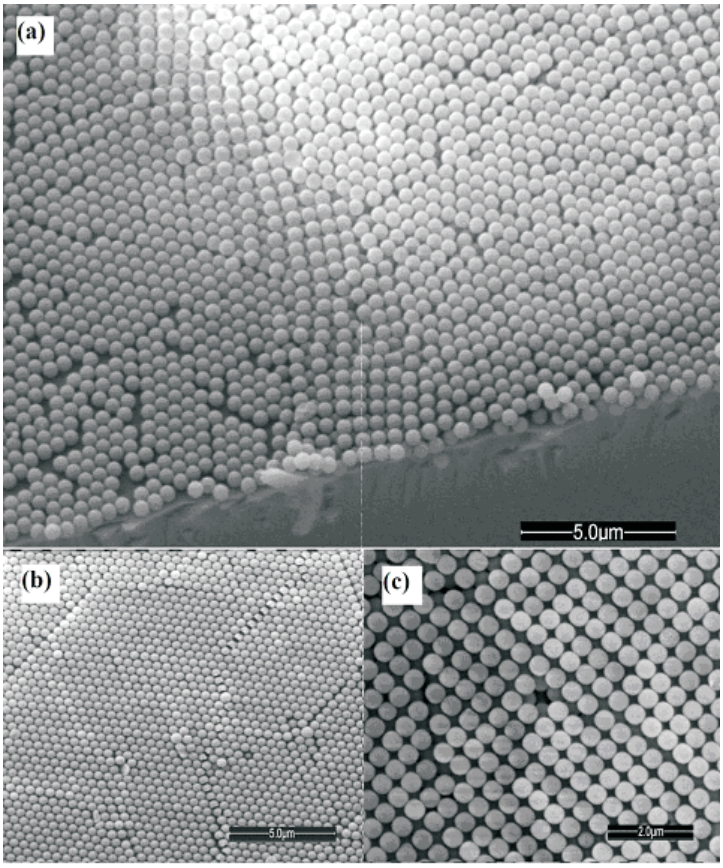

Figure 3.2: SEM images: **(a)** Initial stages of growth at the top of the sample, **(b)** hexagonal areas corresponding to pink regions in figure 3.1**b**, and **c** square areas corresponding to green regions in figure 3.1**b**.

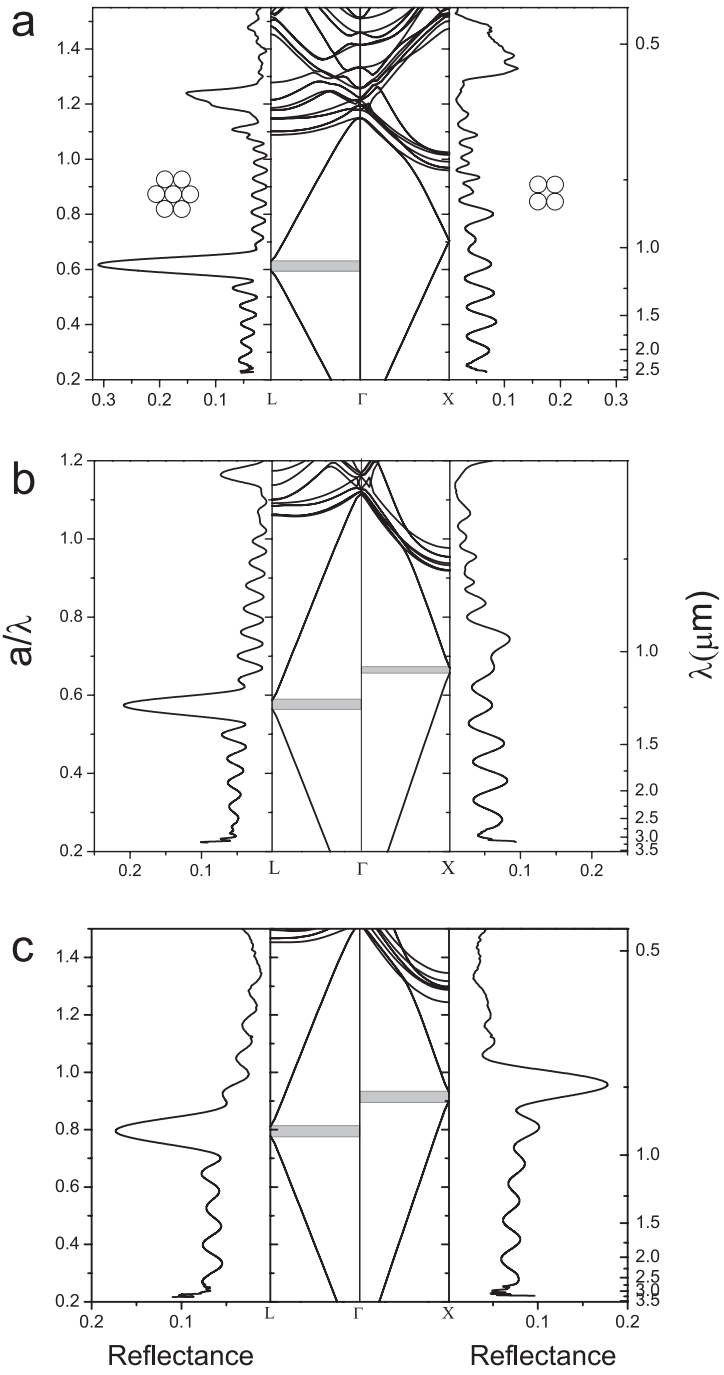

Figure 3.3: **(a)** Left (right) panel shows reflectance collected in hexagonal (square) regions of a bare opal. Central panel shows the corresponding photonic bands. **(b)** Left (right) panel shows reflectance collected in hexagonal (square) regions of a PS−ZnO opal. **(c)** Left (right) panel shows reflectance collected in hexagonal (square) regions of a ZnO inverted opal.

reflectance peak with, approximately, the same intensity as that of the first order maximum along the ΓL direction. This fact is again accounted for by pseudogap widths in either direction in accordance with the calculated bands (0.049 in the ΓX direction and 0.037 in the ΓL direction).

It is also worth mentioning that the high quality of the samples used allows the study of optical features in the high energy regime. In this spectral region interplay between several families of planes strongly modifies the bandstructure of the system and frequency intervals where flat, dispersionless bands develop (e.g. figure 3.1**a**). The group velocity associated with these bands becomes small [24], increasing the interaction time between electromagnetic radiation and the materials forming the crystal. One may benefit from such low group velocity modes to explore enhancement of ZnO emission which could eventually open up routes to fabricate efficient light emitting devices in the UV part of the spectrum.

3.3. Conclusions

In summary, an optical study of the pseudogap occurring in the ΓX and ΓL directions is performed in this chapter, profiting for this purpose from naturally occurring (100) and (111) oriented growth in artificial opals that show facets with square and hexagonal symmetry arrangements respectively. Its dependence on dielectric contrast is demonstrated. An application of bandgap engineering to open an otherwise closed pseudogap which will be very interesting to future refractive applications has been successfully shown. The ability to control the growth of such square layers would redound to the benefit of photonic engineering as it would eliminate a major constrain in artificial opal growth. Work towards this direction is currently being performed.

Chapter 4

Tuning of Quantum dots emission templated on ZnO inverse opals

Light emitters such as organic dyes [109, 110, 111] and semiconductors [112, 113, 114] have been incorporated within the structure of artificial opals during the last few years. Very recently, partial inhibition and enhancement of the spontaneous emission has been shown in inverse titania opals doped with CdSe nanocrystals, matching the first (incomplete) pseudogap [20]. Among the materials for this purpose, ZnO is particularly interesting one. It is a transparent material in a range wider than most infiltrated so far and certainly than most in which photonic bad engineering has been tried. The use of ZnO is important not only for its ample range of transparency but also for its large refractive index. High quality ZnO inverted opals grown by chemical vapour deposition (CVD) (as shown in chapter 2) and atomic layer deposition (ALD) [56] have been reported. Furthermore, the relatively high ZnO refractive index provides enough dielectric contrast in the inverted structure to open additional pGs in the high energy regime which has recently been used for enabling laser emission [28]. The high energy response of photonic crystals [102, 103, 104] presents many of the most remarkable phenomena relating to its photonic nature as anomalous refraction [21], small group velocity [24], and, for certain structures, the opening of a complete PBG [25]. Even though as-grown synthetic opals do not present PBG and their symmetry and topology are fixed by the growth process, they can behave as templates in which different materials can be filled allowing band engineering [97]. This may allow us to modify the band diagram for such systems varying the refractive index contrast of the structure. Careful progressive infiltration with ZnO has revealed peculiar in that many new features develop that were unexpected from previous experience with silica or other oxides (as exposed in chapter 3). Besides, ZnO is of such current interest that its infiltration and characterization in PBG environments is crucial. These two properties along with its lasing action put it in a foremost position which demanded a thorough study

of the possibilities if offers in combination with a PBG environment. Its ample range of transparency allows it to host emitters in a broad spectral range from the infrared to the ultraviolet with no hindrance derived from absorption. All these reasons make ZnO an appropriate template material where quantum dots (QD) can be conformally self-assembled and to optically probe their high energy photonic bands.

In this chapter a large-area, high-quality, new composite material obtained by structuring, in two steps of hierarchical colloidal self-assembly, a ZnO inverted opal with colloidal CdTe nanocrystals is presented. We also provide experimental results of the photonic effect that the original ZnO template produces on the spontaneous photoluminescence (PL) from CdTe QDs embedded in the structure. In particular, we will analyze previously the scarcely explored [115] high-energy photonic bands of the ZnO inverse opal to show that the effect produced shows up as inhibition and enhancement of the QDs emission.

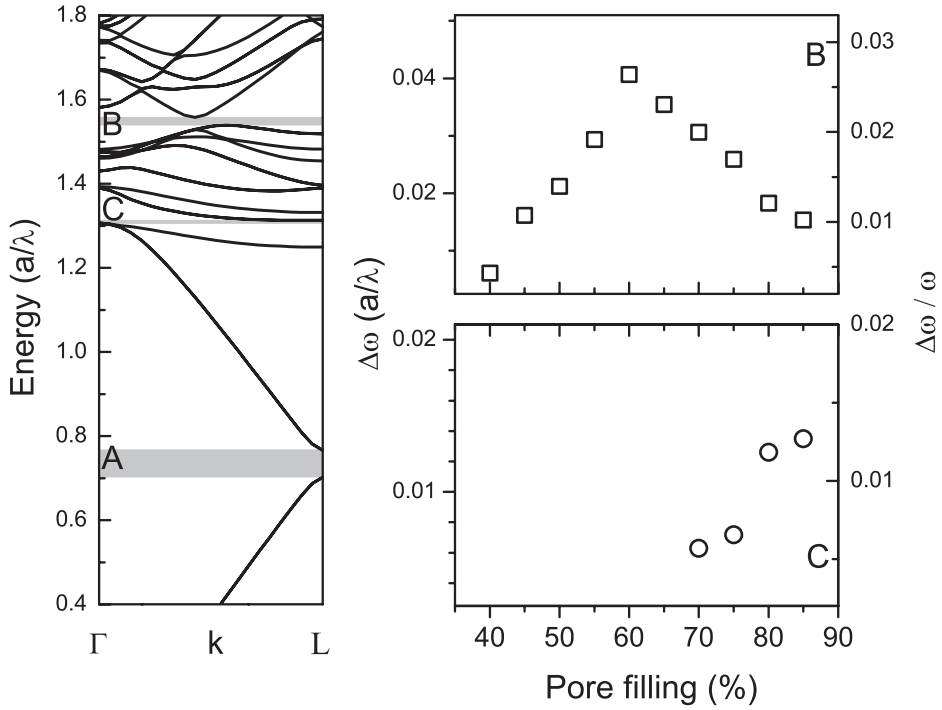

Figure 4.1: **Left panel**: photonic bands with the three pseudogaps opened for 85 % ZnO pore unfilling. **Top right**: spectral width of the second pseudogap (**B**) centered around ($a/\lambda = 1.6$). **Bottom right**: spectral width of the third pseudogap (**C**) opened in the high energy region ($a/\lambda = 1.3$) for greater pore filling fraction.

4.1. ΓL high energy band structure in ZnO inverse opals

In this section, an optical study of the high energy response of ZnO inverted opals is presented. Such systems present, in this frequency interval and for ΓL direction in reciprocal space, the opening of two extra pseudogaps in addition to the lower energy pseudogap present in bare opals. The width of these extra pseudogaps depends on the ZnO fraction present in the opal, which can be controlled in the infiltration process. Experimental evidence of this fact is provided by means of optical reflection and transmission measurements for different filling fractions in good agreement with the calculated bands. In addition, an optical study of the pseudogap appearing in the highest energy interval as a function of sample thickness is performed. The samples exceed the required high quality necessary to resolve their high energy spectral features.

ZnO inverted opals were grown following the method described in chapter 2. Photonic band diagrams corresponding to ZnO inverted opals were obtained using numerical methods [94] as a function of pore filling fraction from 5 % to 85 %. Optical spectroscopy was performed with a Fourier transform infrared spectrometer, as usual in this thesis.

Bands calculated for different ZnO filling fractions in the opals (figure 4.1 left) show how, as a consequence of the increased refractive index contrast, two new pseudogaps are opened in the high energy region of the ΓL direction in addition to the lower energy pseudogap opened in bare opals (which we shall call **A**). For

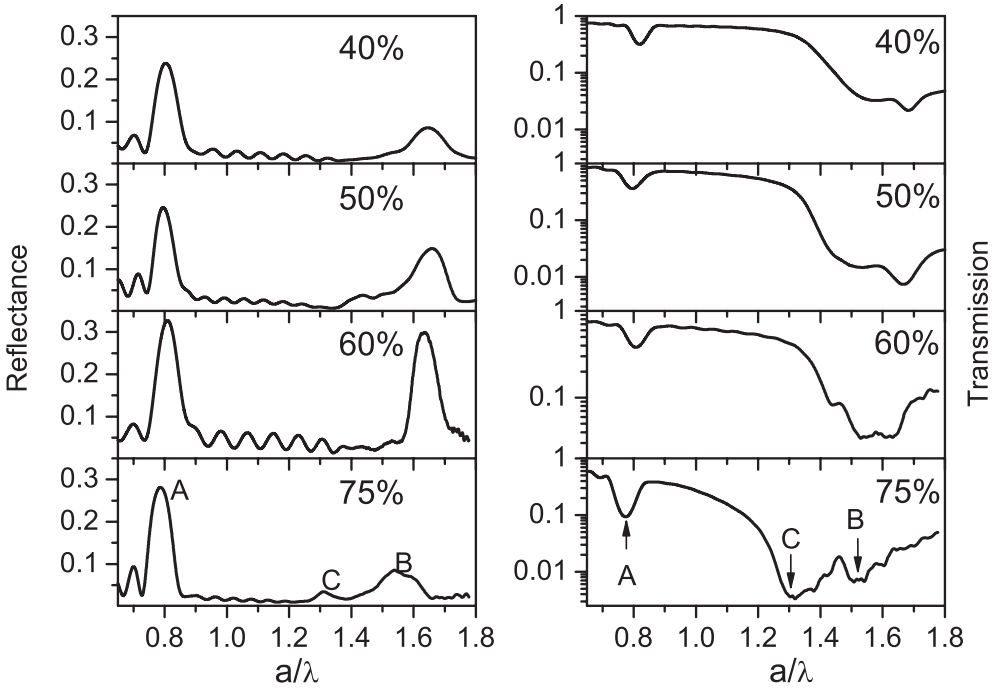

Figure 4.2: Evolution of the three pseudogaps as a function of the pore filling fraction for a fixed thickness (14 layers) as observed in the reflectance and transmittance spectra.

a ZnO pore filling fraction over 40 % a second pseudogap (**B**) appears between the 16th and 17th bands with a spectral position centered around $a/\lambda = 1.6$. This spectral position redshifts with increasing infiltration. The calculated width of this second pseudogap is maximum for 60 % ZnO filling fraction (top panel of figure 4.1), decreasing for further infiltration. In addition to this pseudogap, a third pseudogap (**C**) opens between 5th, 6th bands when the ZnO pore filling fraction reaches 70 %. The spectral position of C pseudogap is centered around $a/\lambda = 1.3$ and varies likewise with the infiltration rate. Its spectral width grows monotonically (lower panel of figure 4.1) with the filling fraction until a complete infiltration (considered for the method used in the process to be 86 % of the pore) is reached.

In order to verify the calculated positions and widths of the B and C pseudogaps appearing in the high energy region, we have infilled samples with ZnO varying the degree of infiltration. We have performed an optical study of the three pseudogaps as a function of ZnO filling fraction (figure 4.2) for a fixed opal thickness (14 layers) by means of reflection and transmission spectroscopy. As

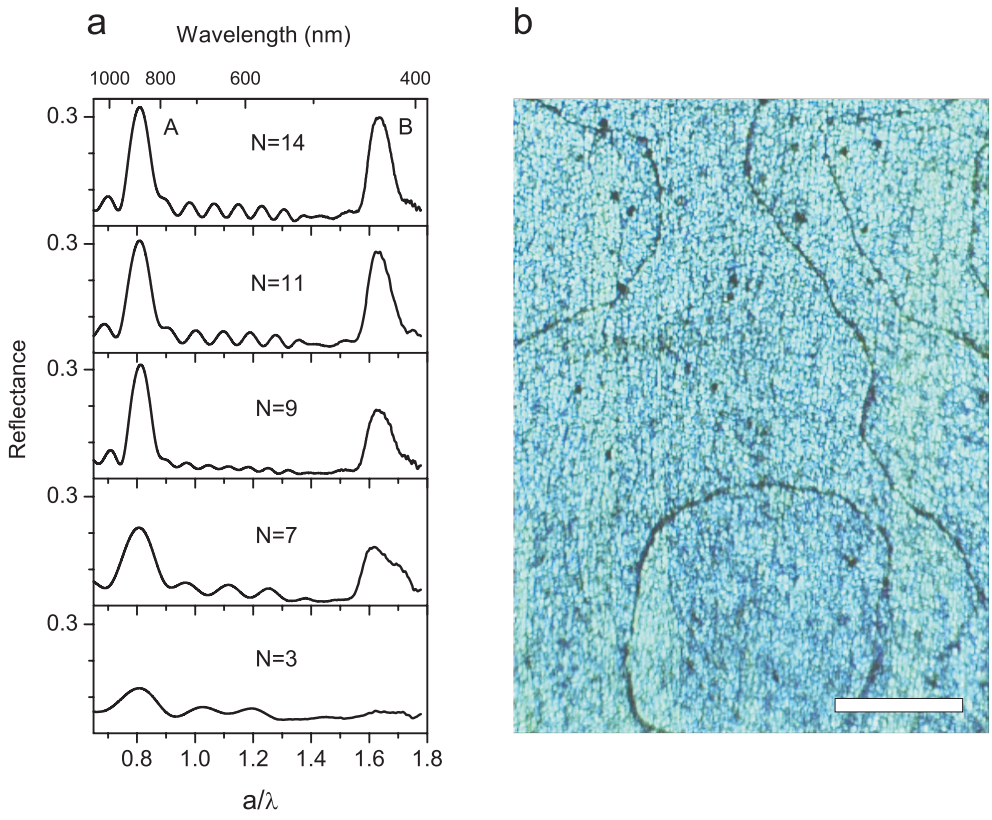

Figure 4.3: **(a)** Evolution of the **A** and **B** pseudogaps as a function of sample thickness for fixed pore filling fraction (60 %). **(b)** Optical microscopy image from the ZnO inverse opal surface. The blue color corresponds to the reflectance peak related to the B pseudogap at 421 nm (these samples have been grown with polystyrene spheres with a diameter $d = 500$ nm). Scale bar is 300 μm

it is known, a pseudogap in the photonic band diagram for a certain direction gives a peak in the reflectance spectra whose intensity grows with the spectral width of the gap. The intensity and the spectral position of the reflectance peak centered around $a/\lambda = 1.6$ evolves in agreement with the calculations. It grows with the ZnO pore filling fraction (> 40 %) having a maximum for a 60 % of ZnO inside the pore and decreasing for greater pore filling fraction. For a 75 % ZnO infiltration, the **C** pseudogap opens around $a/\lambda = 1.3$ in agreement with numerical calculations. The spectral width of the C pseudogap is lower than those of **B** and **A**, which accounts for the intensities of reflectance peaks from each pseudogap. Transmission spectra give complementary information to reflectance ones. In addition to the dip corresponding to the C gap, neighboring dips can be accounted for by diffraction process [104]. We have also performed an optical study of the **B** pseudogap as a function of sample thickness (number of layers) for a fixed filling fraction (60 % for which the width presents a maximum and so does the reflectance intensity). In the evolution of the peak as a function of thickness (figure 4.3**a**) we observe a blueshift which is in agreement with finite size effects for bare opals previously reported [107]. The study of finite size effects shows that, for samples 14 layers thick, these peaks reach a stationary line shape and spectral position, in agreement with the assumption of an infinite-crystal behavior. It is important to point out that, the color of the samples (visible in figure 4.3**b**) is due to light reflectance related to the **B** pseudogap at 431 nm (these

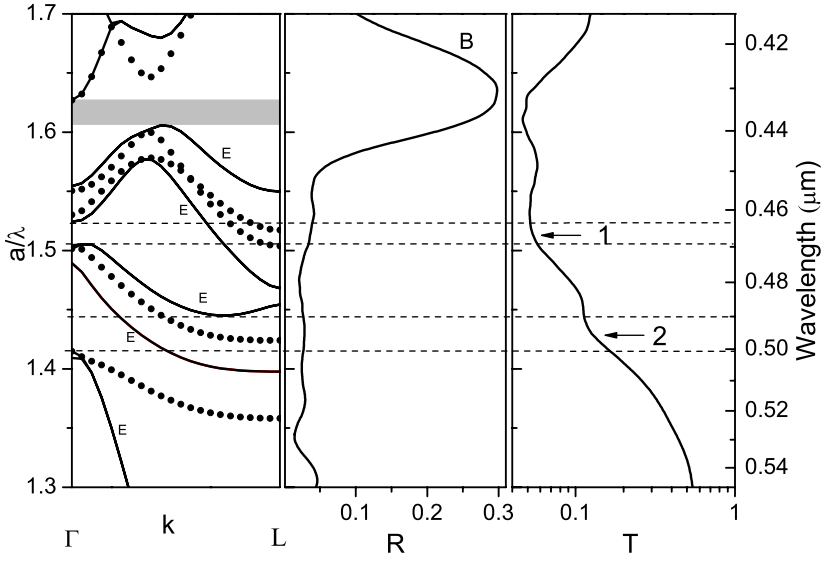

Figure 4.4: **Left panel**: calculated band diagram for 60 % pore filling fraction for which the **B** pseudogap is completely opened. **Right panel**: Reflectance and transmittance spectra are shown for this pore filling fraction. Dashed lines show the spectral ranges where just one mode can be excited.

samples have been grown with polystyrene spheres with a diameter $d = 500$ nm).

For a 60 % ZnO pore filling fraction (for which the **B** pseudogap has maximum width) we have compared reflectance and transmittance spectra with the calculated band diagram in the ΓL direction. It can be observed (figure 4.4) that the 2nd order peaks, both in reflection and transmission, agree in spectral position ($\lambda = 0.43$ μm) with the **B** pseudogap opened as a result of increased refractive index contrast. A spectral region corresponding to diffraction bands ($1.35 < a/\lambda < 1.58$) can be observed in reflectance spectrum which does not present peaks or Fabry-Perot oscillations. In the same frequency interval, transmittance falls and presents some remarkable features. The existence of a lower transmission can be explained attending to the different nature of bands which populate this energy region. Bands can be divided into two groups [103]: bands associated with a homogeneous medium with an effective refractive index (linear bands associated to folding through reciprocal lattice vector parallel to wavevector k) and those associated with diffraction by different sets of planes (diffraction bands). The latter ones represent eigenmodes with non-null components in crystallographic directions other than incident (ΓL in our case). This means that light which couples with these modes will have a moment in other directions of the crystal besides the incident one. Even tough many of these bands are uncoupled due to symmetry reasons [108], allowed modes still exist. We find interesting information about the coupling of these modes with light in reflectance and transmittance spectra (figure 4.4). Different approaches explaining the fea-

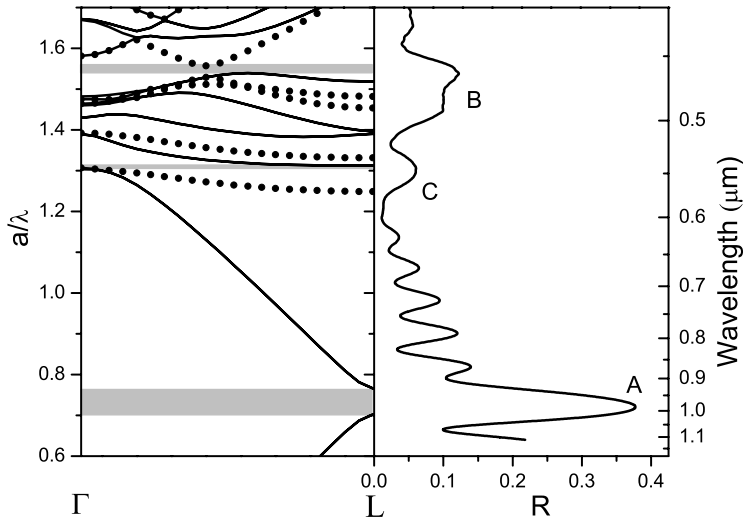

Figure 4.5: **Left panel**: calculated band diagram for a ZnO 85 % pore filling fraction where three pseudogaps are opened. Coupled bands (continuous lines) and uncoupled bands (dotted lines) due to symmetry reasons are shown in the band structure. **Right panel**: reflectance spectrum for this pore filling fraction where three peaks are observed.

tures which appear in the spectra can be found in the literature [103, 102]. In the figure we can observe two dips (**1**, **2**) in transmission which do not correspond to peaks in reflection. These dips appear in spectral regions where just one mode or diffraction band is allowed E labelled states). The absence of features in reflection among the existence of dips in transmission can be understood calculating the structure of the mode excited by the light.

Increasing the ZnO filling fraction over 70 %, a third pseudogap (**C**) can be opened between **A** and **B** ones whose width increases monotonically with the filling fraction. For 85 % filling fraction, the width of **C** pseudogap is enough to observe a peak in the reflectance spectrum (figure 4.5). These narrow peaks can be observed because the quality of the sample is high enough to preserve the gap. It can also be observed that, with a degree of infiltration over 70 %, the first allowed diffraction band (6th band) becomes isolated from the others. The group velocity associated with flat bands becomes small [24], increasing the interaction between electromagnetic radiation and the materials forming the crystal. Such low group velocity modes could be useful to enhance ZnO emission which could eventually open up routes to fabricate efficient light emitting devices in the UV part of the spectrum, which will be subject of study in chapter 9.

4.2. Quantum dots infiltration

Samples were prepared starting from large diameter (700 nm) polystyrene (PS) spheres in order to place the desired photonic features (high energy gaps) matching the QD emission band (around 640 nm for a QD diameter, $d = 4$ nm). The CdTe QDs were synthesized in water following a previously described method by utilizing thioglycolic acid (TGA) as stabilizer [116]. The molar ratio of Cd^{2+} ions to TGA was 1 : 1.3, which allowed the synthesis of high-quality NCs possessing PL quantum yields of up to 50 % without any post-preparative treatment [117]. Figure 4.6 schematically depicts the method used to fabricate the composite material. Thin film opals (figure 4.6**a**) were grown using the common vertical deposition method [45] and then were infiltrated (figure 4.6**b**) with ZnO following a modified CVD method explained in chapter 2, which allows a controlled conformal infiltration with few nanometers precision. The structure was then inverted (figure 4.6**c**) to obtain the ZnO template, eliminating the polymer backbone by calcination. The CdTe QD infiltration (figure 4.6**d**) of the templates (figure 4.6**d**) was performed as follows: the photonic matrix was immersed in a dilute solution of CdTe nanocrystals in doubly distilled water with a concentration of 5.3×10^7 M and was vertically pulled with a step motor. A fine control over the pulling velocity (0.2 $\mu m/$ min) was exerted until the sample was completely removed from the QD colloidal suspension. The sample was finally heated for 3 h at 45 $^{\circ}C$ in order to completely dry it. This leads to an accurate deposition of QDs on the surface of the ZnO shells as figure 4.6**d** schematically reproduces. This process can be repeated as many times as needed. We should remark the fact that QDs are deposited both on the inner and the outer ZnO surfaces. The inner growth is possible because the spherical air cavities are connected by windows produced in

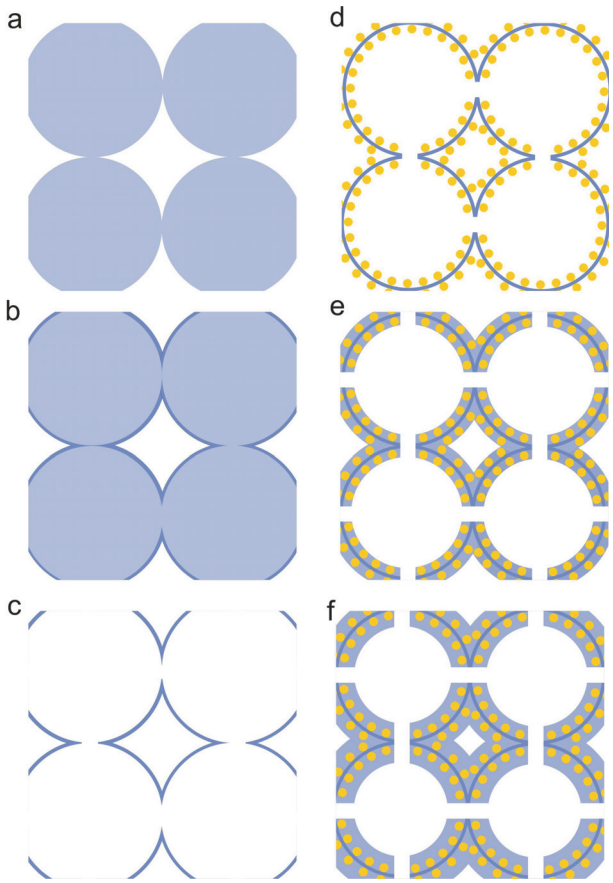

Figure 4.6: Schematic diagram of the method used to fabricate the composite material: **(a)** Growth of a PS opal. **(b)** CVD infiltration of the PS matrix with ZnO. **(c)** Removal of the polymer matrix by calcination. **(d)** CdTe nanocrystals conformal infiltration by dip coating. **(e)**,**(f)** Additional ZnO infiltration by CVD.

the contact points between the original spheres, which remain open after calcination. The size of these windows depends on the degree of sintering and the grown material, in this case ZnO, but typically they are around 10 % of the diameter (70 nm in our case). This interior growth is possible while these windows remain open.

Once the desired amount of QDs are assembled, a thin layer of ZnO can be regrown to bury them (figure 4.6**e**). Additional ZnO infiltrations can be subsequently performed to obtain the desired photonic effects in the final composite (figure 4.6**f**). Optical spectroscopy (figure 4.7) were performed to characterize the sample.

Reflectance (transmittance) shows two peaks (dips) related to the first and the second pGs in the ΓL direction. For the sphere diameters worked with here, the PL emission band overlaps with the second pG of the ZnO photonic matrix. The infiltration of the photonic template with QDs very slightly changes the refractive index distribution, hence the photonic properties of the structure. The optical

properties are so sensitive to these minor changes that they can be used to monitor the process with high precision by measuring the shift of the photonic features. Figure 4.8 shows the specular reflectance, along the ΓL direction (normal to the (111) planes) versus energy in reduced units (a/λ , where a is the lattice parameter and λ is the wavelength in vacuum) for a ZnO inverse opal after several immersions in the QD solution. The maxima in reflectance correspond to the high energy pG that shifts to lower energies after every coating step.

By a sequence of several immersions it is possible to infill the ZnO template with a fine control over the filling fraction thus tuning the photonic bands to the desired specifications for optimal performance. It is important to point out that this spectral displacement depends on the concentration of the QD solution employed. In order to study how the QD are deposited on the surface of the ZnO shells we modelled this process assuming that in each immersion a thin homogeneous layer of CdTe conformal to the ZnO shells is grown. We have calculated [94] the position of the mentioned photonic feature (high energy pG) as a function of the CdTe layer thickness and compared the calculated results with the experimental spectral positions. In figure 4.8**b**, experiment and theory are plotted together showing a good agreement for a 0.5 ± 0.1 nm CdTe layer thickness on either side of the ZnO shell per immersion, for this particular dip coating conditions. The specific calculations of the spectral displacement of the high−energy pG, assuming a CdTe thin-layer deposition, rapidly diverge from the experimental results when the thickness departs from 0.5 nm per immersion. This thickness is related to the initial concentration of the CdTe solution. With higher concentrations, the thickness needed to model the infiltration increases accordingly. The final thickness after 5 immersions, 2.5 nm, is that of a close

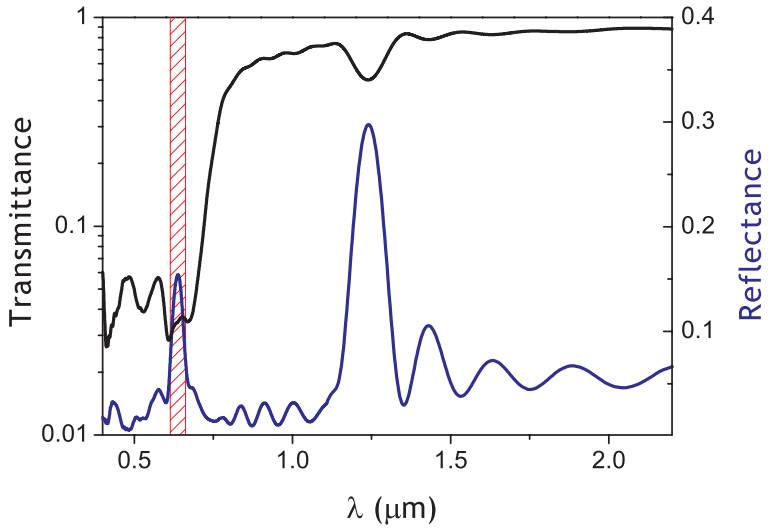

Figure 4.7: Reflectance (blue curve) and transmittance (black curve) of a ZnO inverted opal. First and second order pGs in the ΓL direction are evident. The PL band from the QDs is represented by the dashed area.

packed monolayer [118]. The actual surface on which QDs assemble is, however, extremely rough at the nm scale and, accordingly, the QDs are not close packed. Nevertheless, the surface can be considered flat and smooth as far as the optical properties in the visible range of the spectra are concerned, because ZnO grains (typically 30 nm) are much smaller than wavelengths involved (around 600 nm) which, in case of dielectrics, can be considered negligible.

4.3. Quantum dots emission tuning

We have focused our study of the photonic properties of the new composite material on the high energy regime ($a/\lambda > 1$) where interesting phenomena like slow light or anomalous refraction can take effect and where a full PBG can emerge. Besides, in this spectral range, as opposed to the low energy regime (first stop gap), the interplay between light and PBG environments has remained relatively unexplored. The reason for this is that very high quality samples are needed since, in this regime, the wavelengths involved are smaller than the lat-

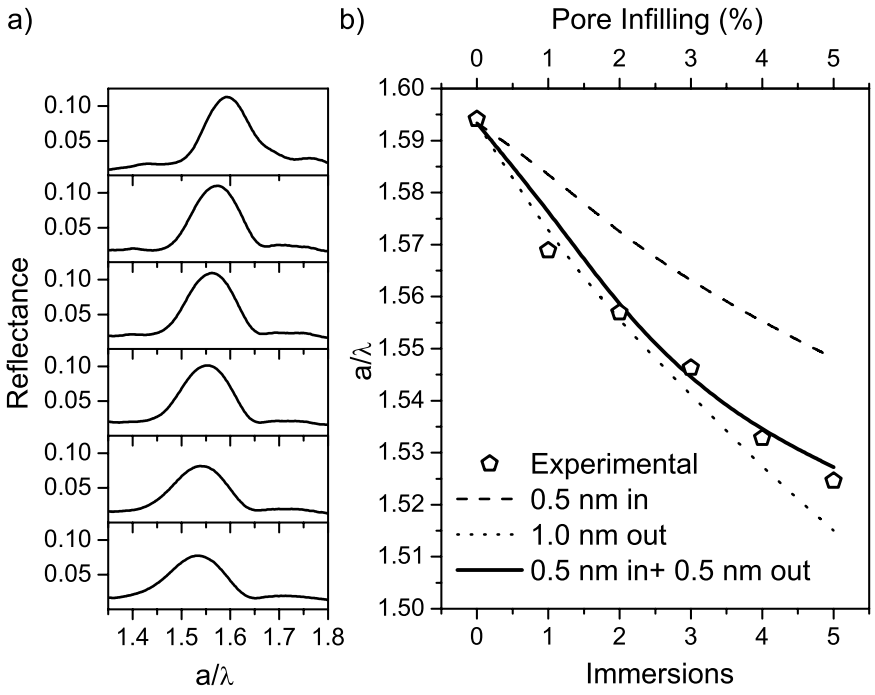

Figure 4.8: **(a)** Spectral displacement of the second-order Bragg peak as a consequence of the QD infiltration. **(b)** Open symbols represent the experimental displacement of the reflectance peak associated with the pG while the solid line represents the evolution of the pG assuming a CdTe thin layer deposition of 0.5 nm (on either side) per immersion.

tice parameter. Therefore, the lattice is explored on a very short range scale where the imperfections are exacerbated. This makes this energy range particularly interesting to test the photonic properties of the new composite. For this purpose, we have used a band engineering strategy [97] (also described in chapter 4) designing composites with given photonic properties by means of accurate infiltrations. A careful balance of the QD infiltration and the posterior ZnO coverage provides a means to accurately match the luminescence to the photonic gaps. In figure 4.9 we show the evolution of the relevant photonic bands for the ZnO/CdTe composite as the additional ZnO layer is increased (following scheme in figure 4.6**f**). The open circles represent photonic bands to which light can not couple due to symmetry restrictions and the solid lines represent the bands that determine the gap [108]. The dashed area represents the energy interval where QD emission takes place and the greyed areas are the effective gap. By varying the degree of infiltration it is possible to tune this pG (see that greyed areas shift with infiltration) sweeping across the whole luminescence band.

In this simulation, panel **(a)** depicts the bands in the case of the initial structure: a ZnO shell 31 nm thick (arising from the original opal after 6 CVD cycles and inversion) coated with a QD layer 1 nm of equivalent thickness as explained

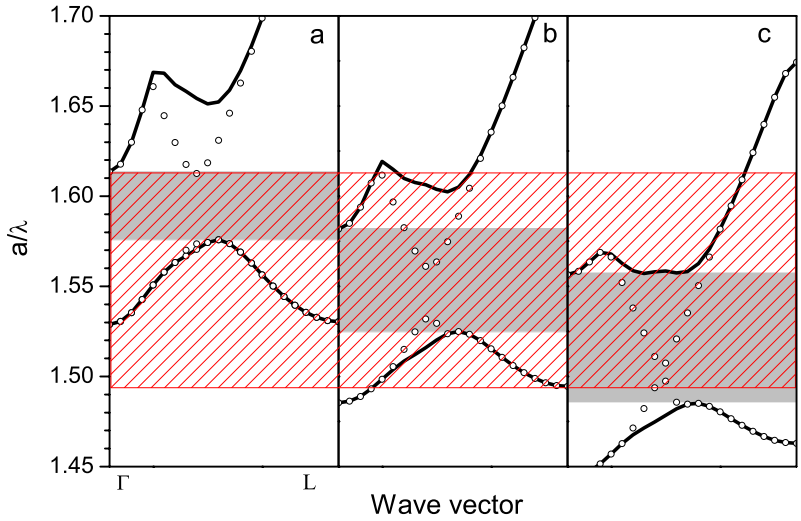

Figure 4.9: Band structure of QD-containing ZnO inverse opals. **(a)** The stage where a 1 nm layer of QDs is added to an inverse opal produced by synthesizing a 31 nm ZnO layer (55 % of the pore) on the opal and inverting. In panel **(b)** an extra ZnO infiltration of 3 nm is added and in **(c)** a further 3 nm layer is grown. The PL band from the QDs is represented by the dashed area and the effective gap by the shaded rectangles. Lines represent the allowed states while dots represent uncoupled bands.

above (two dip coating immersions). Panel **(b)** shows the photonic bands from a structure derived from the latter one by growing a 3 nm thick layer (a single cycle of CVD) on the inner and outer surfaces of the QD decorated shell. Finally, panel **(c)** corresponds to the growth of a further 3 nm thick ZnO layer in an additional single CVD cycle. Although shell thicknesses of quantum dots of the order of 1 nm is invoked, let us remark that this is an effective thickness to simulate the physical infiltration.

The actual properties of these structures are discussed next. The emission properties of the composites prepared were measured and compared with those of the same sources without pG environment. To ensure that the standard PL was free from any effects arising from the interaction of the QDs and the ZnO template we used the PL emission from a pulverized sample rather than a colloidal suspension of QDs. Grinding destroys the photonic lattice and wipes out any pG effects. This system, with no pG properties but the same QD density and material properties as the original sample, is what we shall call standard PL emission. PL measurements were taken at room temperature under 457.9 nm Ar^+ laser line excitation focused onto the back surface of the sample at non-normal incidence. The emitted light from the (111) face of the composed structure was collected with a low-aperture lens ($f/3.5$) and focused onto a spectrometer equipped with a photomultiplier tube.

Figure 4.10 summarizes the results from three samples differing in the amount of ZnO added (increasing from (**a**) to (**c**)) after the QDs were adhered to the

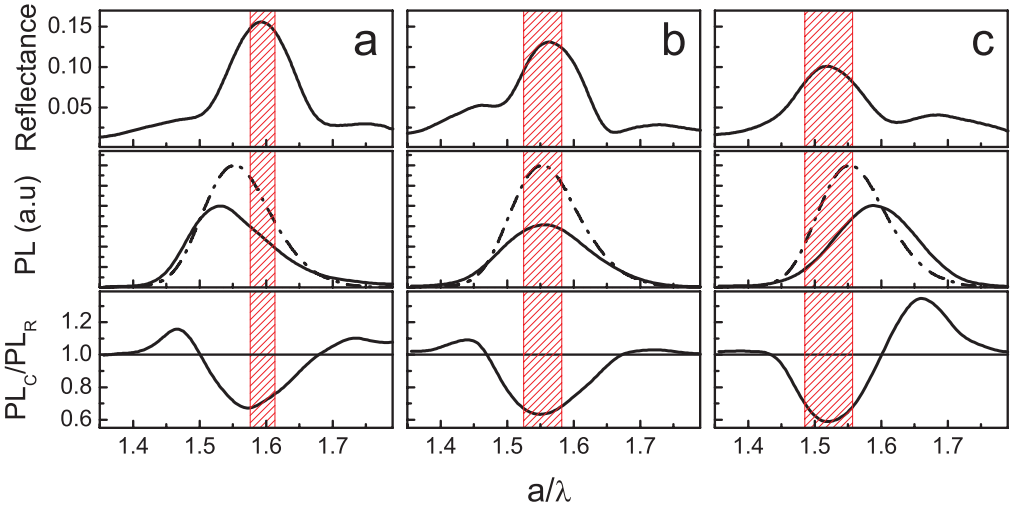

Figure 4.10: Each vertical panel corresponds to a different stage of additional ZnO infiltration. **Upper row**: the calculated spectral position of the reflectance peak in the ΓL direction (dashed area) is shown, with the experimental reflectance, as a function of additional ZnO infiltration. The **center row** shows the comparison between the PL emission in the photonic matrix (PLC, solid line) and the PL of the standard (PLR, dashed line). **Lower row**: Plot of the ratio of PLC/PLR. Values lower than one signify inhibition whereas higher values signify enhancement of the emission.

initial template. In the upper row of plots the reflectance peak is seen to shift to lower energies and broaden as we increase the ZnO content, following the behavior of the calculated pG (dashed areas in the figure). In the middle row, the emission spectra from the reference PLR (dash-dot lines) and composites PLC (solid lines) are plotted. Finally, the ratioed luminescence intensities PLC/PLR are plotted in the bottom row in order to explicitly show the effect. In the stage represented by the panel 4.10**a** (which corresponds to the state of the composite schematically drawn in figure 4.6**d**) the gap overlaps the high energy side of the PL spectrum. Emission in this energy interval is inhibited. The result is a modified emission profile which presents a strong suppression in the high frequencies and an enhancement of low ones compared to the standard PL. An additional infiltration of ZnO in the composite produces a redshift of the photonic features. Panel 4.10**b** corresponds, qualitatively, to the situation drawn in figure 4.6**e** and the corresponding photonic bands are those calculated in figure 4.9**b**. The gap now overlaps with the central frequencies of the PL band which are therefore inhibited. The dip in the radioed PL redshifts as the gap does. In the final panel 4.10**c** (which corresponds to stage drawn in figure 4.6**f** and to the bands in figure 4.9**c**) the gap overlaps with the low energies of the PL band tuning the inhibition to this side of the peak and reinforcing the emission in the high energies. We can see how in passing from figure 4.10**a** to figure 4.10**c** the balance of suppression to enhancement is governed by tuning the photonic bands which in turn is controlled by the amount of material added. We see that initially there is suppression on the high energy side and inhibition on the low, whereas in the final stage the high energies are enhanced at the expense of the low energy range. Among possible mechanisms for PL modifications [119], a process of electronic energy transfer [120] could explain the effect of enhancement attending to the relatively high concentration of emitters inside the composite. One important feature we wish to point out is that the absolute value of reflectance that is causing the enhancement/suppression of the emission is only a few percent. This might not only be caused by the fact that samples are just a few layers thick: this gap, as opposed to the well known fundamental pG at L, produces small reflectivities even in infinitely thick samples. In our analysis we are discounting those bands that cannot couple to incoming plane waves but that are present in the gap. In reality these bands might be actually coupling through defects and lessening the effect. Related to that, we must remark that the high order pG appears at $\lambda = 605$ nm which is smaller than the original PS sphere diameter (700 nm). This implies that this pG is much more sensitive to the presence of defects in the sample than the first order pG.

4.4. Conclusions

In conclusion, a novel structured composite that integrates two very relevant materials such as ZnO and QD in a photonic crystal has been reported in this chapter. Theoretical and experimental evidence of the opening of two extra pseudogaps occurring in the high energy range of ZnO inverse opals is provided. The

high quality of the samples used in this work allows us to perform an optical study of the three pseudogaps by means of reflection and transmission as a function of the pore filling fraction which are accounted for by the calculations. The optical response of the widest high Energy pseudogap as a function of the sample thickness is also presented.The posterior QD infiltration in ZnO inverse opals is performed by an accurate infiltration in two hierarchical steps of colloidal self-assembly. The method to infill a ZnO matrix with CdTe nanocrystals provides a fine control over the pore filling fraction and we prove that the infiltration of nanoparticles behaves, from the structure point of view, as a thin-layer conformal infiltration. This is, in the current state of the art, the only way to control the infiltration of QD. To test this novel composite experimental results of the effect that the photonic matrix has on the spontaneous emission of the PL in the high energy regime are provided. The CdTe QD emission is tuned to this regime of the ZnO template to profit from the wide range of infiltration produced by the large size spheres. The presence of a high energy pG on the spontaneous emission has been experimentally reported as an inhibition for frequencies contained in the gap and enhancement of those on the edge of the gap. Finally, a further careful and progressive infiltration with an extra amount of ZnO has revealed useful to tune this photonic effect through the PL emission spectrum. This novel procedure to build a composite from a photonic template and quantum dots in the same photonic matrix opens a route to heterostructure different materials with different types of nanoparticles.

Part II

Photonic Glasses

Chapter 5

Photonic Glasses

There is a wide range of disordered materials used for photonics. The most commonly systems are those composed by oxides or semiconductor powders such as TiO_2 [121], ZnO [122], $GaAs$ [123], Ge [124]; usually these systems are formed by particles with spherical shape presented both in solid arrangements such as Al_2O_3 [125], ZnO [126], TiO_2 [127, 128] as well as in colloidal suspensions [64, 129]. In all these cases, the particles composing the system are polydisperse in shape, size or both and the individual electromagnetic modes of each building block give rise to an averaged out optical response in wave-vector and frequency [8]. Up to this moment, there are no available disordered materials composed by monodisperse scatterers. In this chapter a novel disordered material for photonics is proposed whose main property is the monodispersity of the building blocks, in this case polymer spheres (see, for example, [130]). A new range of interesting phenomena will be affected by this novel property of the scatters, giving rise to a resonant behavior of diffusion constant, transport mean free path and energy velocity as well as resonant random lasing action in macroscopic arrangements of this kind of scatterers.

5.1. Colloidal stability

A colloid is a two phase (at least) system in which one substance (the internal phase) is divided into minute particles (colloidal particles) with dimensions between 1 nm and several microns dispersed throughout a second substance (the external phase). The size is not the most important property of colloids, the overwhelmingly important property of colloids is their very large surface area. To some degree, they are all surface and their properties are those of their surfaces. The large area emphasizes surface effects relative to volume effects, giving colloids properties different than those of bulk matter.

Different types of colloids can be distinguished depending on the state of matter of each phase. It is possible to find sols (solid in liquids), emulsions (liquid in liquid), foams (gas in liquid), aerosols (liquid or solid in gas) and solid suspensions (solid in solid). In this thesis we only deal with sols composed by

polymer spheres (PMMA or PS) dispersed in a liquid (water). The particles that appear in the sol may be wetted by the water, or may not. Wetting is a typical surface effect and is of paramount importance in a colloidal system. In the first case, the liquid is adsorbed on the surface of the particle and is called lyophilic (hydrophilic if the external phase is water). On the other hand, if the particle does not adsorb the external phase, it is said to be lyophobic.

There are two questions related to the stability of a sol. First, what keeps the particles suspended in the solution? Second, how are the particles kept from agglomerating? A sufficiently small particle acquires a small falling velocity into the solvent, the characteristic time in which the particle settles becomes very long compared to measurements time, and an equilibrium sate may be considered. There is a critical size for a particle, below which it will not settle. For the second question: if two colloidal particles collide, they will stick together and make a bigger particle or, eventually, a cluster. Clusters get larger than the critical size to be suspended by the Brownian movement, and they settle. In most lyophobic colloids, the particles are electrically charged with the same sign, and this keeps them apart, since they repel one another. Since lyophobic sols are stabilized by electric charge, adding extra charge (electrolytes) generally destroys the sol. For example, when rivers reach the sea with their loads of colloidal sediment, the ions in sea water coagulate the sol and the load is deposited forming the delta.

The modelling of the many-body potential of an aqueous colloidal suspension represents a very complicated problem which can be approximated as a (two-body sphere-sphere potential) sum of two terms:

$$U(r) = \phi(r) + U_{VdW}(r) \tag{5.1}$$

where $\phi(r)$ is the electrostatic repulsive potential due to the sphere surface charge and $U_{VdW}(r)$ is the attractive Van de Waals potential (also known as *London dispersion forces*). In this chapter a method will be explained based on this two-body interaction between the spheres to grow completely disordered arrangements of monodisperse ($< 2\%$) dielectric spheres. The growth procedure entails adding electrolytes to the colloidal suspension which attenuates the surface sphere charge and, therefore, $\phi(r)$.

In the limit of low colloidal density, $\phi(r)$ reduces to the well-known $Derjaguin-Landau-Verwey-Overbeek$ (DVLO) repulsion [131, 132] that can be calculated on the basis of the Poisson-Boltzmann equation. In the case of a, so-called, charge colloidal suspension formed by colloidal particles with diameter d and surface charge Z_0 and a collection of point-like charges (electrolytes) with charge Z and concentration, ρ_e, the electrostatic repulsion of any two particles as a function

of the particle-particle distance (r) is given by [133]

$$\begin{aligned} \phi(x) &= \frac{(Z_0 X)^2}{\beta} L_\beta e^{-\kappa} \frac{e^{-\kappa(x-1)}}{x}; \quad x > 1 \qquad (5.2) \\ x &= r/d \\ \beta &= \frac{1}{k_B T} \\ X &\longrightarrow \frac{e^{\kappa/2}}{1+\frac{\kappa}{2}} \\ L_\beta &= \frac{e^2 \beta}{4\pi\varepsilon\varepsilon_0} \\ \kappa &= \kappa_D d = (\sqrt{4\pi L_\beta \rho_e Z^2}) d \end{aligned}$$

This repulsive potential decreases exponentially when increasing the concentration of electrolytes (ρ_e). The *Debye lenght*, $\kappa_D = \sqrt{4\pi L_\beta \rho_e Z^2}$, describes the double layer thickness around the particles, where Z is their charge (Z_i, if there is more than one species of electrolytes) and their concentration ρ_e, ($\rho_{e,i}$). The double layer consist of two types of charges: *charge-determining* ions that control the colloid surface charge and *electrolytes* which are attracted by this charge, screening it partly and decreasing $\phi(r)$. According to this and considering that it is usually the surface charge potential ψ of a charged particle that is experimentally available, the approximate formula $Z_0 = \pi\psi\varepsilon_0\varepsilon(2+\kappa)$ is commonly used (see [132], p. 37).

The *Van der Waals* attractive potential can be expressed as follows

$$U_{VdW}(r) = -\frac{AH(x)}{12} \qquad (5.3)$$

where A is the *Hamaker constant* which depends on the colloid material [134] with values 10^{-19} J to 10^{-20} J and is given as a function of colloid-colloid distance (r) as:

$$\begin{aligned} H(x) &= \frac{1}{x^2-1} + \frac{1}{x^2} + 2ln(1-1/x^2) \qquad (5.4) \\ x &= r/d \end{aligned}$$

Figure 5.1 plots the total interaction, $U(r)$, between two particles as a function of the electrolyte concentration according to the equations equation 5.1, 5.2, and 5.3. The specific parameters used for this particular exemplification are a particle diameter $d = 1220$ nm with a surface potential $\psi = -30$ mV (measured with a standard electrophoretic mobility experiment) and the electrolytes (Ca^{2+} from

$CaCl_2$) added to this suspension have $Z = 2$ and their concentration varies from $\rho_e = 0$ M to $\rho_e = 5 \times 10^{-2}$ M. The *Hamaker constant* for PS microspheres in water is $A = 1.32 \times 10^{-20}$ [135]. As a mater of fact, there is a high probability of flocculation as a result of the collision between two particles if the potential barrier $U_M \leq 10 k_B T$, where r_M is the reduced particle-particle distance at which $U(r)$ has the maximum value. This fact is pointed out in the right panel of figure 5.1, where energies bellow this value are shaded in grey. For electrolyte concentrations for which $U(r_M) \leq 10 k_B T$, the instability of the colloidal suspension is ensured and colloidal flocculation will take place. In this particular case, for an electrolyte concentration $\rho_e = 1 \times 10^{-2}$ M, the potential barrier is $U(r_M) \sim 6 k_B T$ and the Brownian energy is enough to force the colloidal flocculation.

5.2. Experimental procedure

PS spheres employed in this thesis have been synthesized by the Goodwin method [40], which gives rise to a negative surface charge of the particles. PMMA spheres were synthesized following a similar method [41]. In both cases, positive electrolytes are needed to screen the negative surface charge of the colloids (which

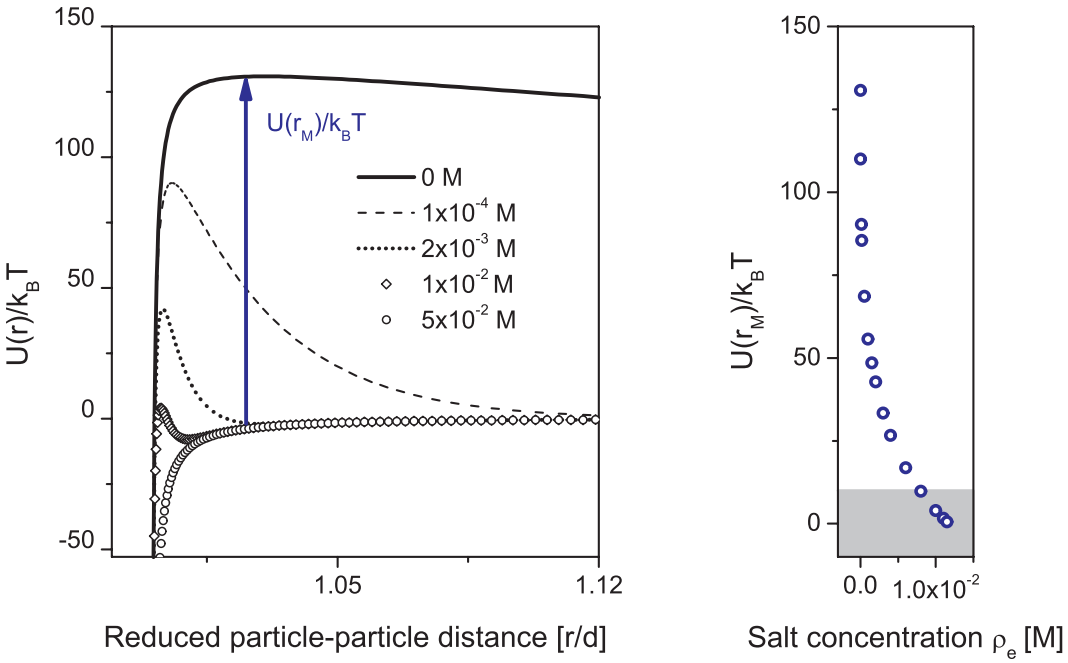

Figure 5.1: **Left panel:** Plot of the total interaction potential between two particles relative to the thermal energy as a function of the concentration of electrolytes in the suspension according to the solution proposed in ref [133]. **Right panel:** The magnitude $U(r_M)$ represents the potential barrier which prevents the colloids from flocculating. This barrier decreases when the electrolyte concentration increases. Energies bellow $10 k_B T$ are shaded in grey. If the potential barrier is lower than this energy, the colloids are able to flocculate. In this particular case, this happens for $\rho_e \geq 7.5 \times 10^{-3}$ M.

otherwise prevent the natural agglomeration) and can be obtained by adding salts (which dissociate producing positive and negative ions in dissolution) or acids (which also dissociate producing protons and also negative radicals). The charge, Z, of the ions or the number of protons dissociated from an acid is an important parameter. The concentration of salt or acid needed to provoke the colloidal flocculation is inversely proportional to their charge. For example, half the concentration of a salt such as $CaCl_2$ (which dissociates producing Ca^{2+} ions) is needed than a salt such as $NaCl$ (which dissociates producing Na^+ ions) to provoke the colloidal flocculation. The attenuation of the repulsive potential gives rise to a net attractive potential between spheres. In this case, the number of effective collisions between spheres increases and clusters are formed by flocculation in the suspension. When the size of the clusters is larger than the critical size they settle. The formation of clusters inhibits the self-assembling process which takes place during the liquid evaporation process and, consequently, a random distribution of disordered clusters is obtained.

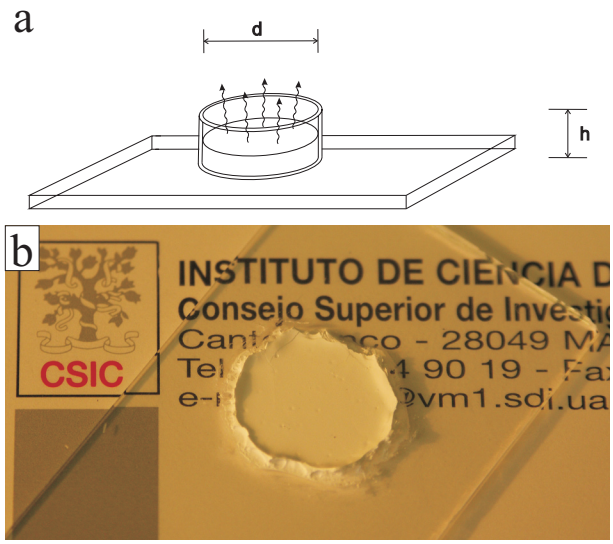

Figure 5.2: **(a)** Schematic of the photonic glass growth method. A methacrylate cylinder of high $h \sim 1$ cm is fixed with impermeable gum to a clean, hydrophilic glass substrate. It is then filled with a charged colloidal suspension previously prepared and shaken under ultrasound. Then it is placed in a oven under constant temperature ($\sim 45°C$) to forced the evaporation of the liquid phase. Finally, the methacrylate cylinder is removed from the glass substrate. **(b)** Picture of a photonic glass grown on a substrate. The sample shows a high degree of planarity, apart from the irregularity of the edge.

In order to control the thickness and the area of the system, a methacrylate cylinder of height h and diameter d is glued with flexible and impermeable gum to a clean hydrophilic glass microscope slide (see schematic figure 5.2**a**). In a typical procedure, a total volume $V_T = 3$ ml of an aqueous suspension of PS spheres with 1220 nm in diameter and $CaCl_2$ is prepared as follows: a $V_s = 2.5$ ml volume of a colloidal suspension of PS spheres with a concentration $\rho_s = 20\ g/l$ ($2\%\ wt$) is added to a volume $V_e = 60\ \mu$l of $CaCl_2$ with a concentration $\rho_e^i = 0.5$

M. To reach the total volume, $V_w = 0.44$ ml of de-ionized water is added. The final concentration of electrolytes in the final suspension is $[Ca^{2+}] = \rho_e^f = 0.01$ M. This aqueous suspension is shaken under ultrasound for 5 min to force the spheres flocculation. The cylinder of diameter $d_c = 2$ cm is then filled with the suspension which is let evaporate in an oven with constant temperature, typically at $T = 45°C$. The sample is left inside the oven for a time long enough as to allow the total evaporation of the liquid. When the liquid is completely evaporated, the cylinder is removed from the substrate, the photonic glass remaining attached to it (see image 5.2**b** and SEM images from the system in figure 5.3). In order to avoid possible cracking (see image 5.3**c**) or peeling of the sample from the substrate, it is important that the cylinder is not touching the substrate, leading a small air chamber between the cylinder, the substrate and the gum. As a matter of fact, a small fraction of colloidal suspension fills this air chamber by capillarity and the sample is more strongly attached to the substrate (see picture 5.2**b**). Proceeding this way, no cracking appears when removing the methacrylate cylinder from the substrate.

The typical thickness obtained in this case is $t = (31 \pm 5)$ μm constant over centimeters (see figure 5.3**b** and 5.3**c**). The following table 5.1 shows the measured thicknesses of five different photonic glasses with five different concentration of spheres where $V_T = 3$ ml, $V_s = 2.5$ ml and $d_c = 2$ cm. The thickness of the photonic glasses is measured using a low magnification objective and measuring the focussing on the substrate and on the glass surface and subtracting both measures.

If the salt concentration is increased, the repulsive barrier is lowered and, consequently, the size of the clusters formed by flocculation is increased. If the salt concentration increases, the number of effective collisions required to attache two particles decreases. Figure 5.4 shows four SEM images corresponding to four different electrolyte concentrations in the colloidal suspension: $\rho_e = 0$ M, figure 5.4**(a)**, 2×10^{-3} M, figure 5.4**(b)**, 1×10^{-2}M, figure 5.4**(c)** and 5×10^{-2} M, figure 5.4**(d)**. It is directly evident how the self-assembly process is inhibited by adding ions to the colloidal suspension.

In the case of $\rho_e = 0$ M **(a)**, the fcc arrangement of spheres is similar to the one obtained by the vertical deposition method (see inset of figure 5.4**a**). For this concentration, the electrostatic barrier is about 130 times the thermal energy, the spheres cannot flocculate but they are self-assemble during the evaporation process. In the case of $\rho_e = 2{\times}10^{-3}$ M, figure 5.4**(b)**, the electrostatic barrier is 20

Table 5.1: Thickness

ρ_s (% wt)	$(t \pm 5)$ μm
2	31
4	66
6	90
8	117
10	150

times the thermal energy and the spheres are randomly distributed but the image still shows traces of short range order as can be appreciated in the inset of the figure 5.4**b**. In this case, the repulsive barrier, $U(r_M) \sim 40k_BT$, is higher than the thermal energy of the particles, but the spheres coagulate and the system looks randomly arranged apart from small ordered clusters. Even by incorporating recent modifications, the DLVO theory does not predict experimental results acceptably well which, generally, show that suspensions have lower stability than predicted [136]. For 1×10^{-2} M, figure 5.4**(c)**, the spheres are homogeneously and randomly distributed in the system, in this case the electrolyte concentration is the optimal to provide a uniform distribution of spheres. Finally, in the case of $\rho_e = 5 \times 10^{-2}$ M, figure 5.4**(d)**, such a high electrolyte concentration gives rise to a totally attractive potential between colloids which enhances the number of

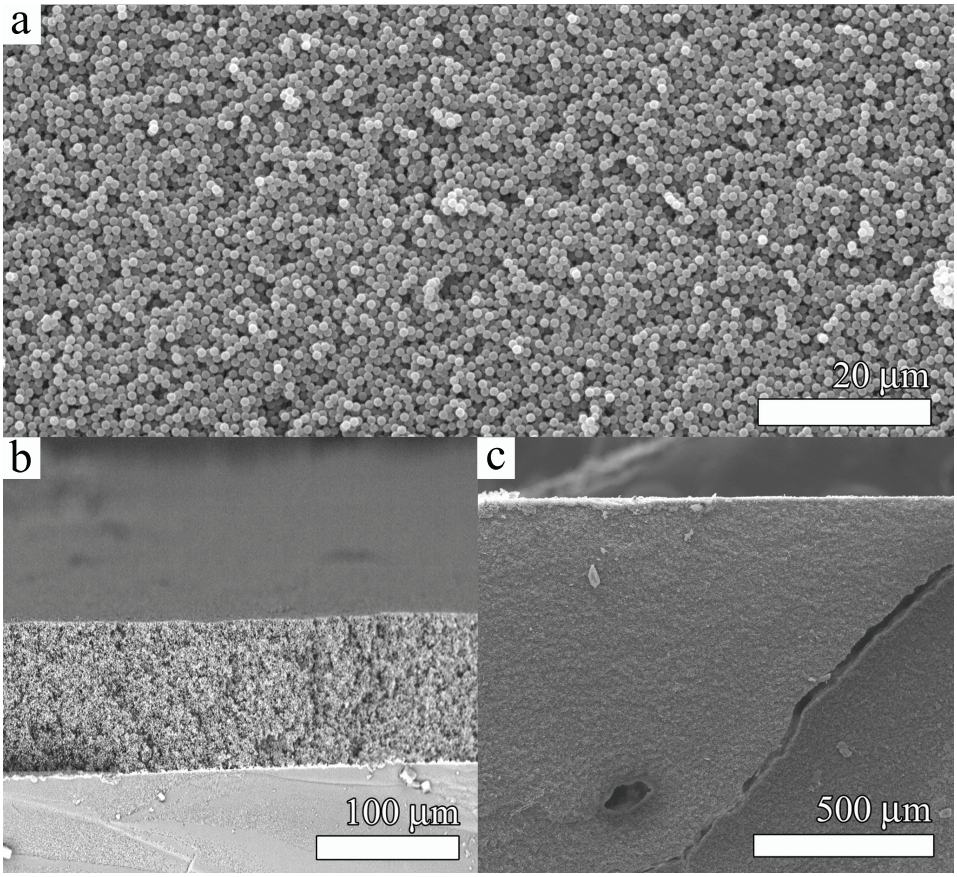

Figure 5.3: SEM images from different parts of a photonic glass made with PS spheres with $d = 1220$ nm. **(a)** image shows the surface of the sample. The random arrangement of the spheres is here revealed. **(b)** and **(c)** images show cleaved edges of the sample. In both cases, the images revealed the planarity of the surface over millimeters. The crack visible in image **(c)** is produced when removing the methacrylate cylinder from the glass substrate.

effective flocculating collisions and the formation of bigger clusters (see inset of figure 5.4**d**).

Filling fraction f as the volume occupied by the spheres divided by the total volume of the system. The size of the clusters has an important effect on f of the system and may strongly affects the physical magnitudes which describe light transport. It has been shown that, increasing the electrolyte concentration, glasses where clusters present increasing sizes can be grown. Figure 5.5 plots the average f from different photonic glasses as a function of the electrolyte concentration from 0.74 (the expected theoretical volume for a perfect fcc structure, [137]) to 0.55. These measurements have been performed weighting and measuring the total volume of the samples. The volume occupied by the PS spheres is estimated by weighting the substrate before and after the sample growth. By

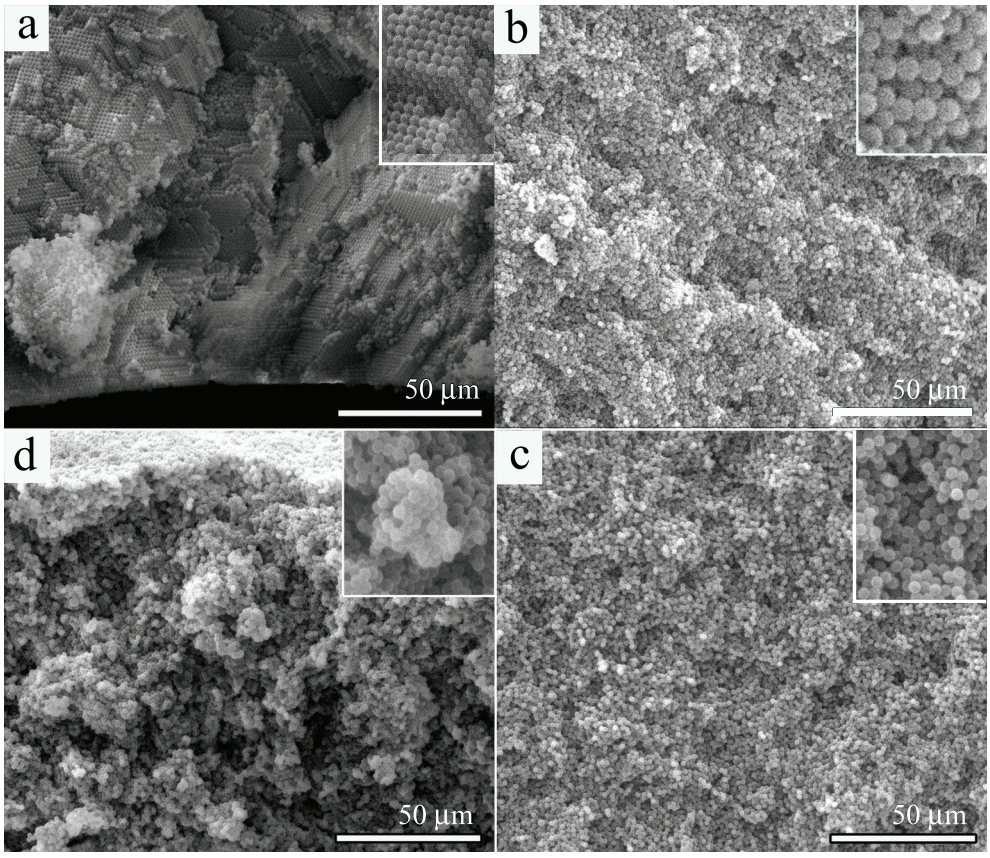

Figure 5.4: SEM images from colloidal suspensions of PS spheres with $d = 1220$ nm naturally sedimented and after liquid phase evaporation. The colloidal suspensions have been prepared with different electrolyte concentrations: **(a)** $\rho_e = 0$ M, shows an ordered fcc arrangement of spheres (see crystallographic in the inset of the figure). **(b)** $\rho_e = 2 \times 10^{-3}$ M, spheres are randomly distributed but still show ordered clusters (see inset). **(c)** $\rho_e = 1 \times 10^{-2}$ M, the image shows a uniform random arrangement of spheres similar to the one in figure 5.3a. Finally, **(d)** $\rho_e = 5 \times 10^{-2}$ M, image shows a very inhomogeneous random distribution of spheres.

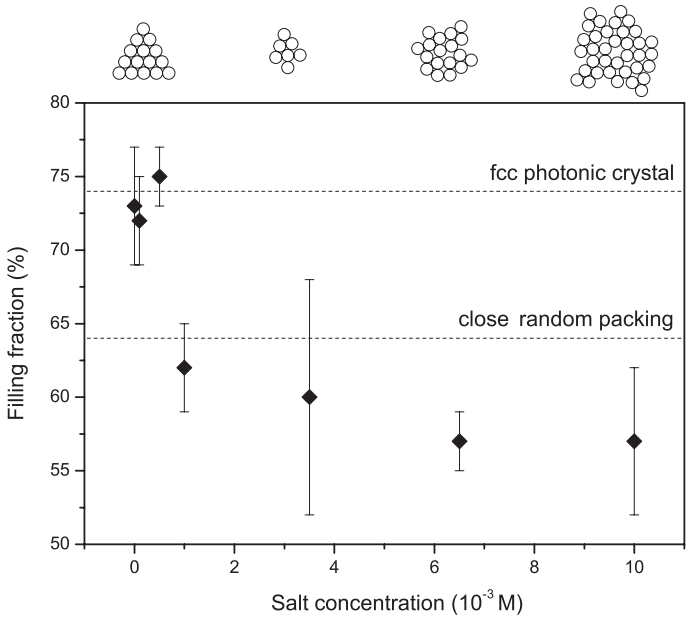

Figure 5.5: Plot of the average *f* of a photonic glass as a function of electrolyte (salt) concentration. Spheres which composed the glass are 1220 nm diameter. Filling fraction can be estimated by weighting the samples when their geometry is known. A concentration 0 M gives rise to a well known opal-based photonic crystal where the total volume occupied by the spheres is $74\ \%$ of the total volume of the unit cell in an fcc lattice.

doing so, we can estimate the sample weight. Furthermore, the total volume of the glass is obtained by measuring the thickness and sides of the samples with the microscope. Large bar errors come from total volume measurements. In particular, the measurement of the glass sides introduces huge error in the final filling fraction value regarding the irregularity of the sample edges (see figure 5.2**b**).

5.3. Study of topological disorder in photonic glasses

The degree of topological disorder in photonic glasses has been measured by means of two different characterization methods; the first one consist in the analysis of the image autocorrelation function which allows to estimate the correlation length, ℓ_c, of the sample surface. The second one is provided by optical spectroscopy and consist in the measurement of reflectance and transmittance which permits the analysis of the bulk disorder in the sample. Both methods provide an accurate characterization of the disorder degree in photonic glasses.

5.3.1. Correlation lenght

In order to obtain a measure of the ordering of the system, the autocorrelation function, $F(\tau)$ has been analyzed from a SEM image of a photonic glass surface

and compared it with the same function from both an ordered sample as well as a TiO_2 powder sample (see figure 5.6). The autocorrelation function describes the correlation of the contrast function, $c(r)$, and gives a measure of the translational symmetry in the system:

$$F(\tau) \quad = \quad \int_{-\infty}^{+\infty} c(\vec{r}) * c(\vec{r}+\tau) d\vec{r} \tag{5.5}$$

If the particles have the same shape and size (monodisperse) and are arranged with a regular distance between first neighbors (that is, a certain local order) the function presents a maximum at the corresponding distance. Accordingly, the auto-correlation function of a random and isotropic arrangement of monodisperse objects, i.e. without positional correlation, is a delta function in the case of point-like objects or a decaying function if the objects have a certain size.

The left panel in figure 5.6 shows a comparison of SEM images of the three different systems and, on the central panel, a normalized plot profile of $F(\tau)$ from the corresponding system. The first system is an opal-based photonic crystal, the second one is a photonic glass and the third one is composed by TiO_2 powder. The autocorrelation function from an ordered structure presents a periodic dis-

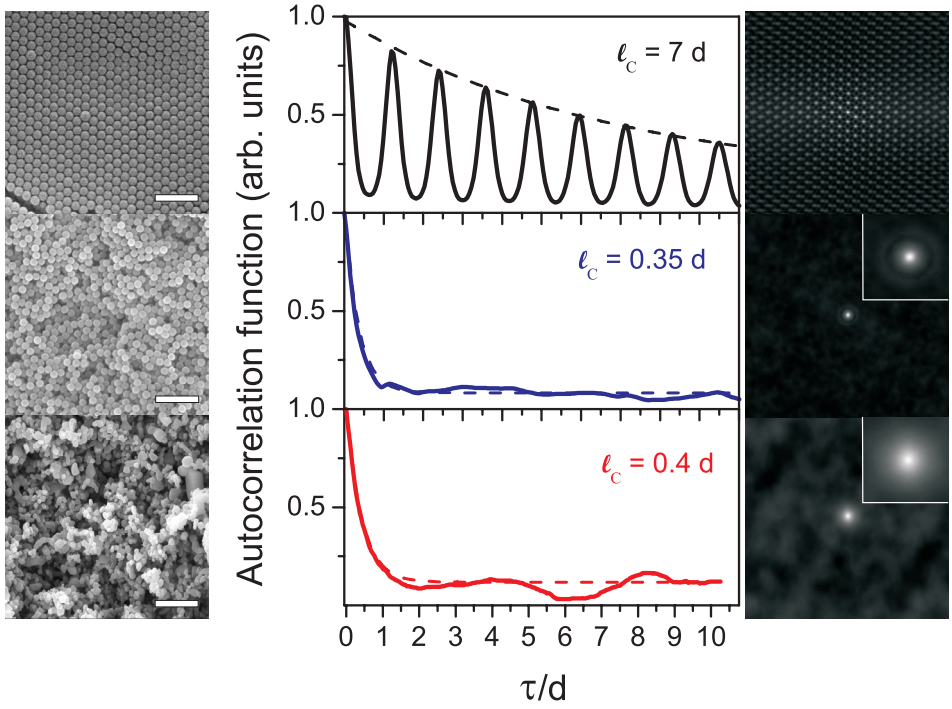

Figure 5.6: **Left panel:** SEM images of an opal-based photonic crystal, a photonic glass and TiO_2 powder. Scales bar are 1 μm. **Right panel:** Autocorrelation function of the surface SEM images from the three different systems. A plot profile of a cut in the autocorrelation function shows the order degree of each sample, characterized with a correlation length ℓ_c for each system.

tribution of maxima due to its long range correlation (translational symmetry). The autocorrelation function of an infinite image composed by point-like objects randomly arranged is a Dirac-delta. In the case of a photonic glass (monodisperse scatterers randomly arranged), $F(\tau)$ clearly presents a decaying intensity as a mark of the randomness of the sphere distribution. In addition, at the position corresponding to the nearest neighbor distance ($\tau/d = 1$), a small hint of a peak appears in all directions of the autocorrelation image (see inset of figure 5.6) as a sign that no sphere can stand in air without being attached at least to one other sphere. Despite the randomness of the sample, this is a weak correlation due to the solid nature of the system and may disappear if the spheres were, for example, in a colloidal suspension. TiO_2 powder is composed by scatterers polydisperse in shape and size randomly arranged; $F(\tau)$ from this system is similar to the one from a photonic glass, apart from the fact that, in this last case, there is no presence of the peak associated to the scatterer-scatterer contact in the autocorrelation function. This absence is due to the polydispersity of the scatters in the powder sample and consequently the many-body first neighbor's distances. This particular feature in the autocorrelation function is a clear sign of a system composed by touching monodisperse objects randomly arranged.

Note also that dependence on distance of the autocorrelation functions also gives a measure of the relative order in the three structures. The decay in the autocorrelation function can be characterized by a correlation length as $F(\tau) \propto \cos(\tau/d)\ e^{-\tau/\ell_c}$ which is the distance from a point beyond which there is no further correlation of structural order. From a fit of the envelope function $e^{-\tau/\ell_c}$, the values of the three systems correlation lengths are $\ell_c = 7\ d$ in the case of the crystal and $\ell_c = 0.35\ d$, $\ell_c = 0.4\ d$ in the case of the glass and the powder respectively.

5.3.2. Optical spectroscopy

In order to probe the amount of bulk disorder, optical tests are conducted where specular and ballistic reflectance (R) and transmittance (T) are measured. Optical spectroscopy is a powerful method to probe the order of the samples. When the material composing the colloidal particles is transparent (i.e not absorbing [57]) and the wavelength involved is larger than the particles diameter (the energy range of work is below the onset of diffraction), the magnitude $R+T$ can be used as a very sensitive measure of the order [59, 60] (see Appendix A). The measure of R alone is not enough to characterize a photonic band gap material since it only probes a thickness $L_0 \lesssim L_B$, where L_B is the Bragg length [59]. A high amount of imperfections such as vacancies, lattice displacements or stacking faults or the very absence of a lattice produce an extra source of elastic light scattering with a different propagation direction, contrary to the case of interference-built straightforward transmission or diffraction, when allowed ($a/\lambda > 1$. This sort of diffuse scattering is, in this particular case, the only source for a decrease in transmission and reflection. Diffuse intensity (D) is estimated as $D = 1 - R - T$, from measurements with normal incidence white light in the low energy regime ($a/\lambda < 1$, where a is the lattice parameter and

λ is the wavelength of light in vacuum) for a certain crystallographic direction: (1,1,1) (normal to the surface of the samples). A defect-free infinite colloidal photonic crystal must accomplish $D = 0$. In particular, for energies contained in the bandgap, the crystal must present 100 % reflectance (0 % transmittance) and, consequently, 0 % diffuse intensity. In real samples, even in a very high quality one, this is not fulfilled as imperfections are always present. In contrast, a completely randomly arranged system should present $D = 1$. For $\ell_s > L$ the ballistic beam is exponentially attenuated, where ℓ_s is the scattering mean free path and L is the sample thickness, according to Lambert-Beer's law (discussed in the appendix A). A high value for D is a strong indication of disorder and, in contrast, a modulationof D for energies contained in the bandgap is a sign of residual order. Following this, even apparently very disordered samples according to surface SEM inspection were discarded after detecting a decrease in D in the regions of the bandgap.

Figure 5.7 shows D as a function of the reduced frequency (a/λ) for four different colloidal suspensions naturally deposited on a substrate and after the evaporation of the water. D has been measured as a function of electrolyte concentration (ρ_e) added to the colloidal suspension in the form of $CaCl_2$ salt. According to the figure, an increase of electrolyte concentration in the colloidal suspension gives rise to an enhancement of D. In particular, the dip present at $a/\lambda \sim 0.6$ corresponds to the pseudogap along the ΓL direction [59] and

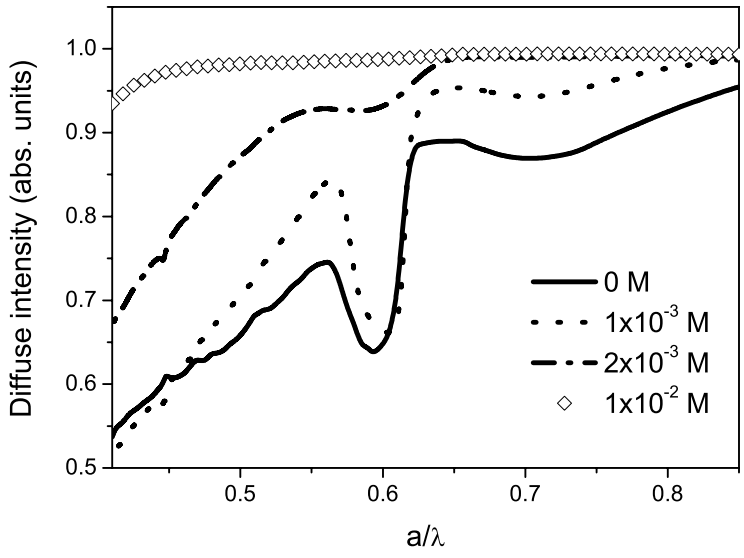

Figure 5.7: Plot of diffuse intensity, $D = 1 - R - T$, measured in different samples as a function of the electrolyte concentration in the initial colloidal suspension. Photonic features, as the main gap, remain till the concentration of salt is enough to force the spheres flocculation thus preventing them from self-assembling.

it is remarkable how the dip associated with it disappears upon increasing the electrolyte concentration. As figure 5.7 reveals, a concentration $\rho_e = 2\times10^{-3}$ M is not enough to sufficiently attenuate the electrostatic barrier for which the spheres are still able to self-assemble and the sample still shows traces of order. This is already pointed out in the electrostatic barrier estimation done in figure 5.1. Despite the fact that SEM image of figure 5.4**b** shows a relatively high degree of disorder in the sample, the presence of photonic crystal features can be explained attending to the fact that such a low concentration of salt in the sample is not enough to force a complete flocculation of the spheres, which are still allowed to self-assemble in the evaporation process. This is a remarkable fact as the only inspection of the sample surface is not enough to ensure the total randomness of a sample and to discard possible order remains. Nevertheless, a concentration higher than 1×10^{-2} M is enough to provoke the spheres agglomeration preventing them from ordering by self-assemble. This is in agreement with the estimations done in figure 5.1 and with SEM image of figure 5.4**c** and confirmed by the experimental measurement of D.

The comparison of optical spectroscopic analysis with the autocorrelation function analysis highlights now how, a high value of D does not ensure a fully random distribution of the system. On the contrary, an autocorrelation function analysis alone gives only information from the analyzed surface. Both analysis methods together are complementary and determine the degree of disorder of the system.

5.4. Conclusions and future work

In conclusion, the realization of photonic glasses, solid random distributions of monodisperse spheres, which are a new photonic material, has been presented. The system is qualitatively different from opals with poor degree of order and short-range periodicity like, as they are fully disordered systems with no long-range correlations. The growth method used is based on the colloidal charge interaction, it provides very thick and completely random samples which can also be used as templates to grow higher refractive index materials such as ZnO or Si. These samples may be a perfect playground to investigate light diffusion in a resonant random media, resonant random laser and Anderson localization of light.

Chapter 6

Light transport through Photonic Glasses

While (ordered) periodic photonic media, i.e. photonic crystals, take advantage of the periodicity in the dielectric constant and the consequent long-range correlation to mold the flow of light [3, 4]. Disordered ones, with no positional order, can still strongly affect light transport [8, 5, 138, 139, 140, 141, 143]. Typical non-absorbing materials are homogeneous and non-dispersive, i.e., they are clear and transparent, and phase and energy travel with the same velocity. Optical propagation is then determined by the shape of the interfaces between various such materials (e.g. a curved surface boundary acts as a lens). If the material is absorptive, dispersion is introduced (brought about by the Kramers-Kroenig relations) whereby the phase velocity looses most of its usefulness and group velocity (at which pulses travel) takes over to describe the transport of energy. Differently, non-absorbing but nanostructured materials can create a new class of systems in which the dispersion is controlled via light interference. Photonic band gap materials, for instance, are systems where extinction is built up from multiple interference (Bragg reflection) creating a region of extinction and anomalous dispersion. In this way, the relevant velocities can be engineered to, for instance, create devices for dispersion compensation. An entirely new scenario is presented when disorder is added to the mixture.

The system proposed in the chapter 5, the photonic glass, is composed by monodisperse scatterers. In the introduction it was pointed out how such a scatterer, a single dielectric microsphere with size comparable to the wavelength of light in the visible (a Mie sphere for the visible), can sustain electromagnetic resonances. The description of the Mie solution to the light scattering problem with a dielectric sphere is briefly outlined in the introduction (section 1.1.1).

Combining these electromagnetic modes of a single spherical scatterer with the monodispersity of the system (see figure 6.1), it will be possible to observe resonances in the light transport from the macroscopic system. Those resonances will be probed by static and dynamic experiments as an extended optical characterization of photonic glasses. A detailed optical study of the resonant behavior

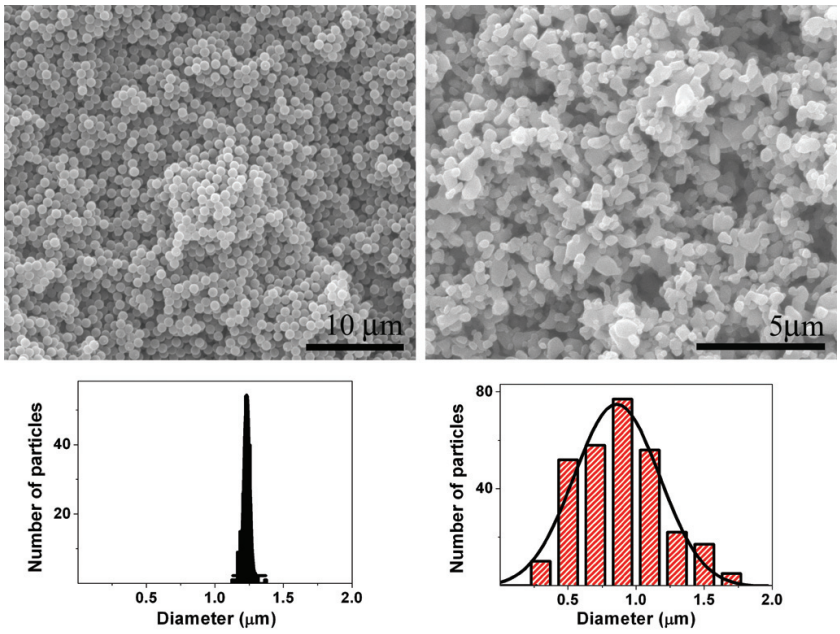

Figure 6.1: **Top: (Left)** SEM image from the photonic glass surface composed by PS spheres with a diameter of $d = 1200$ nm. **(right)** SEM image from TiO_2 powder surface with an average particle diameter $d = 850$ nm. **Bottom:** Corresponding histogram of particle sizes from the photonic glass **(left)** and TiO_2 powder **(right)**

of diffuse light transport through such a system will be provided and, by means of independent static and dynamic measurements, resonances will be shown in the transport mean free path, diffusion constant and also energy velocity of light. In this chapter, experimental results will be referred to equations explained in the diffusion approximation section establish in the introduction (1.2.1).

6.1. Static measurements

Figure 6.2 schematically sketches the set up used to perform static measurements: an integrating sphere which consists of a hollow cavity with its interior coated for high diffuse reflectance. Photonic glasses slabs with different thicknesses are placed on the integrating sphere entrance aperture and illuminated with white light provided by a Tungsten lamp. The sample is optically very thick; therefore, ballistic or unscattered light propagating through it is exponentially attenuated. It can be therefore assumed that only diffusive light comes out at any angle from the sample and enters the integrating sphere.

Figure 6.3 shows a direct measurement of the total diffuse light transmission through different photonic glass slabs (thickness $L \sim 100$ μm) upon white light illumination in the range 500 nm to 920 nm. In order to be able to compare the optical response of different sphere sizes (790 nm, 930 nm, 1000 nm and 1220 nm), the measurements have been plotted as a function of reduced energy units

$(d \cdot n/\lambda)$, where n is the refractive index.

Oscillations in transmission and its spectral dependence are due to the existence of modes for the electromagnetic field in the spheres. The spectral positions of these Mie modes depend exclusively on spheres diameter, d, and on its refractive index, n. These electromagnetic modes are excited when the electromagnetic field wavelength is comparable with the optical diameter of the spheres.

Figure 6.3**a** shows a clear and simple evidence of the resonant behavior of light transport in a broad energy interval. In order to remark this fact and also to clarify the conditions under which the modes can be collectively excited, the resonant behavior of these four different spheres sizes has been compared with two different no-resonant dielectric random systems. Figure 6.3**b** plots the total transmission through two reference samples which, for two different reasons, do not exhibit resonant behavior. As figure 6.3**b** points out, there is no trace of resonances in the transport of light for these two reference systems. The first one (dashed curve) is a photonic glass composed by PS spheres with a diameter of 200 nm. The small size of the spheres compared to the light wavelength illumination $(d \cdot n/\lambda) \sim 0.4$ whose modes have energies in other range. Therefore, those spheres behave, upon this particular light energy illumination, as point-like scatterers giving rise to Rayleigh scattering (where scatterer structure can be neglected) instead of Mie scattering (where resonances can be sustained). Resonances are expected in other energy ranges (in the UV) for this particular system. The second one (solid curve) is composed by TiO_2 non-spherical powders with a polydispersity about 36 % (see inset of the figure 6.3**b**) and a mean diameter of about 850 nm. A different situation arises with the non-resonant light transport through TiO_2 powder. In this case, TiO_2 particles are large enough $(d \cdot n/\lambda \sim 2.5)$ to sustain Mie modes in this wavelength interval. However, figure 6.3**b** shows no trace of oscillations in the light transport because resonances are smoothed out by polydispersity and the arbitrary non-spherical shape of the scatterers. As shown in the introduction 1.1.1, Mie modes are defined by the morphology of

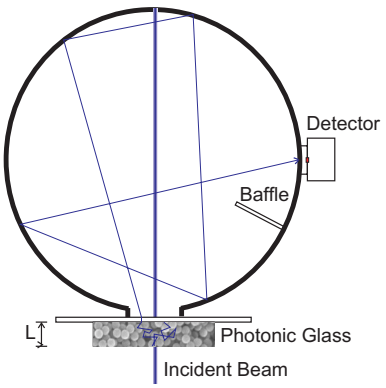

Figure 6.2: Cartoon of the experimental set up to perform static measurements. A slab of photonic glass with thickness L is placed at the entrance of an integrating sphere and illuminated with white light. Diffuse light is measured at the detector.

the scatterer. When the scatterers are non-spherical and also polydisperse, as in the TiO_2 case, each building block sustains resonances for different wavelengths. This smoothes out the collective response giving rise to an overall non-resonant behavior.

6.1.1. Resonant mean free path

In order to completely characterize these systems, total transmission, $T(L, \lambda)$, was measured as a function of the slab thickness (L, from 50 μm to 1600 μm) for a fixed sphere diameter ($d = 1220$ nm) and over an extended wavelength range ($500 \text{ nm} < \lambda < 920$ nm). $T^{-1}(L, \lambda)$ is shown in Figure 6.4. From the experiments it is possible to fit the values of $\ell_t(\lambda)$, the transport mean free path, and $\ell_a(\lambda)$, the

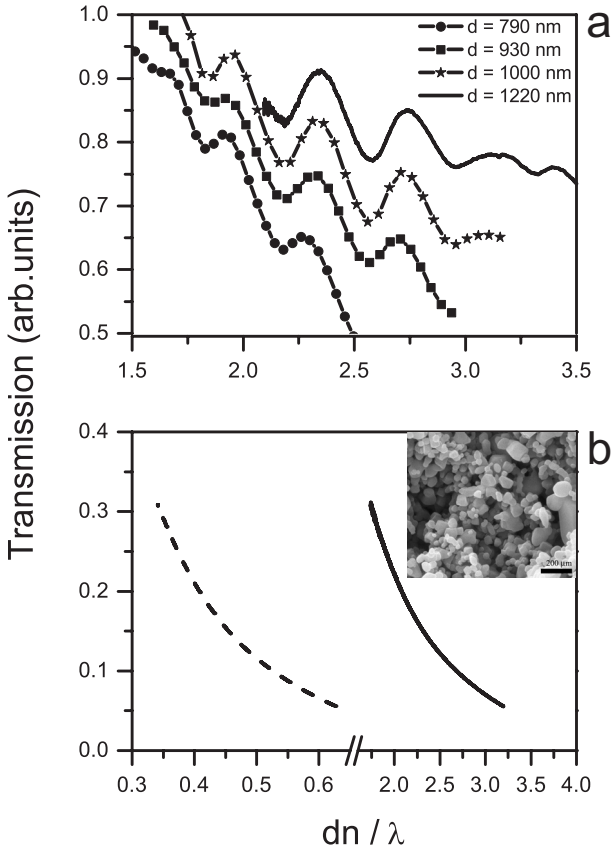

Figure 6.3: **(a)** Normalized total transmission of white light through photonic glasses as a function of the reduced parameter $d{\cdot}n/\lambda$. Samples are composed by spheres with four different diameters and thickness is about 100 μm in all cases. **(b)** Total transmission of white light through two different reference samples as a function of the reduced parameter $d{\cdot}n/\lambda$. The dashed-line represents total transmission through photonic glasses made of PS spheres of $d = 200$ nm. Solid-line represents total transmission through a powder made of polydisperse TiO_2 of averaged $d = 850$ nm (SEM inset of the sample where scale bar represents 200 nm). Both present no-resonant light transmission.

absorption length. When light propagates diffusively and in absence of absorption ($\ell_a >> L$) the function $1/T(L,\lambda)$ is directly proportional to the slab thickness, L (figure 6.5**a**). This is usually called photonic Ohm's law and is outlined in the stationary solution to the diffusion equation (see introduction 1.2.2). From this set of samples, represented in figure 6.4**a**, we can obtain $\ell_t(\lambda)$ by fitting the experimental results with the stationary solution of the diffusion equation (1.21) (see introduction 1.2.2). Figure 6.6 shows this fit for the extended wavelength range. It reveals a clear resonant behavior of $\ell_t(\lambda)$. In the curve, a triangle and a square mark the spectral positions of a minimum and a maximum of $\ell_t(\lambda)$ respectively.

The scattering cross section is enhanced when a Mie mode is excited in a sphere. The scattering is more efficient at those wavelengths and, therefore, the transport mean free path becomes minimum.

6.1.2. Absorption

Absorption provokes an exponential dependence of $1/T(L,\lambda)$ on the slab thickness (pointed out in figure 6.4**b**) and must be carefully characterized. Absorption provokes extinction ($T \propto e^{-\ell_a L}$) which should be distinguished from diffusion ($T \propto 1/L$). Figure 6.5**b** plots the value of $1/T(L,\lambda)$ as a function of

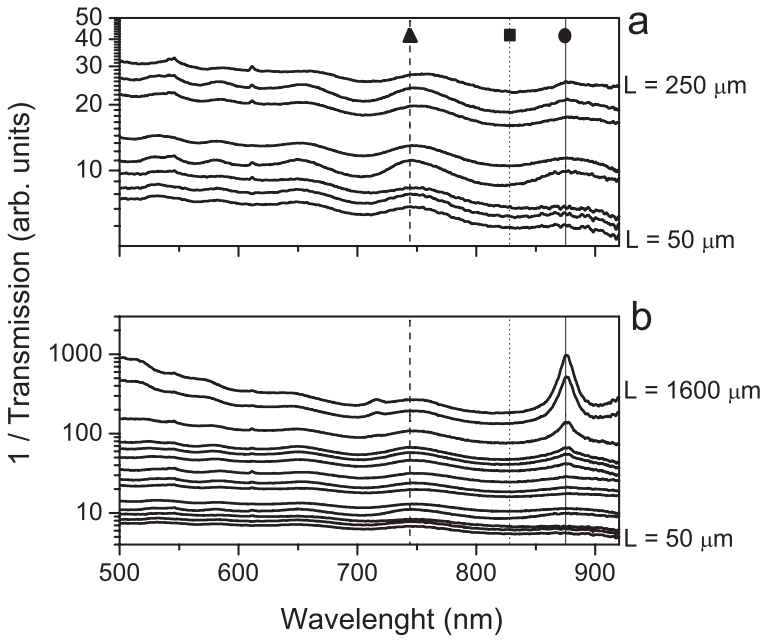

Figure 6.4: Total light transmission of white light trough photonic glasses made of PS spheres with $d = 1220$ nm as a function of wavelength. **(a)** For low values of L ($(\ell_a > L)$). In this case, thicknesses vary from 50 μm to 250 μm. **(b)** For high values of L ($\ell_a < L$), up to 1600 μm, transmission shows a linear dependence on thickness except for those wavelengths were absorption is not negligible. Three particular wavelengths are marked with a triangle ($\lambda_1 = 744$ nm), a square ($\lambda_2 = 828$ nm) and a circle ($\lambda_3 = 875$ nm)

slab thickness (L) at three particular wavelengths which have been previously marked in figure 6.4 with a triangle ($\lambda_1 = 744$ nm), a square ($\lambda_2 = 828$ nm) and a circle ($\lambda_3 = 875$ nm). In the first and second cases, $\lambda_1 = 744$ nm and $\lambda_2 = 828$ nm, the function $1/T(L, \lambda)$ presents a linear dependence on L while in the third case, $\lambda_3 = 875$ nm, presents an exponential dependence. Wavelengths λ_1 and λ_2 correspond to a minimum and a maximum of a Mie resonance, respectively. The different slopes agree with the photonic Ohm's law with negligible absorption ($\ell_a(\lambda_1, \lambda_2) > L$) and different ℓ_s. Contrary to these cases and when L is large enough (see the difference between figures 6.5**a** and **b**), a clear absorption peak is revealed at wavelength λ_3. This can be easily seen in figure 6.4**b** and is made more apparent in figure 6.5**b**, where the function $1/T(L, \lambda)$ presents a clear exponential dependence on L.

In order to clarify and distinguish Mie resonances from absorption peaks, the same transmission experiments have been performed for different spheres diameters. Figure 6.7 shows the total light transmission through three particular photonic glass slabs composed by different sphere sizes with diameters 200 nm, 1000 nm and 1200 nm respectively. These slabs are thick enough to present the

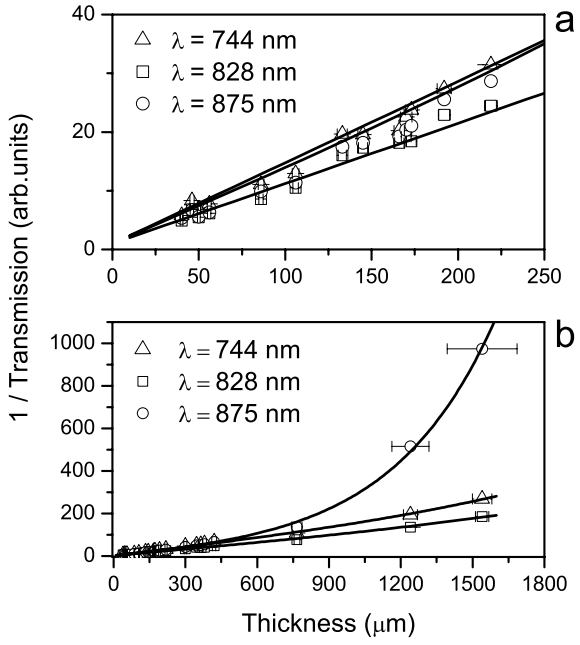

Figure 6.5: Plot of T^{-1} as a function of the thickness for three different wavelengths. **(a)** For low L ($\ell_a >> L$), linear dependence is clearly shown for λ = 744, 828 and 875 nm as an indication of the validity of the Ohm's law for this wavelengths which present, however, different slopes that provide ℓ_t. **(b)** For high L ($\ell_a < L$), exponential behavior is revealed for $\lambda = 875$ nm related to a water absorption band.

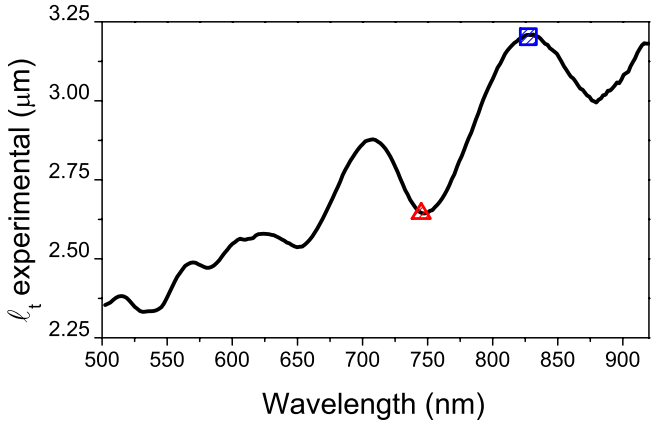

Figure 6.6: Experimental transport mean free path in a photonic glass made of PS spheres of $d = 1220$ nm. The data are obtained by fitting the L dependence of experimental T^{-1} curves. Two particular minimum and maximum wavelengths are marked with a triangle ($\lambda_1 = 744$ nm) and a square ($\lambda_2 = 828$ nm), respectively.

peak absorption at $\lambda_3 = 875$ nm. Therefore $\ell_a(875\text{ nm}) < L$ in all these cases. This peak is independent on the sphere diameter and, for this reason, it cannot originate from a Mie resonance, which only depends on the geometric parameters of the scatterers. In addition, as a photonic glass slab composed by spheres with $d = 200$ nm cannot sustain collective Mie resonances, we deduce that the peak must be due to a discrete absorption. It is shown that, for certain wavelengths, the system presents discrete absorptions which are revealed in optical spectroscopic measurements only when $\ell_a < L$. At this point it is necessary to estimate the value of this diffusive length in the energy range where experiments have been performed. Figure 6.8 shows the diffusive absorption length, $\ell_a(\lambda)$, obtained by fitting the experimental curve of the function $T(L, \lambda)$ with the corresponding equation 1.21. Valuable information is revealed in this plot: (**i**) the mean value of the absorption length (ℓ_a) is about 1 mm, (**ii**) two dips at wavelengths $\lambda = 730$ nm and $\lambda = 875$ nm appear in the function $\ell_a(\lambda)$, for which ℓ_a presents values about 900 μm and 500 μm respectively and, consequently, absorption is maximum, (**iii**) a UV absorption tail is pointed out at higher energies (lower wavelengths), where ℓ_a presents a steady decay. The exponential dependence of the function $1/T(L, \lambda)$ on L is related to UV PS absorption [57] at high energies. The sphere's material has no absorption [57] at lower energies . According to this, the peaks at $\lambda = 730$ nm and $\lambda = 875$ nm are attributed to near infrared states of residual liquid water in the sample due to overtones and combination bands of fundamental vibrations occurring in the mid infrared [145]. To rule out other possible effects of the salt used to destabilize the colloidal suspension, we have grown different photonic glasses varying the growth conditions. As said in chapter 5, an extra amount of charge is enough to attenuate the electrostatic potential into a total attractive

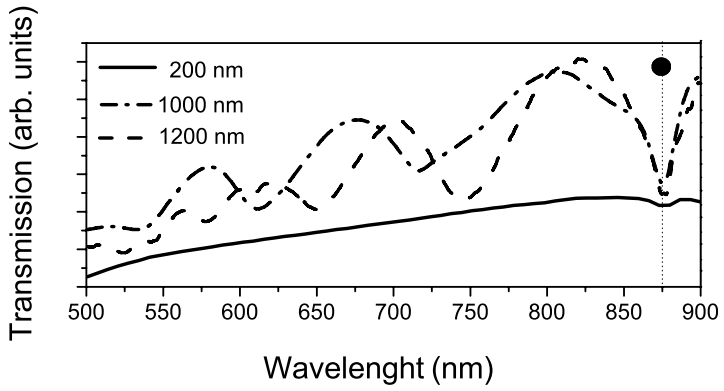

Figure 6.7: Total white light transmission through photonic glasses composed by PS spheres with 200 nm (continuous full line), 1000 nm (dashed-dot line) and 1200 nm (dash-dotted line) as a function of wavelength. All the spectra present an absorption peak at $\lambda = 875$ nm related to water. The spectral position is marked with a circle, as in figures 6.4 and 6.5.

potential. To verify that no discrete absorption peaks were due to salt, photonic glasses with different kind of salts ($CaCl_2, NaCl, K_2CO_3, MgSO_4$ and Na_2CO_3) and also with an acid (HCl) have been grown. Their optical response is always the same and show the same absorption peaks which, therefore, cannot be due to the salt or PS.

A short comment about absorption in photonic glasses compared to other photonic systems is needed. As previously settled, light transport through highly

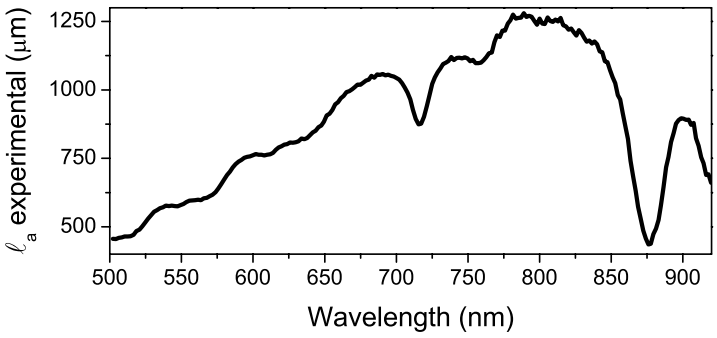

Figure 6.8: Plot of the absorption length, ℓ_a, from a photonic glass made of PS with $d = 1220$ nm. It clearly shows two absorption peaks at $\lambda = 875$ nm, $\lambda = 730$ nm related to liquid water vibrations.

disordered materials is diffusive as opposed to to ballistic or unscattered transport through non-diffusive materials. Although absorption disturbs the optical properties of all photonic systems, its effects are more evident in diffusive materials. Opal-based photonic crystal is a paradigmatic system where light transport is, in principle, ballistic in spite of being grown with the same building blocks as a photonic glass. Absorption effects which can be neglected or unobservable, for example, in a photonic crystal, should be taken into account and carefully characterized in photonic glasses. This fact is explained attending to the different light transport properties which take place in each one. In a diffusive material, the characteristic absorption length is ℓ_a whereas in a non-diffusive material absorption is characterized with the length ℓ_i, which is the distance that light travels before being attenuated a factor e. According to equation 1.17 (see introduction, 1.2.1), ℓ_i is always longer than ℓ_a and, therefore, light should propagate much longer ballistic distance in photonic crystal to become attenuated the same factor as in a photonic glass.

An estimation of the main values of both ℓ_a and ℓ_t can be performed, and also the main value of ℓ_i. At the wavelengths for which absorption peak has been observed, a value of $\ell_a \sim 800$ μm gives rise to $\ell_i \sim 0.7$ μm (with a value of $\ell_t \sim 3$ μm), attending to the fact that $\ell_a = \sqrt{(\ell_t \cdot \ell_i)/3}$ (see introduction, 1.2.1). The big difference (three orders of magnitude) between the absorption length (ℓ_i) and the diffusive absorption length (ℓ_a) is remarkable. This fact suggests that, to observe the same absorption effects in a pass-band photonic crystal it should be necessary to build a photonic crystal 1000 times thicker than a photonic glass, that is, around 1 m thick. This estimation is performed in a pass-band whereas the optical performances of a photonic crystal are expected to be enhanced in the photonic gap edge, as will be shown in chapter 8.

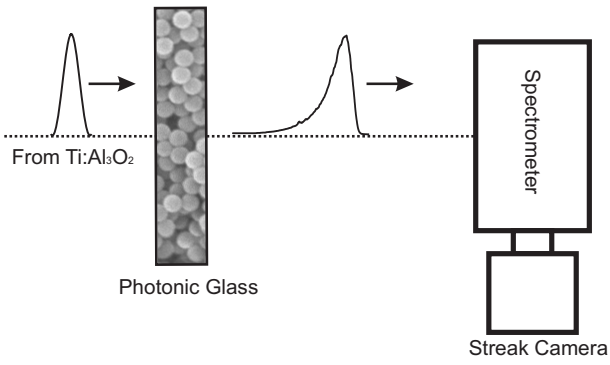

Figure 6.9: Experimental set up to perform dynamical measurements. A ultrashort laser pulse is sent to the sample. A spectrometer collects the pulse temporally spread by the sample and sends it to a streak camera.

6.2. Dynamic measurements

Once the static photonic properties of photonic glasses have been examined, the dynamic transport parameters will be probed. In the experimental set up to perform a time-resolved measurement (schematically shown in figure 6.9) a streak camera has been used which permits to monitor the time evolution of a very short laser pulse in its propagation through the glass. In particular, the experiment has been performed with 2 ps pulses provided by a $Ti : Al_2O_3$ laser tuneable within 700 - 920 nm. An example of a time-resolved transmission measurement is plotted in figure 6.10**a** for two different wavelengths, $\lambda_1 = 744$ nm and $\lambda_2 = 828$ nm, which correspond to the minimum and the maximum of a Mie resonance analyzed in the previous section. The different slope of $T(t, \lambda)$ at long times

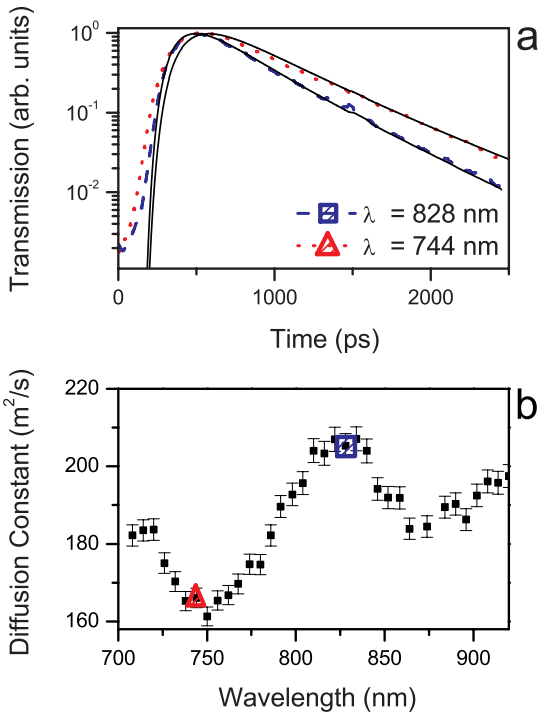

Figure 6.10: **(a)** Time-resolved transmission measurements at $\lambda = 744$ nm and $\lambda = 828$ nm where the different slope of $T(t)$ gives rise to a minimum $(\mathcal{D}(744) = 166\ m^2/s)$ and maximum $(\mathcal{D}(828) = 205\ m^2/s)$ in the diffusion constant. In this case $L = 1120\ \mu$m. (black full lines represent the fit of the experimental measurements with the diffusion equation). **(b)** Experimental diffusion constant in a photonic glass made of PS spheres with $d = 1220$ nm obtained by fitting experimental $T(t)$ curves. Two particular wavelengths are marked with a triangle $(\lambda_1 = 744$ nm), a square $(\lambda_2 = 828$ nm), corresponding to the particular measurements shown in **(a)**.

(the time decay) at this two different wavelengths accounts for the presence of a Mie resonance. The thickness of the photonic glasses used in these time-resolved experiments is about 1 mm. Figure 6.10**b** evidences the resonant behavior of $\mathcal{D}(\lambda)$. Its value has been obtained fitting the experimental time dependence of $T(t)$ with the dynamical solution of the diffusion equation 1.23 (1.2.3). The solution to the diffusion equation, with appropriate boundary conditions, fits well the experimental data. The value of $\ell_a(\lambda)$ has been obtained independently from static measurements, using Ohm's law, and can be introduced in the equation as a known parameter. This provides an accurate estimation of the value of $\mathcal{D}(\lambda)$. Absorption accounts for a correction of only few %, in average, but is crucial on the absorption peak (at $\lambda = 875$ nm). It can be concluded that the resonant behavior of $\mathcal{D}(\lambda)$ is due to Mie modes and presents maxima and minima at the same spectral positions as in the static measurements of $\ell_t(\lambda)$.

6.3. Coherent backscattering

The measurements carried so far have been analyzed in the context of the diffusion approximation. The transport mean free path has been measured in the past sections by means of the photonic Ohm's law. In order to support this optical study, and to show an interference effect, coherent light backscattering measurements will be provided in this section. We will obtain a value of ℓ_t by means of the coherent backscattering cone. The phenomenon of coherent backscattering of light from random systems is an interference effect which survives multiple scattering and constitutes a correction to the diffusion approximation. Also known as weak localization of light, it can be detected since it manifests as an enhancement of light intensity in the backscattering direction. This enhancement is usually called *cone of coherent backscattering*. Several observations of this physical phenomenon have been performed in colloidal suspensions [138, 139], powders [146], cold-atom gases [144] or randomized laser materials [147] to give just a few

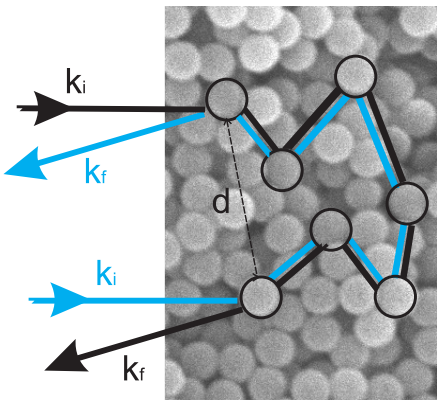

Figure 6.11: Counter-propagating light paths that give rise to coherent light backscattering.

examples.

The physical origin of the light backscattering enhancement is in the interference between two paths which undergo exactly the same, direct and reverse, random walk. Reciprocity is what ensures the equality of the direct and reverse paths amplitudes. If we place a source with a long coherence time (an excited atom, for example) inside the system, there will be, at certain points of the sample, an enhancement of light due to this interference process which attenuates the diffusion propagation. For this reason, this process is called weak localization. If the random system is illuminated by an external laser beam, the backscattered intensity results from interference between the amplitudes associated with the various scattering paths inside the system; for any two points in the sample surface, two exactly direct and reverse random walks start from and end in both points (see scheme in figure 6.11). The interference pattern from these two points in the sample surface is the same as in the two slit Young's interference experiment:

$$I(\theta, \varphi) = I_0(1 + \xi \cos \mathbf{d} \cdot \Delta\mathbf{k}) \tag{6.1}$$

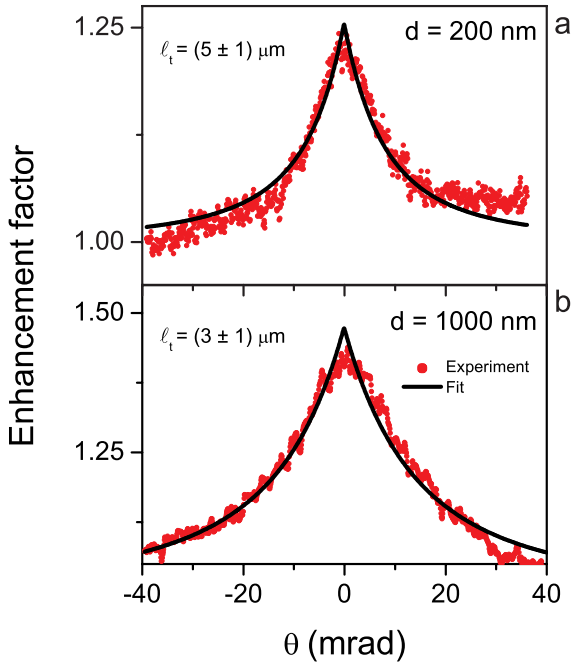

Figure 6.12: Plot of the coherent backscattering cone measured from photonic glasses composed by PS spheres with diameters d = 200 nm **(a)**, and d = 1000 nm **(b)**. The shape of the experimental cone is fitted with the theoretical curve which provides the estimate of the transport mean free path in both cases.

where I_0 is the total intensity, ξ is the interference contrast and θ and φ are the angles with respect to the backscattering direction. Maximum interference ($\xi = 1$) is obtained when the counterpart optical paths have the same amplitude and only at $\theta = 0$. The cone of light backscattering is the Fourier transform of the probability for a photon to return to the sample surface, when it is illuminated by a point-like source. An accurate optical set up to collect the backscattering cone is explained in appendix C. The top of the cone is build up with long diffusive optical paths with far entrance-exit surface points (short spatial frequency distributions). The phase difference between two paths is

$$\Delta\phi = \frac{2\pi}{\lambda_0}(\mathbf{d} \cdot \Delta\mathbf{k}) \tag{6.2}$$

and, in the small θ limit into:

$$\Delta\phi \approx \frac{2\pi}{\lambda_0}\theta|\mathbf{r}_N - \mathbf{r}_1| \tag{6.3}$$

where the term $|\mathbf{r}_N - \mathbf{r}_1|$ is basically the mean separation between the first and last scattering events of a photon inside the system, which is of the order of ℓ_t:

$$\Delta\phi \approx \frac{2\pi}{\lambda_0}\theta\ell_t \tag{6.4}$$

The width of the backscattering cone is, therefore, determined by the average distance between the first and last scattering event and, thereby, by ℓ_t as:

$$W \simeq \frac{0.7}{2\pi}\frac{\lambda_0}{\ell_t} \tag{6.5}$$

The backscattering cone detection is an accurate method to measure the transport mean free path. We will use it is as a complementary measurement of ℓ_t in two different photonic glasses made with PS spheres with diameters $d = 200$ nm and 1000 nm at a fixed wavelength $\lambda_0 = 632$ nm. This experiment carried out with a broad spectral range laser would provide the same information as that of the total transmission (photonic Ohm's law). Figure 6.12 shows coherent backscattering cones from two photonic glasses composed by spheres with diameters $d = 200$ nm (figure 6.12**a**) and $d = 1000$ nm (figure 6.12**b**). The value of ℓ_t is estimated from equation 6.5.

The values of ℓ_t obtained from the backscattering cone, $\ell_t = (3 \pm 1)$ μm for $d = 1000$ nm and $\ell_t = (5 \pm 1)$ μm for $d = 200$ nm, are in agreement with those obtained with the total transmission measurement. The low enhancement factor and the large error of the measurements are due to the relative high noise of the measurements which have the only objective to confirm the measurements obtained in previous sections. This shows the sensitivity of such measurement and the convenience of the total transmission measurements performed in previous sections.

The advantage of this procedure is that, with one measurement on one sample, we can obtain the value of ℓ_t, contrary to the case of the total transmission where several samples are needed to perform an accurate fit of the solution to the

diffusion equation. The disadvantage of the backscattering cone, apart from the accuracy needed to obtain an acceptable enhancement factor, is that we obtain ℓ_t at one wavelength and we can not resolve the resonances.

6.4. Discussion

The appropriate velocity which describes light diffusive transport in photonic glasses is the energy velocity. A discussion about the possible resonant behavior of this magnitude can be found in the literature [67, 148, 149]. Figure 6.13 represents the energy velocity, v_E, obtained from independent measurements of $\ell_t(\lambda)$ (static) and $\mathcal{D}(\lambda)$ (dynamic) and the help of the expression:

$$\mathcal{D} = \frac{1}{3} v_E \, \ell_t \tag{6.6}$$

the experimental value is below the average value of the group velocity obtained from the sample average refractive index $v_g = c/\langle n \rangle \sim 0.77c$ while showing clear resonances. Qualitatively, the minima of $\ell_t(\lambda)$, for which the scattering strength is maximum, correspond to wavelengths that excite a Mie mode, and therefore experience a longer dwell time. This turns into a minimum transport velocity (figure 6.13). For comparison, at the bottom of figure 6.13 the lack of velocity resonance of a TiO_2 powder sample is shown. It is measured in the same experimental conditions. For ideal microspheres, the single particle resonances are $10 - 20$ % wide in wavelength, and therefore they are expected to be washed

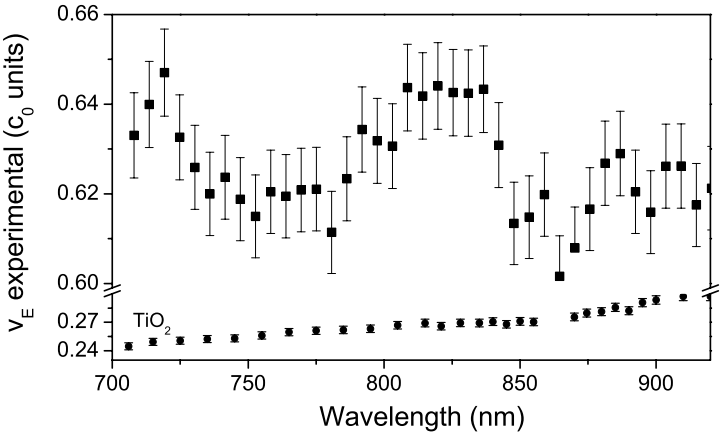

Figure 6.13: Experimental values of the energy velocity as a function of the wavelength for a photonic glass made of PS sphere with diameter $d = 1220$ nm and for TiO_2 powder. For the photonic glass, a full oscillation of around 5 % amplitude is shown. The averaged medium group velocity is $0.77c$. For the TiO_2 powder, flat velocity dispersion is shown, obtained with the same procedure (note the different scales on the y-axis).

out for $f > 5 - 10$ % (see the lower curve in figure 6.13). Recently, Stoerzer et al [150] have reported a wavelength dependent diffusion constant in $15 - 20$ % polydisperse, irregularly shaped titania powders, which in the light of the findings presented in this thesis is unlikely to be the result of Mie resonances. The importance of the morphology of the sphere is evident, as a broad size distribution or a random shape of the dielectric resonator are expected to wash out the resonant properties [151, 152]. Figure 6.14**a** shows the comparison between the experimental and theoretical plots of $\ell_t(\lambda)$ obtained by using the analytical Mie solution to the Maxwell's equations for a single dielectric sphere. This theory can be rigorously applied to the single scattering regime or in the case of dilute systems and independent scattering events. The partial disagreement between experimental and theoretical data comes from the fact that this system, the photonic glass, cannot be considered diluted with a filling fraction of 0.55. When the scatterers density is very low, a multiple scattering theory with a single scatter t-matrix should be appropriate [144]. This holds roughly until the optical (and not physical) sizes of the scatterers start to overlap. Then, the modes start to interact and this fact should necessarily affect the scattering matrix of the sphere. Finally, it is expected that the resonances will disappear when the scatterers occupy a volume fraction of 100 %. The coherent-potential approximation [149], which is a mean field theory and a first order in scattering density, predicts that the scattering resonances weaken at high *fs* and even disappear for $f \sim 50 - 60\%$. Nevertheless, at a filling fraction as high as 0.55, it is still possible to experimentally observe resonances in the transport mean free path and transport velocity, as shown here. It is interesting to look further into the physics involved in the resonant behavior at intermediate filling fractions. When optimizing light diffusion, one often wants to increase the refractive index contrast and to maximize the scatterers density in order to minimize the scattering mean free path. The price to be paid when increasing f is to induce both correlations in the scatterers relative positions (in the close-packing limit, only the crystalline fcc lattice is allowed) and interaction between the Mie modes inside scatterers. As long as the suspensions are dilute, the scatterers can be considered independent and intraparticle scattering (represented by the form factor *F(q)*) is sufficient to describe the system. If the concentration increases, however, in addition to intraparticle scattering, interparticle scattering (represented by the structure factor *S(q)*) must be taken into consideration. The relation between transport mean free path and the microscopic scattering properties is given by [18, 140]:

$$\frac{1}{\ell_t} = \frac{\pi}{k^6} \int_0^{2k} \rho \cdot F(q) \cdot S(q) \cdot q^3 dq \tag{6.7}$$

where ρ is the number density and q the single-scattering wave vector. One can work with a modified structure factor, *S(q)*, in order to fit the data [128] or confront a new calculation of *F(q)* taking into account the possible interactions between the modes of a sphere and near neighbors. Figure 6.14**b** shows the comparison between the experiment and the calculation of *S(q)* obtained in the Percus-Yevick approximation for hard spheres [153] (since there is no preferred direction in this random system, S depends only on k and not on q):

$$S(k) = 1 + (2\pi)^3 \frac{6f}{(\pi R)^3} \frac{C(k)}{1 - (2\pi)^3 \frac{6f}{(\pi R)^3} C(k)} \tag{6.8}$$

where R is the sphere radius and f the filling fraction of the system and:

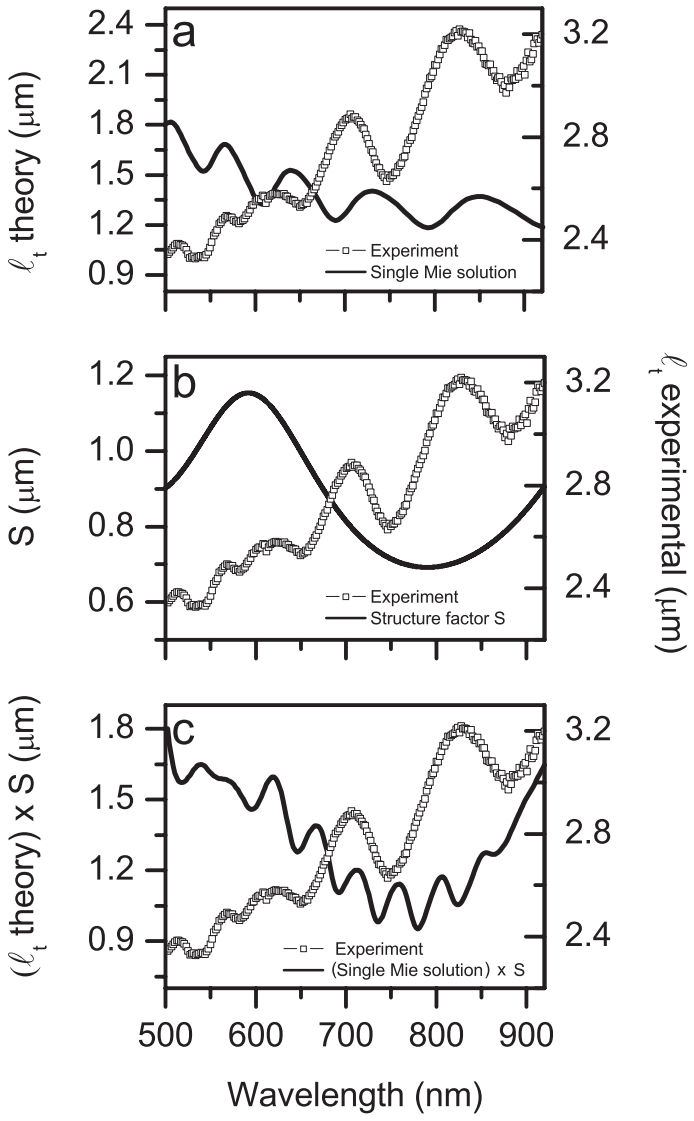

Figure 6.14: **(a)** Plot of the experimental transport mean free path (stars) and the theoretical prediction based on the Mie solution to the single-sphere [67] for ideal PS spheres (continuous line) with diameter is $d = 610$ nm **(b)** Experimental (open squares) transmission from the same spheres as previous figure compared with the Percus-Yevick structure factor for hard spheres *S(q)* (continuous line) with $f = 0.5$. **(c)** Plot of the experimental transport mean free path (stars) and the combination of the Mie solution to the single-sphere with the Percus-Yevick structure factor for hard spheres *S(q)* with $f = 0.5$ (continuous line).

$$C(k) = \frac{4\pi a^3}{f^{\,2}(2\pi)^3}[\frac{\alpha+\beta+\gamma}{(2ka)^2}\cos(2ka) - \frac{\alpha+\beta+\gamma}{(2ka)^3}\sin(2ka) + \\ -2\frac{\beta+6\gamma}{(2ka)^4}\cos(2ka) + \frac{2\beta}{(2ka)^4} + \frac{24\gamma}{(2ka)^5}(\cos(2ka)-1] \qquad (6.9)$$

$$\begin{aligned} \alpha &= \frac{(1+2f)^2}{(1-f)^4} \\ \beta &= -6f\frac{(1+f/2)^2}{(1-f)^4} \\ \gamma &= \frac{f(1+2f)^2}{2(1-f)^4} \end{aligned}$$

It evidences how *S(q)* alone cannot account for the resonances which appear in the transmission spectrum. A combination of the Mie solution to the single-sphere with the Percus-Yevick structure factor for hard spheres *S(q)* cannot account for the resonances of the experimental ℓ_t measurement (figure 6.14**c**). A solution to this problem could be a multiple scattering theory with a modified single scatterer *F(q)* which takes into account the possible interactions with nearest neighbors.

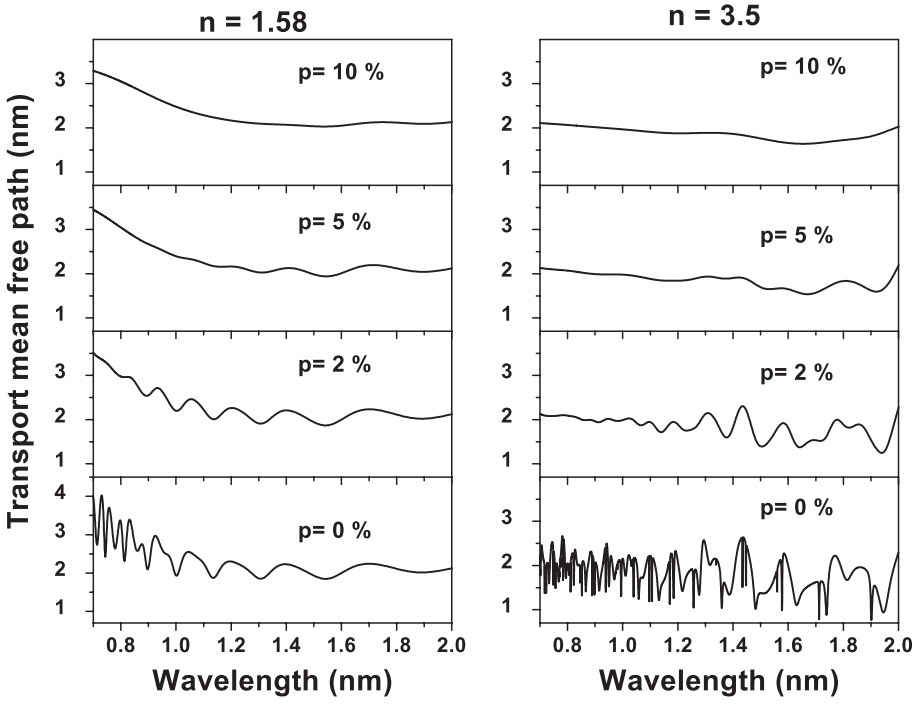

Figure 6.15: Analytical calculations of the transport mean free path, ℓ_t, for four values of sphere polydispersity, *p*, and for two different values of sphere refractive index. Sphere diameters are 1 μm and *f* = 0.5.

Indeed, the calculation of an adequate *F(q)* may be convenient to accurately account for the strength of the resonances.

Finally, polydispersity and refractive index contrast of the structure are important in determining the visibility of the resonances. Figure 6.15 shows the plot of ℓ_t simulated for four different values of sphere polydispersity and two different values of sphere refractive index corresponding to PS and Silicon. It is calculated by assuming a normally distributed spheres radii which defines the polydispersity. This distribution is then convoluted with the analytical solution for a single sphere, which yields the macroscopic frequency dependence of the scattering parameters. Figure 6.15 shows how, increasing the polydispersity, the resonances are washed out. Even in the case of a high refractive index contrast, a polydispersity of 5 % is enough to smooth all the main spectral features. This theoretical prediction agrees with the measurements presented here, which show how a high polydispersity gives rise to non-resonant light transport (Figure 6.3b) even in the case of high refractive index contrast, as in the case of TiO_2.

6.5. Conclusions

In conclusion, an ample optical characterization of photonic glasses is presented in this chapter, as far as transport is concerned. With independent experiments (static and dynamic), a resonant behavior in diffuse light transport is observed: resonant transport mean free path, diffusion constant, and energy velocity. This observation opens new and encouraging routes in the field of light transport through disorder media as photonic glasses can be powerful systems to be used as a new playground for light diffusion. This novel material joins light dispersion and diffusion in the same system, a combination that can be crucial to control the diffuse flow of light in analogy to what photonic crystals do for ballistic light. For example, phenomena such as Anderson localization of light or random lasing in combination with resonances in ℓ_t acquire promising possibilities in this novel framework. Photonic glasses by themselves and integrated with photonic crystals may give rise to new applications in future photonic devices.

Chapter 7

Resonance-driven Random Laser

Among all the possible applications of disordered nanophotonics, random lasing is one of the most intriguing and fascinating. Proposed by Letokov [63] in the sixties and experimentally observed for the first time by Lawandy [64] and co-workers, a random laser is basically the combination of a random assembly of elastic scatterers and a gain medium. In such a system light is multiply scattered and amplified. In a standard laser, light scattering hampers the functionalities, disturb the process and is generally regarded as a parameter to minimize. In a conventional laser, light amplification is obtained by (resonant) feedback provided by an optical cavity, therefore, scattering induces light losses and increases the lasing threshold. On the contrary, in a random laser, multiple scattering of light is the *sine qua non* condition to reach threshold and lase, playing the role of the cavity as a (non-resonant) feedback mechanism. The lasing emission is determined by the interplay between losses and gain. In a random system, light travels long diffusive paths inside the medium, getting the chance of being amplified. Unlike ordinary lasers, the resulting light emission is multidirectional and not really monochromatic, but the threshold behavior [64], the photon statistics [154, 155] and relaxation oscillations [156, 157] are very similar to those of standard lasers. This phenomenon is usually observed in random matrices composed by very polydisperse scatterers in shape and size such as powdered laser crystals [158], ceramics [159], organic composites [160], and even biological tissue [161]. In all those systems, the scattering parameters, the transport mean free path or the diffusion constant, which define the diffusion transport, are monotonically dependent on the light wavelength for a wide range of energy. Thus, the lasing output is selected a priori by the gain properties.

In order to tailor lasing properties, modern nanophotonics propose a route to exert a control over the lasing parameters through the material nanostructure itself. In the particular case of random lasers, there are two main lacks of desired functionalities, which are emission directionality and wavelength tunability.

In this chapter it will be shown how to control light diffusion with the optical

resonances of the monodisperse scatterers composing the system. The resonant behavior in the diffuse light though a photonic glass allows to control the laser emission via the diameter of the spheres and their refractive index. Such a system is a dispersive random device with a priori design lasing peak within the gain curve.

7.1. Gain medium

A crucial factor in realizing a random laser is the gain medium, the medium which provides light emission and amplification. Most of the materials used to that purpose can be described as a three of four electronic level systems. When the material is optically excited, electrons promote to some high energy level and decay in a very short time interval to a metastable state. Is between this metastable state and the ground state where laser transitions occur. Usually, materials which can be optically pumped are considered. Among those gain materials we find mainly semiconductors with photoluminescence properties as ZnO [154] or organic molecules, organic *dyes* [64]. Photoluminescence semiconductors usually present a high refractive index contrast and are used also as the scattering material, as in the case of ZnO. Organic dyes, however, present a low refractive index and should be embedded in a multiple scattering system. These organic materials present high quantum efficiencies and a wide Stokes shift, which together with their versatility and small size (organic chains with few nanometers) make them very good candidates to be laser materials in a random medium. Among them, the *DCM* (4-dicyanomethylene-2-methyl-6-p-dimethylaminostyryl-4H-pyran) dye molecule is known as one of the best laser dyes. However, gain molecules is that they present a large quantum efficiency when in dissolution. For random lasing this is a hampering factor since, when in dissolution, the scattering medium and the gain medium together with the solvent commonly present a low refractive index contrast which attenuates the multiple scattering of light. To solve this issue, organic dyes are usually embedded in the scattering medium in solid phase. This disturbs highly the luminescence functionalities of the dyes

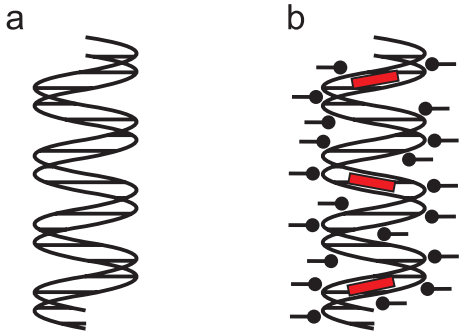

Figure 7.1: Schematic diagram for the gain medium. **(a)** Representation of DNA helices. **(b)** Inclusion of DCM organic dye into the helices of the DNA.

(they present quenching or result damaged under high pump energies). In order to avoid these eventualities, organic are intercalated into the helices of the biopolymer doxyribonucleic acid (DNA) [162]. This process, which is schematically plotted in figure 7.1, prevent dye quenching but also provide a way to dissipate dye vibrations heat to DNA strands. Proceeding this way, the intensity of the fluorescence is greatly enhanced (even amplified spontanous emission has been reported for this dye configurations [163]) and no dye damage is reported for a wide pump energy values. In this work we will use DCM-intercalated into DNA helices or strands, *DCM@DNA*, as gain medium. The analysis of the laser properties of such material are, however, out of the scope of this work [164].

7.2. Conventional Random Laser in a TiO_2 matrix powder

A random system, composed by particles with arbitrary shape and size, has a transport mean free path that is spectrally flat (non-resonant) at least for $\Delta\lambda \sim 100 \sim$ nm. Under this condition, conventional random lasing occurs at a wavelength where $\ell_g(\lambda)$ has its minimum, i.e. at the maximum of the gain

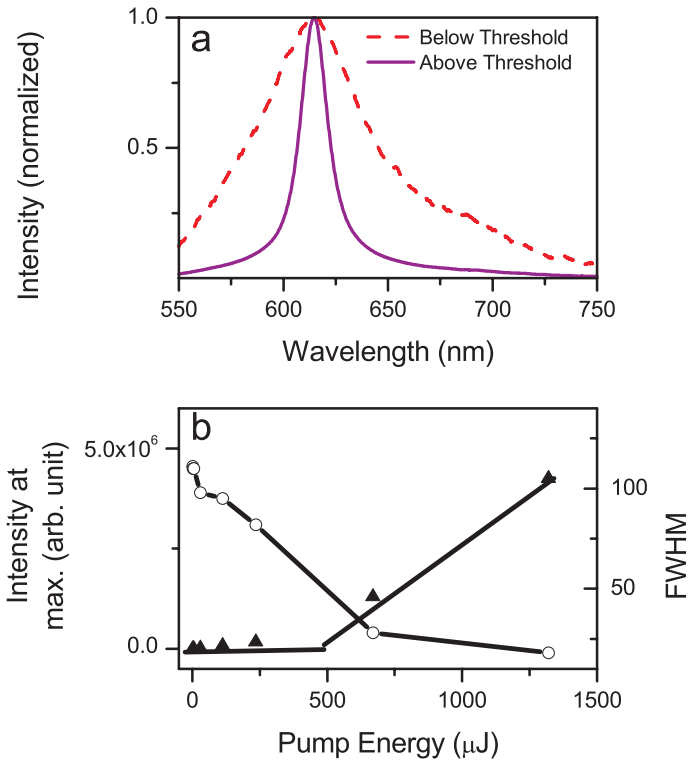

Figure 7.2: **(a)** Emission intensity bellow (dashed curve) and above (continuous curve) the threshold in the case of DCM@DNA embedded in a TiO_2 matrix. The lasing mode is defined by the gain maximum. **(b)** Emission intensity and its full width at half maximum (FWHM) as a function of pumping energy. A clear threshold appears at a 500 μJ per pulse. Pumping spot size is 2 mm

curve. Figure 7.2 shows conventional random lasing from the organic emitter, DCM@DNA, shown in previous section and embedded in a TiO_2 powder matrix. This system is optically pumped by a frequency doubled Q-switched pulsed Nd:YAG laser (9 ns pulse duration), with $10 \sim Hz$ repetition rate. The spot size was fixed at 2 mm diameter, to access a large gain volume (much larger than ℓ_t). The diffuse emission was monitored with a miniature spectrometer with a resolution of 0.5 nm. The scattering strength of such a system is relatively high due to the high refractive index contrast between TiO_2 particles ($n = 2.5$) and air ($n = 1$), where n is the refractive index. Figure 7.2**a** shows the normalized output intensity below (red curve) and above threshold (violet curve). As the pump power increases, the emission peak becomes narrower due to the preferential amplification of the frequencies close to the maximum of the gain curve. In such a system the lasing modes are selected from those at the spectral position of the minimum gain length, ℓ_g. The amount of DCM@DNA was 0.02 wt % for all samples considered here, of which 1% was DCM. Even with such a low concentration of organic emitter, 2×10^{-4} wt %, it is possible to achieve a lasing threshold in the output intensity at 500 μJ, which corresponds to ~ 60 $\mu J/mm^2$ per pulse (figure 7.2**b**). As previously mentioned, wavelength tunability is a great challenge in every lasing device, in particular it is an issue in random lasers. Since gain is fixed and determined by the emitter properties, in order to obtain a random system where lasing modes do not depend strictly on the gain length it is necessary to exploit the ability of the medium to sustain electromagnetic modes. The idea is to exploit resonances in scattering coefficients [11], present when the sizes of the scatterers are comparable with the wavelength of the incident light. This resonances are also present in the TiO_2 microparticles which compose the powder, but due to their different shape and size, the modes are averaged in a macroscopic non-modal response. On the contrary, in a monodisperse scatterers-composed system, each scatterer sustains the same modes at the same energy, giving rise to a macroscopic resonant behavior. A possible candidate for that purpose is the *photonic glass* (see chapter 5); static and dynamic measurements of light diffusion in such systems have shown matching resonances for $\ell_t(\lambda)$ and the diffusion constant of light $\mathcal{D}(\lambda)$ (see chapter 6).

7.3. Resonant Random Laser based on Photonic Glasses

In a photonic glass, the lasing wavelength becomes very sensitive to the diameter of the constituent spheres and follows the resonances of the system, as will experimentally shown. To that purpose, a set of photonic glasses composed by spheres with different diameters were used as the basis of an amplifying system by embedding dry organic laser dye. The emitter embedded in the different photonic glasses, DCM−special couple into the DNA strands, is the same as the one used in the case of TiO_2 powder, with the same concentration. DNA hosts charge ions in certain strand positions. The whole emitter has, therefore, a net charge due to this fact, about 3×10^{-6} M charge concentration. This extra amount of charge, when added to the colloidal suspension of microspheres, force the flocculation of

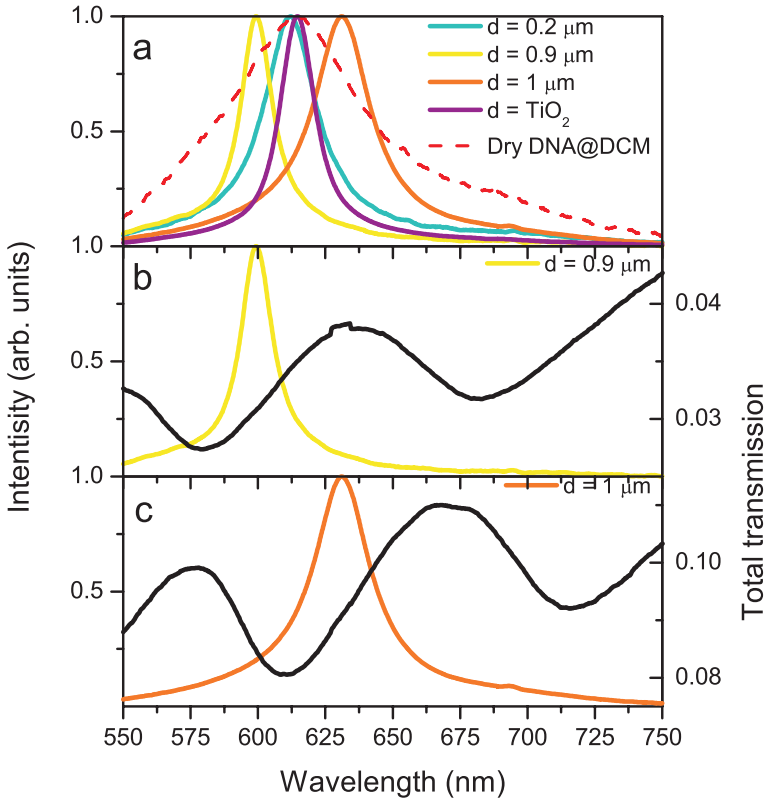

Figure 7.3: **(a)** Random laser emission from photonic glasses with different sphere diameter compared with the pure dry dye fluorescence and a reference sample made with TiO_2 powder doped with DCM@DNA). The pump energy for every sample is around 10 mJ. **(b)** and **(c)** Emission intensity and total transmission for photonic glasses respectively with $d = 0.9$ μm and $d = 1.0$ μm. Lasing occurs close to the transmission minimum.

the colloidal particles (see chapter 5).

The optical pumping and the diffuse emission was monitored equally as in the case of TiO_2-embedded random laser. The multiple light scattering condition was ensured by using samples of thickness L larger than 100 μm, which is much larger than the typical mean free path in such photonic glasses, $\ell_t \cong 2 - 3$ μm, for visible light (see chapter 6). Figure 7.3 shows in more detail how the modes sustained by the scatterers affect lasing action. As a reference we consider a photonic glass of very small spheres with $d = 0.2$ μm (figure 7.3**a**, light blue curve) as well as the polydisperse TiO_2-based random laser (violet curve). Both systems, for different reasons, do not show resonances in the static or dynamic measurements (see chapter 6). Both lase nearly at the same wavelength, close to the maximum of the gain curve. In the same figure (panel **a**), instead, one can observe a controlled overall shift of the lasing wavelength of about 35 nm between different photonic glasses composed with spheres with diameters $d = 0.9$ μm (yellow curve) and $d = 1.0$ μm (orange curve). Lasing modes from both systems

are shifted with respect to the gain maximum which can be explained in terms of Mie modes. Figures 7.3**b** and 7.3**c** compare the lasing wavelength dependence with the sample total transmission. For these two photonic glasses, the Mie resonances are pronounced and in phase opposition, even if the difference in the diameter is only ~ 0.1 μm. The minimum in transmission corresponds to a minimum both in ℓ_t and $\mathcal{D}$ and with a maximum in the scattering strength. Light at this wavelength populates a Mie mode in the structure and dwells longer in the spheres, enhancing the light/dye interaction. According to that, the system tends to lase where the scattering strength is maximum, even far from the gain maximum. The limited gain puts a limit on the wavelength shift induced by the scattering resonance. Figure 7.4 shows the images corresponding to the emission of both systems above threshold and points out the spectral shift, distinguishable by naked eye observation in the color of the lasing emission.

To prove this concept and to confirm that, indeed the transport resonances determine heavily the lasing wavelength, the spheres of the photonic glass with the gain medium DCM@DNA are dispersed in ethanol solution (spheres concen-

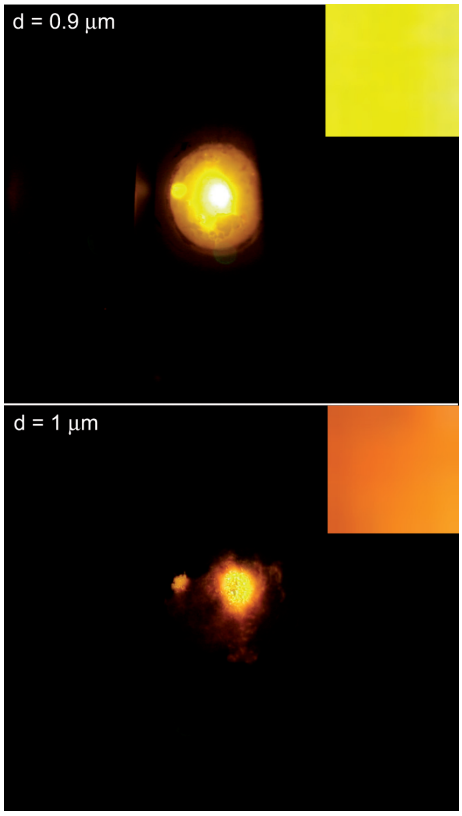

Figure 7.4: Real image of the lasing mode from $d = 0.9$ μm and $d = 1.0$ μm photonic glasses doped with DCM@DNA with a pump energy around 10 mJ in both cases. The spectral difference between both lasing emissions (~ 30 nm) is distinguishable by naked eye.

tration 5 vol%). In such a way, the refractive index contrast and, therefore, the Mie resonances are washed out. In previous works [65, 68], colloidal suspensions of spheres of particles mixed with the laser dye have been used for random lasing. This makes the contrast so low that the Mie resonances disappear. Figure 7.5**a** shows such an effect. The straight curve represents total light transmission for a photonic glass composed by spheres with $d = 1.0$ μm, while the dashed curve represents the total light transmission through the colloidal suspension of the same spheres in ethanol. The figure clearly reveals that the resonances are totally damped. The corresponding emission spectra are plotted in figure 7.5**b**, where the colors represent the same sphere diameters as for the samples in figure 7.3**a**. Figure 7.5 points out the fact that by destroying the collective Mie modes of the system, the tunability of the lasing emission also disappears, as expected, and it is no longer possible to select the lasing wavelength with the sphere diameter. As in a conventional random laser, the lasing modes are only defined by the gain maximum.

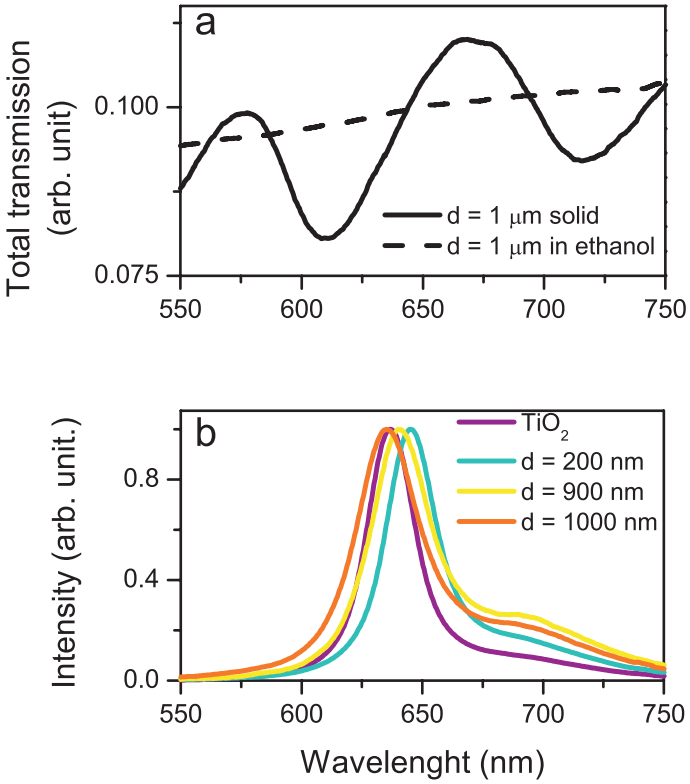

Figure 7.5: **(a)** Total integrated transmission for a photonic glass with $d = 1$ μm (continuous curve) and from a colloidal suspension of the same spheres (5 vol% of concentration) in ethanol (dashed curve). The refractive index of the host medium increases respectively from 1 (air) to 1.36 (ethanol). **(b)** Random laser emission for different spheres suspension in ethanol with DCM@DNA as optical active medium, with an external pump energy fixed at 10 mJ. In this case the total spectral separation of the emission maxima for the different suspensions is only 7 nm.

7.4. Threshold dependence on Mie resonances

The existence of resonant modes in the system not only affects the lasing mode tunability but also the threshold value of the photonic glass-based random laser [**?**]. The presence of a maximum in the scattering strength and, correspondingly, a minimum in the transport parameters as ℓ_t and $\mathcal{D}$ corresponds to a maximization of the light scattering. For certain wavelengths, the multiple scattering of light is optimized, minimizing the pump energy necessary to reach the inversion of population and, thus, the lasing. Figure 7.6**a** compares the threshold for the photonic glasses used in this work and figure 7.6**b** shows a measurement of the transport mean free path obtained from experimental measurement of coherent light backscattering [138, 139] from the same samples. All the samples measured here were pumped under the same conditions. The threshold value for four different systems is shown in figure 7.6**a**, all are composed with spheres of the same material, but with different diameters and polydispersity. Apart from the diameter, a very important parameter to take into account is the monodispersity of the scatterers. A high polydispersity value washes out the macroscopic resonant response (see chapter 6). In this measurement we have used three photonic glasses composed by very monodisperse microspheres (< 2 %) and one with a high polydispersity (represented by the bar error). This last sample is grown by mixing spheres of the same material with slightly different diameters. We intentionally introduce the polydispersity in the system to obtain a very polydisperse reference sample composed by the same material as the other photonic glasses. The diameter of the spheres is normalized to the lasing wavelength emission (λ_{lasing}) and the polydispersity is represented by the error bar on the diameter variable.

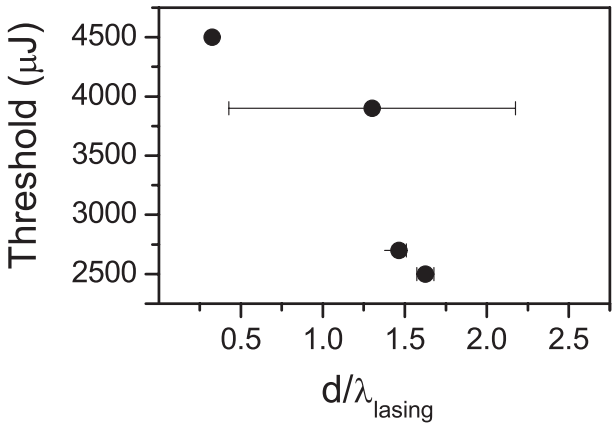

Figure 7.6: Threshold for various photonic glasses: a standard sample with $d = 0.2$ μm which is not able to sustain Mie resonances in the visible, two photonic glasses with $d = 0.9$ μm and $d = 1.0$ μm which are capable to sustain Mie resonances within the gain curve and a polydisperse arrangement (~ 42 %) of PS spheres for which a threshold appears at 3.9 mJ. This plot points out how the existence of resonant modes for light within the gain spectral range reduces the pump energy necessary to achieve population inversion.

Three of those systems have a main diameter closed to the lasing wavelength. This fact places Mie modes in such an energy interval. In the particular case of the photonic glass composed by spheres with $d = 200$ nm, the small size of the spheres pushes the modes to much higher energies. Therefore, those spheres behave, upon this particular light energy illumination, as point-like scatters giving rise to Rayleigh scattering (where scatterer structure is negligible) instead of Mie scattering (where resonances are featured). Resonances are expected in other energy ranges (in the UV) for this particular small sphere diameter. With this considerations, it is easily observed how random lasing has a lower threshold for those photonic glasses where Mie modes are present (for this particular energy range), as in the case of $d = 0.9$ μm and $d = 1.0$ μm. These photonic glass-based random lasers need about half pumping energy than the two reference samples: the photonic glass composed by small microspheres (with $d = 0.2$ μm) and a very polydisperse arrangement of the same kind of spheres with a main diameter about $d = 0.8$ μm. It is also important to mention that these two reference samples lase at the same spectral position of the TiO_2 conventional random laser. Therefore, Mie modes are not only a way to control random lasing wavelength but also a way to optimize random lasing threshold.

7.5. Conclusions and future work.

In this chapter, random laser action from a three-dimensional system with resonant transport features has been presented. The experiments shown here demonstrate that Mie resonances can strongly effect random lasing and determine both the lasing emission wavelength and threshold for photonic glasses. The concurrence of disorder with scattering strength, gain and monodispersity is what allows this fact. The high contrast of the dielectric in air secures strong light-matter interaction; the dye hosted in DNA helices lends amplification; finally the resonances spectrally select the modes and minimize the lasing threshold of the laser. In the experiments the laser dye was always distributed on the surface of the spheres. This work shows that it is possible to control spectrally both light diffusion and random lasing emission, opening a novel route to active disorder based photonic devices.

Part III

From Photonic Crystals to Photonic Glasses

Chapter 8

Light transport through vacancy-doped photonic crystals

Usually, defects in photonic crystals are regarded as undesirable features that spoil optical quality and performance. However, they can also be viewed as an enriching factor since, when controlled, they can be used to build up cavities, waveguides etc. being the basis of future circuits of light. This only happens when a strict control is exerted on defects amount, position, shape, and other morphological characteristics [166]. The essential property of, for example, semiconductor materials which form the basis of modern electronics and optoelectronics is that their electrical conductivity can be tuned over several orders of magnitude by the addition of impurities to the crystal lattice [167]. Since the control of conductivity is performed by adding impurities to the semiconductor material, lattice imperfections has been a critical issue in the field of microelectronics. These include both extrinsic (intentional) and intrinsic (unintentional) impurities such as vacancies and interstitials. The point defects can, eventually, be optically active and act as either radiative or non-radiative recombination centers thus affecting the optical properties of the material [169], as we have seen in ZnO photoluminescence mesurements in chapter 2.

Attending to the mature semiconductors technology and in order to fulfil the promise that photonic crystals hold for nanophotonic applications, the engineering in a controlled way of (extrinsic) defects appears as an important challenge. In the particular case of opal-based photonic crystals, the amount of (intrinsic) defects produced by self-assembly is partly out of control and the achievement of the highest quality possible is a common goal of the colloidal community, for which many routes have been tested.

Important consequences on light transport parameters such as the scattering mean free path or the diffusion constant will be reported in this chapter. Even far from the localization regime, the scattering properties of Bloch modes, the periodic electromagnetic modes of a photonic crystal, are expected to be profoundly

different from the diffusive modes encountered in conventional random media. Pioneering experiments on coherent backscattering [178, 179], and diffuse light transport in photonic crystals have been searching for signatures of Bloch-mode mediated scattering but have merely shown standard light diffusion. Moreover, the experiments have been interpreted using a model that assumes no photonic modal dispersion [182], but rather a modified reflectivity at the system boundaries. Up to now, the role of the photonic crystal modes and the effect of the modified density of states on light scattering are largely unknown.

In this chapter, a new route to introduce controlled amount of extrinsic defects in lattice positions of photonic crystals will be shown. The method to introduce vacancies in lattice positions of opal-based photonic crystals will be explained. Then, a careful characterization of morphologic disorder degree will be carried out by means of SEM images analysis as well as optical spectroscopy as function of the density of vacancies. Finally, light transport will be studied through these systems. In this case, static and dynamic measurements will be shown together contrary to what has be done in chapter 6, we will here firstly analyze the scattering mean free path, ℓ_s, and the diffusion constant, $\mathcal{D}$, in photonic crystals as a function of the density of vacancies. At this point, we will return to total white light transmission measurements which suggests, in the light of the previous analysis, a kind of transition from ballistic to diffuse light transport as a function of vacancy-density. A comparison between completely random arrangements of spheres (photonic glasses) and photonic crystals with a high amount of vacancies will be finally presented.

8.1. Vacancy-doped photonic crystals

In chapter 5, a way to obtain a random solid ensemble of spheres has been extensively outlined. In addition, an alternative route to grow a disordered distribution of monodisperse spheres will be shown in this section. For that purpose, a binary colloidal crystal will be engineered in what it is called an *alloy photonic crystal* or *vacancy-doped photonic crystal*. Binary photonic crystals have been object of interest in the past years [170, 171, 172]. They consist of both large (L) and small (S) spheres that alternately self-organize into two- or three-dimensional superlattices. Compared to those crystals which are composed by single-species spheres, binary crystals exhibit a rather rich phase behavior that depends on the volume fractions of the large and small spheres, and on the diameter ratios of the small to large spheres.

Going a step beyond, and selectively etching one of the spheres (either large or small ones), those that we will call dopants in the following, a system composed by monodisperse scatterers can be obtained. Figure 8.1 schematizes the process and the results obtained. Binary colloidal suspensions of PMMA and PS spheres were ordered by vertical deposition [45]. The total colloidal concentration is typically set as 0.15 *wt* % and the growth conditions are the same as for the case of the photonic crystals as explained in chapter 2. The density of dopants (PS spheres, in this case) is tune by changing over the partial PS con-

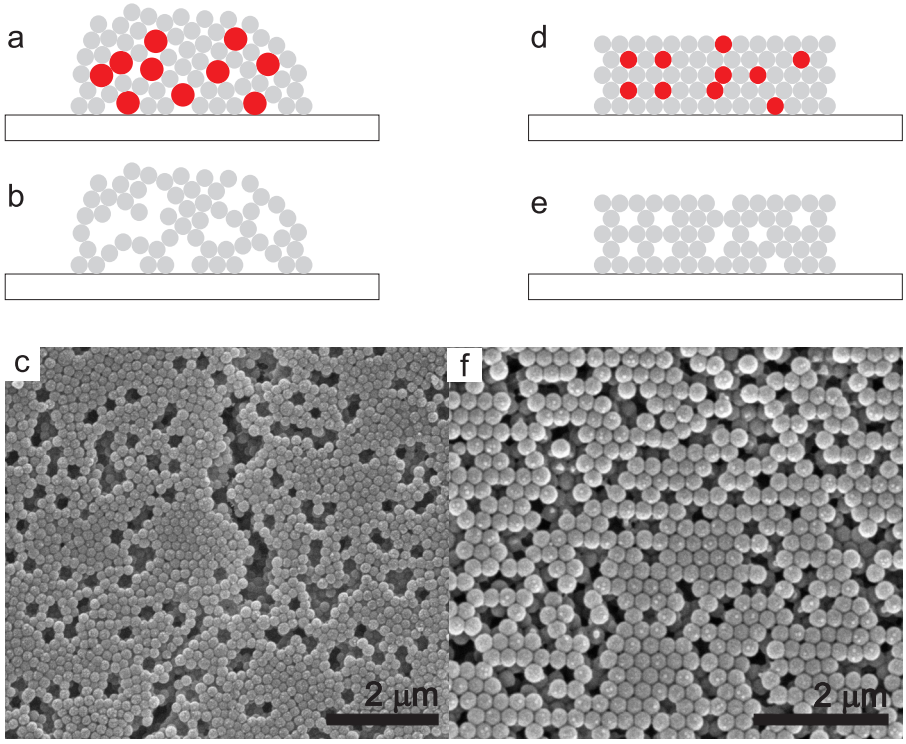

Figure 8.1: **(a)** A diagram schematizes the film growth by vertical deposition when PS (red) and PMMA (grey) spheres are mixed together in the initial colloidal suspension with different diameters. By removing the dopant spheres (PS), thin disordered films are obtained **(b)**. The vacancies are the original positions of the PS spheres before selectively etching them with Cyclohexane. These are visible in a SEM image **(c)** of a disordered film grown by this method using PS and PMMA spheres with diameters 457 nm and 237 nm, respectively. **(d)** and **(e)** show the same process when PS and PMMA spheres have the same diameter. In that case, the lattice remains undisturbed after the dopants removal. **(f)** SEM image of thin disordered film grown by this method with PS and PMMA spheres with the same diameter (237 nm).

centration in the initial colloidal suspension. For example, if a 10 % final vacancy density is needed, a partial PS spheres concentration of 0.015 wt % and PMMA concentration of 0.135 wt % will be mixed to obtain a total 0.15 wt % colloidal suspension. Once the alloy colloidal crystal is grown, PS is removed by a chemical selective etching. In particular, PS selective removal is performed by immersing the samples in 99 % pure Cyclohexane for at least 4 h. This very easy procedure completely removes PS spheres from their lattice positions, leaving the PMMA spheres undisturbed. Figure 8.1 schematizes the two possible final systems which can be obtained following this procedure. Figure 8.1**a**, 8.1**b** and 8.1**c** shows the process when using two original PS (red) and PMMA (grey) spheres with different diameters ($d_{PMMA}/d_{PS} = 0.6$). If the spheres diameters are initially different ($0.3 < d_{small}/d_{large} < 0.7$), the thin film grows very disordered [173] and the resulting system is a random and disordered thin film composed by PMMA spheres,

as shown in figure 8.1**a**. By selectively removing the dopants (PS spheres), a disorder arrangement of PMMA spheres is obtained (figure 8.1**b**). SEM image of the surface of such system is shown in figure 8.1 **c**. The ratio between PS diameter and PMMA diameter has a paramount importance. If one of both spheres is too small, an ordered superlattice can arise from the self-assembling process [170]. On the contrary, if the spheres diameters are initially equal figure 8.1**d**, a different kind of disordered system is obtained. In that case, the system grows ordered and the selective removal of the dopants do not alter the structure lattice (figure 8.1**e**). SEM image figure 8.1**f** shows a colloidal crystal composed by 30 % of PS spheres and 70 % of PMMA spheres after PS etching. In that case, both spheres PMMA and PS have the same diameter $d = 237$ nm, within the polidispersity of each of the spheres (< 2 %).

The selective dissolution of PS spheres in an colloidal alloy crystal can be optically monitored. This can be done by estimating the effective refractive index of the sample for a given thickness and following its evolution as a function of etching time. The optical response of a photonic crystal for (low) energies far from the pseudogap are equal to those of an homogenous medium with an effective refractive index. For that energy range, light cannot probe the nanostructure of the system. From the spectral separation of the Fabry-Perot fringes in the

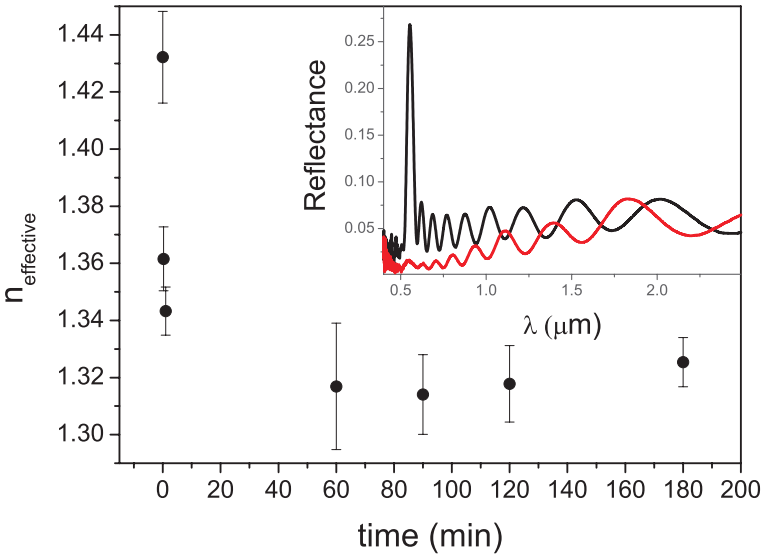

Figure 8.2: Effective refractive index (n_{eff}) of the system as a function of PS etching time. The concentration of PS and PMMA spheres are known and the thickness of the sample, *L*, can be then calculated from the Fabry-Perot fringes in the reflectance spectrum (black curve in the inset of the figure). By dissolving the PS spheres, n_{eff} reduces. This variation is accounted for by the blueshift in the Fabry-Perot fringes. The evolution of n_{eff} can be estimated with the help of *L* and the Fabry-Perot fringes of the etched sample (red curve in the inset of the figure). The PS removal has a characteristic time of about few minutes. n_{eff} reaches a stationary value when PS spheres are completely removed from the sample.

transmittance or reflectance spectra, the thickness of the sample can be accurately estimated. Local reflectance maxima due to the Fabry-Perot resonances will appear at (for an opal on a substrate with a refractive index higher than that of the opal [174]):

$$m\lambda = 2Ln_{eff} \Longrightarrow \frac{1}{\lambda} = \frac{m}{2Ln_{eff}} \tag{8.1}$$

where m is the resonance order, L is the sample thickness and n_{eff} is the effective refractive index. Plotting the inverse wavelength as a function of the resonance order, a linear relation is obtained. From the slope of the relation between m and λ the thickness of the sample can be calculated. The thickness of the as-grown system, composed by PS and PMMA spheres (figure 8.1**d** can be estimated from the known partial concentration of each sphere and from their refractive index: $n_{PS} = 1.59$ and $n_{PMMA} = 1.4$. With this initial estimation of the thin film thickness, which does not vary during the etching process, it is then possible to study the evolution of the etching process by monitoring the effective refractive index as a function of the etching time using equation 8.1. n_{eff} is constant when the PS spheres are completely removed from the lattice. Figure 8.2 plots the evolution of n_{eff} as a function of the etching time in thin film initially composed by a 60 % of PMMA spheres and a 40 % of PS spheres both with a diameter $d =$ 237 nm. The figure reveals that, for a etching time interval longer than 1h, n_{eff} reaches a constant value and, therefore, the PS spheres are completely dissolved. This process occurs in few minutes; the effective refractive index strongly reduces in the first minutes of the etching process. The inset of figure 8.2**b** shows the reflectance spectrum from the composite before (dark curve) and after PS removal (red curve). Apart from the disappearance of the reflectance peak related to the first pG in the ΓL direction (which will be object of attention in the following sections), a blue shift in the Fabry-Perot fringes point out a change in n_{eff}. The final system is a vacancy doped photonic crystal (figure 8.1**e**), where the amount of vacancies is determined by the initial relative concentration of PS/PMMA spheres in the initial colloidal suspension. These samples have typically the same dimensions of a thin photonic crystal film, that is, few micrometres thick and few centimeters wide. The homogeneity of the final structure after etching might be useful to study the effect of controlled induced extrinsic disorder.

8.2. Study of topological disorder in vacancy-doped photonic crystals

The degree of disorder in vacancy-doped photonic crystals is evaluated by means of two characterization methods; firstly, the analysis of the image autocorrelation function which allows an estimate of the correlation length ℓ_c, of the sample surface (the distance from a point on the sample beyond which there is no positional correlation), and secondly white light optical spectroscopy (specular measurement of reflectance and transmittance) which permits to probe the superficial and bulk disorder in the sample. Both methods provide an indication of the

disorder degree as a function of the density of vacancies included in the samples. A complete characterization requires the study of light transport parameters like the scattering mean free path, ℓ_s, or the diffusion constant, $\mathcal{D}$.

8.2.1. Correlation length

The analysis of the autocorrelation function, $F(\tau)$, from a SEM image of a photonic glass surface has already been used to measure the degree of disorder in those systems (see chapter 5). As explained in that case, the autocorrelation

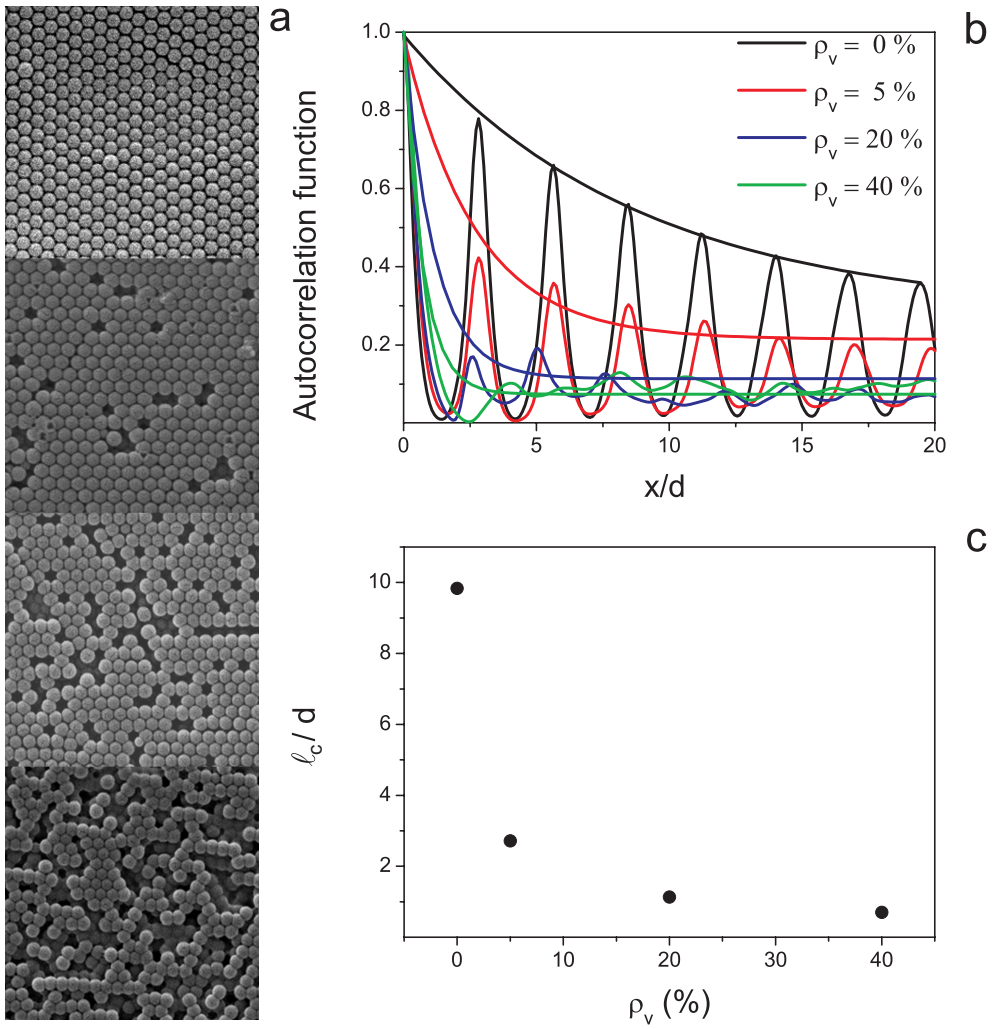

Figure 8.3: **(a)** SEM images of opal-based photonic crystals doped with a different vacancy density: $\rho_v = 0\ \%, 5\ \%, 20\ \%$ and $40\ \%$. **(b)** Autocorrelation function, $F(\tau)$, of the surface SEM images from the four different systems. A plot profile of a cut in the autocorrelation function accounts for by the order degree of each sample. **(c)** Correlation length ℓ_c calculated for the four samples as the autocorrelation function decay length $F(\tau) \propto e^{-\tau/\ell_c}$.

function describes the correlation of the contrast function, $c(r)$, of an image (in this case the surface of a given sample) and gives a measure of the translational symmetry in the system. The same analysis will be used in the case of photonic crystals doped with a given density of vacancies. All the samples analyzed in this section are composed by particles which are equal in shape and size (monodisperse) and are arranged with a regular distance between first neighbors (as that one shown in figure 8.1**f**). In this case, the lattice remains undisturbed after the PS etching process and it presents a long-range correlation. There is, therefore, a strong correlation imposed by the lattice survival. As will be shown, the effect of addition of vacancies is the increase the disorder and the decrease of the correlation length of the system.

Figure 8.3**a** shows a comparison of four SEM images from different opal-based photonic crystals grown with PMMA spheres with a diameter $d = 237\ nm$ and doped with $\rho_v = 0\ \%, 5\ \%, 20\ \%$ and $40\ \%$ vacancies in lattice positions. Figure 8.3**b** shows the autocorrelation function, $F(\tau)$, for an arbitrary given direction and from the corresponding system and figure 8.3**b** shows the corresponding correlation length, normalized to the sphere diameter. The autocorrelation function from the vacancy-free (*perfect*) ordered structure presents a periodic distribution of maxima due to its long range correlation (translational symmetry). By doping the system with vacancies, this maxima are strongly attenuated, pointing out an increasing disorder in the system. Note also that dependence on distance of the autocorrelation functions also gives a measure of the relative order of the four different structures. The periodicity of the crystals yields an oscillating spatial correlation which is damped on different length scales, depending on the amount of imperfections. The decay in the autocorrelation function can be characterized by a correlation length as $F(\tau) \propto \cos(\tau/d)\ e^{-\tau/\ell_c}$ which is the distance from a point beyond which there is no further correlation of structural order. The oscillations present in the autocorrelation of the SEM images are on the same length scale, corresponding to the periodicity of the structure (the same in the four cases), but the decay of the envelope shows an increasing disorder with the density of vacancies. From a fit, the values of the four systems correlation lengths are $\ell_c \sim 10\ d$ in the case of the perfect crystal and $\ell_c \sim 3\ d$, $\ell_c = 1\ d$, $\ell_c = 0.7\ d$ for a vacancy concentration of a 5 %, 20 % and 40 % respectively.

8.2.2. Optical spectroscopy

In this section light transport though opal-based photonic crystals doped with a controlled amount of vacancies will be analyzed by means of static measurements. The static measurements will comprise specular transmission and reflection with white light (from 400 nm to 900 nm) in the direction perpendicular to the sample surface (ΓL).

An optical and morphological study of disorder in the composite alloy crystal (figure 8.1**a**), the intermediate system where PS spheres are not removed from the sample, can be found in the literature [173]. The aim of the work presented in this chapter is, nevertheless, to obtain disordered thin films composed by *monodisperse* scatterers. It is, therefore, mandatory to selectively remove one of the species

and to study the degree of disorder in the bulk of the system. The analysis of the autocorrelation function from SEM images of the samples surfaces carried out in the previous section only gives information from the sample boundaries, the surfaces. The analysis carried out in the present section will affront the measurement of the amount of remaining order in the bulk of the structure. To that purpose, optical tests are conducted where specular reflectance ($R = I_R/I_0$) and transmittance ($T = I_T/I_0$) are measured in the direction perpendicular to the sample (along the ΓL crystallographic direction). As explained in chapter 5, section 5.3.2, the magnitude $R + T$ can be used as a measure of the order of the structure. Intrinsic disorder in opal-based photonic crystals has been analyzed by this means in the past [59, 60]. In this section we will applied this method to characterize the intentionally (extrinsic) disorder added to the samples. Diffuse

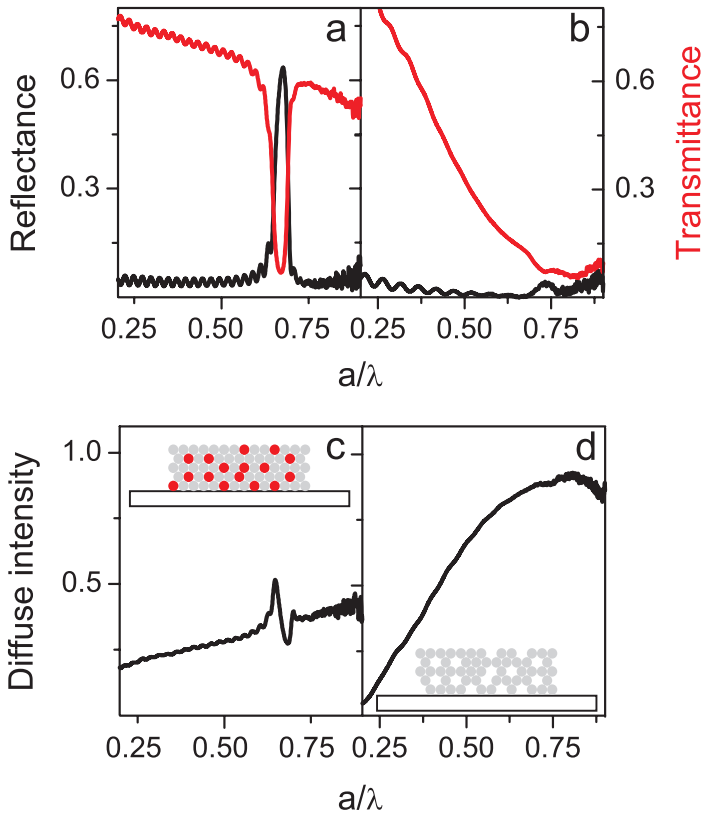

Figure 8.4: **(a)** and **(b)** figures show the reflection and transmission measured from the 0 % and 40 % vacancy doping, respectively. **(c)** and **(d)** figures show diffuse light intensity from the corresponding samples before and after PS removal, respectively. Notice the presence (disappearance) of the gap before (after) PS spheres removal. The inset of figures **(c)** and **(d)** shows a scheme of the corresponding system.

intensity, D, can be calculated from the relation $D = 1 - R - T$ (see appendix A). R and T measurements with normally incident white light in the low energy regime ($a/\lambda < 1$, where a is the lattice parameter and λ is the wavelength of light in vacuum) for a certain crystallographic direction will be carried out for that purpose. Since PS and PMMA absorbance for the considered frequencies is negligible [57, 58], only the presence of a certain amount of vacancies in lattice positions gives rise to diffuse light scattering and extinction.

The main consequence of the inclusion of vacancies in photonic crystals in their optical properties is shown in figure 8.4. Figure 8.4**a** and **b** shows reflectance and transmittance measurements from samples doped with a 0 % and 40 % of vacancies, respectively. The most evident effect of the inclusion of vacancies in the photonic crystal is the disappearance of the reflectance peak related to the pG in the ΓL direction (direction along which the measurements are performed). This effect is also revealed by the diffuse intensity measurement, D, from both samples (figures 8.4**c** and 8.4**d**). Before etching, D presents the usual features for a finite opal such as the monotonic increase for frequencies outside the gap, the presence of a gap at about $a/\lambda \sim 0.6$ for polymeric spheres, an enhancement in the low energy edge and an inhibition of frequencies inside the gap [59]. The transition between order and disorder is performed by removing the PS spheres and it is highlighted by the disappearance of any hint of gap or band-edges features and by the enhancement of D for all frequencies. The reason for the disappearance of the photonic features related to the pG is that, when increasing disorder, constructive and destructive interference, which is at the basis of light propagation through photonic crystals, is averaged out giving rise to an effective medium behavior. In such a case, only UV absorption tail is left at higher energies related to UV PS absorption [57]. The complete disappearance of a gap-related peak (dip) in reflectance (transmittance) is the fingerprint of bulk disorder in the samples. This measurement, together with the analysis of the sample surface correlation length, gives a preliminary characterization of the effect that the inclusion of vacancies in random positions of the lattice has on the optical properties of the samples.

8.3. Scattering mean free path

Let's go deeper in this direction and let's quantify the effect that these vacancies have on light scattering and, in particular, their effect on the scattering mean free path and the diffusion constant. In the case of the perfect lattice, the waves scattered by each sphere interfere in such a way to cause total transparency for a large energy interval. From the light propagation point of view, the vacancies act as scatterers which produce diffuse light, making the pass-band opaque and the band gap transparent. This effect will be quantified in this section by the direct measurement of the scattering mean free path as a function of the vacancies density.

For that purpose, the scattering mean free path (ℓ_s) in the visible and near infrared range for one specific direction has been measured. Furthermore, a strong chromatic dispersion of ℓ_s and value of up to $\sim 100-500$ μm, that is to say ~ 300

times the lattice parameter, a, is reported. Figure 8.5 shows a scheme of the experimental set-up. The opal-based photonic crystals doped with vacancies (from 0 % to 40 %) are probed along the ΓL crystallographic direction (perpendicular to the sample surface). Specular reflectance ($R = I_R/I_0$) and transmittance ($T = I_T/I_0$) are measured. Spectra (as those shown in figures 8.4**c** and 8.4**b**) are taken in adjacent regions, as shown in figure 8.5**a**, along a line perpendicular to the crystal growth direction and parallel to the meniscus between the colloid and the substrate. This is done to be sure that growth has taken place under exactly the same conditions and at the same instant. Adjacent regions of different thickness (films with different amount of stacked layers, drawn in figure 8.5**a**) are visible by optical microscope inspection as terraces on the sample surface, as in figure 8.5**b**. The thickness of such films is assessed by measuring the density of Fabry-Perot fringes that occur for the interference of the light reflected from the front and rear faces of the sample. This precise measurement has been crucial to provide the exact thickness, L, of the tested region in the sample and has been confirmed by simply counting terraces along the photonic crystal (counting the number of terraces in the vertical direction whose separation is known with an uncertainty equal to that of sphere diameter. The actual thickness is, therefore, given with an uncertainty of < 2 %, the sphere polydispersity.

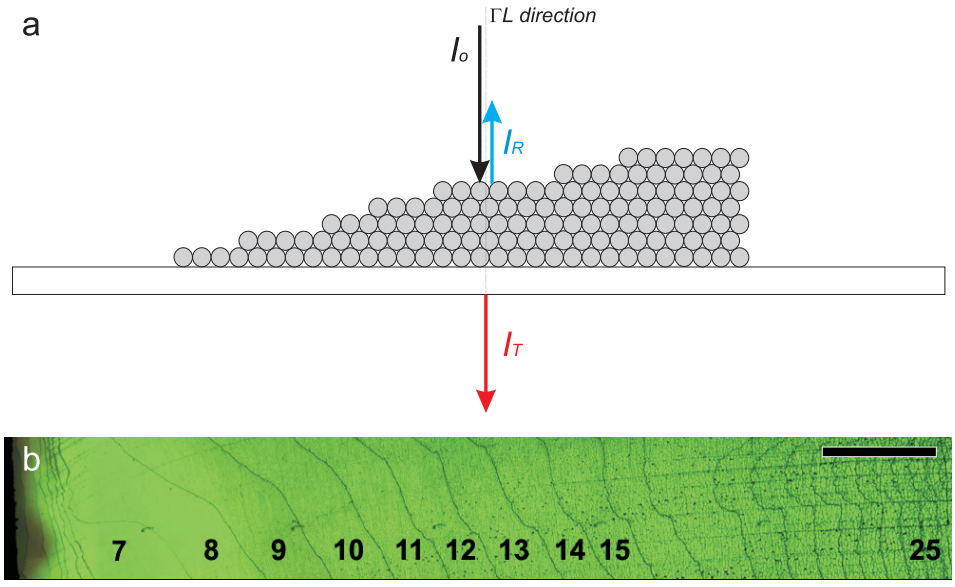

Figure 8.5: **(a)** Scheme of the scattering mean free path measurement set up. Specular reflectance and transmittance are measured along the ΓL direction (perpendicularly to the sample surface) in adjacent terraces with known thickness. **(b)** Optical image made combining 8 images of the opal surface from a microscope, in which the different layers are distinguishable as terraces. The measurements have been performed from 1 to 67 layers, which are clearly distinguishable from each other by eye inspection with the help of the microscope, on adjacent areas, along horizontal lines perpendicular to the crystal growth direction.

The analysis carried out over the reflectance and transmittance measurements takes into account the fact that light impinging on a perfect photonic crystal can be absorbed, reflected, diffracted or transmitted. In our case, and in the particular spectral range of interest, absorption effects can be neglected as confirmed by measuring the absorption length ($\ell_a \sim 10m$) in the visible range for a photonic glass composed by the same polymer spheres (see chapter 6, section 6.1). Diffraction can be totally excluded as we are considering energies below the onset of diffraction ($a/\lambda \sim 1.12$) for details see appendix A. If any degree of topological disorder is added, some light will be scattered off a Bloch mode, leading to what is commonly known as diffuse light. In the case treated here, scattering is the only phenomenon that can account for light missing from the sum of ballistic transmittance T and reflectance R. Under these conditions, the diffuse light in photonic crystals is then quantified by $D = 1 - (T + R)$, as previously discussed. Lambert-Beer law for photonic crystals can be written as:

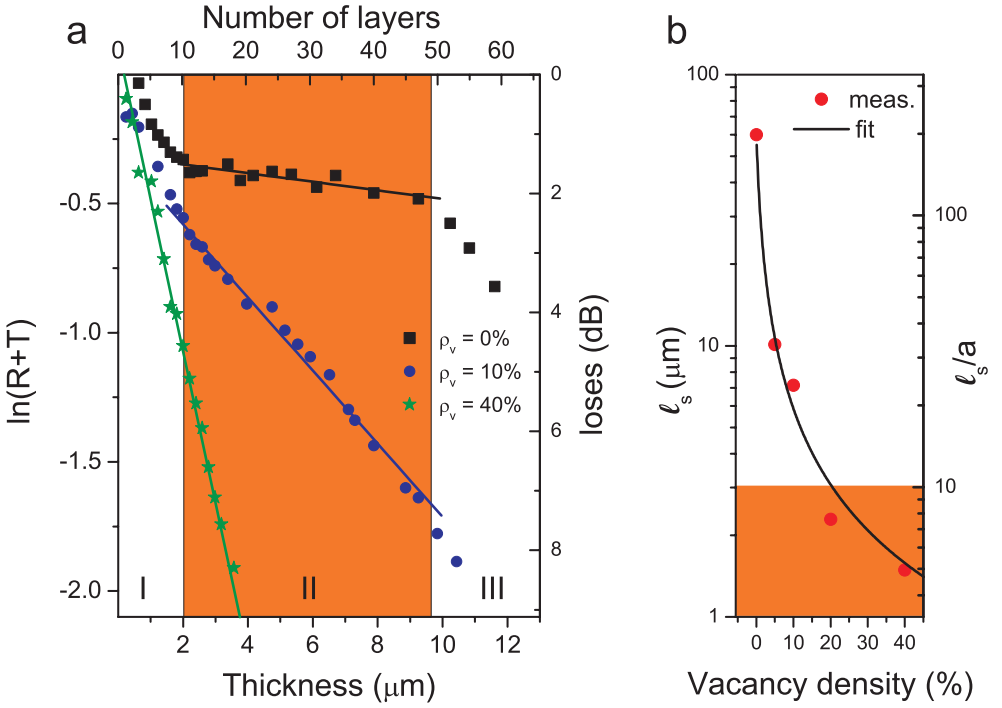

Figure 8.6: Lambert-Beer's law in photonic crystals. **(a)** Plot of $ln(R+T)$ as a function of the sample thickness, at $\lambda = 633$ nm, for different vacancy density doped photonic crystals (from 0 % to 40 % vacancies doping), made of PMMA spheres of 237 nm diameter, and refractive index 1.4. The slope is the inverse of the scattering mean free path. Three regions are distinguishable, from low to high thickness: (I) interface effects; (II) the opal is complete, and the scattering losses grow slowly and exponentially; (III) thick and cracked opal. **(b)** Represents ℓ_s obtained from the slope of the linear fit, for regime II, compared to the Bragg length (L_B) in the case of $\rho_v = 0$ % as shaded area.

$$R(L) + T(L) = \exp(-\frac{L}{\ell_s}) \tag{8.2}$$

(deduced in more detail in A, section A.1). Scattering losses are characterized through the scattering mean free path which, in a random medium, is defined as $\ell_s = 1/\sigma\rho_s$, where σ is the scattering cross-section and ρ_s is the scatterers number density. ℓ_s is not only a measure of the quality of a photonic structure but also the basic length-scale of a more complex picture of multiple scattering and light diffusion. While quantities like the transport mean free path, ℓ_t, or the diffusion constant, $\mathcal{D}$, are meaningful only in the context of the diffusion approximation, ℓ_s has a full meaning in any microscopic picture, regardless of the transport regime. In our system, the degree of extrinsic disorder can be very precisely and uniformly tuned (see scanning electron microscopy (SEM) images in figure 8.1**a** and 8.1**b**), while keeping the sample thickness precisely controlled. This allows us to develop a setup to measure Lambert-Beer's law for photonic crystals.

8.3.1. Scattering mean free path vs. vacancy doping

Figure 8.6**a** shows the measured $ln(T + R)$ for three different degrees of vacancy doping, i.e. for different degrees of extrinsic disorder, at a wavelength $\lambda = 633$ nm and for spheres with diameter d = 237 nm ($a/\lambda = 0.52$). In this type of representation, the slope yields directly $(-\ell_s)^{-1}$ according to equation 8.2. This wavelength is chosen to exemplify a spectral region where no photonic band features are present, as, at such a low energy, the photonic crystal band dispersion is the same as in a uniform homogeneous effective medium. In figure 8.6**a** three scattering regimes are clearly distinguishable. For thicknesses lower than ca. 10 layers, regime (**I**), light scattered is due to surface effects and the slope of the linear fit decreases. Top (crystal-air) and bottom (crystal-substrate) interfaces are sources of light scattering of about $\sim$ 25-30 %. The interfaces present additional defects, for example different stacking patterns [48], high lattice displacements and, even stacking order arrangements [47], which are been already discussed in the context of optimal self-assembling of the spheres in the colloidal meniscus [50]. When the second regime (**II**) sets in, the slope $(-\ell_s)^{-1}$ reach a stationary value that characterizes the photonic crystal. Equation 8.2 holds and scattering losses scale with sample thickness like $\sim \exp(L/\ell_s)$. In this range of thicknesses, where self-assembly has reached a stationary and optimal behavior [59], it is possible to determine the quality of the crystal from the scattering mean free path. If we extrapolate to zero thickness the exponential fit yields a non-zero value for the losses, which means that there are some intrinsic scattering losses associated with the surfaces of the crystal. As the crystal grows thicker, the absolute value is dominated by surface losses but, for thicknesses in regime **II**, ℓ_s is determined from crystal bulk variation. Finally, for larger thicknesses, a third scattering regime (**III**) appears in figure 8.6**a**. Apparently, for thick samples the self-assembling process loses its effectiveness and the intrinsic disorder grows strongly. This effect may be attributed to several reasons such as a possible different drying condition of the crystal caused by the evaporation

of the solvent or a mechanical instability of the sample that we found starts to crack after ~ 50 layers and to lift from the substrate.

The physical picture we propose can be checked against consistency if additional disorder is added to the photonic crystals. This can be done by doping the original photonic crystal with a controlled concentration of vacancies. In this way, the scattered light increases when the extrinsic disorder (vacancies) increases. At a wavelength of 633 nm the values of ℓ_s for different vacancy density, calculated from the fit to the Lambert-Beer law, are plotted as a function of vacancy density in figure 8.6**b**. Basically, in a photonic crystal without vacancies, ℓ_s depends only on the intrinsic thermodynamically-induced disorder, whereas in a controlled vacancy-doped photonic crystal, ℓ_s can be artificially decreased through extrinsic disorder. As can be readily appreciated, the *perfect* crystal (that with 0 % added vacancies) is far from perfect but it presents a scattering mean free path of several hundreds of times the lattice constant (in this case $a = 0.33\ \mu m$) and, in particular, much larger than the Bragg length [59], that in our case is $\ell_B = (3.8 \pm 0.3)\ \mu m$. It can also be noticed that, the addition of a very little amount of defects rapidly decreases the mean free path, hence the quality of the crystal. In this figure, the inverse scattering mean free path scales linearly with the vacancy concentration ρ_v. We can expressed ℓ_s as:

$$\ell_s^{-1} = \rho_0\sigma_0 + \rho_v\sigma_v \tag{8.3}$$

where ρ_0 and ρ_v are the density of intrinsic and intentionally added scatterers and ρ_0 and ρ_v their scattering cross-section respectively. Equation 8.3 assumes independent scattering from the vacancy doping. Using equation 8.3 we can fit $\ell_s(\rho_v)$ as a function of the vacancy concentration, ρ_v (in %) and get a good agreement with experimental data. From this fit we can estimate $\sigma_v = (0.016 \pm 0.002)\ \mu m^2$, which is about 3 times smaller than the geometrical cross section of the sphere and compatible with its Mie cross section ($\sigma_{Mie} \sim 2\pi R^2$ for $R \sim \lambda$, where R is the sphere radius [10]).

8.3.2. Scattering mean free path vs. energy

The analysis carried out so far has been done at wavelengths away from any photonic band gap features: that is, in a spectral region where the material acts just as an effective medium and the addition of vacancies (scatterers) is just a source of scattering. In order to study the effect of the photonic crystal modes on light scattering it is necessary to investigate the energy dependence of ℓ_s, which can be done by plotting the scattering mean free path as a function of wavelength, as presented in figure 8.7.

Here a resonant behavior of ℓ_s is visible. This strong dispersion is the signature of the effect of the photonic crystal. Before going into the details of this profile, it is worth carrying out a quantitative analysis of the scattering strength in our photonic crystals. In the low energy side of the pG, ℓ_s takes on a value of the order of $\sim 100\ \mu$m for sphere diameter $d = 237$ nm and $\sim 500\ \mu$m for $d = 600$ nm (not shown here), the largest values reported so far. Previous experiments [178, 179, 180] have measured ℓ_t, the transport mean free path, from very thick

(~ 200 μm) photonic crystals grown by natural sedimentation or centrifugation [178], and found values in the range $7\ \mu\text{m} < \ell_t < 20\ \mu\text{m}$. It is important to point out that ℓ_s is in always smaller than ℓ_t since it is defined as:

$$\ell_t = \frac{\ell_s}{1 - \langle \cos\theta \rangle} \tag{8.4}$$

where θ is the angle with respect to the forward direction. Therefore, these reported values of ℓ_t constitute an upper bound for the scattering mean free path. The values found in our experiments represent a much higher degree of ordering than previous reports.

Figure 8.7 presents the energy dependence of ℓ_s in a logarithmic scale. Far from the band-gap, $\ell_s(\omega)$ varies as $\sim \omega^{-2}$. This $\sim \omega^{-2}$ dependence has been confirmed also in previous experiments [182] and attributed to Rayleig-Gans type of scattering [10]. Figure 8.7 shows how, at the band-edges, $\ell_s(\omega)$ has a sharp decrease of a factor of up to 4 to $\ell_s(a/\lambda = 0.59) = 111$ μm and then it shoots up almost an order of magnitude in the band-gap to $\ell_s(a/\lambda = 0.62) = 80 \pm 40$ μm. Such an 8-fold increase occurs within just 0.03 in a/λ or ~ 27 nm in wavelength, around the photonic band-gap. Again, as a comparison, we show in figure 8.7 the frequency dependence of ℓ_s for the 10 % and the 40 % vacancy photonic

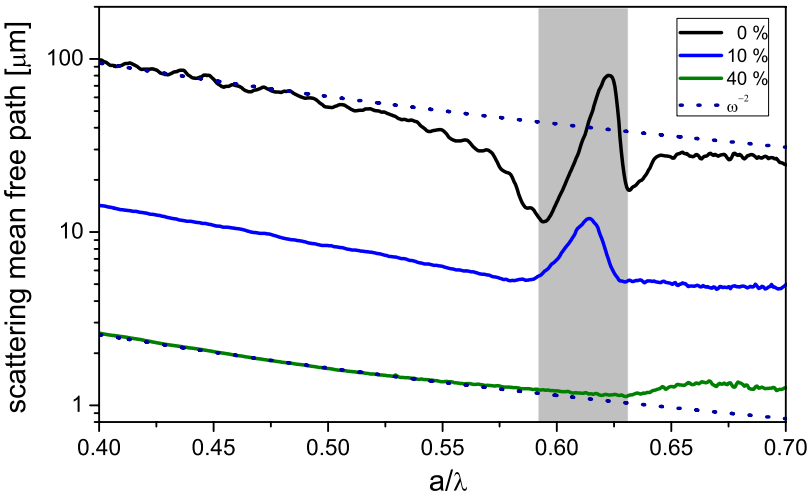

Figure 8.7: Dispersion of the scattering mean free path. Figure shows ℓ_s as a function of the light wavelength for samples grown with spheres 237 nm in diameter. The position of the pseudo-gap is shaded in cyan. A strong decrease of ℓ_s at the band-edge and a strong increase in the band-gap is the effect of the photonic crystal dispersion. The same analysis performed on 10 % and 40 % vacancy doped photonic crystals shows how the dispersion smooths rapidly to turn into a slight variation associated with the first Mie resonance of the disordered medium. The dotted line shows the ω^{-2} dependence of ℓ_s far from the band-gap.

crystal, the latter can be considered fully disordered. As the vacancy doping is increased, the profile is smoothed. Firstly the band-edge effect on ℓ_s disappears, as these states are very sensitive to disorder (we will return to this assumption later on this chapter). Then, for the 40 % vacancy case, the effects on $\rho(\omega)$ are washed out and the only feature in ℓ_s occurs at the position of the first Mie resonance of the individual dielectric spheres. This weak energy dependence of ℓ_s is likely to be the only residual effect in a very disordered opal, as those grown by natural sedimentation or centrifugation [42, 178]. Disordered opals present only superficial ordering visible in the Bragg iridescences from the first layers but are largely bulk-disordered and exhibit standard light diffusion. This may be the reason why previous experiments have reported very small values of mean free paths and no evidence of strong frequency dependence.

8.3.3. Scattering mean free path and density of states

The polarizability tensor of a small spherical particle of volume V placed at position $\mathbf{r}$ can be written as [181]:

$$\alpha = 3V[\mathbb{I} - 3iV\beta(\frac{\omega}{c})^2 Im\mathbb{G}(\mathbf{r},\mathbf{r}')]^{-1} \tag{8.5}$$

where $\mathbb{I}$ is the unit dyadic, $\mathbb{G}(\mathbf{r},\mathbf{r}')$ is the green tensor of the system at the working frequency, and β is the Clausius - Mossotti factor of the scatterer. From this, the power scattered by the particles is:

$$P \approx \varepsilon_0(3V\beta\omega/c)^2 E^+_{inc}(\mathbf{r}) Im\mathbb{G}(\mathbf{r},\mathbf{r}) E^+_{inc}(\mathbf{r}) \tag{8.6}$$

where $E_{inc}(\mathbf{r})$ is the field polarizing the scatterer. If the external field is a plane wave with wave-vector $\mathbf{k}$ and amplitude $\mathbf{E}_0$ and taking into account the reciprocity theorem, the field exciting the scatterer can be expressed using the $\mathbf{k}$ component of the green tensor $\mathbb{G}_k(\mathbf{r})$ as $E_{inc}(\mathbf{r}) = \mathbb{G}_k(\mathbf{r})\mathbf{E}_0$. We will assume that the imaginary part of the green tensor can be approximated by $Im\mathbb{G}(\mathbf{r},\mathbf{r}) \approx \mathbb{I}\pi c^2/(2\omega)\rho_{\mathbf{k}}(\omega)$. Noting aslo that the $\mathbf{k}$ contribution to the local density of states (or *projected* density of states), denoted by $\rho_{\mathbf{k}}(\mathbf{r},\omega)$, is proportional to $|\mathbb{G}_{\mathbf{k}}(\mathbf{r})\mathbf{E}_0|^2$, we obtain a (spatially averaged) scattering cross section:

$$\sigma_{\mathbf{k}}(\omega) \sim F(\omega)\omega^2\rho(\omega)\rho_{\mathbf{k}}(\omega) \tag{8.7}$$

where $F(\omega)$ is a form factor which takes into account corrections beyond Rayleigh scattering. In this simple model, the form factor can be replaced by a Rayleigh-Gans factor $F(\omega) \sim \omega^{-2}$ and the polarizability of the scatterer $\alpha(\omega)$ can be considered independent of frequency. Any lack of isotropy is neglected in the dispersion relations of the photonic crystal. This result states that the scattering cross-section, and hence the scattering mean free path, has a strong dependence on the light wavelength and the total and projected density of states $\rho(\omega)$ and $\rho_{\mathbf{k}}(\omega)$, respectively. This dependence typically disappears in ordinary random media for which the photonic modes are isotropic, and with smooth energy dependence.

Figure 8.8**a** shows the inverse of the total density of states, $\rho(\omega)$, which induces the dispersion in ℓ_s. While the total density (dark blue dotted line) has a very weak modulation at the gap, the density of states $\rho_{\mathbf{k}}(\omega)$ for propagation parallel to $\mathbf{k} = (111)$ (along the ΓL crystallographic direction) which is proportional to the inverse of the group velocity in that direction, $v_g(\mathbf{k} = (111))$, has a strong variation at the gap (violet full line). Of course in an infinite crystal the inverse of the group velocity diverges at the band edges and is not defined in the gap [24], but for finite crystals a shape that closely resembles the scattering enhancement is experimentally and numerically found.

Figure 8.8**b** shows the enhancement factor in the scattering mean free path for two different samples composed by PMMA spheres with diameters d = 237 nm (black curve) and d = 600 nm (green curve). The enhancement factor is obtained by normalizing the experimental curve, calculated from the fitting of the measurements, to the value of the scattering mean free path measured at $a/\lambda \sim 0.4$. At this low energy, which is spectrally considerably far from the photonic pseudo-gap of the photonic crystal, light does not probe the nanostructure of the system and just propagates thought the crystal as in an effective medium with an effective refractive index. The enhancement factor points out the existence of a photonic pG and reveals the variation of the density of states in the photonic crystal as compared with the effective medium. A clear resonant behavior is evident. The variation in ℓ_s is 8-fold for d = 237 nm and 20-fold for d = 630 nm, which we attribute to the superior quality of the lattice in the last particular

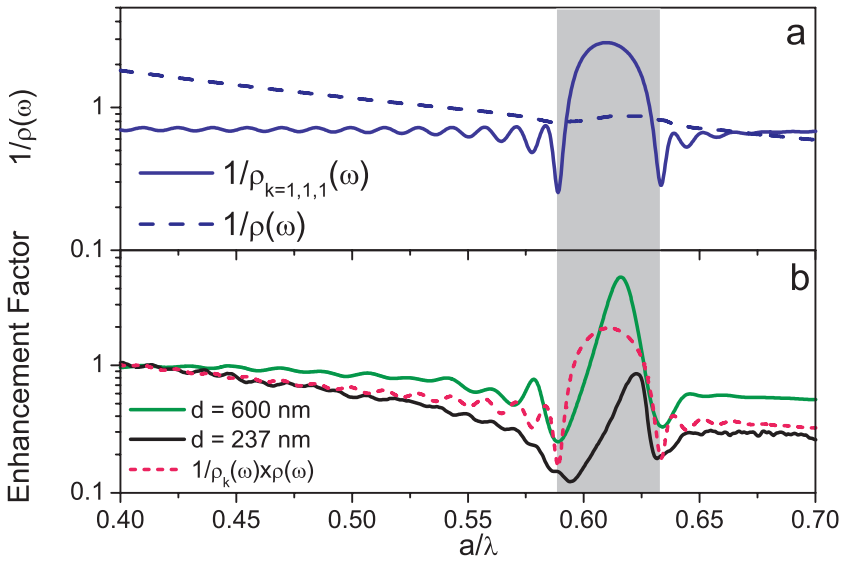

Figure 8.8: **(a)** Inverse of the theoretical density of states for an fcc arrangements of spheres along the incident direction (ΓL direction). Both the inverse of the total $\rho(\omega)$ and the projected $\rho_{\mathbf{k}=(1,1,1)}(\omega)$ are plotted. **(b)** Enhancement factor, $\ell_s(a/\lambda)/\ell_s(a/\lambda = 0.4)$, for two opals with two different sphere diameters and no vacancy doping. The dashed pink curve is the product $[\rho(\omega)\rho_{\mathbf{k}}(\omega)]^{-1}$, which qualitatively reproduces the measured profiles. The position of the pseudo-gap is shaded in cyan.

sample. In figure 8.8**b** we plot also $1/\rho(\omega)\rho_{\mathbf{k}}(\omega)$ (dashed pink curve) that, from equation 8.7, is expected to reproduce the shape of energy dependence of $\ell_s(\omega)$. A fair agreement between theory and experiment is obtained, and the qualitative behavior is well captured by our simple model. Notice that $\rho(\omega)$ measures the number of modes available for propagation into all directions, and hence is the quantity that controls the light emission from an isotropic light source embedded in the photonic crystal. In polymeric opal photonic crystals, as the one discussed here, $\rho(\omega)$ has only a minor variation of around 10 % in the pG. The directional $\rho_{\mathbf{k}}(\omega)$, which describes a single direction, has a large variation of an order of magnitude: it increases sharply at the band-edge and decreases considerably in the middle of the gap. Although both contribute to the strong variation of ℓ_s, it is evident that the principal factor responsible for a change in $\ell_s(\mathbf{k} = (111))$ is $\rho_{\mathbf{k}}(\omega)$ in the direction $\mathbf{k} = (111)$. Our simple and qualitative model accounts quite well for the shape of the measured $\ell_s(\omega)$ although it does not account for the asymmetry of its dispersion in the pG. This effect is related to the available scattering states in other crystallographic directions close to the incident one. For light incident in the ΓL direction, scattered photons in the low energy band-edge find allowed states in adjacent directions when a small momentum is acquired (like from scattering in an impurity). At the high energy band-edge, the additional momentum needed for a scattered photon to find an accessible state in other directions is larger and the process for this frequency becomes less probable than the former. This is the reason that, qualitatively, explains why ℓ_s grows more slowly in the low energy side of the gap and presents such an asymmetry. These measurements indicates the need for a more complete theoretical model that should account for all the modes in all directions with the right scattering probability.

An increase of ℓ_s in the band-gap and a decrease at the band-edge reflects the modified phase space available (Δk) for light scattering when the photonic modes are concentrated around few k-directions or when the available scattered state one reduced. This is consistent with John's seminal prediction of a need for a modified Ioffe-Regel criterion [37] for scattering in photonic crystals, to include Δk. In addition, here we show that as the phase-space is modified, also ℓ_s is altered, light scattering in photonic crystals is richer than in conventional amorphous media.

8.4. Diffusion constant

Static measurements reveal the resonant behavior in the scattering mean free path and its dependence on the projected density of states in the photonic crystal, but a crucial information about the dynamic response of light pulses though the system is also of paramount importance to characterize the transition from order to disorder. As shown in chapter 6, sectionb6.2, time-resolved measurements of light transport diffusion offer valuable information. In the previous section, the static transmission of scattered light has been analyzed, which is at the basis of light diffusion. A light pulse incident on an homogeneous material with wave-

length independent transmission, like a constant refractive index thin film, will be transmitted preserving its shape; if the same pulse encounters a bandgap environment, as in the case of photonic crystals, it experiences delays and deformations of its envelope due to the complicated dispersion of the group velocity in these systems. In this section, the time-resolved response of transmitted diffuse light though photonic crystals with a controlled amount of vacancies will be analyzed. In chapter 6, section 6.2, a streak-camera set up was used to monitor the time decay of diffuse light with ps-resolution; however, in this section, a non-linear optical gating technique will be used to measure the time decay of diffuse light, as the needed resolution is in the range of fs.

8.4.1. Time-resolved spectroscopy by non-linear optical gating

The time which light spends to travel thought a thin film with thickness of the order of microns (structured or not) is of hundreds femtoseconds (fs). This is out of the range of typical streak cameras. A streak camera cannot go beyond few picoseconds. We are brought to employ very short laser pulses and an accurate technique to detect very short time intervals (see also [184]).

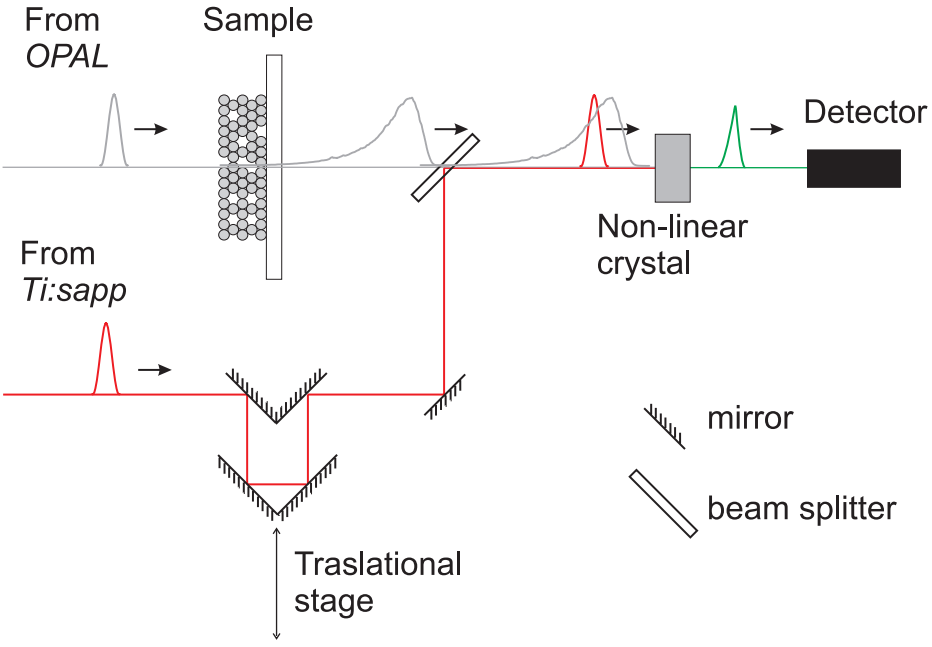

Figure 8.9: Scheme of the non-linear optical gating. Two synchronous pulses are generated by the *OPAL* laser at 1500 nm and 810 nm (grey and red pulses, respectively). The infrared (grey) pulse is used to probe the sample and generate diffuse light. The reference (red) pulse is spatially delayed in a controlled translational stage. Diffuse and reference pulses are then mixed together in a non-linear crystal generating a third pulse with frequency sum of the frequencies of generator pulses. Since the intensity of this later pulse is proportional to the product of the two, diffuse and reference, pulses intensities at a given time, the whole process works as an optical gate.

An optical gating technique has been employed to measure time decay of diffuse light through the samples analyzed in this chapter. Optical gating solves the problem of detecting very short optical pulses by converting time intervals into space distances via the space-time relation $x = ct$ (for light in vacuum 10 fs correspond to 3 μm). Figure 8.9 schematizes the set up used to that purpose. A *probe* and a *reference* pulses are provided by an optical parametric oscillator (Spectra Physics, *OPAL*) which yields short pulses tunable within 1450 to 1600 nm (average power 100 mW). The *OPAL* is pumped by a Ti:Sapphire laser at center wavelength 810 nm (pulse duration 130 fs, average power 2.0 W, repetition rate 82 MHz). More details about the pulse source can be found in appendix B). In our case, the probe pulse is generated at 1500 nm (grey pulse in figure 8.9) and it is used to probe the samples. A second *reference* pulse, residual of Ti:Sapp laser, is synchronously generated with the probe pulse at wavelength 810 nm (red pulse in figure 8.9) and it is delayed spatially in a controlled manner with the help of a translation stage with accuracy of microns. The first pulse probes the sample and gives rise to diffuse light (schematically drawn as a deformed grey pulse in figure 8.9). It is then mixed with the reference pulse in a non-linear crystal, giving rise to a third generated sum frequency pulse (green pulse in figure 8.9). The generated pulse frequency is sum of the diffuse and reference pulses frequencies. Since the efficiency of the sum-generation at the non-linear crystal is proportional to the product of the two diffuse and reference pulses intensities at a given time, the whole process works as an optical gate. Delaying spatially the reference pulse, it is possible to scan the diffuse pulse in time. Then, the problem of resolving tens of fs translates into resolving μm which is a more easily done by using the translation stage. The details of the set up used to measure time of flight of diffuse light though vacancy-doped photonic crystals can be found in appendix B

Figure 8.10 shows the measurement of the time-resolved light transmission, through thin film opals grown with PMMA spheres with a diameter $d = 630$ nm at two different energies and for a fixed vacancy density, $\rho_v = 0$. The spheres used in this section have a diameter slightly larger than those used in the previous section and this is due to the fact that both PMMA spheres come from two different batches.

The measurements have been performed at $a/\lambda_1 = 0.56$ (black circle in figure 8.10**a**) and $a/\lambda_2 = 0.59$ (red circle figure 8.10**b**). The reference pulse is plotted in both figures with a blue curve in order to compare the diffuse decay with the time delay of the reference beam. The thicknesses of the samples used in these time-resolved experiments are about 21 μm ($\sim$ 40 layers). The value of the diffusion constant is obtained by fitting the experimental time profile of $T(t)$ with the dynamical solution of the diffusion equation 1.23 (1.2.3). The diffusion constant at λ_2 is $\mathcal{D}(\lambda_2) = 220\ m^2/s$. Contrary to this, the time decay of the diffuse light at λ_1 is on the order of the of the probe and reference pulses (150 fs, blue curve in figure 8.10**a**) and it is not possible to fit the decay time and to obtain a measurement of the diffusion constant at that energy by means of the non-linear optical gating technique. In order to explain this fact, ℓ_s has been measured at these two different wavelengths, $\lambda_1 = 1590$ nm and $\lambda_2 = 1500$ nm,

for samples grown with these spheres. Figure 8.11**a** shows the corresponding spectral positions of these two probe wavelengths with respect to the theoretical density of states of the sample. The first probe wavelength (λ_1) corresponds to the value $a/\lambda_1 = 0.56$ (marked by black square). The second probe wavelength corresponds to $a/\lambda_2 = 0.59$ (marked with a red circle). Figure 8.11**a** plots the theoretical density of states projected along the ΓL direction, $\rho_{\mathbf{k}=(1,1,1)}(\omega)$, for an fcc arrangements of spheres. It is easy to observe that the first energy probe (black square) lies in a photonic pass band along the ΓL direction and the second energy probe (red circle) coincides with the spectral position of the low energy band-edge in the same crystallographic direction (figure 8.11**b**). As explained in the previous section, this fact has an important effect on the measurement of the scattering mean free path. To explicitly point it out, figure 8.11**c** shows the variation of the ℓ_s as a function of the vacancy density (ρ_v) at both energies. At λ_1, ℓ_s varies from 53 μm, in the case of the perfect opal, to 3 μm, for $\rho_v = 40$ % (a ten fold reduction). This strong variation (plotted as a dashed black curve in the figure) happens in the case of λ_1 lying on the pass band, far from any photonic feature. Contrary to this strong variation, at λ_2, figure 8.11**c** shows a more attenuated variation of the scattering mean free path when the sample is probed at the band-edge (plotted as a dashed red curve). In that case, the value of the scattering mean free path varies from 25 μm, for the perfect opal, to 4 μm, in the case of $\rho_v = 40$ %, which is nearly half the variation as in the case of λ_1. This fact can be due to the modified phase space available Δk, which enhances light scattering

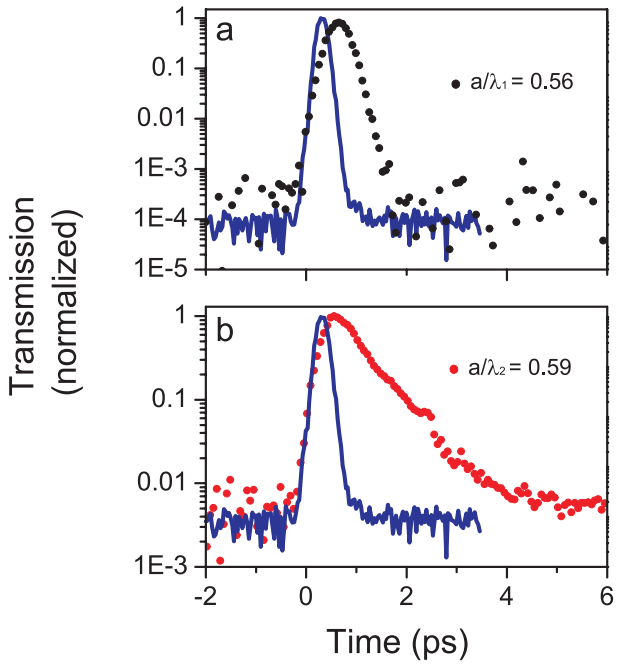

Figure 8.10: Plot of the time-resolved diffuse transmission through photonic crystals with $\rho_v = 0$ % at different energies: $a/\lambda_1 = 0.56$ **(a)** and $a/\lambda_2 = 0.59$ **(b)**, together with the pulse reference (blue curve).

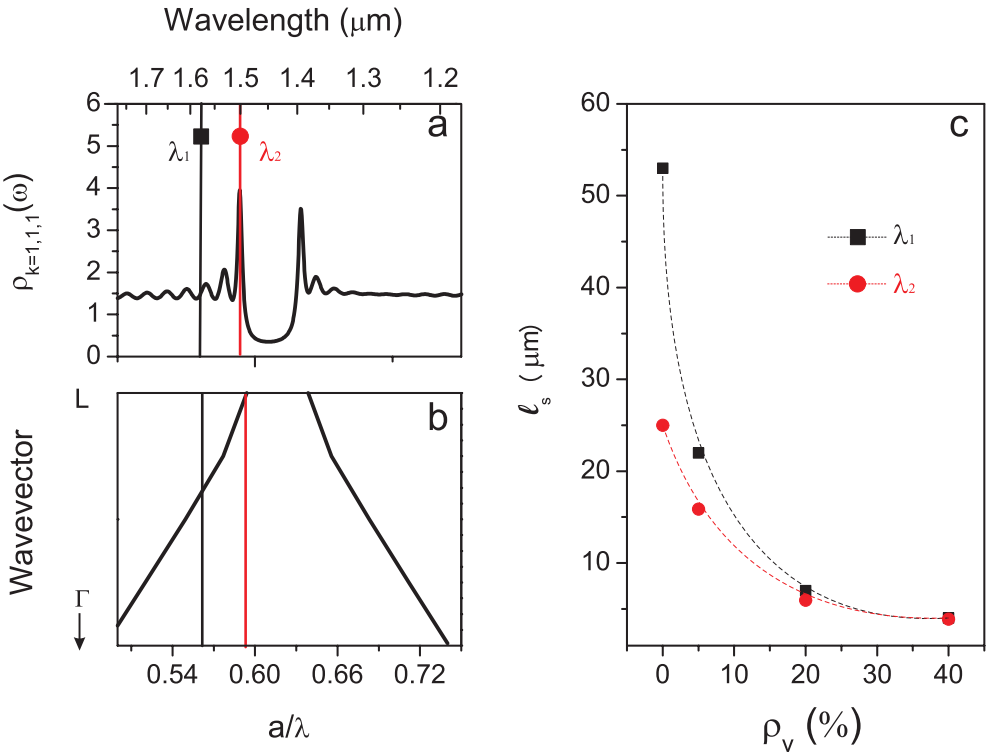

Figure 8.11: **(a)** Theoretical density of states along the ΓL direction for the case of $\rho_v = 0$. The measurement of the diffusion constant is performed at a fixed energy value (red circle), $a/\lambda_2 = 0.59$, which coincides with the band-edge in this particular crystallographic direction. Black square represents an energy value at the pass band, far from any photonic feature. **(b)** Photonic band diagram along the ΓL direction which shows the actual spectral position of the λ_1 (black line, pass band) and λ_2 (red line, low energy band-edge). **(c)** Scattering mean free path, ℓ_s, measured at two different spectral positions, at the pass-band (black squares) and at the band-edge (red circles) as a function of the vacancy density, ρ_v. The variation of ℓ_s is more attenuated in the case of the band-edge (red line) than in the pass-band (black line).

(pointed out in figure 8.11**c**). This light scattering enhancement gives rise to a subsequent light diffusion enhancement. Attending to these measurements, a photonic effect related to the density of states in the *perfect* photonic crystal may be the reason for which the diffusion constant is too large to be measured at λ_1. In the pass-band of the photonic crystal, light scattering is very inefficient and light propagation is mainly ballistic or unscattered. On the contrary, in the band-edge, where light scattering and diffuse light are enhanced, the diffusion constant is too high and the time decay is of the order of the reference pulse to be measured.

From the time dependence we obtain $\mathcal{D}$. Figure 8.12 shows the experimental diffusion constant at a fixed fixed wavelength $\lambda_2 = 1500$ nm which corresponds to $a/\lambda_2 = 0.59$ and as a function of the vacancy density, ρ_v. The experimental measurements are fitted by an exponential decay (dashed black curve) as $\mathcal{D} \propto$

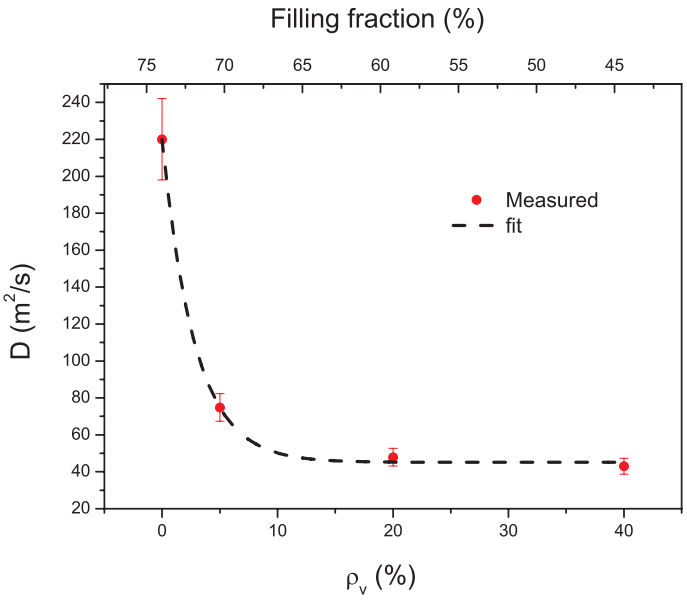

Figure 8.12: Plot of the diffusion constant of light, $\mathcal{D}$, as a function of the vacancy density, ρ_v measured at $\lambda_1 = 1500$ nm. The system is composed by PMMA spheres with $n = 1.42$ and a diameter $d = 630$ nm.

$e^{-\rho_v/\alpha_0}$, where $\alpha_0 \sim 3$. The figure 8.12 shows a reduction of the diffusion constant as a consequence of the increased amount of disorder in the samples induced by the inclusion of vacancies in lattice positions. The value of the diffusion constant varies from $\mathcal{D}(\rho_v = 0\ \%) = 220\ m^2/s$ to $\mathcal{D}(\rho_v = 40\ \%) = 43\ m^2/s$. The introduction of 40 % of vacancies in the sample constitutes a very disturbing effect on the photonic properties of the sample which may completely destroy any photonic feature (as shown in figure 8.6**b**). The final disordered system has a diffusion constant value which is about 20 % of that from the most perfect photonic crystal (no doped with vacancies). It seems plausible that, at wavelength λ_2, these variation may be artificially attenuated by a low diffusion constant value for $\rho_v = 0$ % due to light interference in the structure, as suggest recent theoretical analysis of the diffusion constant where disorder is intentionally added to a photonic crystal [38]; a 70 % variation of $\mathcal{D}$ is found in such studies in the onset of strong light localization. In our case, we are probably far from this phase transition due to the low refractive index of the structure. An exceptional reduction of the diffusion constant in photonic crystals with a certain amount of intrinsic disorder has also been measured very recently [186] which is explained, also, in terms of interference effects on the diffusion parameters.

8.5. Total white light transmission: from crystals to glasses

A smooth transition between order and disorder has been characterized through the analysis of the scattering mean free path in section 8.3 and the diffusion con-

stant in section 8.4. It has also be shown how the density of states $\rho(\omega)$ of the system has a crucial role in the light scattering though photonic crystals. The possibility of exerting a high control over this magnitude is of paramount importance since it is what governs directly the light transport as well as light emission in nanostructured dielectrics [3, 32]. Along this thesis we have seen that, by modifying the vacuum modes, photonic crystals change the available phase space for light propagation opening frequency gaps in which propagation in some (or even all) directions is inhibited, while the density of states, $\rho(\omega)$, near the band-gap edge frequencies is increased. However, even in the highest quality photonic crystals intrinsic disorder triggers light scattering that, for thick enough crystals, provokes that ballistic transport of light is replaced by diffusion. Strong evidence that the density of states significantly modifies light scattering has been provided in the previous section. As pointed out by John [4], a dramatic change in light diffusion may occur for frequencies in or around the band-gap and eventually Anderson localization of light can be reached, the photonic conductor becoming an insulator. Even far from localization, the study of the transition from ballistic to diffuse light propagation is a challenge itself. In this section, experimental measurements which suggest such a transition will be analyzed in an opal-based photonic crystal when it is doped with vacancies.

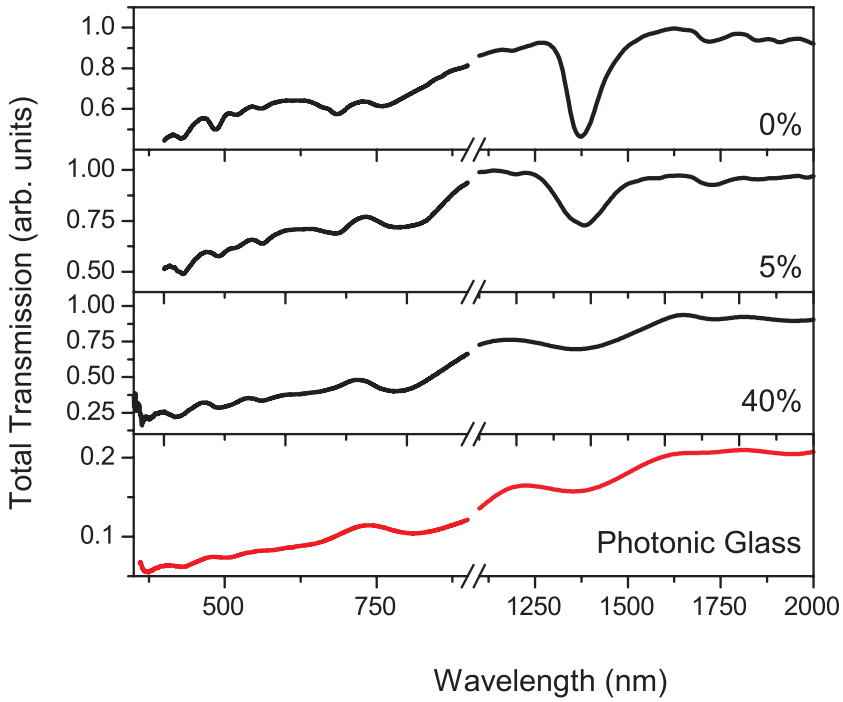

Figure 8.13: Total light transmission through opal based photonic crystals doped with a given density of vacancies (black curves) and through a photonic glass grown with the same spheres (red curve). The measurements are taken in the high and low energy range. In particular, the figure shows the evolution of the dip related to the pseudogap in the ΓL direction.

To that purpose, total transmission is measured with the help of an integrating sphere which consists of a hollow cavity with its interior coated for high diffuse reflectance. A schematically sketch can be seen in chapter 5, section 6.1. Photonic crystal thin films with different concentration of vacancies are placed on the integrating sphere entrance apperture and illuminated with monochromatic visible and infrared light. Light illumination is performed perpendicularly to the sample surface.

In order to estimate the ratio between the sample thickness and the scattering mean free path, we will use the value of ℓ_s measured at the pass band (black squares in figure 8.11**c**). Total transmission measurements are performed with the integrating sphere on large areas of mm^2, where it is not possible to select an individual thickness in the sample (contrary to the case of ℓ_s measurement). For this reason, we will assume a mean value of the sample thickness of 21 μm. With this value of L, we can estimate the ratio L/ℓ_s. This is an important parameter to characterize the light transport regime in each sample. Attending to the definition of ℓ_s (see chapter 1, section 1.2.1), L/ℓ_s becomes an estimation of the average number of scattering events which take place in the sample, as shown in table 8.1. The number of scattering events which light performs in the sample (in the pass band, at an energy far from any photonic feature) increases with the vacancy density ρ_v. From an average value of no scattering events in the case of the most perfect opal-based photonic crystals to the 5 average scattering events in the case of $\rho_v = 40$ %. This important estimation gives a first crucial information about the kind of light transport regime which takes place in the samples. From ballistic light transport, in the case of non-doped crystals, to the case of quasi multiple scattering light transport, in the case of $\rho_v = 40$ % doped crystals.

Table 8.1: Average number of scattering events

ρ_v (%)	ℓ_s (μm)	L/ℓ_s
0	40 ± 4	0.5
5	22 ± 2	1
20	7.0 ± 0.7	3
40	4.0 ± 0.4	5.3

The enhancement of light scattering is here pointed out: without changing the crystal structure, just by the addition of vacancies in the lattice which act as scatterers, we can control *and fine tune* the light scattering regime from ballistic to multiple scattering. This as already suggested in the measurement of the scattering mean free path compared to the Bragg length L_B (figure 8.6**b**). In this section we will try to analyze this transition more deeply and to compare the transport parameters of the doped crystal with the photonic glass. Figure 8.13 shows a direct measurement of the total light transmission through different photonic crystals films (thickness $L \sim 20$ μm) upon white and infrared light illumination in two ranges from from 980 nm to 2000 nm and 500 nm to 900 nm, in order to be able to probe both the low and the high energy photonic

dispersion relation of the samples. The density of vacancies varies from $\rho_v = 0$ % to $\rho_v = 40$ % (black curves) and it is compared with the total diffuse light transmission from photonic glasses (red curves) grown with the same spheres. In photonic glasses, the transport mean free path has been measured (see chapter 6) to be $\ell_t \simeq 3$ μm. Although, ℓ_s is smaller than ℓ_t, the values of ℓ_s for the crystal highly doped with vacancies and for the photonic glass are on the same order, $\ell_s(\rho_v = 40\ \%) = 2$ μm (figure 8.6**b**).

The first fact which is necessary to point out is that, in the cases of $\rho_v = 0$ % and $\rho_v = 5$ % we are measuring ballistic light transport. For these low vacancy densities, the samples present a low value of scattering events (table 8.1) and

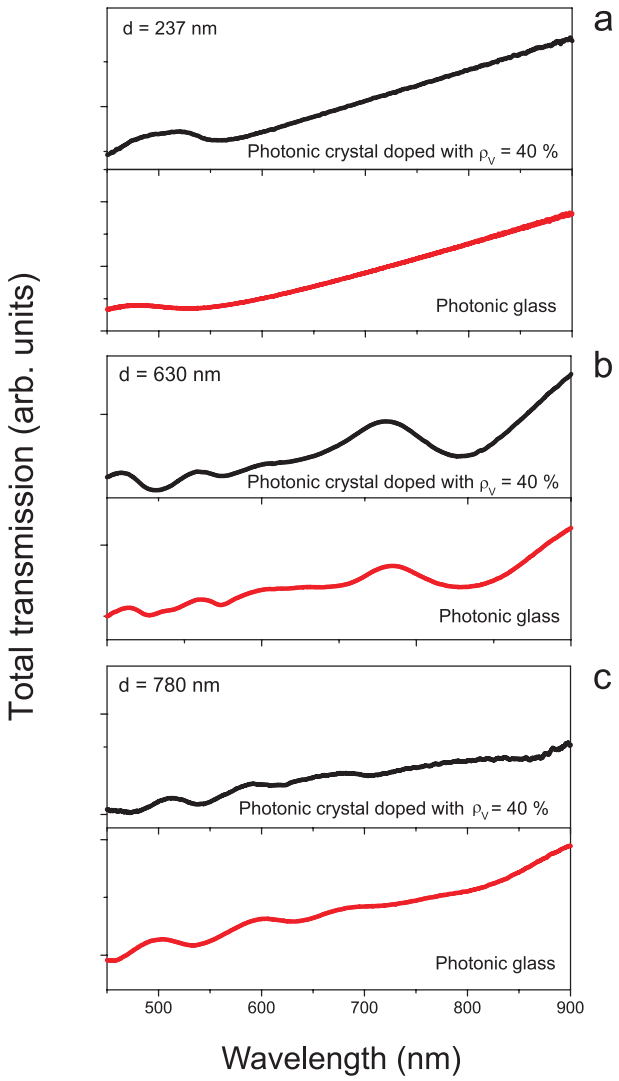

Figure 8.14: Total light transmission through opal-based photonic crystals with a 40% of vacancies in lattice positions compared to photonic glasses made with the same spheres with diameters d = 237 nm **(a)**, d = 630 nm **(b)** and d = 780 nm **(c)**.

light propagates through the sample ballistically. Most of the photons propagate without being scattered by the lattice. Figure 8.13**b** shows a dip in the case of $\rho_v = 0$ % and, the same but attenuated, in the case of $\rho_v = 5$ %. This dip in transmission is related to the ΓL pseudogap. As previously said, light illumination is performed perpendicularly to the sample surface and, therefore, ballistic light only probes the ΓL crystallographic direction, giving rise to a deep in transmission. This dip, as extensively shown in this thesis and, in particular, in the introduction, originates from light interference and can be described in terms of Bloch-modes propagation and band-gaps. In the case of $\rho_v = 40$ %, the optical thickness of the sample can be considered large, attending to table 8.1. In this case, ballistic light is exponentially attenuated as dictated by the Lamber-Beer law and only diffuse light escaping from the sample can be measured. For such a high amount of vacancies, the dip related to the photonic pseudogap transforms into a Mie resonance related to the Mie modes of the dielectric spheres. I hypothesize is that there is a transition from Bloch-modes mediated light transport (in the case of $\rho_v = 0$ %) to Mie-modes mediated light transport (in the case of $\rho_v = 40$ %). Although it cannot be completely assured with these measurements, it is plausibly suggested when comparing with total light transmission through a photonic glass. The total diffuse light transmission through a photonic glass (red curve) grown with the same PMMA spheres with the same diameter reveals such a behavior (see also chapter 6, section 6.1). The total light transmission from a crystal doped with $\rho_v = 40$ % and from a photonic glass are indistinguishable (figure 8.13).

In order to support and to give additional experimental evidences to this *thesis*, figure 8.14 compares the total light transmission through photonic crystals doped with $\rho_v = 40$ % and through photonic glasses made with the same PMMA spheres for three different diameters, d = 237 nm, d = 630 nm and d = 780 nm. Figure 8.14 shows, clearly, that light transmission presents the same features in the case of both systems. From these static measurements it is not possible to distinguish a photonic crystal doped with a $\rho_v = 40$ % from a photonic glass, even if in the first case a long correlation still exist in the structure. Although this measurements are not enough to ensure a complete transition between ballistic to diffuse light transport, they suggest such a transition.

8.6. Conclusions

In conclusion, we show that the controlled smooth transition from ballistic to diffuse transport in photonic crystals can be induced by the introduction of extrinsic disorder. It was also found that the strength of scattering is closely related to the density of states, which induces immense, up to 20-fold, variations in the scattering mean free path. The measurement of this magnitude was made possible by a simple method that estimates scattering strength from simple straight-line transmittance and reflectance measurements. We propose ℓ_s as a robust, easy to measure, figure of merit in assessing the quality of photonic crystals for technological applications. In particular, our samples which are grown

in no special-care conditions like glove boxes or clean rooms, exhibit scattering losses as small as $\sim$ 86 dB/cm casting an optimistic light on photonic crystal future applications. The possibility of controlling light scattering and diffusion in nanostructured optical media has important implications not only to test the quality of photonic devices, but also to properly address the proximity to the onset of Anderson localization in disordered lattices, or for the spectral control of lasing emission from disordered/ordered active media. Complete photonic band-gap materials, like Si inverted opals, would amplify the effect here presented and would be proper candidates to observe Anderson localization of light. Moreover, and beyond the fundamental questions related to light transport, the majority of microelectronic devices, from conducting wires to p-n junctions, are based on rather perfect metallic atomic lattices and exploit carrier diffusion as their functional component. In the photonic domain, the control of light diffusion in imperfect ordered dielectrics is an unexplored route that might lead to photonic devices based on the interplay between order and disorder.

Chapter 9

Laser emission in ZnO nanostructures

Along this thesis, it has been pointing out that conventional optics and modern nanophotonics mold the flow of light in a different fashion. Conventional optics makes use of homogenous materials and engineers light emission and light propagation through the material boundaries whereas modern photonics makes use of nanostructured dielectrics where light properties are controlled with the nanostructured itself. This is, for example the case of laser emission. Both in the introduction and also in chapter 7, it has been widely explained how conventional lasers are composed by a gain medium which is able to radiate photons by means of an external pumping mechanism and an optical cavity which provides the necessary resonant feedback to reach a threshold [61]. The optical cavities used in those lasers are mirror-based Fabry-Perot resonators. Light modes are built up with the help of mirrors and threshold is achieved with the resonant feedback mediated by the cavity. Cavity losses are the main limiting factor and define the well-known parameter β-factor, the amount of spontaneous emission that contributes to the lasing mode. Smaller β, smaller energy needed to make a gain medium laser. Modern nanophotonics propose different strategies to minimize the value of β and to obtain very efficient lasing emission spending less energy than in homogenous gain media. In nanostructured gain media, light modes are provided by light interference with an ordered dielectric structure (photonic crystal-based lasing emission *Bloch lasing* [72]) or by light multiple scattering (as in the case of *random lasers* [63]). In both approaches, ordered (in two- [190] and three- [28] dimensions) and disordered (powders [154] or very low quality ordered structures [189]), light-mater interaction is enhanced artificially with the help of the material nanostructure, the material is engineer to simultaneously play the role of gain medium and optical cavity in conventional lasers, providing laser modes feedback.

In this chapter lasing measurements on ZnO ordered and disordered nanostructures will be shown. Bloch lasing in high energy photonic bands of *ZnO* inverse opal will be reported as well as experimental evidence of random lasing in

two different ZnO disordered nanostructures: ZnO inverse photonic glasses and ZnO inverse photonic crystals doped with a high amount of vacancies. A playground to study the transition from Bloch to Random lasing will be provided. Both lasing emission approaches will be quantitatively compared and the basis to a further study of the transition from Bloch to random lasing will be proposed.

9.1. Bloch laser in ZnO inverse opals.

We will firstly analyze lasing emission in ZnO inverse opals obtained with the infiltration method shown in chapter 2. Figure 9.1 schematizes the optical set up used to that purpose: ZnO inverse opals are optically pumped by a frequency tripled Q-switched pulsed Nd:YAG laser (9 ns pulse duration), with 10 Hz repetition rate. The spot size was fixed at 1 mm diameter. The pumping beam and the emission beam are along the direction perpendicular to the sample surface and probe the photonic band structure along the ΓL crystallographic direction. The ZnO emission was monitored along the same direction with the help of a beam splitter and a miniature spectrometer with a resolution of $0.5 \sim$ nm. The pump energy per pulse is measured with the help of a powermeter, as figure 9.1 shows.

ZnO inverse opals without vacancies are pumped at high energy photonic bands ($a/\lambda > 1$), where light couples with small slope photonic bands [59]. UV ZnO lasing is demonstrated at room temperature for these samples as figure 9.2 shows. This measurements confirm those reported by M. Scharrer *et al.* [28] for similar ZnO structures. Such structure, inverse ZnO opal with high refractive index contrast $n \simeq 2$, simultaneously confines light and provides optical gain.

Figure 9.2 shows the comparison of the experimental lasing emission results (right panels of figure 9.2**a**, 9.2**b** and 9.2**c**) and the calculated photonic band

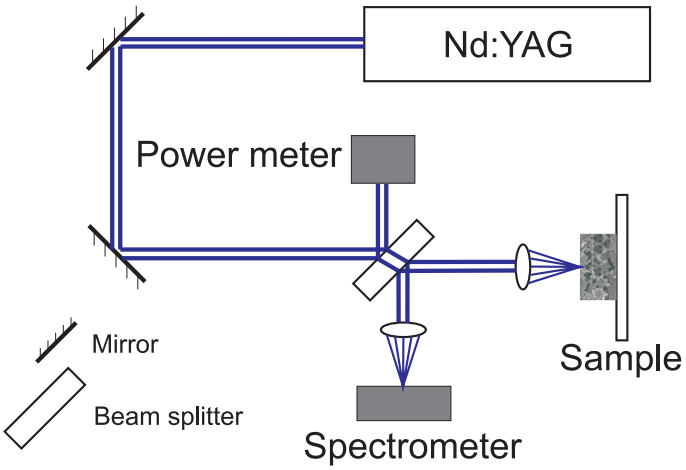

Figure 9.1: Schematic of the optical set up used to measure emission from ZnO inverse opals. Pumping and emission are along the (111) crystallographic direction of the ordered nanosctructure.

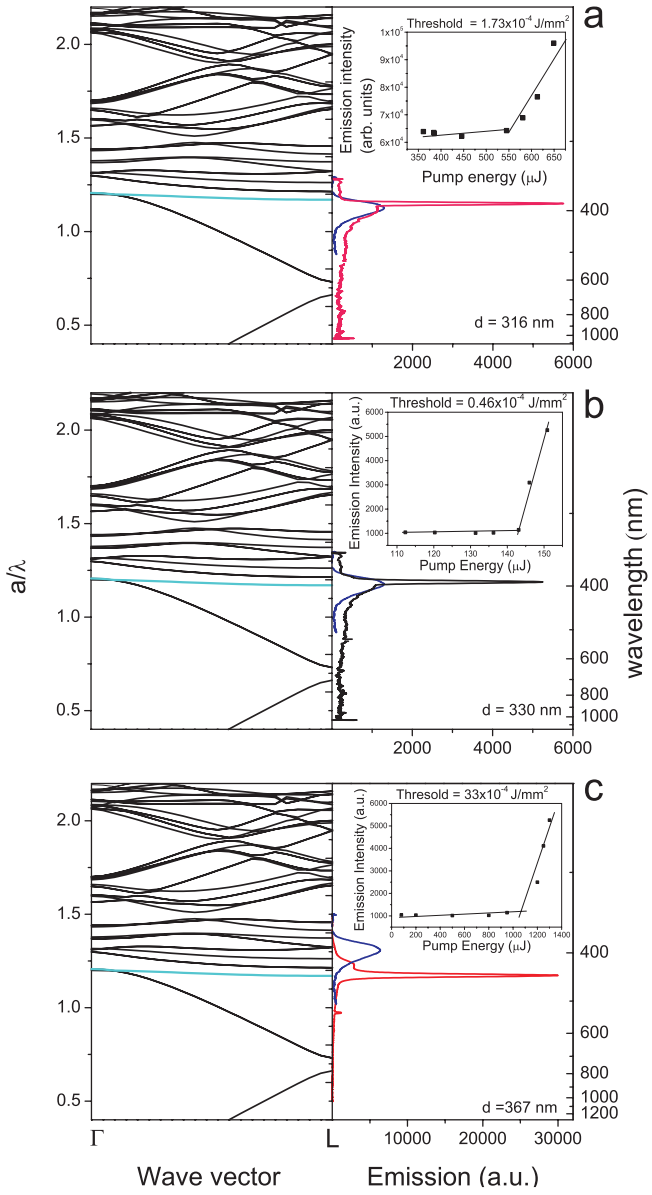

Figure 9.2: Comparison between experimental measured ZnO lasing in three different ZnO inverse opals with different original polymer sphere diameters and the photonic band structure in the ΓL direction assuming a ZnO refractive index $n = 2.5$ at the resonance. The spheres diameters are **(a)** $d = 316$ nm, **(b)** $d = 330$ nm and **(c)** $d = 367$ nm. ZnO emission below threshold is also shown in the figure (blue curve) and compared to the lasing mode. The increase in the sphere diameter is translated into a redhift of the first high-energy flat band (blue) with respect to the ZnO PL spectrum. This gives rise to a redshift of the lasing mode from 386 nm **(a)** to 392 nm **(b)** and finally to 442 nm **(c)**. Inset in right panels of the three figures show the emission intensity versus pump energy, evidencing the existence of a threshold for the three cases.

structure for each structure at panels of the corresponding figures. These measurements reveal that ZnO lasing emission occurs in high-order photonic bands with so-called abnormally low group velocity [24]. As explained in the introduction, section 1.4.2, at photonic band edges or at weakly dispersive, so-called, *flat* high energy bands, the slope of the dispersion relation minimizes for a certain range of wavevector k values. A reduction of $\mathbf{v}_g$ creates a standing wave like an ordinary cavity. This leads to a stronger light-matter interaction and to an enhancement of the optical response of the system. This demonstrates that the high-order band structure of three-dimensional photonic crystals can be used to effectively confine light and, for example, to enhance ZnO emission. In particular, at the low-frequency edge of the third pseudogap in the high energy range of ZnO inverse opals (labelled **C** in chapter 4) there is an isolated non degenerate band (blue curve in left panels of figure 9.2) with extraordinarily low dispersion. Right panels of figures 9.2**a**, 9.2**b** and 9.2**c** show ZnO emission above threshold which coincides with the spectral position of this flat photonic band for three different PMMA original sphere diameter: $d = 316$ nm (9.2**a**), $d = 330$ nm (9.2**b**) and $d = 367$ nm (9.2**c**). Different original PMMA sphere diameters have been chosen to tune the *blue* flat photonic band through ZnO photoluminiscence (PL). Profiting from the relatively wide spectrum of ZnO PL, it is possible to probe lasing emission from 380 nm to 440 nm by varying the sphere diameter. Light in such a weakly dispersive *blue* band has a very low group velocity v_g which provides light amplification. In order to proof that this is the origin of the ZnO lasing emission, the original PMMA sphere diameter is increased (from figure 9.2**a** to 9.2**c**). *Blue* flat band redshifts with respect to the ZnO PL spectrum as a consequence of that diameter increasing. *Blue* flat band tunes the ZnO PL from 386 nm **(a)** to 392 nm **(b)** and finally to 442 nm **(c)**. In all these cases, the lasing emission coincides with the spectral position of the flat band. Even in the latter case, for original PMMA spheres diameter $d = 367$ nm, for which the *blue* flat band is spectrally far from the maximum ZnO PL, it is still possible to observe ZnO lasing mediated by the low group velocity provided by that mode. Inset of figures **(a)**, **(b)** and **(c)** show the emission intensity versus pump energy, evidencing the existence of a threshold for the three cases.

Figure 9.3**a** shows ZnO emission above threshold from the three ZnO inverse opals shown in figure 9.2. Lasing emission of the three inverse opals is compared with ZnO emission below threshold (dashed dark blue curve in figure 9.3). Figure 9.3 points out the spectral redshift of the lasing emission originated from the spectral shift of the lasing mode (*blue* flat band in figure 9.2) with respect to the ZnO PL. This reveals that it is possible to tune Bloch lasing in ZnO ordered nanostructures just by varying the lattice constant. The existence of resonant modes for light (in this case, *blue* flat band) within the gain spectral range reduces the pump energy necessary to achieve population inversion. This effect has already been observed in resonant random laser (see chapter 7). The lasing threshold is, therefore affected, by the interplay between ZnO gain and the spectral position of the lasing mode (*blue* flat band). Figure 9.3**b** shows this effect: varying the lattice constant (by increasing sphere diameter) is translated into an lower ZnO gain and the lasing mode overlapping, which gives rise to lasing

threshold increasing.

9.2. Synthesis of ZnO disordered nanostructures

In order to compare previous Bloch lasing in ZnO ordered nanostructures with random lasing in ZnO disordered nanostructures, we will present in this section two different ways to obtain such systems. The chemical vapor deposition presented in chapter 2 to accurately infiltrate opal-based photonic crystals with ZnO will be used in this section to infiltrate disordered nanostructures which are the two approaches presented in this thesis: photonic glasses and photonic crystals highly doped with vacancies. The relatively high ZnO refractive index $n \simeq 2$ provides enough dielectric contrast to improve the effect of multiple scattering on light propagation compared to the polymeric original systems, but in addition to that, UV light photoluminescence of ZnO at room temperature (shown in chapter 2) is a great motivation to use ZnO. By means of the mentioned CVD-method,

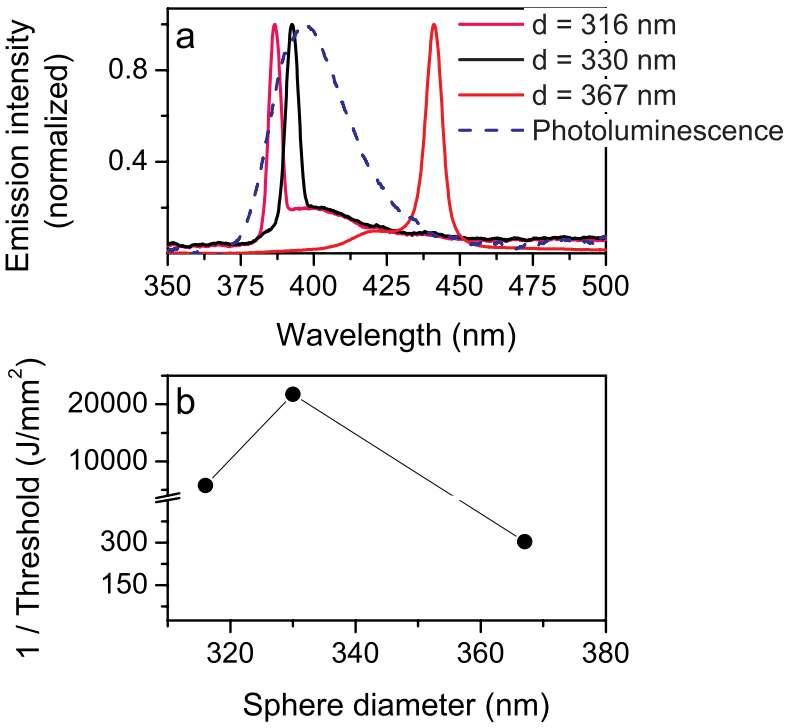

Figure 9.3: **(a)** Detail of the redshift of the lasing emission in ZnO inverse opals produced by the increase in the original PMMA sphere diameter from $d = 316$ nm to $d = 367$ nm. **(b)** Inverse of the lasing threshold for the corresponding spheres diameters. The spectral distance from the lasing mode (the first weakly dispersive photonic band, in this case) and the maximum in the ZnO PL gives rise to an increasing in the lasing threshold.

ZnO will be infiltrated in both systems and inverse ZnO disordered structures will be obtained. In the former case, photonic glasses grown with PMMA spheres as explained in chapter 5 will be infiltrated with ZnO. In the latter case, PMMA opal-based photonic crystals doped with a high amount of vacancies as explained in chapter 8 will be also infiltrated with ZnO. In order to obtain the inverse structures in both cases, the polymeric backbone will be removed by calcination.

9.2.1. ZnO inverse photonic glasses

In order to compare ZnO lasing in both disordered macrostructure, we used the same PMMA sphere diameter to grow both templates. In the first case, a photonic glass composed by PMMA spheres with $d = 367$ nm is synthesized following the process explained in chapter 5. Then, the template is infiltrated with ZnO following the chemical vapor deposition method explained in chapter 2. If the PMMA spheres are then calcinated, ZnO random distributed shells are obtained (figure 9.4**a**). The inset of figure 9.4**a** shows cracked ZnO shells in detail. If the cycles in the CVD process are long enough (typically few minutes bubbling H_2O and $ZnO(CH_3CH_2)_2$ simultaneously) the sample can be totally infilled by ZnO, obtaining a random distribution of air spheres embedded in ZnO (figure 9.4**b**).

In order to optically monitor the different stages of the process, we have analyzed total transmission with the help of an integrating sphere. This method has been used in this thesis in chapters 6 and 8. To that purpose we have used a photonic glass template composed by spheres with diameter $d = 1220$ nm. The sample is placed in the entrance of the integrating sphere and it is illuminated in the range 500 nm to 920 nm. Figure 9.5 shows the measurement of diffuse light through the different systems obtained in the process. The initial template (figure 9.5**a**), the photonic glass, is optically thick and, therefore, ballistic light is exponentially attenuated into the sample. Only diffuse light is collected by

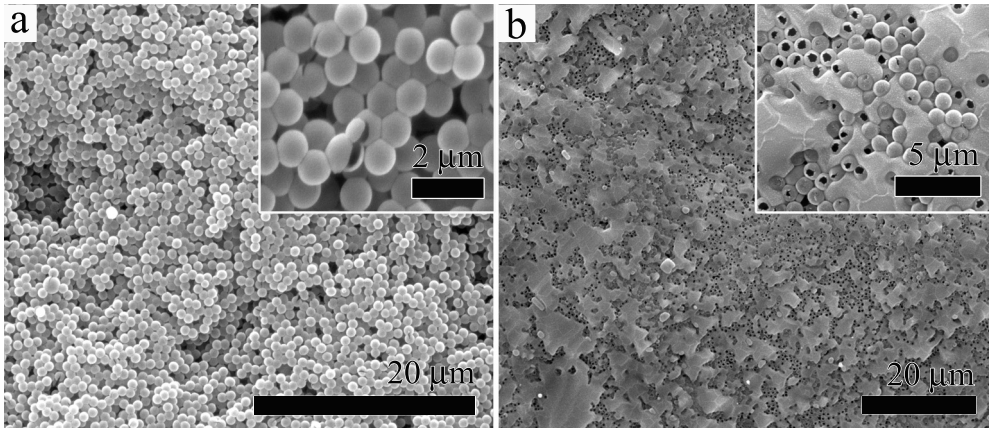

Figure 9.4: SEM images from ZnO inverse photonic glasses. **(a)** ZnO shells randomly embedded in air. **(b)** Air spheres randomly embedded in ZnO.

the detector. It presents the typical resonances in transmission related to the Mie modes of the spheres. The particular sphere diameter $d = 1220$ nm used to perform this measurements is selected to resolve such resonances in this particular energy range. In the case of spheres diameter $d = 367$ nm, no resonances can be measured in transmission for this energy window. When the template is infiltrated with ZnO, the spectral position of the resonances slightly redshifts, as figure 9.5**b** shows. In this case, the resonances are still observable in total transmission. When the polymer backbone is removed and a random distribution of ZnO shells is obtained, the resonances strongly attenuate in this energy range (figure 9.5**c**). The reason is that the Mie modes are strongly confined at the highest refractive index material which, in the case of the direct photonic glass is that one which composes the spheres (see introduction, section 1.1.1). When the spheres are removed, the field is then confined in the material which composes the shells, ZnO in this case, and the resonances are shifted to other energies.

9.2.2. ZnO inverse opals doped with vacancies

The second approach to obtained a disordered ZnO nanostructure is based on the infiltration of vacancy-doped photonic crystals. As shown in chapter 8, a controlled amount of vacancies can be introduced in a polymer opal. If a ZnO chemical vapor deposition is carried out on such system, the material only grows conformally on the polymer spheres. The lattice vacancies remain unaltered and,

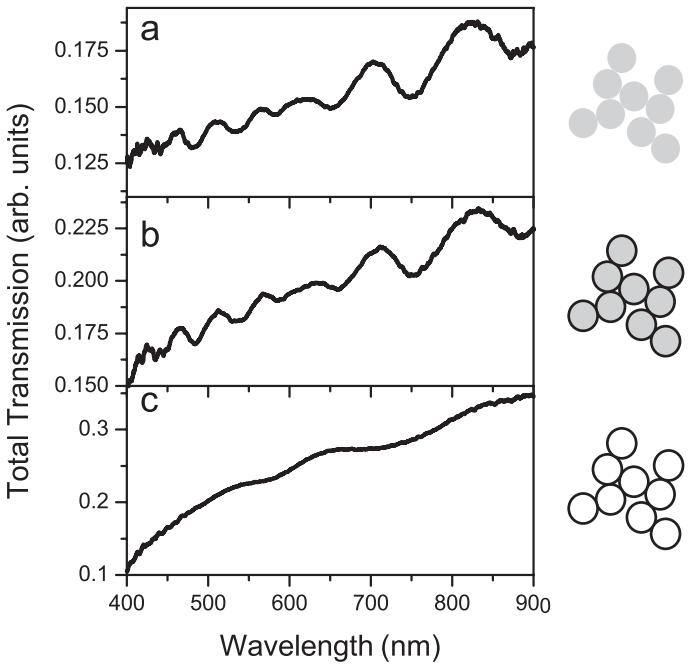

Figure 9.5: Total diffuse light transmission measurements through a photonic glass composed by PMMA spheres with $d = 1220$ nm **(a)**, through the same system infiltrated with ZnO **(b)** and through the inverse structure: a ZnO inverse photonic glass **(c)**

when the polymer background is removed by means of a temperature-based annealing process, the resultant ZnO inverse structure replicates the vacancy-doping of the original structure. Figure 9.6 schematizes this process: a photonic crystal composed by PMMA spheres (grey spheres in figure 9.6**a**) is doped with a controlled amount of PS spheres (red spheres in the figure). The samples used in this chapter have been grown using PMMA spheres with $d = 367$ nm and PS spheres with the same diameter has been used as the dopants. The total colloidal initial concentration is typically 0.15 wt % and the relative concentrations of PMMA and PS spheres are 60 % and 40 % respectively. A selective removal is exerted over PS spheres by immersing the system in 99 % pure Cyclohexane. This selectively dissolves PS spheres, leaving PMMA spheres intact in their lattice positions (figure 9.6**b**). Then, ZnO infiltration by means of chemical vapor deposition is performed over the system, giving rise to a composite PMMA-ZnO material doped with vacancies (figure 9.6**c**). ZnO only grows conformally on the surviving PMMA spheres. Consequently, it will tend to form small lumps (in regions where a PS sphere was removed) embedded in a network of ZnO of $f = 26$ %. Finally, PMMA spheres are removed by calcination at $T = 450\ ^{\circ}C$, giving rise to a ZnO-shells inverse structure doped with vacancies (figure 9.6**d**).

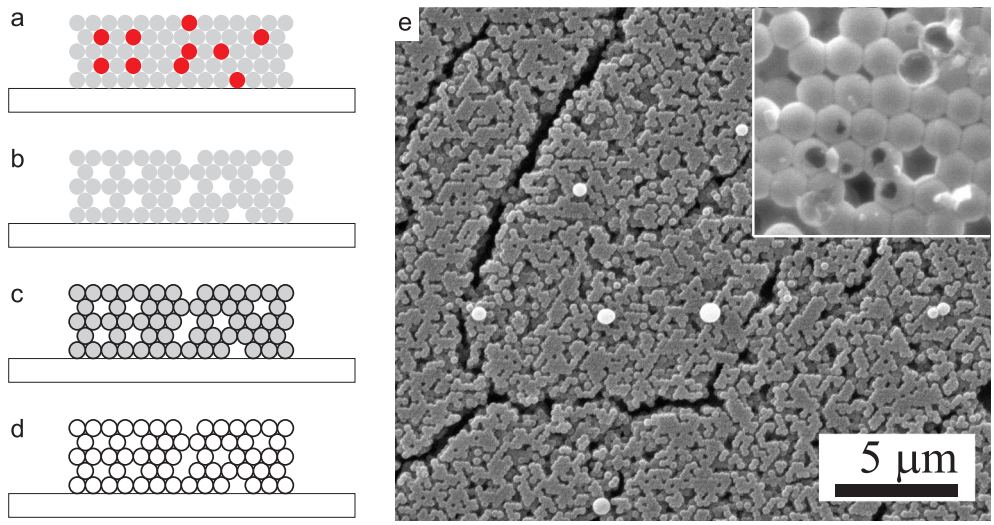

Figure 9.6: Schematic of the ZnO infiltration process in vacancy-doped photonic crystals. **(a)** Binary crystals are grown with PMMA (grey) and PS (red) spheres with a controlled partial concentrations of each other. **(b)** PS spheres are removed by selectively dissolution in 99 % pure Cyclohexane. PMMA spheres remain intact. **(c)** ZnO infiltration by means of chemical vapor deposition provides PMMA-ZnO composite opals doped with vacancies. **(d)** Polymeric backbone removal by calcination gives rise to a ZnO inverse opal doped with vacancies. The final vacancy concentration is the original PS concentration in the initial binary crystal. **(e)** SEM images from ZnO inverted opals doped with vacancies. The vapor-based infiltration process allows a ZnO conformal growth on PMMA spheres leaving the vacancies intact. This permits the replication of the vacancy doping in the final ZnO inverse structure.

Figure 9.6**e** shows a SEM image from the final ZnO inverse opals doped with vacancies. The inset of the figure shows how the ZnO shells are grown conformally to the PMMA spheres and also how the vacancies remain in the final ZnO inverse structure. The vacancy concentration that can be introduced in this system is limited by the mechanical stability of the system and is always lower than a 40 %. A concentration higher than $\rho_v > 40$ % gives rise to very mechanically intestable PMMA structures. Apart from this limitation, a wide range of ZnO inverse opals with vacancy concentration from $\rho_v > 0$ % to $\rho_v > 40$ % can be grown to probe their optical properties.

9.3. Random laser in ZnO disordered nanostructures.

Differently to the case of ordered ZnO inverse opals, where lasing emission mediated by Bloch modes has been shown, random lasing is determined by diffusive modes. In this section, random lasing from the both different ZnO disordered nanostructures presented previously will be shown. In particular, we will use ZnO inverse photonic glasses and ZnO inverse opals doped with a high amount of vacancies ($\rho_v = 40$ %). Random lasing in very low quality ZnO inverse opals [189] has been already shown in the past. However, random lasing emission can be measured in our systems due to the high amount of disorder introduced in a controlled way. The samples are optically pumped in the same manner as ordered ZnO structures and lasing emission is collected with the same set up configuration (see figure 9.1).

Figure 9.7 shows ZnO emission above threshold in the case of a ZnO inverse photonic glass (orange curve) and in the case of a ZnO inverse opal doped with $\rho_v = 40$ % vacancies (black curve). Both systems are grown with original PMMA spheres with diameter $d = 367$ nm. Lasing emission from both systems appear at the same spectral position, $\lambda = 391$ nm, contrary to the case of ZnO inverse opal without vacancies, where lasing emission occurs at $\lambda = 442$ nm. Both ZnO random structures present conventional random lasing emission. It is here important to remark the crucial difference between random lasing emission observed in photonic glasses in chapter 7 with random lasing emission observed here in ZnO inverse photonic glasses. In the first case, lasing modes are determined both by the gain curve and the resonant modes present in the sample. ZnO inverse photonic glasses do not present resonances in transmission, as shown in figure 9.5**c**. This important difference can be explained attending to the fact that, the electromagnetic field resonates in the high refractive index material which, in the case of direct photonic glasses composed by polymer spheres is the polymer itself. In the case of inverse ZnO photonic glasses, the high refractive index material is the ZnO shells. The total transmission of such a system is monotonically dependent on energy over the ZnO gain spectrum, as shown in figure 9.5**c**. No resonant modes can be measured at the energy range where ZnO PL takes place and random lasing is completely determine by ZnO gain curve (dashed dark blue curve in figure 9.7). As the pump power increases, the emission peak becomes narrower due to the preferential amplification of the frequencies close to the maximum of

the gain curve. The lasing modes are selected from those at the spectral position of the minimum gain length, ℓ_g, as occurs in the case of TiO_2-based random laser in chapter 7. The same can be explained in the case of ZnO inverse opals doped with a high amount of vacancies. Although the direct opal doped with vacancies presents resonant modes in its total transmission (see section 8.5 in chapter 8), the inverse structures do not present these resonances any more for the same reason of the ZnO inverse photonic glass explained previously. Total transmission does not present resonances within the ZnO gain spectrum for both ZnO disordered nanostructures and, therefore, lasing modes are completely determine by ZnO gain curve. A small blueshift (~ 5 nm) can be observed in figure 9.7 for both lasing emissions with respect to the maximum of the ZnO gain curve which cannot be explained at this point. Lasing threshold is $4 \times 10^{-5}\ J/mm^2$ per pulse, in the case of ZnO inverse photonic glass, and $3.2 \times 10^{-5}\ J/mm^2$ in the case of ZnO inverse photonic crystal doped with $\rho_v = 40$ % vacancies.

9.4. Transition from Bloch to Random ZnO laser mediated by vacancy doping

Both Bloch lasing and random lasing have been observed in ZnO inverse structures. In the first case, the lasing emission is determined by the lattice

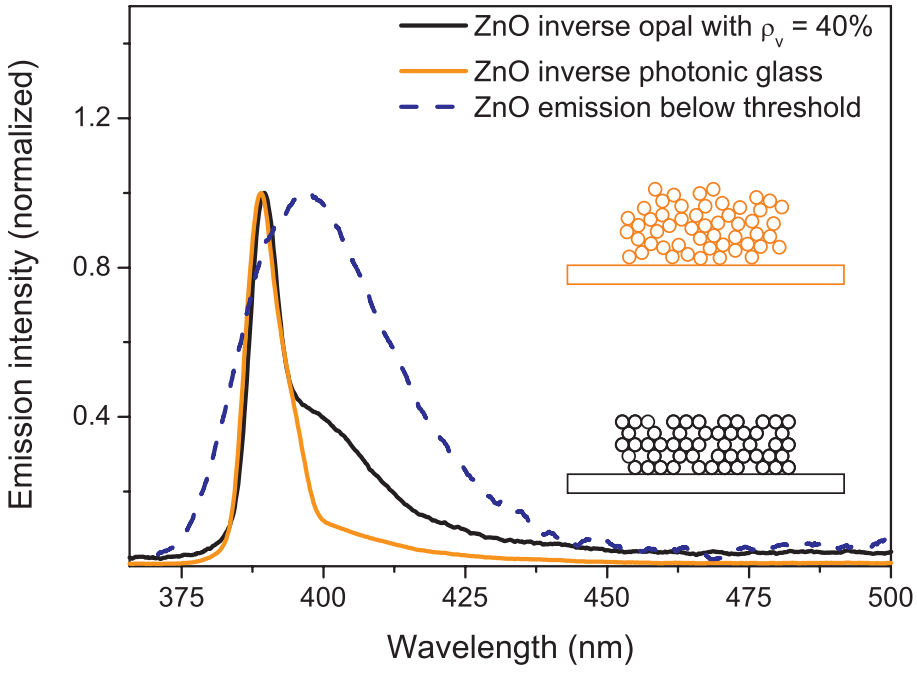

Figure 9.7: ZnO lasing emission in ZnO inverse photonic glass (orange curve) and ZnO inverse opal doped with $\rho_v = 40$ % (black curve). Lasing modes from both systems are spectrally very closed ($\lambda = 389$ nm). This is due to the fact both systems do not present resonances within the ZnO gain spectrum and show conventional random lasing.

constant of the crystal (sphere diameter) whereas in the second case, no control can be exerted over the lasing emission. It appears at the same spectral position for a random distribution of ZnO shells and for a ZnO inverse opal doped with a high amount of vacancies. In this section, the transition from Bloch lasing emission in the ordered structure to random lasing emission in the disordered one will be shown. For that purpose, we will use a ZnO inverse opal with no vacancy doping and a ZnO inverse opal doped with a high amount of vacancies $\rho_v = 40$ %, both grown with an original PMMA sphere diameter $d = 367$ nm. Figure 9.8 shows ZnO emission above threshold in the case of a *perfect* ZnO inverse opal (red curve) and a ZnO inverse opal doped with vacancies (black curve). Lasing emission is determined, in the case of the ZnO ordered nanostructure (red curve), by the interaction between the lasing mode (*blue* flat photonic band shown in figure 9.2) and ZnO gain spectrum. In particular, it appears at $\lambda = 442$ nm. On the contrary, no resonant modes are present in the disordered ZnO photonic crystal doped with vacancies, as discussed in previous section. Lasing modes in such a structure are diffuse open modes as those of a conventional random laser. Emission above threshold (black curve) is, therefore, determined by the gain length ℓ_g and the lasing mode appears, therefore, spectrally very close ($\lambda = 390$

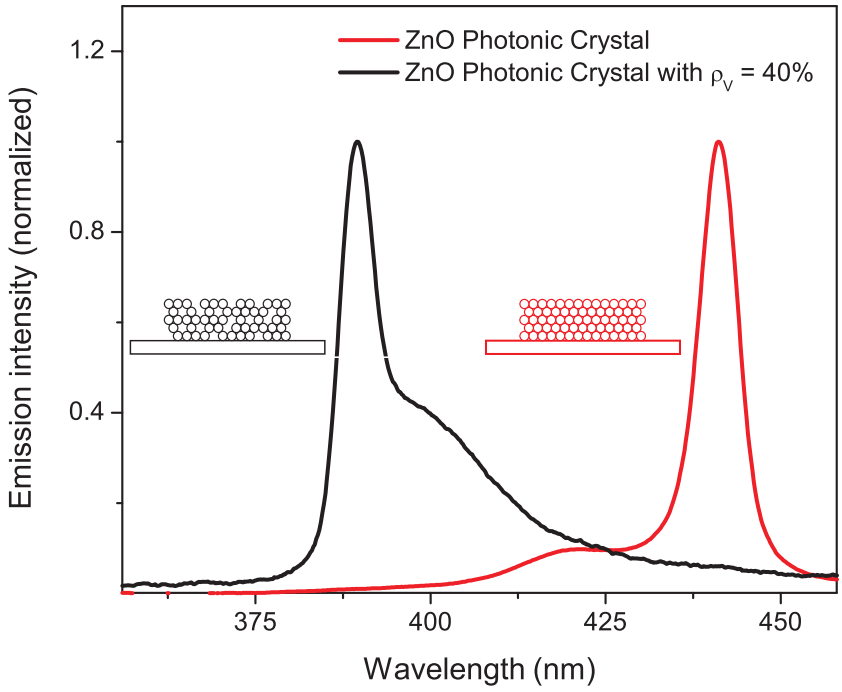

Figure 9.8: ZnO emission above threshold from ZnO inverse opal without vacancies (red curve) and with a $\rho_v = 40$ % vacancy doping (black curve). Both systems are grown with an original PMMA sphere diameter $d = 367$ nm. The spectral shift of the lasing mode from $\lambda = 442$ nm to $\lambda = 390$ nm suggests a transition from Bloch lasing in the case of the ordered structure to random lasing, in the case of the disordered structure.

nm) to the gain maximum ($\lambda = 395$ nm). Lasing threshold in both structures is achieved at $3.3 \times 10^{-3} J/mm^2$ in the case of $\rho_v = 0$ % and $3.2 \times 10^{-5} J/mm^2$ in the case of $\rho_v = 40$ %.

Figure 9.8 suggests how, just by adding a certain amount of vacancies to the ordered system, it is possible to observe a transition from Bloch to random lasing emission. PMMA sphere diameter has been particularly selected to obtain lasing emission in the ZnO inverse opal spectrally far from the maximum ZnO gain. This enhances the transition between both types of lasing in ZnO nanostructures revealed, in spectral measurements, as a lasing emission shift from the spectral position of the first flat band to the spectral position determined by the ZnO gain curve. Both are, respectively, the lasing modes in the ordered and disordered ZnO nanostructures.

9.5. Conclusions and future work.

This chapter summarizes the spectral measurements of ZnO lasing from different ZnO nanostructures, ordered and disordered. Here we show UV lasing in ZnO inverse opals mediated by high-energy weakly dispersive photonic bands. By varying the original polymer sphere diameter it is possible to tune the lasing mode though the ZnO gain spectrum. It is also shown that, the spectral distance between the lasing mode (the flat photonic high-energy band) and the maximum in the ZnO gain curve strongly affects the value of the lasing threshold which increases with this spectral distance (and with the sphere diameter). We also show UV random lasing in ZnO inverse photonic glasses and ZnO inverse opals doped with a high amount of vacancies. Lasing emission from both disordered ZnO nanostructures are spectrally very close to each other and to the maximum of the ZnO gain curve. The transition from Bloch lasing to Random lasing is suggested in the case of ZnO inverse opals with and without vacancy doping.

Spectral measurements shown in this chapter are not enough to assure such a lasing mechanism transition. In the future, the range of vacancy doping density from $0\ \% < \rho_v < 40\ \%$ should be investigated to analyzed the intermediate system. Time-resolved measurements of and photon statistics of ZnO lasing in both cases as well as in the intermediate system may be crucial to ensure a complete control exerted over the lasing mechanism with just the controlled extrinsic disorder of the structure.

Appendix A

Light scattering in Photonic Crystals

Light impinging on a perfect dielectric lattice as, for example, an opal-based photonic crystal, can be reflected (I_R) or scattered (I_S) in the bulk of the system. Moreover, light scattering in such a system can be elastic (due to light-lattice interaction, when lattice constant is on the order of light wavelength) or inelastic (absorption by the material composing the spheres). Polystyrene (PS) and polymethil-metacrilate (PMMA) spheres do not absorb light in the spectral range of work (450 nm $< \lambda <$ 2 μm) used in this thesis [57, 58]. On the following, we will discard absorption effects and, therefore, only elastic scattering will be taken into account.

In the particular case of light propagating normal to the surface of the system (see figure A.1), it undergoes a constructive interference imposed by the periodicity of the lattice. This limits light propagation directions to the incidence one (I_T) or along certain diffraction directions determined by the lattice (I_{diff}, with different diffraction patterns, in the figure two of them have been exemplified).

Diffraction patterns are a very particular case of the speckle pattern of the system due to the underlaying lattice structure. Light is scattered in directions different than the incidence one by constructive interference. This regime of light scattering occurs, in the case of photonic crystals, in the, so-called, high energy photonic bands [103]. Let us consider light incident perpendicular to the sample surface with a given incident wavevector k_i. Whether grown by natural sedimentation [43] or vertical deposition [45], artificial opals present their surface parallel to the (111) family of crystallographic planes, that is, along ΓL crystallographic direction. Light wavevector k_i is, therefore, along ΓL direction.

Figure A.2 shows the scattering diagram in the reciprocal space. In particular, the repeated Brillouin zone of an fcc structure is shown. Figure A.2 also shows the photonic band structure along the ΓL direction. Scattered light wavevector (red arrow) k_o is restricted by two conditions: the energy conservation and the conservation of the parallel component of the incident wavevector k to the sample boundary (imposed by the boundary conditions of the Maxwell equations).

The first one imposes that, both incident and transmitted wavevectors lie on a dispersion surface, which for one homogenous-like medium is plotted by circle centered at the origin. The second imposes that the scattered wavevector, k_o, can be folded back to the incident one, k_i, by some reciprocal lattice vector, G in such a way to conserve the parallel component of k_i to the system boundary. In the case of k_i along ΓL direction, the parallel component is null. Figure A.2 schematizes the scattering process for three different light frequencies **(1)**, **(2)** and **(3)** where isofrequency surfaces are plotted as circles with three different colors. In the first case **(1)** (blue circle), incident and scattered light wavevectors are restricted to be equal. Light can only propagate straightforward in the incident direction. This corresponds to light coupling with a, so-called, linear photonic band (pointed out in the band diagram). In the second case **(2)**, equi-energy surface (pink circle) lies on a Bragg plane and a Bragg diffraction takes places. A pseudogap is opened for this particular frequency ω_2 as pointed out in the photonic band diagram. Finally, in the third case **(3)**, incident wavevector is large enough (yellow circle) to be folded by a reciprocal lattice vector G_i into scattered wavevectors lying in other directions than the incident one. This physical process occurs when light couples to a, so-called, diffraction band [103], as pointed out in the band diagram. This is the origin of light diffraction in photonic crystals.

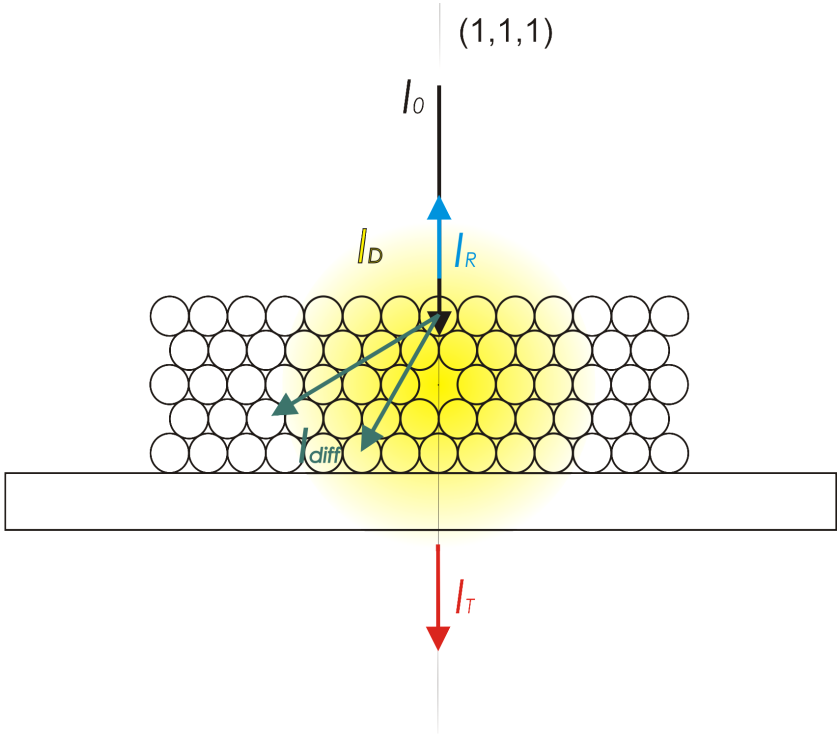

Figure A.1: Schematic of the possible propagation light channels for light impinging normally to the sample surface with intensity I_0. Disregarding inelastic scattering (i.e absorption) of the material composing the spheres, light can be reflected (I_R), diffracted (I_{diff}), straightforward transmitted (I_T) or diffused by inhomogeneities (I_D).

For low energies, as in cases **1** and **2**, for which $a/\lambda < 1$ the, so-called, onset of diffraction, only linear bands are available and diffraction can not be built for these energies.

Scattering in perfect and infinite photonic crystals is, therefore, given by:

$$I_S = I_T + I_{diff} \tag{A.1}$$

However, if the lattice is not perfect, that is, there is a certain amount of disorder such as vacancies, displacements, polydispersity in the spheres size, etc, there is an extra source of elastic scattering allowed in the crystal. If the lattice is not translational invariant, there is no more wavevector k conservation. In this case, the propagation direction is not restricted and the light scattering is diffuse (I_D). This type of light propagation is the origin of what is commonly known as light diffusion. For light impinging on a photonic crystal in a certain direction and measured in the same direction, I_D is a source of light loss in that particular direction and can be used as an extremely sensitive measurement of the amount of disorder in the system [59, 60].

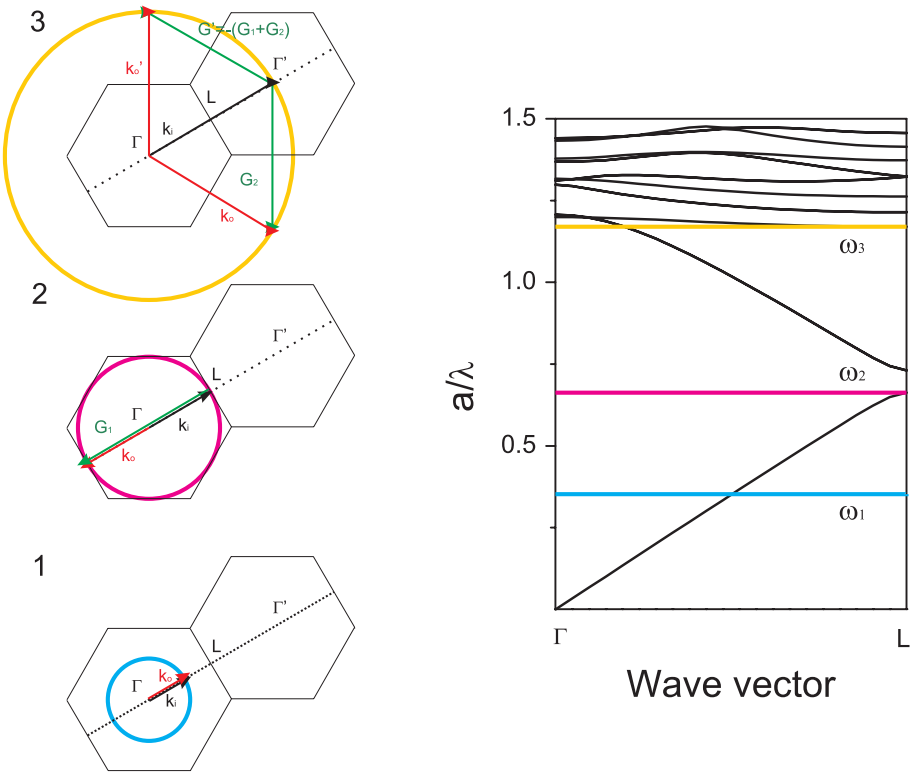

Figure A.2: **(Left)** Schematic of the scattering diagram in reciprocal space: incident (scattered) light wavectors represented by black (red) arrows. Light scattering process is represented for three particular frequencies and for the case of incident wavevector lying in the ΓL direction. The diagrams are for negligible refractive index contrast. **(Right)** Photonic band structure along this particular crystallographic direction is also plotted to point out light-bands coupling in the three different cases.

Scattering in an imperfect photonic crystal is, therefore, given by

$$I_S = I_T + I_{diff} + I_D \tag{A.2}$$

According to the previous discussion, in the case of a non-perfect lattice, non-absorbing sphere material and below the onset of diffraction ($I_{diff} = 0$), light can only by reflected, transmitted or diffused by inhomogeneities:

$$I_0 = I_R + I_S = I_R + I_T + I_D \tag{A.3}$$

A.1. Lambert-Beer law for Photonic Crystals

I_0 is the intensity entering the sample at $z = 0$, I_z is the intensity entering the infinitesimal slab at z, dI is the intensity scattered in the slab, and I is the intensity of light leaving the sample. Then, the total opaque area on the slab due to the scatterers is $\sigma\rho_s A dz$, where σ is the scattering cross section and ρ_s the scatterer density. The fraction of scattered photons will be $\sigma\rho_s dz$ so,

$$\frac{dI}{I_z} = -\sigma\rho_s dz \tag{A.4}$$

which solution is:

$$I_z = I_0 exp(-\sigma\rho_s z) \tag{A.5}$$

where $\ell_s = 1/\sigma\rho_s$ is the scattering mean free path. In the case of independent absorbing scatters, the extinction length of the ballistic light beam is:

$$\frac{1}{\ell_{ext}} = \frac{1}{\ell_s} + \frac{1}{\ell_{abs}} \tag{A.6}$$

In this thesis, as discussed previously, we deal with non-absorbing materials in the spectral range of work (at least as a first approximation). Therefore, Lambert-Beer's law reads:

$$I(L) = I_0 \exp(-\frac{L}{\ell_s}) \tag{A.7}$$

where I_0 is the light intensity impinging the system and $I(L)$ is the light intensity leaving the system in the same direction (ballistic beam propagation). According to what has been discussed in the previous section, in the case of a non-perfect lattice, non-absorbing sphere material and bellow the onset of diffraction, for light incident normal to the system surface, the light intensity at a given thickness L inside the sample is:

$$I(L) = I_0 - I_D \tag{A.8}$$

here, the only source of light losses in the direction of incidence is the diffuse light I_D. According to A.3, A.7 and A.8 it is easy to obtain:

$$I_R + I_T = I_0 \exp(-\frac{L}{\ell_s}) \tag{A.9}$$

and taking into account $R = I_R/I_0$ and $T = I_T/I_0$:

$$R(L) + T(L) = \exp(-\frac{L}{\ell_s}) \tag{A.10}$$

A very sensitive and precise measure of the scattering mean free path of the system can be obtained by measuring reflectance, $R(L)$, and transmittance, $T(L)$, from a photonic crystal with a certain amount of lattice disorder, composed by non-absorbing material and for energies bellow the onset of diffraction as a function of the system thickness. This is limited if a very precise measurement of L is possible.

Appendix B

Optical gating technique

Optical gating uses the non linear optical properties of frequancy sum to a reference laser beam (ω_1) with the diffuse light signal beam (ω_2) transmitted though the sample in a 3 mm thick non-linear BBO (beta barium borate) crystal to produce a sum frequency signal. Since the efficiency of the sum-generation is proportional to the product of the two laser beam intensities at a given time, the whole process works as an optical gate, with a variable time delay.

Figure B.1**a** shows the probe beam sorce, which is obtained by an Argon laser, which pumps a Ti:Sapp laser, which at the same time pumps an optical parametric oscillator (called *OPAL*). The Argon laser is used to pump a Titanium Sapphire crystal, hence, in order to exploit all the absorption spectrum, the Argon is kept multi-line. Ti:Sapp laser works with a center wavelength 810 nm (pulse duration 130 fs, average power 2.0 W, repetition rate 82 MHz) and the pumped *OPAL* yields short pulses tunable from 1450 to 1600 nm (average power 200 mW). This beam (ω_1) is used to probe the sample. The reference pulse at 810 nm (ω_2) is obtained from the Ti:Sapp beam (450 mW average power). Both signal beams can be distinguished in figure B.1**a** as the probe beam (grey) and the reference beam (red).

Figure B.1**b** shows the optical set up to analyzed diffuse light though the samples. The probe beam (grey) probes the sample with a certain angle with respect to it surface whereas the reference beam is delayed with a translation stage. The spatial delay introduced in the reference beam is of the order of microns. Both signal beams, the reference and the diffuse light from the sample are mixed in the non-linear crystal generating green light (ω_3) (figure B.1**c**). The energy conservation requires that $\omega_3 = \omega_1 + \omega_2$, while the momentum conservations $k_3 = k_1 + k_2$. The radiation can be emitted in every direction but the phase-coherence between the waves determines a strongly peaked output in a certain direction.

The phase-matching condition, turns into a relation between the refractive indexes n_e and n_o, that the waves experience in the material:

$$k_{e3}(\theta) = k_{o1} + k_{o2} \tag{B.1}$$

or

$$n_e(\omega_3)\omega_3 = n_o(\omega_1)\omega_1 + n_o(\omega_2)\omega_2 \tag{B.2}$$

Phase-matching cannot be fulfilled in a normally dispersive medium, as the refractive index is a monotonic function of wavelength. In the case of the BBO non-linear crystal, phase-matching is obtained changing the angle between light

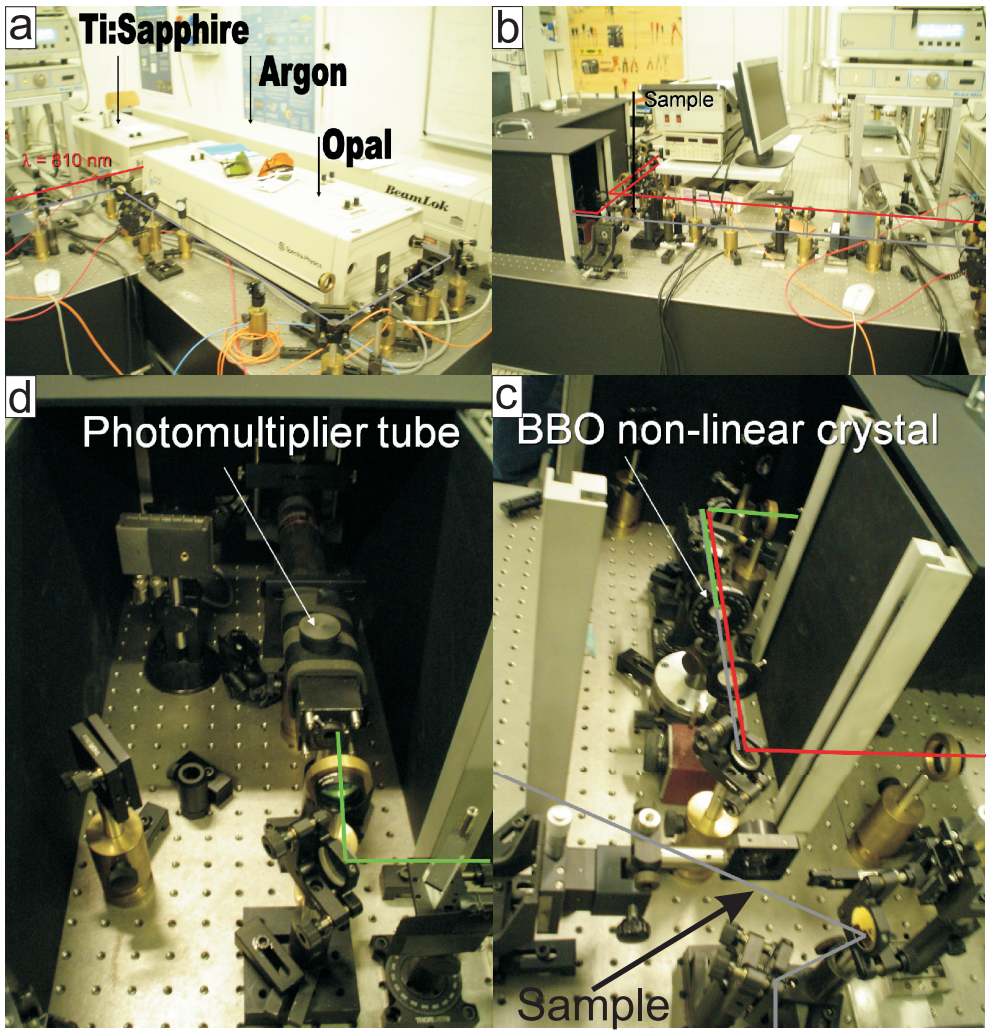

Figure B.1: **(a)** Reference beam (ω_2) and probe signal beam (ω_1) are generated by a Ti:Sapp laser and an optical parametric oscillator (*OPAL*) respectively. The OPAL is pumped with the Ti:Sapp laser. **(b)** The signal provided by the *OPAL* , within 1400 nm and 1600 nm, probes the sample whereas the reference beam (810 nm) is delayed spatially with a controlled translation stage. The spatial delay is of the order of microns. **(c)** The diffuse beam from the sample and the delayed reference beam are mixed together in the BBO non-linear crystal, generating green light (ω_2). The efficiency of this sum-generation is proportional to the product of the two laser beam intensities, the whole process works as an optical gate, with a variable time delay. **(d)** The green beam is finally detected by a photodiode.

propagation and the optical axes, as the extraordinary refractive index is angle-dependent (equation B.3) so it can be tuned to satisfy equation B.2.

$$n_e(\theta) = \frac{n_o n_e}{sqrtn_e^2 cos\theta^2 + n_o^2 sin\theta^2} \tag{B.3}$$

As mentioned previously, the sum-generation efficiency is proportional to the product of the two beams intensities. In other words, the intensity of the green generated light ($I_{\omega 3}$) is directly proportional to the cross correlation between the two incoming pulses ($I_{\omega 1,2}$):

$$I_{\omega 3}(t) \int I_{\omega 1}(t-\tau) I_{\omega 2}(t) d\tau \tag{B.4}$$

A delay line on the reference beam path allows to tune the time delay between signal and reference, and thus the longitudinal spatial overlapping. This technique allows for measuring in a time window equal to the pulse duration, 130 fs. The constant time profile of the generated signal at 510 - 540 nm allows for a time resolution of less than 100 fs. The sum frequency signal is detected by a photodiode and a standard lock-in technique is used to suppress noise (figure B.1**d**).

Appendix C

Coherent backscattering technique

The technique to record backscattered light needs to be very accurate. The backscattering cone is a very sensitive measurement. Although the physical phenomenon and its interpretation is rather simple, a reasonable enhancement factor of the backscattered light is necessary to estimate ℓ_t with accuracy. The theoretical enhancement factor for light backscattered at $\theta = 0$ is two for weak scattering in the helicity conserving polarization, but many set-up artifacts reduce considerably this factor. These artifacts are from reflections in boundaries and surfaces which introduce noise in the measurement to diffusion in other materials different than the sample itself. It is, therefore, crucial to be careful and screened all the possible reflectance surfaces. When working with visible light, light can be screen with the use of black surfaces which absorb light losses from the laser beam.

Figure C.1 schematizes the set up built up to measure the coherent enhanced backscattering. The coherent beam is provided by a He-Ne laser at $\lambda_0 = 632$ nm. All the cone measurements are done at this wavelength. The laser beam is polarized vertically and it is formed by several EM modes. It is very important to illuminate the samples with a plane wave beam in order to have a flat background. To spatially clean the laser mode, a spatial filter composed by a microscope and a pin hole is used. The laser beam is then collimated with the help of a lens **(1)** and its diameter is selected with a diaphragm. With the help of a beam splitter, the beam illuminates the sample. In order to average over a large number of scattering configurations, the sample is rotated in the plane perpendicular to the beam propagation. The backscattered light from the sample surface is then focused with the help of a lens **(2)** into a CCD camera, which records the backscattering cone. The enhancement factor of the backscattering cone is defined as the ratio of the total intensity at exact backscattering to the diffuse background intensity at exact backscattering. The diffuse background intensity is the intensity which would be expected from an incoherent addition of the scattered waves. Light polarization is a very important issue. Single scattering events invert the helicity of incoming light whereas multiple scattering events

randomized the light polarization. Light which is singly scattered reduces the cone enhancement and should be eliminated from the measurement. A way to do that is to properly place a quarter-wave plate **(a)** in the incoming laser beam. This converts the linearly polarization into circular polarization. Single scattering events will flip the helicity of circular polarized scattered light whereas higher scattering orders will convert incoming circular polarization into elliptically polarized one. By placing an additional quarter-wave plate **(b)** in the backscattered beam, it is possible to transform singly scattered light with circular polarization into vertically polarized light. The only requirement is the second quarter-wave plate **(b)** to be orthogonal to the initial one **(a)**. Finally, singly scattered light can be eliminated from the backscattered beam by placing an horizontal axis polarizer. This proceeding significantly improves the set up performance and the backscattering cone measurement. An example of a backscattering cone obtained with this set up is shown in figure C.2, where the experiment is performed on a piece of paper. The inset of figure C.2 shows the cone of light backscattered recorded by the CCD. The value of the transport mean free path is obtained by fitting the the experimental backscattered light with the function:

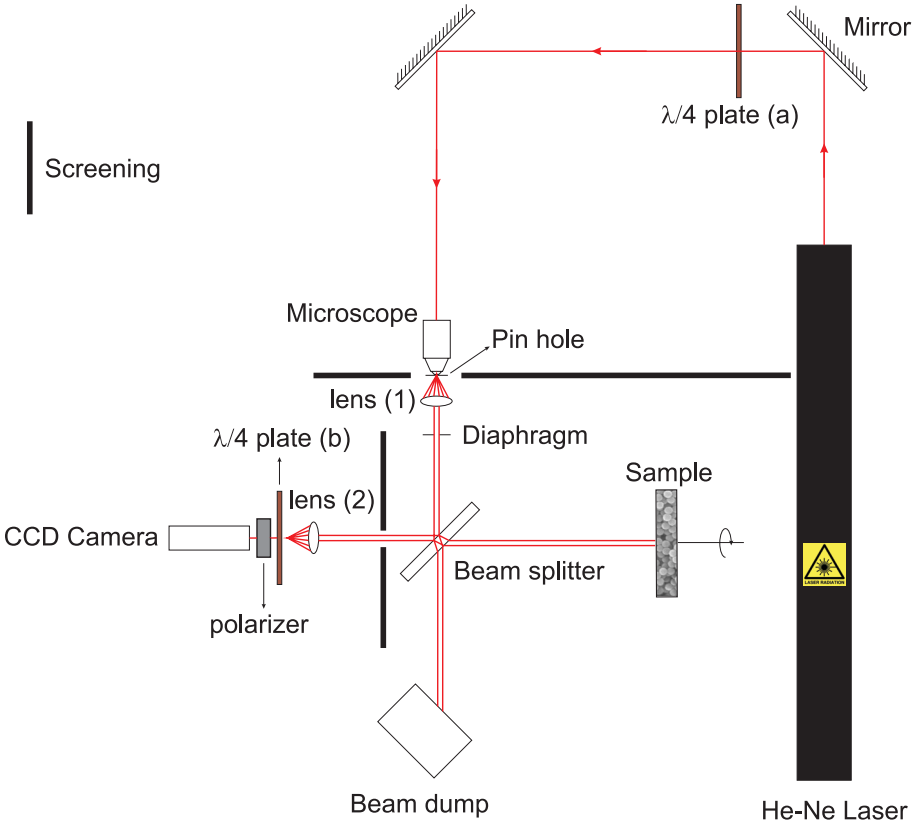

Figure C.1: Set up of the backscattering cone measurement.

$$\gamma_C(\theta) = \frac{3}{2\ell_t^3 \alpha u} \frac{\alpha + u(1 - exp(-2\alpha\xi))}{(u+\alpha)^2 + \eta^2} \tag{C.1}$$

$$\begin{aligned} \eta &= k(1-\mu_S) \\ u &= \frac{1+\mu_S^{-1}}{2\ell_t} \\ \xi &= \frac{2}{3\ell_t} \\ \mu_S &= \cos\theta \\ \alpha &= k\sin\theta \end{aligned} \tag{C.2}$$

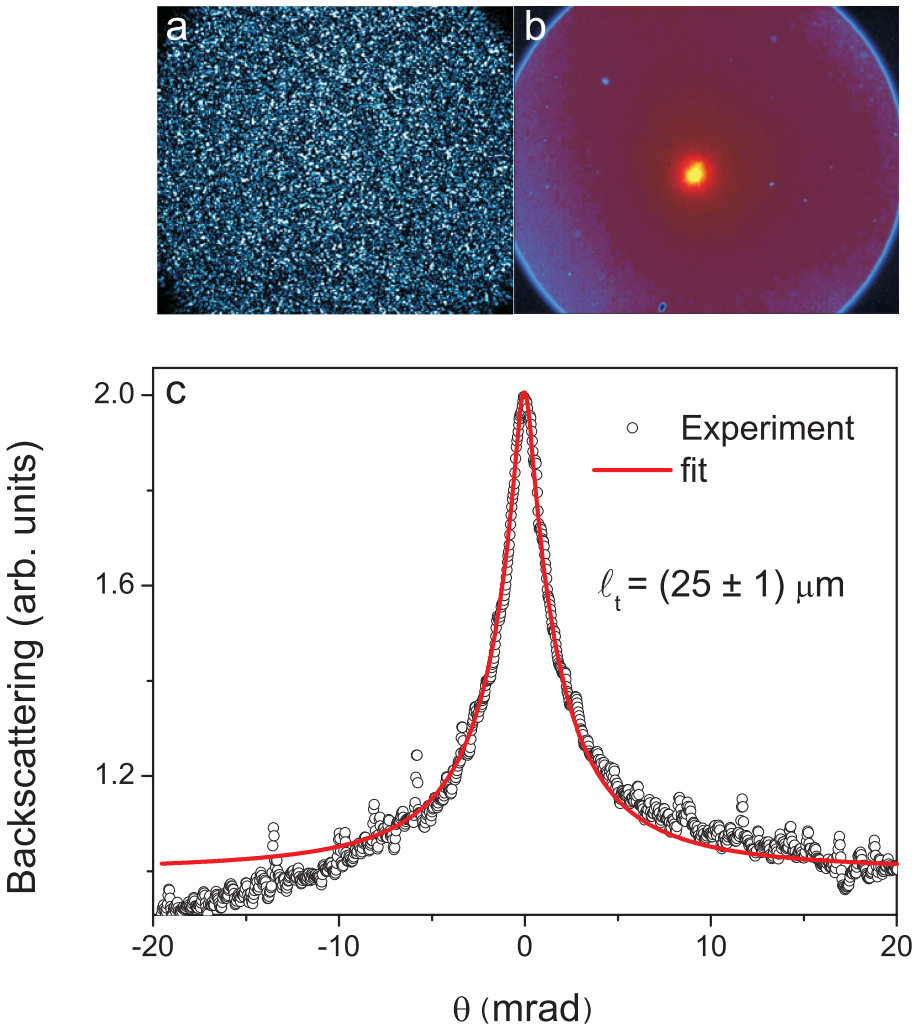

Figure C.2: **(a)** Speckle pattern **(b)** Average speckle pattern which shows the cone of backscattering and **(c)** fit of the backscattering cone from paper.

where $\gamma_C(\theta)$ is the so-called cross term, a contribution from the interference between reciprocal light paths [138, 139]. This function, which derivation is out of the scope of this thesis, can be obtained assuming that the random walk in the three orthogonal propagation directions is uncoupled. For more details, please check [191].

Bibliography

[1] T. Young, *A Course of Lectures on Natural Philosophy and the Mechanical Arts* (1807, republished 2002 by Thoemmes Press).

[2] L. de Broglie, *Recherches sur la théorie des quanta (Researches on the quantum theory)*, Thesis, Paris (1924).

[3] E. Yablonovitch, *Inhibited spontanous emission in solid-state physics and electronics*, Phys. Rev. Lett. **58**, 2059 (1987).

[4] S. John, *Strong localization of photons in certain disordered dielectric superlattices*, Phys. Rev. Lett. **58**, 2486 (1987).

[5] Locatization for electrons: P.W. Anderson, *Absence of diffusion in certain random lattices.* Phys. Rev. **109**, 1492, (1958). Localization for photons: P. W. Anderson, *The question of classical localization: a theory of white paint?*, Philos. Mag. B **52**, 505 (1985).

[6] R. Dalichaouch, J. P. Armstrong, S. Schultz, P. M. Platzman, S. L. McCall, *Microwave localization by two-dimensional random scattering*, Nature **354**, 53 (1991).

[7] A. Z. Genack, N. Garcia, *Observation of photon localization in a three-dimensional disordered system*, Phys. Rev. Lett. 1991, 66 2064.

[8] P. Sheng, *Introduction to Wave Scattering, Localization, and Mesoscopic Phenomena* Academic Press, San Diego (1995).

[9] I. Newton, *A treatise of the reflections, refractions, inflections and colours of light* (Opticks) London (1704); reprinted by Dover, New York (1952).

[10] H. C. Van de Hulst, *Light scattering by small particles*, Dover publications, (2002).

[11] G. Mie, *Beiträge zur Optik trüber Medien, speziell kolloidaler Metallösungen,* Ann. Phys. **25**, 377 (1908).

[12] J. W. S. Rayleigh, Scientific Papers **5**, 617 (1912).

[13] Simulations were performed with meep [A. Farjadpour, D. Roundy, A. Rodriguez, M. Ibanescu, P. Bermel, J.D. Joannopoulos, S. G. Johnson, G. Burr, Opt. Lett. **31**, 2972 (2006).

[14] M.I. Antonoyiannakis, R. Pendry, *Mie resonances and bonding in photonic crystals*, Europhys. Lett. **40**, 613 (1997).

[15] D. J. Durian, *Influence of boundary reflection and refraction on diffusive photon transport. Phys. Rev. E* **50**, 857-866 (1994).

[16] N. Garcia, A. Z. Genack, A. A. Lisyansky, *Measurement of the transport mean free path of diffusing photons.* Phys. Rev. B **46**, 14475 (1992).

[17] J. X. Zhu, D. J. Pine, D. A. Weitz, *Internal reflection of diffusive light in random media*, Phys. Rev. A **44**, 3948 (1991).

[18] M. S. Patterson, B. Chance, B. C. Wilson, *Time resolved reflectance and transmittance for the non-invasive measurement of tissue optical properties*, Appl. Opt. **28**, 2331 (1989).

[19] A. Fick, *Über Diffusion*, Poggendorff's Annalen der Physik und Chemie, **94**, 59 (1855).

[20] P. Lodahl, A. F. van Driel, I. S. Nikolaev, A. Irman, K. Overgaag, D. Vanmaekelbergh, W. L. Vos, *Controlling the dynamics of spontaneous emission from quantum dots by photonic crystals*, Nature **430**, 654 (2004).

[21] S. Noda, M. Fujita, T. Asano, *Spontaneous-emission control by photonic crystals and nanocavities*, Nature Photonics **1**, 449, (2007)

[22] A. F. Koenderink, W. L. Vos, *Light Exiting from Real Photonic Band Gap Crystals is Diffuse and Strongly Directional*, Phys. Rev. Lett. **91**, 213902 (2003).

[23] M. Notomi, *Theory of light propagation in strongly modulated photonic crystals: Refractionlike behavior in the vicinity of the photonic band gap*, Phys. Rev. B **62**, 10696 (2000).

[24] K. Sakoda, *Optical Properties of Photonic Crystals*, Springer, Berlin 2001.

[25] A. Blanco, E. Chomsky, S. Grabtchak, M. Ibisate, S. John, S. W. Leonard, C. López, F. Meserger, H. Míguez, J. P. Mondia, G. A. Ozin, O. Toader, H. M. van Driel, *Large-scale synthesis of a silicon photonic crystal with a complete three-dimensional bandgap near 1.5 micrometres*, Nature **405**, 437 (2000).

[26] C. López, *Materials Aspects of Photonic Crystals*, Adv. Mater. **15**, 1679 (2003).

[27] J. F. Galisteo-López, M. Galli, M. Patrini, A. Balestreri, L. C. Andreani, C. López, *Effective refractive index and group velocity determination of 3D photonic crystals by means of white light interferometry*, Phys. Rev. B **73**, 125103 (2006)

[28] M. Scharrer, A. Yamilov, X. Wu, H. Cao, R. P. H. Chang, *Ultraviolet lasing in high-order bands of three-dimensional ZnO photonic crystals*, Appl. Phys. Lett. **88**, 201103, (2006).

[29] S. John, J. Wang, *Quantum electrodynamics near a photonic band gap: Photon bound states and dressed atoms*, Phys. Rev. Lett. **64**, 2418 (1990).

[30] T. Quang, M. Woldeyohannes, S. John, G.S. Agarwal, *Coherent Control of Spontaneous Emission near a Photonic Band Edge: A Single-Atom Optical Memory Device*, Phys. Rev. Lett. **79**, 5238 (1997).

[31] S. Y. Zhu, Y. P. Yang, H. Chen, H. Zheng, M. S. Zubairy, *Spontaneous Radiation and Lamb Shift in Three-dimensional Photonic Crystals*, Phys. Rev. Lett. **84**, 2136 (2000).

[32] E. M. Purcell, *Spontaneous emission probabilities at radio frequencies*, Phys. Rev. **69**, 681 (1946).

[33] Y. Yamamoto, F. Tassone, H. Cao, *Semiconductor Cavity Quantum Electrodynamics*, Springer, New York (2000).

[34] K. J. Vahala, *Optical microcavities*, Nature **424**, 839 (2003).

[35] A. Kress, F. Hofbauer, N. Reinelt, M. Kaniber, H. J. Krenner, R. Meyer, G. Bohm, J. J. Finley, *Manipulation of the spontaneous emission dynamics of quantum dots in two-dimensional photonic crystals*, Phys. Rev. B **71**, 241304 (2005).

[36] D. Englund, D. Fattal, E. Waks, G. Solomon, B. Zhang, T. Nakaoka, Y. Arakawa, Y. Yamamoto, J. Vuckovic, *Controlling the Spontaneous Emission Rate of Single Quantum Dots in a 2D Photonic Crystal*, Phys. Rev. Lett. **95**, 013904 (2005)

[37] A. F. Ioffe, A. R. Regel, Prog. Semicond. **4**, 237, (1960).

[38] C. Conti, A. Fratalocchi, *Dynamic light diffusion, three-dimensional Anderson localization and lasing in inverted opals*, Nature Physics **4**, 794, (2008).

[39] J. B. Jones, E. R. Segnit, J. V. Sanders, *Structure of Opal*, Nature 204, 990 (1964).

[40] J.W. Goodwin, J. Hearn, C. C. Ho, R. H. Ottewill, *Studies on the preparation and characterisation of monodisperse polystyrene laticee. Colloid Polym. Sci.* **252**, 464 (1974).

[41] M. Mueller, R. Zentel, T. Maka, S. G. Romanov, C. M. Sotomayor Torres, *Dye-Containing Polymer Beads as Photonic Crystals*, Chem Mater. **12**, 2508 (2000).

[42] V. N. Astratov et al. *Optical spectroscopy of opal matrices with CdS embedded in its pores: Quantum confinement and photonic band gap effects.* Nuovo Cimento Della Societa Italiana Di Fisica D-Condensed Matter Atomic Molecular and Chemical Physics Fluids Plasmas Biophysics **17**, 1349 (1995).

[43] R. Mayoral, J. Requena, J. S. Moya, C. López, A. Cintas, H. Miguez, F. Meseguer, L. Vázquez, M. Holgado, A. Blanco *3D long-range ordering in an SiO2 submicrometer-sphere sintered superstructure*, Adv. Mater. **9**, 257 (1997).

[44] H. Míguez, F. Meseguer, C. López, A. Blanco, J. S. Moya, J. Requena, A. Mifsud, V. Fornés, *Control of the photonic crystal properties of fcc-packed submicrometer SiO2 spheres by sintering*, Adv. Mater. **10**, 480 (1998).

[45] P. Jiang, J. F. Bertone, K. S. Hwang, V. L. Colvin, *Single-crystal colloidal multilayers of controlled thickness*, Chem. Mater. **11**, 2132 (1999).

[46] J. F. Galisteo Lopez, *An optical study of opal based photonic crystals*, Thesis, ISBN 84-689-2810-0, Madrid (2005).

[47] N. D. Denkov, O. Velev, P. Kralchevski, I. Ivanov, H. Yoshimura, K. Nagayama, *Mechanism of Formation of 2-Dimensional Crystals from Latex-Particles on Substrates*, Langmuir **8**, 3183 (1992).

[48] X. Checoury, S. Enoch, C. López, A. Blanco, *Stacking patterns in self-assembly opal photonic crystals*, Appl. Phys. Lett. **90**, 161131 (2007).

[49] N. Denkov, O. Velev, P. Kralchevski, I. Ivanov, H. Yoshimura, K. Nagayama, *Mechanism of formation of two-dimensional crystals from latex particles on substrates*, Langmuir **8**, 3183 (1992).

[50] P. Pieranski, L. Strzelecki, B. Pansu, *Thin Colloidal Crystals*, Phys. Rev. Lett. **50**, 900 (1983).

[51] H. S. Sozuer, J. W. Haus, R. Inguva, *Photonic Bands - Convergence Problems with the Plane-Wave Method*, Phys, Rev, B **45**, 13962 (1992).

[52] O. D. Velev, E. W. Kaler. *Structured porous materials via colloidal crystal templating: From inorganic oxides to metals* Adv. Mater. **12**, 531 (2000).

[53] K. M. Kulinowski, P. Jiang, H. Vaswani, V. L. Colvin, *Porous metals from colloidal templates*, Adv. Mater. **12**, 833 (2000).

[54] P. N. Bartlett, P. R. Birkin, M. A. Ghanem, *Electrochemical deposition of macroporous platinum, palladium and cobalt films using polystyrene latex sphere templates*, Chem. Comm. 1671 (2000).

[55] B. H. Juarez, C. Lopez, C. Alonso, *Formation of zinc inverted opals on indium tin oxide and silicon substrates by electrochemical deposition*, Journal of Physical Chemistry B **108**, 16708 (2004).

[56] M. Scharrer, X. Wu, A. Yamilov, H. Yamilov, H. Cao, R. P. H. Chang, *Fabrication of inverse opal ZnO photonic crystals by atomic layer deposition*, Appl. Phys. Lett. **86**, 151113 (2005).

[57] T. Inagaki, E. T. Arakawa, R. N. Hamm, M. W. Williams, *Optical properties of polystyrene from the near-infrared to the x-ray region and convergence of optical sum rules*, Phys. Rev. B, **15**, 3243 (1997).

[58] M. A. Khashan, A. Y. Nassif, *Dispersion of the optical constants of cellulose triacetate irradiated by gamma rays in a wide spectral range 0.2Ű3 ţm*, Opt. Comm. **188**, 129 (2001).

[59] J. F. Galisteo-Lopez, E. Palacios-Lidon, E. Castillo-Martinez, C. Lopez, *Optical study of the L gap in thickness and orientation controlled artificial opals*, Phys. Rev. B **68**, 115109 (2003).

[60] V. N. Astratov, A. M. Adawi, S. Fricker, M. S. Skolnick, D. M. Whittaker, P. N. Pusey, *Interplay of Order and Disorder in the Optical Properties of Opal Photonic Crystals*, Phys. Rev. B **66**, 165215 (2002).

[61] A. E. Siegman, *Lasers.*, Stanford University, University Science Books, Oxford (1986).

[62] M. A. Noginov, *Solid-state random lasers.*, Springer, Berlin (2005).

[63] V. S. Letokhov, *Generation of light by a scattering medium with negative resonance absorption. Sov. Phys. JETP* **26**, 835 (1968).

[64] N. M. Lawandy, R. M. Balachandran, A. S. L. Gomes, E. Sauvain, *Laser action in strongly scattering media*, Nature **368**, 436 (1994).

[65] D.S. Wiersma, A. Lagendijk, *Light diffusion with gain and random lasers. Phys. Rev. E* **54**, 4256 (1996).

[66] A. Lagendijk, B. van Tiggelen, *Resonant multiple scattering of light*, Phys. Rep. **270**, 143 (1996).

[67] M.P. van Albada, B.A. van Tiggelen, A. Lagendijk, A. Tip, *Speed of propagation of classical waves in strongly scattering media*, Phys. Rev. Lett. **66**, 3132 (1991).

[68] K. L. van der Molen, A. P. Mosk, A. Lagendijk, *Intrinsic intensity fluctuations in random lasers*, Phys. Rev. A, **74**, 053808 (2006).

[69] E. Türeci, L. Ge, S. Rotter, A. Douglas Stone, *Strong Interactions in Multimode Random Lasers*, Science, **320**, 643 (2008).

[70] O. Painter, R. K. Lee, A. Scherer, A. Yariv, J. D. O'Brien, P. D. Dapkus, I. Kim, *Two-dimensional photonic band-gap defect mode laser*, Science 284, 1819 (1999).

[71] G. van Soest, A. Lagendijk, *Beta factor in a random laser*, Phys. Rev. E, **65**, 047601 (2002).

[72] M. N. Shkunov, Z. V. Vardeny, M. C. DeLong, R. C. Polson, A. A. Zakhidov, R. H. Baughman, *Tunable, Gap-State Lasing in Switchable Directions for Opal Photonic Crystals*, Adv. Funct. Mater. **12**, 21 (2002)

[73] K. Sakoda, *Enhanced light amplification due to group-velocity anomaly peculiar to two- and three-dimensional photonic crystal*, Opt. Express **4**, 167 (1999).

[74] Jr. H. C. Casey, M. B. Panish, *Heterostructure Lasers: Part A, Fundamental Principles* Academic, New York (1978).

[75] K. Sakoda, K. Ohtaka, T. Ueta, *Low-threshold laser oscillations due to group velocity anomaly peculiar to two- and three-dimensinal photonic crystals*, Optics Express **4**, 481 (1999).

[76] D. C. Look, *Recent advances in ZnO materials and devices*, Mater. Sci. Eng. B **80**, 383 (2001).

[77] Z. K. Tang, G. K. L. Wong, P. Yu, M. Kawasaki, A. Ohtomo, H. Koinuma, Y. Segawa, *Room-temperature ultraviolet laser emission from self-assembled ZnO microcrystallite thin films*, Appl. Phys. Lett. **72**, 3270 (1998).

[78] Y. Li, G. W. Meng, L. D. Zhang, F. Phillipp, *Ordered semiconductor ZnO nanowire arrays and their photoluminescence properties*, Appl. Phys. Lett. **76**, 2011 (2000).

[79] M. H. Huang, S. Mao, H. Feick, H. Q. Yan, Y. Y. Wu, H. Kind, E. Weber, R. Russo, P. D. Yang, *Room-Temperature Ultraviolet Nanowire Nanolasers*, Science, **292**, 1897 (2001).

[80] Z. W. Pan, Z. R. Dai, Z. L. Wang, *Nanobelts of Semiconducting Oxides*, Science, **291**, 1947 (2001).

[81] B. D. Yao, Y. F. Chan, N. Wang, *Formation of ZnO nanostructures by a simple way of thermal evaporation*, Appl. Phys. Lett. **81**, 757 (2002).

[82] P. X. Gao, Z. L. Wang, S*elf-assembled Nanowire-Nanoribbon Junction Arrays of ZnO*, Phys. Chem. B **106**, 12653 (2002).

[83] M. C. Larciprete, C. Sibilia, S. Paoloni, M. Bertolotti, F. Sarto, M. Scalora, *Accessing the optical limiting properties of metallo-dielectric photonic band gap structures*, J. Appl. Phys. **93**, 5013 (2003).

[84] X. Wu, A. Yamilov, X. Liu, S. Li, V. P. Dravid, R. P. H. Chang, H. Cao, *Ultraviolet photonic crystal laser*, Appl. Phys. Lett. **85**, 3657 (2004).

[85] E. W. Seelig, B. Tang, A. Yamilov, H. Cao, R. P. H. Chang, *Self-assembled 3D photonic crystals from ZnO colloidal spheres, Mater*, Chem. Phys. **80**, 257 (2003).

[86] S. M. Abrarov, Sh. U. Yuldashev, S. B. Lee, T. W. Kang, *Dominant ultraviolet-blue photoluminescence of ZnO embedded into synthetic opal*, J. Lumin. **109**, 25 (2004).

[87] V. V. Ursaki, I. M. Tiginyanu, V. V. Zalamai, V. M. Masalov, E. N. Samarov, G. A. Emelchenko, F. Briones, *Photoluminescence and resonant Raman scattering from ZnO-opal structures*, J. Appl. Phys. **96**, 1001 (2000).

[88] H. Yan, C. F. Blandford, J. C. Lytle, C. B. Carter, W. H. Smyrl, A. Stein, *General Synthesis of Periodic Macroporous Solids by Templated Salt Precipitation and Chemical Conversion*, Chem. Mater. **12**, 1134 (2000).

[89] T. Sumida, Y. Wada, T. Kitamura, S. Yanagida, *Macroporous ZnO films electrochemically prepared by templating of opal films*, Chem. Lett. **30**, 38 (2001).

[90] M. Ritala, M. Leskela, J. Dekker, C. Mutsaers, P. J. Soininen, J. Skarp, *Perfectly conformal TiN and Al_2O_3 films deposited by atomic layer deposition*, Chem. Vap. Deposition **5**, 7 (1999).

[91] J. W. Elam, Z. A. Sechrist, S. M. George, *ZnO/Al_2O_3 nanolaminates fabricated by atomic layer deposition: growth and surface roughness measurements*, Thin Solid Films **414**, 43 (2002).

[92] B. Sang, M. Konagai, *Growth of Transparent Conductive Oxide ZnO Films by Atomic Layer Deposition*, Jpn. J. Appl. Phys. Part 2 **35**, L602 (1996).

[93] H. Yoshikawa, S. Adachi, *Optical Constants of ZnO*, Jpn. J. Appl. Phys. Part 1 **36**, 6237 (1997).

[94] The photonic band structure was calculated using the software *MIT PHOTONIC BANDS*, G. Johnson, J. Joannopoulos, Opt. Express **8**, 173 (2001).

[95] K. Vanheusen, C. H. Seager, W. L. Warren, D. R. Tallant, J. A. Voight, *Correlation between photoluminescence and oxygen vacancies in ZnO phosphors*, Appl.Phys. Lett. 68, 403 (1996).

[96] H. Miguez, E. Chomski, F. García-Santamaría, M. Ibisate, S. John, C. López, F. Meseguer, J. P. Mondia, G. A. Ozin, O. Toader, H. M. van Driel, *Photonic Bandgap Engineering in Germanium Inverse Opals by Chemical Vapor Deposition*, Adv. Mater. **13**, 1634 (2001).

[97] F. García-Santamaría, M. Ibisate, I. Rodríguez, F. Meseguer, C. López, *Photonic Band Engineering in Opals by growth of Si/Ge multilayer shells*, Adv. Mater. **15**, 10 (2003).

[98] I. Tarhan, G. H. Watson, *Analytical expression for the optimized stop bands of fcc photonic crystals in the scalar-wave approximation*, Phys. Rev. B **54**, 7593 (1996).

[99] E. Palacios-Lidón, A. Blanco, M. Ibisate, F. Meseguer, C. López, J. Sánchez-Dehesa, *Optical study of the full photonic band gap in Silicon inverse opals*, Appl. Phys. Lett. **81**, 4925 (2002).

[100] A.Y. Vlasov, X.-Z. Bo, J.C. Sturm, D.J. Norris, *On-chip natural assembly of silicon photonic bandgap. crystals*, Nature **414**, 289 (2001).

[101] Q. B. Meng, C. H. Fu, Y. Einaga, Z. Z. Gu, A. Fujishima, O. Sato, *Assembly of highly ordered three-dimensional porous structure with nanocrystalline TiO2 semiconductors*, Chem. Mater. **14**, 83 (2002).

[102] H. Miguez, V. Kitaev, G. A. Ozin, *Band spectroscopy of colloidal photonic crystal films*, Appl. Phys. Lett. **84**, 1239 (2004).

[103] J. F. Galisteo-López, C. López, *High-energy optical response of artificial opals*, Phys. Rev. B **70**, 035108 (2004).

[104] F. Garcia-Santamaria, J. F. Galisteo-López, P. V. Braun, C. Lopez, *Optical diffraction and high-energy features in three-dimensional photonic crystals*, Phys. Rev. B **71**, 195112 (2005).

[105] A. Blanco, H. Míguez, F. Meseguer, C. López, F. López-Tejeira, J. Sánchez-Dehesa, *Photonic band gap properties of a CdS-in-opal system*, Appl. Phys. Lett. **78**, 3181 (2001).

[106] J. F. Bertone, P. Jiang, K. S. Hwang, D. M. Mittleman, V. L. Colvin, *The Thickness Dependence of the Optical Properties of Ordered Silica-Air and Air-Polymer Photonic Crystals*, Phys. Rev. Letters, Phys. Rev. Lett. **83**, 300 (1999).

[107] J. F. Galisteo-López, E. Palacios-Lidón, E. Castillo-Martínez, C. López, *Optical study of the L gap in thickness and orientation controlled artificial opals*, Phys. Rev. B **68**, 115109 (2003).

[108] F. López-Tejeria, T. Ochiai, K. Sakoda, J. Sánchez-Dehesa, *Symmetry characterization of eigenstates in opal-based photonic crystals*, Phys. Rev. B **65**, 195110 (2002).

[109] E. P. Petrov, V. N. Bogomolov, I. I. Kalosha, S. V. Gaponenko, *Spontaneous Emission of Organic Molecules Embedded in a Photonic Crystal*, Phys. Rev. Lett. **81**, 77 (1998).

[110] M. Megens, J. E. G. J. Wijnhoven, A. Lagendijk, W. L. Vos, *Fluorescence lifetimes and linewidths of dye in photonic crystals*, Phys. Rev. A **59**, 4727 (1999).

[111] C. López, A. Blanco, H. Míguez, F. Meseguer, *Photonic crystals for laser action*, Opt. Mater. **13**, 187 (1999).

[112] A. Blanco, C. López, R. Mayoral, H. Míguez, F. Meseguer, A. Mifsud, J. Herrero, *Photonic crystal properties of packed submicrometric SiO_2 spheres*, Appl. Phys. Lett. **73**, 1781 (1998).

[113] Y. A. Vlasov, N. Yao, D. J. Norris, *Synthesis of Photonic Crystals for Optical Wavelengths from Semiconductor Quantum Dots*, Adv. Mater. **11**, 165 (1999).

[114] S. G. Romanov, D. N. Chigrin, C. M. Sotomayor Torres, N. Gaponik, A. Eychmüller, A. L. Rogach, *Emission stimulation in a directional band gap of a CdTe-loaded opal photonic crystal*, Phys. Rev. E **69**, 046606 (2004).

[115] L. Bechger, P. Lodahl, W. Vos, *Directional Fluorescence Spectra of Laser Dye in Opal and Inverse Opal Photonic Crystals*, J. Phys. Chem. B **109**, 9980 (2005).

[116] N. Gaponik, D. V. Talapin, A. L. Rogach, K. Hoppe, E. V. Shevchenko, A. Kornowski, A. Eychmüller, H. Weller, *Thiol-Capping of CdTe Nanocrystals: An Alternative to Organometallic Synthetic Routes*, J. Phys. Chem. B **106**, 7177 (2002).

[117] A. Shavel, Thesis, Hamburg, (2005).

[118] The filling fraction of a monolayer of close packed spheres is $f = 0.6$, so that the effective thickness of a monolayer of particles with $d = 4\ nm$ is $f \times d = 2.4\ nm$.

[119] M. Barth, A. Cruber, F. Cichos, *Spectral and angular redistribution of photoluminescence near a photonic stop band*, Phys. Rev. B **72**, 085129 (2005).

[120] C. R. Kagan, C. B. Murray, M. Nirmal, M. G. Bawendi, Electronic *Energy Transfer in CdSe Quantum Dot Solids*, Phys. Rev. Lett. **76**, 1517 (1996).

[121] N. Garcia, A. Z. Genack, *Observation of nonclassical optical diffusion*, Phys. Rev. Lett. **63**, 259 (1989)

[122] H. Cao, Y. G. Zhao, H. C. Ong, S. T. Ho, J. Y. Dai, J. Y. Wu, R. P. H. Chang, *Ultraviolet lasing in resonators formed by scattering in semiconductor polycrystalline films*, Appl. Phys. Lett. **73**, 3656 (1998).

[123] D. S. Wiersma, P. Bartolini, A. Lagendijk, R. Righini, *Localization of light in a disordered medium*, Nature, **390**, 671 (1997).

[124] J. Gomez Rivas, R. Sprik, L. D. Noordam, C. W. Rella, A. Lagendijk, *Midinfrared scattering and absorption in Ge powder close to the Anderson localization transition*, Phys. Rev. E, **62**, R4540 (2000).

[125] N. Garcia, A. Z. Genack, *Anomalous photon diffusion at the threshold of the Anderson localization transition*, Phys. Rev. Lett. **66**, 1850 (1991).

[126] X. H. Wu, A. Yamilov, H. Noh, H. Cao, E. W. Seelig, R. P. H. Chang, *Random lasing in closely packed resonant scatterers*, JOSA B, **21**, 159 (2004).

[127] R. H. J. Kop, P. de Vries, R. Sprik, A. Lagendijk, *Observation of Anomalous Transport of Strongly Multiple Scattered Light in Thin Disordered Slabs*, Phys. Rev. Lett. **79**, 4369, (1997).

[128] M. Reufer, L. F. Rojas-Ochoa, S. Eiden, J. J. Saenz, F. Scheffold, *Transport of light in amorphous photonic materials*, Appl. Phys. Rev. **91**, 171904 (2007).

[129] L. F. Rojas-Ochoa, J. M. Mendez-Alcaraz, J. J. Saenz, P. Schurtenberger, F. Scheffold, *Photonic Properties of Strongly Correlated Colloidal Liquids*, Phys. Rev. Lett. **93**, 073903 (2004).

[130] Y. Xia, B. Gates, Y. Yin, Y. Lu, *Monodispersed Colloidal Spheres: Old Materials with New Applications*, Adv. Matter. **12**, 693, (2000)

[131] B. V. Derjaguin, L. Landau, *The stability of colloid systems*, Acta Physicochim. URSS **14**, 633 (1941).

[132] E. J. W. Verwey, J. T. G. Overbeek, *Theory of the Stability of Lyophobic Colloids*, Elsevier, Amsterdam 1948.

[133] K. L. Wu, S. K. Lai, *Theoretical Studies of the Early Stage Coagulation Kinetics for a Charged Colloidal Dispersion*, Langmuir **21**, 3238 (2005).

[134] J. Israelachvili, *Intermolecular and Surface Forces*, Academic Press, London (1985).

[135] R. H. Ottewill, J. N. Shaw, *Stability of monodisperse polystyrene latex dispersions of various sizes*, Discussions Faraday Soc. **42**, 154, (1966).

[136] J. L. Baldwin, B. A. Dempsey, *Mean Free Path of Brownian Motion and Implications for Coagulation of Charged Nano-particles*, Colloids and Surfaces A: Physicochemical and Engineering Aspects **177**, 111 (2001).

[137] D. A. Weitz, *Packing in the Spheres*, Science **303**, 968 (2004).

[138] M. P. van Albada, A. Lagendijk, *Observation of Weak Localization of Light in a Random Medium*, Phys. Rev. Lett. **55**, 2692 (1985).

[139] P. E. Wolf, G. Maret, *Weak Localization and Coherent Backscattering of Photons in Disordered Media*, Phys. Rev. Lett. **55**, 2696 (1985).

[140] S. Fraden, G. Maret, *Multiple light scattering from concentrated, interacting suspensions*, Phys. Rev. Lett. **65**, 512 (1990).

[141] M. P. van Albada, J. F. de Boer, A. Lagendijk, *Observation of long-range intensity correlation in the transport of coherent light through a random medium*, Phys. Rev. Lett. **64**, 2787 (1990).

[142] P. Sebbah, B. Hu, A. Z. Genack, R. Pnini, B. Shapiro, *Spatial-Field Correlation: The Building Block of Mesoscopic Fluctuations*, Phys. Rev. Lett. **88**, 123901 (2002).

[143] F. Scheffold, G. Maret, *Universal Conductance Fluctuations of Light*, Phys. Rev. Lett. 81, 5800 (1998).

[144] G. Labeyrie, E. Vaujour, C. A. Muller, D. Delande, C. Miniatura, D. Wilkowski, R. Kaiser, *Slow Diffusion of Light in a Cold Atomic Cloud*, Phys. Rev. Lett. **91**, 223904 (2003).

[145] J. A. Curcio, C. C. Petty, *Near infrared absorption spectrum of liquid water*, J. Opt. Soc. Am. **41**, 302 (1951).

[146] M. Kaveh, M. Rosenbluh, I. Edrei, I. Freund, *Weak localization and light scattering from disordered solids*, Phys. Rev. Lett. **57**, 2049 (1986).

[147] D. S. Wiersma, M. P. van Albada, A. Lagendijk, *Coherent backscattering of light from amplifying random media*, Phys. Rev. Lett. **75**, 1739 (1995).

[148] C. M. Soukoulis, S. Datta, E. N. Economou, *Propagation of classical waves in random media*, Phys. Rev. B **49**, 3800 (1994).

[149] K. Busch, C. M. Soukoulis, *Transport properties of random media: An energy-density CPA approach*, Phys. Rev. B **54**, 893 (1996).

[150] M. Storzer, C. M. Aegerter, G. Maret, *Reduced transport velocity of multiply scattered light due to resonant scattering*, Phys. Rev. E **73**, 065602(R) (2006).

[151] S. C. Hill, R. E. Benner, *Morphology-dependent resonances*, in P. W. Barber, R.K. Chang (Eds.), *Optical Effects associated with small particles* World Scientific, Singapore (1988).

[152] G. H. Watson, P. A Fleury, S. L. McCall, *Searching for photon localization in the time domain*, Phys. Rev. Lett. **58**, 945 (1987).

[153] L. Tsang, J. A. Kong, K. H. Ding, C. O. Ao, *Scattering of electromagnetic waves: Numerical simulations* John Wiley and Sons, New York (2001).

[154] H. Cao, Y. Ling, J. Y. Xu, C. Q. Cao, *Photon statistics of random lasers with resonant feedback*, Phys. Rev. Lett. **86**, 4524 (2001).

[155] L. Florescu, S. John, *Photon statistics and coherence in light emission from a random laser*, Phys. Rev. Lett. **93**, 013602 (2004).

[156] C. M. Soukoulis, J. Xunya, J. Y. Xu, H. Cao, *Dynamic response and relaxation oscillations in random lasers*, Phys. Rev. B **65**, 041103 (2002).

[157] K. L. van der Molen, A. P. Mosk, A. Lagendijk, *Relaxation oscillation in long-pulsed random lasers*, arXiv:physics/0703045v1 (2007).

[158] V. M. Markushev, V. F. Zolin, C. M. Briskina, *Powder laser*, Zh. Prikl. Spektrosk, **45**, 847 (1986).

[159] M. Bahoura, K. J: Morris, M. A. Noginov, *Threshold and slope efficiency of* $Nd_{0.5}La_{0.5}Al_3(BO_3)_4$ *ceramic random laser: effect of the pumped spot size*, Opt. Comm. **201**, 405 (2002).

[160] S. Klein, O. Cregut, D. Gindre, A, Boeglin, K. D. Dorkenoo, *Random laser action in organic film during the photopolymerization process*, Opt. Express **3**, 5387 (2005).

[161] R. C. Polson, Z. V. Vardeny, *Random lasing in human tissues.* Appl. Phys. Lett. **85**, 1289 (2004).

[162] J. P. Jacopsen, J. B. Pedersen, D. E. Wemmer, *Site selective bis-intercalation of a homodimeric thiazole orange dye in DNA oligonucleotides*, Nucl. Acid Res. **23**, 753 (1995).

[163] Y. Kawabe, L. Wang, S. Horinochui, N. Ogata, *Amplified Spontaneous Emission from Fluorescent-Dye-Doped DNA-Surfactant Complex Films*, Adv. Mater. **12**, 1281 (2000).

[164] M. Ibisate *et al.* In preparation.

[165] J. Ripoll, C. M. Soukoulis, E. N. Economou, *Optimal tuning of lasing modes through collective particle resonance*, J. Opt. Soc. Am. B, **21**, 141 (2004).

[166] P. V. Braun, S. A. Pruzinsky, F. Garcia-Santamaria, *Introducing defects in 3D photonic crystals: State of the art*, Adv. Mater, **18**, 2665 (2006).

[167] C. Kittel. *Introduction to Solid State Physics*, John Willey and Sons, New York (1967).

[168] K. V. Shalimova, *Physics of Semiconductors*, Mir, Moscow (1975).

[169] P. Y. Yu, M. Cardona, *Fundamentals of Semiconductors* Springer-Verlag, Berlin Heidelberg (1996).

[170] K. P. Velikov, C. G. Christova, R. P. A. Dullens, A. van Blaaderen, *Layer-by-Layer Growth of Binary Colloidal Crystals*, Science, **296**, 106 (2002).

[171] V. Kitaev, G. Ozin, *Self-assemble surface patterns of binary colloidal crystals*, Avd. Mat. **15**, 75 (2003).

[172] D. Wang, H. Moehwald, *Rapid fabrication of binary colloidal crytals by stepwise spin-coating*, Avd. Mat. **16**, 244 (2004).

[173] E. Palacios-Lidon, B. H. Juárez, E. Castillo-Martinez, C. Lopez, *Optical and Morphological Study of Disorder in Opals*, J. Appl. Phys. **97**, 063502 (2005).

[174] M. Born, E. Wolf, *Principles of Optics*, Pergamon Press (1986).

[175] M. Stoerzer, P. Gross, C. M. Aegerter, G. Maret, *Observation of the Critical Regime Near Anderson Localization of Light*, Phys. Rev. Lett. **96**, 063904 (2006).

[176] A. A. Chabanov, M. Stoytchev, A. Z. Genack, *Statistical signatures of photon localization*, Nature **404**, 850 (2000).

[177] T. Schwartz, G. Bartal, S. Fishman, M. Segev, *Transport and Anderson localization in disordered two-dimensional photonic lattices*, Nature **446**, 52, (2007).

[178] A. F. Koenderink, M. Megens, G. van Soest, W. L. Vos, Ad Lagendijk, *Enhanced backscattering from photonic crystals*, Physics Letters A **268**, 104 (2000).

[179] J. Huang, N. Eradat, M. E. Raikh, Z. V. Vardeny, A. A. Zakhidov, R. H. Baughman, *Anomalous Coherent Backscattering of Light from Opal Photonic Crystals*, Phys. Rev. Lett. **86**, 4815 (2001).

[180] Y. A. Vlasov, M. A. Kaliteevski, V. V. Nikolaev, *Different regimes of light localization in a disordered photonic crystal*, Phys. Rev. B **60**, 1555 (1999).

[181] L.D. Landau, E.M. Lifshitz, *Course of Theoretical Physics, Electrodynamics of Continuous Media*, vol. **8**, Pergamon, New York (1984).

[182] A. F. Koenderink, Ad Lagendijk, Willem L. Vos, *Optical extinction due to intrinsic structural variations of photonic crystals*, Phys. Rev. B **72**, 153102 (2005).

[183] K. Busch, S. John, *Photonic band gap formation in certain self-organizing systems*, Phys. Rev. E **58**, 3896 (1998).

[184] R. Sapienza, P. Costantino, D. S. Wiersma, M. Ghulinyan, C.J. Oton, L. Pavesi, *Optical Analogue of Electronic Bloch Oscillations*, Phys. Rev. Lett. **91**, 263902 (2003).

[185] R. W. Boyd, *Nonlinear Optics*, Academic Press, London (1992).

[186] C. Toninelli, E. Vekris, G. A. Ozin, S. John, D. S. Wiersma, *Exceptional Reduction of the Diffusion Constant in Partially Disordered Photonic Crystals*, Phys. Rev. Lett. **101**, 123901 (2008).

[187] K. L. van der Molen, P. Zijlstra, A. Lagendijk, A. P. Mosk, *Laser threshold of Mie resonances*, Opt. Lett. **31**, 1432 (2006).

[188] J. Ripoll, C. M. Soukoulis, E. N. Economou, *Optimal tuning of lasing modes through collective particle resonance*, J. Opt. Soc. Am. B **21**, 0740 (2004).

[189] L. K. Teha, C. C. Wong, H. Y. Yang, S. P. Lau, S. F. Yu, *Lasing in electrodeposited ZnO inverse opal*, Appl. Phys. Lett. **91**, 161116 (2007).

[190] X. Wu, A. Yamilov, X. Liu, S. Li, V. P. Dravid, R. P. H. Chang, H. Cao, *Ultraviolet photonic crystal laser*, Appl. Phys. Lett. **85**, 3657 (2004).

[191] E. Akkermans, P. E. Wolf, R. Maynard, *Coherent backscattering of light by disordered media: analysis of the peak line shape*, Phys. Rev. Lett. **56**, 1471 (1986).

Conclusiones generales

- Se han obtenido ópalos inversos de ZnO mediante deposición en fase vapor de ópalos directos constituidos por microesferas poliméricas. Se han estudiado las propiedades ópticas del sistema directo, el compuesto y el inverso. Por último se ha medido la fotoluminiscencia de la estructura final. Se ha realizado un estudio de la misma en función de la estructura cristalina mediante procesos de recocimiento de temperatura variable.

- Se ha utilizado el método de infiltración de ZnO en ópalos directos como medio para investigar diferentes zonas cristalográficas de las muestras. En particular se han estudiado las direcciones cristalográficas (111) y (100) que corresponden con las direcciones ΓL y ΓX del espacio recíproco.

- Se ha realizado un estudio óptico de reflectancia y transmitancia de ópalos inversos de ZnO en la zona de alta energía ($a/\lambda > 1$). Se han relacionado los resultados experimentales con la estructura de bandas fotónicas del sistema. Se ha observado y controlado la aparición de intervalos de energía prohibida en la zona de alta energía.

- Se ha realizado la infiltración física de puntos cuánticos de CdTe en ópalos inversos de ZnO. Se ha observado que dicha infiltración puede monitorizarse ópticamente, controlando de esta forma la cantidad aproximada de nanoparticulas en la estructura. Se ha estudiado el efecto que la estructura fotónica ejerce sobre la fotoluminiscencia de las nanoparticulas.

- Se ha crecido una estructura desordenada formada por esferas iguales en tamaño y forma. Se ha llamado vidrio fotónico. Se ha estudiado la propagación de luz difusa a través de dicho sistema, constatándose el comportamiento resonante tanto en el camino libre medio de transporte como en la constante de difusión. Se ha hecho uso de dicha propiedad para ejercer control sobre la emisión de laser aleatorio.

- Se han introducido intencionadamente vacantes en un ópalo polimérico. Se ha estudiado el efecto que estos defectos extrínsecos tienen en la propagación de la luz, en particular sobre el camino libre medio y la constante de difusión. Se ha realizado una ulterior infiltración de dichos sistemas con ZnO. Se ha observado emisión laser en el caso del sistema sin dopaje que corresponde a una baja velocidad de grupo y que es efecto debido enteramente a la estructura fotónica del sistema. Por otro lado, se ha observado emisión

laser aleatoria en el caso del sistema fuertemente dopado observándose una transición de uno a otro tipo de emisón laser a través del dopaje de las muestras.

Agradecimientos

Esta es, para mucha gente y para mí mismo, la parte más importante de todo lo que he escrito hasta ahora. Siempre he dicho que yo quería hacer una tesis para agradecérsela a alguien. Y no es del todo una broma. Todo lo que hacemos, lo que pensamos, lo que vivimos lo hacemos por y para el *otr@* y, como ya pensaban los griegos, lo importante es la travesía, porque no hay ningún puerto final al que llegar.

En primer lugar quiero agradecer a mi director de tesis, Cefe López, su apoyo y su confianza puesta en mí durante estos años. Gracias a él, esta ha sido una experiencia vital y profesional de primera magnitud. Es mérito suyo el haber creado un grupo de trabajo formado por personas de gran profesionalidad y humanidad, un caldo de cultivo en el que hacer un buen trabajo es algo casi trivial y, por supuesto, un placer. Gracias también a mi tutor en la Universidad Autónoma de Madrid, profesor José Manuel Calleja por su ayuda. Agradezco del mismo modo al Ministerio de Educación y Ciencia del gobierno de España por prestarme su ayuda económica para realizar este trabajo así como al patronato de huérfanos del ejército del Aire su cuya ayuda económica para que yo pudiera estudiar Física en Madrid.

También quiero destacar mi agradecimiento a Riccardo Sapienza. Él ha sido para mi un gran estímulo; me ha enseñado y me ha contagiado su emoción y su entusiasmo incomparables, grazie davvero. Mi agradecimiento a Álvaro Blanco, por sus chistes malísimos, sus buenísimos consejos y su gran cercanía; a Juan Galisteo y Bea Juárez, que tanta ayuda me proporcionaron cuando empecé, dentro y fuera del laboratorio y tan buenos momentos me dieron cuando escribían sus tesis; ahora comprendo que no tenía ni p. gracia. A Martín con el que he recorrido gran parte de este tiempo con mucha complicidad, profesional y personal, a Marta Ibisate, Paco Gallego, Luis Froufe, Lola Golmayo y Ainhoa Altube que, como ya he dicho, forman un grupo de una gran profesionalidad y humanidad. Quiero agradecer también a Marisa, a Ana, a Eva, a toda la gente de teatro y del instituto que han hecho todo tan fácil y divertido, gracias a todos. También quiero acordarme de Sarah Núñez por su complicidad en todo este camino. A ver si, con el tiempo, recordamos todo lo que sentimos durante estos años de precariedad.

I also want to remember and thank the people from Florence during my stay there. Als eerste zou ik Diederik Wiersma willen bedanken to give me the opportunity to join his group. A tutti i ragazzi del *group meeting* Pierre, Jacopo, Stefano, Ribo e Francesca. Tutti hanno fatto il mio tempo a Firenze facile e

divertente...come la lingua italiana. Grazie a tutti, davvero. Spezialmente voglio riccordare Costanza e Silvia que hanno stato e ci sonno due care amiche.

En el plano laboral, me gustaría agradecer a R. Serna, por su ayuda con las medidas de elipsometría. También a J. Benito Rodríguez por su ayuda con la espectroscopía de barrido y a Isabel Pastoriza, por su ayuda con las medidas de movilidad, ambos pertenecen al grupo de Luis Liz con el que formamos parte de una unidad asociada. Quiero agradecer también al profesor Luis Viña y a M. Dolores Martín por su colaboración y ayuda en las medidas de constante de difusión de los vidrios fotónicos.

Por último quiero agradecer de forma más personal a mi familia y amigos. Esta tesis está dedicada a la memoria de mi padre, que falleció cuando era estudiante de físicas. También a mí madre, cuya fortaleza y vitalidad siempre me ha parecido admirable y sobrehumana. Es la fuerza de la vida la que habla a través de ella. Al resto de mi familia, a mi hermano Marci, a Asun, a mi tio Marcial y a mi abuela María por su apoyo y su cariño. Finalmente, gracias a todos mis amigos: Ana, Loreto, Marta, Juanmi, Reyes, Maripandi, Dj Lou, Angela, Borja, Toni@Andrés, Paloma, María Broccone (la española, como ninguna) que han sido y son para mi una aunténtica segunda familia. Y por último quiero agradecer a Fidel (que vino, vio y venció) por su apoyo y su ayuda. Gracias.